frontiers | Research Topics

Women in carbon science and technology

Edited by
Irma Kuljanishvili, Aruna Ivaturi, Glaura Silva, Maria F. Pantano, Marinella Striccoli and Gabriela Borin Barin

Published in
Frontiers in Carbon

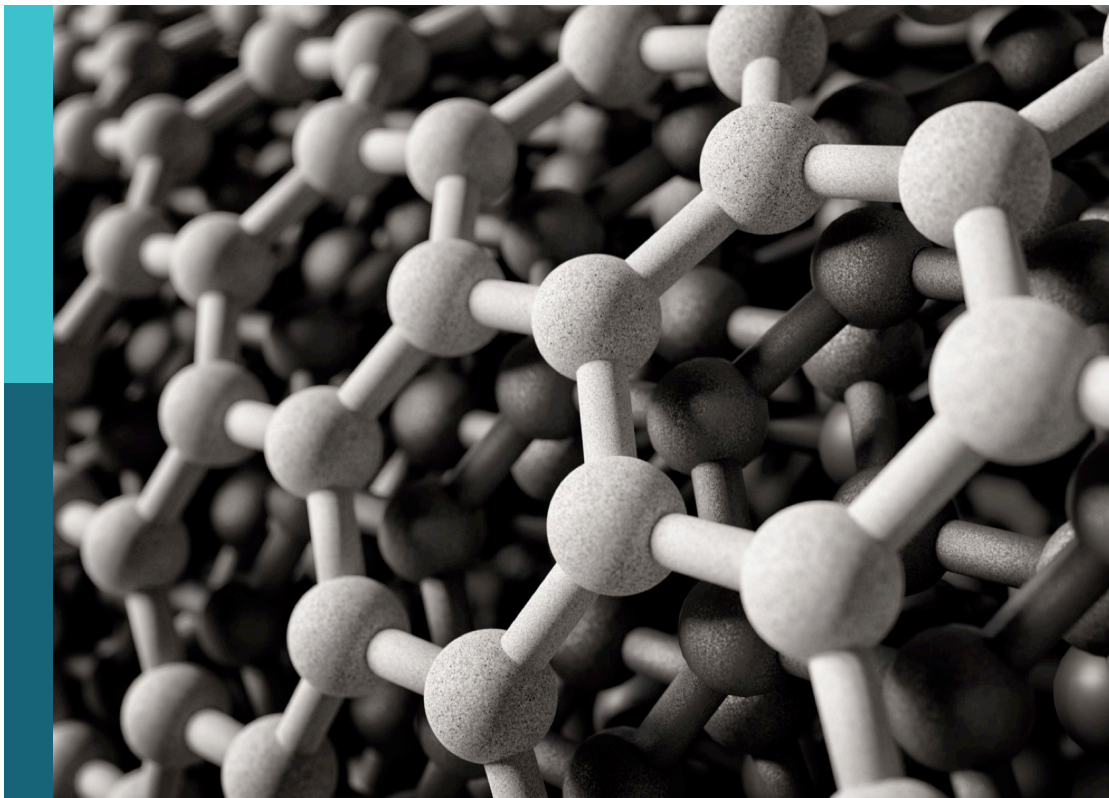

ISSN 1664-8714
ISBN 978-2-8325-5858-4
DOI 10.3389/978-2-8325-5858-4

About Frontiers

Frontiers is more than just an open access publisher of scholarly articles: it is a pioneering approach to the world of academia, radically improving the way scholarly research is managed. The grand vision of Frontiers is a world where all people have an equal opportunity to seek, share and generate knowledge. Frontiers provides immediate and permanent online open access to all its publications, but this alone is not enough to realize our grand goals.

Frontiers journal series

The Frontiers journal series is a multi-tier and interdisciplinary set of open-access, online journals, promising a paradigm shift from the current review, selection and dissemination processes in academic publishing. All Frontiers journals are driven by researchers for researchers; therefore, they constitute a service to the scholarly community. At the same time, the *Frontiers journal series* operates on a revolutionary invention, the tiered publishing system, initially addressing specific communities of scholars, and gradually climbing up to broader public understanding, thus serving the interests of the lay society, too.

Dedication to quality

Each Frontiers article is a landmark of the highest quality, thanks to genuinely collaborative interactions between authors and review editors, who include some of the world's best academicians. Research must be certified by peers before entering a stream of knowledge that may eventually reach the public - and shape society; therefore, Frontiers only applies the most rigorous and unbiased reviews. Frontiers revolutionizes research publishing by freely delivering the most outstanding research, evaluated with no bias from both the academic and social point of view. By applying the most advanced information technologies, Frontiers is catapulting scholarly publishing into a new generation.

What are Frontiers Research Topics?

Frontiers Research Topics are very popular trademarks of the *Frontiers journals series*: they are collections of at least ten articles, all centered on a particular subject. With their unique mix of varied contributions from Original Research to Review Articles, Frontiers Research Topics unify the most influential researchers, the latest key findings and historical advances in a hot research area.

Find out more on how to host your own Frontiers Research Topic or contribute to one as an author by contacting the Frontiers editorial office: frontiersin.org/about/contact

Women in carbon science and technology

Topic editors

Irma Kuljanishvili — Saint Louis University, United States
Aruna Ivaturi — University of Strathclyde, United Kingdom
Glaura Silva — Federal University of Minas Gerais, Brazil
Maria F. Pantano — University of Trento, Italy
Marinella Striccoli — Consiglio Nazionale delle Ricerche - CNR, Italy
Gabriela Borin Barin — Swiss Federal Laboratories for Materials Science and Technology, Switzerland

Citation

Kuljanishvili, I., Ivaturi, A., Silva, G., Pantano, M. F., Striccoli, M., Borin Barin, G., eds. (2025). *Women in carbon science and technology*. Lausanne: Frontiers Media SA. doi: 10.3389/978-2-8325-5858-4

Table of contents

frontiers | Frontiers in Carbon

TYPE Editorial
PUBLISHED 17 December 2024
DOI 10.3389/frcrb.2024.1521817

OPEN ACCESS

EDITED AND REVIEWED BY
Anirudha Sumant,
Argonne National Laboratory (DOE),
United States

*CORRESPONDENCE
Irma Kuljanishvili,
irma.kuljanishvili@slu.edu
Maria F. Pantano,
maria.pantano@unitn.it

RECEIVED 02 November 2024
ACCEPTED 18 November 2024
PUBLISHED 17 December 2024

CITATION
Kuljanishvili I, Pantano MF, Borin Barin G, Striccoli M, Goulart Silva G and Ivaturi A (2024) Editorial: Women in Carbon Science and Technology-"The Many Shades of Carbon". *Front. Carbon* 3:1521817. doi: 10.3389/frcrb.2024.1521817

Editorial: Women in Carbon Science and Technology-"The Many Shades of Carbon"

Irma Kuljanishvili[1]*, Maria F. Pantano[2]*, Gabriela Borin Barin[3], Marinella Striccoli[4], Glaura Goulart Silva[5] and Aruna Ivaturi[6]

[1]Department of Physics, Saint Louis University, St. Louis, MO, United States, [2]Department of Civil, Environmental and Mechanical Engineering, University of Trento, Trento, Italy, [3]Department of Advanced Materials and Surfaces, Empa, Swiss Federal Laboratories for Materials Science and Technology, Dübendorf, Switzerland, [4]CNR-IPCF Institute for Physical and Chemical Processes, Bari, Italy, [5]Technology Center in Nanomaterials and Graphene (CTNano/UFMG), Belo Horizonte, Brazil, [6]Department of Pure and Applied Chemistry, University of Strathclyde, Glasgow, United Kingdom

KEYWORDS

carbon based applications, carbon dots, carbon based composites, carbon nanotubes, graphene oxide

Editorial on the Research Topic
Women in carbon science and technology

This Research Topic features work presented by women principal and lead authors, established and internationally recognized in the field of carbon science and technology, as well as early career investigators, and captures the spirit of collaboration and interdisciplinary nature of carbon-related research.

The advent of carbon nanomaterials in their diverse dimensionalities, from carbon dots and fullerenes to single- or multi-walled carbon nanotubes (SWCNTs or MWCNTs), graphene (single or few-layered) and graphene derivatives (graphene oxide, graphyne, or graphane), has introduced a myriad of new opportunities for both fundamental and applied scientific research and sparked industrial applications (De Volder et al., 2013). Indeed, carbon nanotubes and graphene possess a unique set of impressive mechanical, optical, electrical, and thermal properties (Geim and Novoselov, 2007), which make them ideal building blocks for the next-generation of technologies. At the same time, the recent discovery of intensely fluorescent and eco-friendly carbon nanoparticles in the visible range offers numerous applications in sensing, bio-imaging, energy conversion, electronics, and nanomedicine (Liu et al., 2020).

Because carbon is one of the most versatile materials, it can be processed from a variety of sources, both naturally and synthetically, and added to other materials, heterostructures, and matrices to fabricate novel carbon-based composites with enhanced and/or tailored properties.

This Research Topic of articles presents several original works as well as a review article, which describe and address challenges associated with carbon nanomaterials, in the ways they are synthesized or processed, as well as their uses in a wide range of applications, from flexible sensors to biomedical devices to sustainable water treatments, just to name a few. With reference to this latter application field, by carbon nanotubes/nanofibers were synthesized on an ultrabasic rock, such as serpentinite, to obtain a composite material for removing organic pollutants, such as sulfentrazone, from water (Diogo et al.). Also, other forms of carbon materials were shown to be an effective water treatment remedy, and the mechanisms by which multidimensional graphene nanostructures adsorb a common contaminant like paracetamol were elucidated (Matos et al.).

One main trust related to graphene applications is its efficient dispersion in solutions; this is often addressed by the use of graphene derivatives, such as graphene oxide (GO), which offers an exciting opportunity to be efficiently mixed with other materials, such as polymers, due to the presence of several functional groups. To this end, GO was shown to be incorporated into PEDOT:PSS and PEDOT for the production of conductive inks, later used as active layers in flexible methanol sensor devices (Neves et al.). New fabrication processes involving GO reinforced polymers, for example, ultrahigh molecular weight polyethylene (UHMWPE), were shown to be scalable and, therefore, compatible with industrial settings (Amurin et al.).

In general, to tune the properties of carbon nanomaterials, including their ability to be successfully interfaced with other materials, their chemical structure has to be modified by proper functionalization strategies, which can be investigated through theoretical and experimental approaches. For example, the theoretical investigation of the electronic properties, such as the band structure and the spatial distributions of the electronic states in quantum corrals resulting from fractal architectures of carbon atoms, can guide the synthesis of novel fractal nanostructures, highlighting new functionalization possibilities (Late and Latgé). Additionally, the structure of GO contains oxygenated functional groups that can act as anchor points for various species, such as biomolecules or medicines, through different synthetic approaches, as reported by Gonçalves et al.. In general, the biomedical and medical fields can significantly benefit from the applications of carbon nanomaterials, because of their intrinsic biocompatibility. For example, carbon dots can be directly incorporated into polyvinyl alcohol (PVA) to produce fluorescent films for wearable bio-chemical sensors or therapeutic remedies (Silva et al.). They could serve as both colorimetric pH sensors to monitor pH changes characterizing wound healing processes or as antioxidants in the wound treatment for developing bioactive dressings. On the other hand, understanding the potential toxicity of carbon nanomaterials, heterostructures, and other derivatives, is an area of intense investigation because they are, often, interfaced with human body and biological samples. In this respect, researchers investigated the behavior of normal and cancer affected cells, their viability and spreading on the bed of SWCNTs and heterostructures of SWCNTs and ZnO nanowires (Luc et al.). While both materials were biocompatible, the concentration of released Zn^{+} ions indicated to play a critical role. In a different study, the biodistribution of polyethylene glycol-functionalized SWCNTs was analyzed after intravenous delivery to assess their capability to cross biological membranes and reach specific rat brain sites, such as brain cortex parenchyma, without acute toxic effects (Bruch et al.).

In this Research Topic, the diversity of carbon nanomaterials and their wide-ranging applications reflect the dynamic nature of the field. The innovative research presented here not only advances fundamental science but also opens new avenues for technological and biomedical applications. We hope this body of work continues to inspire collaboration and progress in carbon-based research and technology.

This Research Topic is dedicated to Professor Mildred Dresselhaus (1930–2017), whose lifelong commitment to science and technology, pioneering work in the field of carbon research, and inspiring mentorship and support of women in science have earned her a loving attribute of "Queen of Carbon" (Chung, 2017).

Author contributions

IK: Writing–original draft, Writing–review and editing. MFP: Writing–original draft, Writing–review and editing. GB: Writing–review and editing. MS: Writing–review and editing. GG: Writing–review and editing. AI: Writing–review and editing.

Funding

The author(s) declare that no financial support was received for the research, authorship, and/or publication of this article.

Conflict of interest

The authors declare that the research was conducted in the absence of any commercial or financial relationships that could be construed as a potential conflict of interest.

The author(s) declared that they were an editorial board member of Frontiers, at the time of submission. This had no impact on the peer review process and the final decision.

Generative AI statement

The author(s) declare that no Generative AI was used in the creation of this manuscript.

Publisher's note

References

Chung, D. D. L. (2017). Mildred S. Dresselhaus (1930–2017). *Nature* 543, 316. doi:10.1038/543316a

De Volder, M. F. L., Tawfick, S. H., Baughman, R. H., and Hart, A. J. (2013). Carbon nanotubes: present and future commercial applications. *Science* 339 (6119), 535–539. doi:10.1126/science.1222453

Geim, A. K., and Novoselov, K. S. (2007). The rise of graphene. *Nat. Mater.* 6, 183–191. doi:10.1038/nmat1849

Liu, J., Li, R., and Yang, B. (2020). Carbon dots: a new type of carbon-based nanomaterial with wide applications. *ACS Cent. Sci.* 6 (12), 2179–2195. doi:10.1021/acscentsci.0c01306

frontiers | Frontiers in Carbon

TYPE Original Research
PUBLISHED 02 November 2023
DOI 10.3389/frcrb.2023.1291283

OPEN ACCESS

EDITED BY
Duncan John Mowbray,
Yachay Tech University, Ecuador

REVIEWED BY
Julio Cesar Chacón Torres,
Yachay Tech University, Ecuador
Camilo Zamora-Ledezma,
Catholic University San Antonio of Murcia, Spain

*CORRESPONDENCE
Glaura Goulart Silva,
glaurag@ufmg.br

RECEIVED 08 September 2023
ACCEPTED 17 October 2023
PUBLISHED 02 November 2023

CITATION
Amurin LG, Oliveira PND, Pereira AFTS, Ribeiro NC, Rezende DBD and Silva GG (2023), Ultrahigh molecular weight polyethylene-reduced graphene oxide composite scaling up to produce wear resistant plates.
Front. Carbon 2:1291283.
doi: 10.3389/frcrb.2023.1291283

Ultrahigh molecular weight polyethylene-reduced graphene oxide composite scaling up to produce wear resistant plates

Leice Gonçalves Amurin[1], Poliane Neves De Oliveira[1,2], Ana Flávia Tavares S. Pereira[1,2], Nirvana Cecília Ribeiro[1,3], Daniel Bastos De Rezende[1,2] and Glaura Goulart Silva[1,2]*

[1]Technology Center in Nanomaterials and Graphene (CTNano/UFMG), Belo Horizonte, Brazil, [2]Federal University of Minas Gerais (UFMG), Belo Horizonte, Brazil, [3]Federal Center for Technological Education of Minas Gerais (CEFET-MG), Belo Horizonte, Brazil

Maintaining the properties of nanocomposites obtained at the laboratory scale when evolving to pilot and industrial scales is a great challenge. In this work, the route for a 3000-fold increase in scale between the laboratory and production in an industrial environment was conducted in two stages—Pilot 1 and Pilot 2—to obtain polymeric nanocomposite plates for pilot testing. The nanocomposite was based on ultrahigh molecular weight polyethylene (UHMWPE) and reduced graphene oxide (rGO), and several different operations were optimized for complete scale-up, i.e., 1) production of reduced graphite oxide (rGrO); 2) exfoliation of rGrO; 3) milling of rGO with UHMWPE in a ball mill to produce masterbatch; and 4) RAM extrusion to produce the plates. All these steps were accompanied by characterizations that show the quality of the nanomaterial, masterbatch and nanocomposite plates. The gains in nanocomposite properties with 0.25 wt% rGO with respect to UHMWPE were ~45% in elastic modulus, ~50% in hardness, ~25% in impact strength and 15% in abrasion wear (two-body test). The nanocomposite surfaces after wear tests are more hydrophobic than UHWWPE. The Pilot 1 results were generally superior to the Pilot 2 results, probably due to the very different thicknesses of the plates, i.e., 10 mm in Pilot 1 and 40 mm in Pilot 2. The improvement in different properties confirms the multifunctionality of the nanocomposite UHMWPE/rGO now produced on a pilot scale.

KEYWORDS

nanocomposite, reduced graphene oxide, ultrahigh molecular weight polyethylene, wear resistance, scale up

1 Introduction

The masterbatch process has broad application because of its ability to easily produce composites in the plastic industry with convenience and minimal air pollution (Li et al., 2007). Color, flame-retardant, reinforcing, conducting and so forth masterbatches have been widely applied with conventional and advanced additives (Herrera-Ramírez et al., 2017). Reis *et al.* (dos Reis et al., 2023) showed an efficient methodology for obtaining polymer nanocomposites containing carbon nanomaterials from the dilution of a masterbatch.

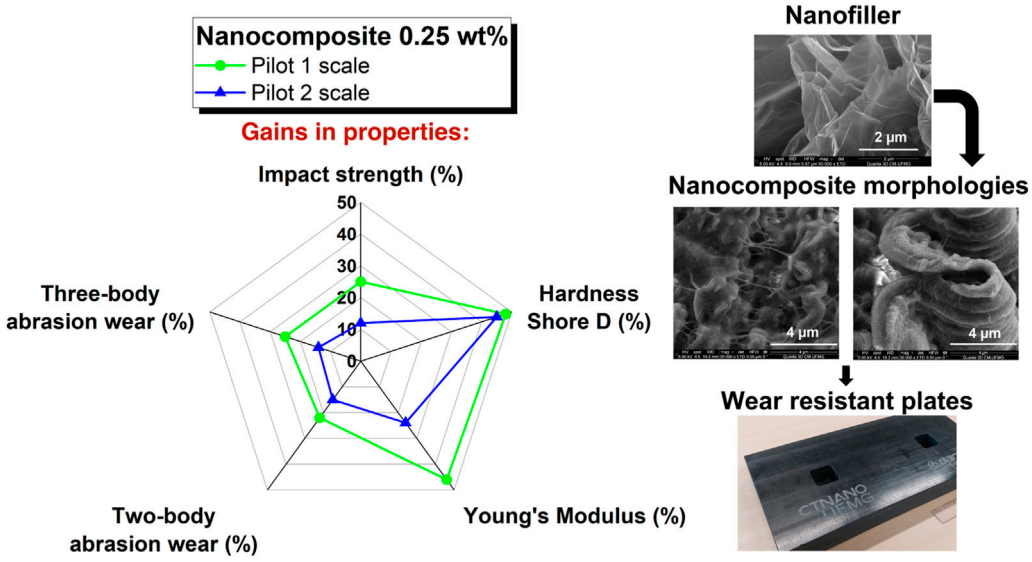

GRAPHICAL ABSTRACT

Polymeric nanocomposites have been proposed to solve the usual trade-off between stiffness and toughness occurring with the addition of conventional fillers (Zhang et al., 2022; Greenfeld and Wagner, 2015). Among the most explored nanofillers are carbon nanomaterials (Spitalsky et al., 2010; Potts et al., 2011), and graphene has been applied when wettability and tribological properties are the main goals (Friedrich, 2018; Gao et al., 2022).

Graphene oxide (GO) and reduced graphene oxide (rGO) have been proposed as important candidates in the large commercial interest in graphene products (Park et al., 2017). GO can be considered functionalized graphene with a distribution of epoxy, ether, aldehyde, ketone, alcohol, and carboxylic acid groups (Dreyer et al., 2010). rGO can have different degrees of oxygen functionalities removed, thus showing behavior similar to that of GO or pristine graphene in some cases. The quality of the dispersion of GO or rGO is one of the critical parameters to harness the exceptional properties of these nanofillers in polymeric composites (Johnson et al., 2015).

Ultrahigh molecular weight polyethylene (UHMWPE) is an engineering thermoplastic applied in bearings, valves and linings for mining, steel and food industries, and biomedical materials (Visco et al., 2016; Li et al., 2018). The mechanical and tribological properties of UHMWPE-rGO composites were investigated recently by our group (Amurin et al., 2022; Soares et al., 2022). Significant increases in wear resistance in the abrasion and sliding modes were observed with the addition of a maximum of 0.50 wt% rGO. Moreover, the hardness and stiffness also improved in these nanocomposites. These results were obtained on a laboratory scale involving the test of approximately 0.5 kg of nanocomposite. The challenge posed after the initial results was to demonstrate the scalability of the nanocomposite production with reproducibility of the properties obtained in the laboratory.

The work facing this challenge is reported herein, and it was designed in two steps: 1) **Pilot 1** was proposed to increase the production of nanocomposite to 90 kg and involved the preparation of a masterbatch with 3 wt% of rGO and the process of RAM extrusion to produce composite plates with 10 mm thickness by dilution of the masterbatch. This process was quite different from the laboratory scale (Amurin et al., 2022), where the molded composite plates were obtained by compression molding in the final concentrations for the study (0.10, 0.25, and 0.50 wt%). Therefore, the complete characterization of the samples was repeated in Pilot 1 for nanocomposites at 0.10 and 0.25 wt% rGO obtained from the masterbatch with 3 wt% dilution. The 0.50 wt% nanocomposite did not advance for the Pilot 1 study because the laboratory characterization already ruled out this composition due to a decrease in properties, probably associated with an increase in the aggregation of rGO (Amurin et al., 2022). Thereafter, 2) **Pilot 2** was pursued with the production of the masterbatch to allow the processing of 1,500 kg of the nanocomposite at 0.25 wt% of rGO. In this stage, an important difference was also applied: the plates had a larger thickness, 40 mm, four times the value of Pilot 1. Characterizations were also undertaken in the plates produced, and the results indicated that the main requirements of wear resistance and mechanical properties were achieved after the complete scale-up study that increased the amount of nanocomposite produced at the laboratory scale by 3.000x. Shirvanimoghaddam *et al.* (Shirvan et al., 2023) described the challenges in obtaining multifunctional polyethylene nanocomposites with a low content of nanofiller and how research seeks to develop scale-up processes to avoid cluster formation, which can promote negative effects on nanocomposite performance.

Therefore, this work reports a process that includes 1) production of reduced graphite oxide (rGrO); 2) exfoliation of rGrO in the liquid phase to obtain the nanofiller rGO and introduction of UHMWPE in the liquid phase; 3) milling of rGO with UHMWPE in a ball mill to produce masterbatch; and 4) RAM extrusion to produce the plates in two different stages, Pilot 1 and Pilot 2. All these steps were accompanied by characterizations that show the quality of the nanomaterial, masterbatch and nanocomposite plates.

2 Experimental part

2.1 Materials

Ultrahigh molecular weight polyethylene (UHMWPE - GUR 4152 - Celanese) has specific characteristics of a high-performance semicrystalline polymer, such as an average molar mass greater than 7.6 x 10^6 g mol^{-1}, a density of 0.930 g cm^{-3}, an intrinsic viscosity of 28 dL g^{-1} and a particle size of the polymeric powder of approximately 180 μm (Celanese, 2022). The thermogravimetric analysis curve (Supplementary Figure S1A), differential scanning calorimetry (Supplementary Figure S1B) and FTIR spectra (Supplementary Figure S1C) of the UHMWPE are reported in the Supplementary Material.

Graphite powder (Gr) (Grafine 72,140–Nacional de Grafite) is a fine crystalline powder that has a carbon content ≥72%, moisture ≤0.3%, a guaranteed ash limit corresponding to ≤28%, an apparent density equal to 0.38 g cm^{-3} and a surface area corresponding to 5.3 m^2 g^{-1} (de Grafite, 2023).

2.2 Synthesis and exfoliation of the filler

Graphite oxide (GrO) was synthesized from graphite according to the modified Hummers method (Hummers and Offeman, 1958) and then thermally reduced and expanded via a rotary furnace in a semicontinuous process, in which reduced and expanded graphite oxide (rGrO) was obtained (dos Reis et al., 2020). The rGrO had a granulometry limited to less than 600 μm to control reproducibility and quality of the filler, defined from the granulometric classification via dry sieving with mesh openings of 600 μm, 300 μm, 90 μm, 75 μm, and 45 μm (Pavitest–Contenco).

The filler rGrO was preexfoliated in a liquid medium (ethanol) via mechanical agitation in a high shear mixer for 30 min at a rotation speed of 4,500 rpm in a suspension with a concentration of 5 g L^{-1} and a volume of 1,200 mL for Pilot 1 and 2,400 mL for Pilot 2. Then, the preexfoliated filler was simultaneously subjected to exfoliation in an ultrasonic bath at 60 C and mechanical agitation (300 rpm) for 2 h, resulting in reduced graphene oxide (rGO).

2.3 Nanocomposite preparation

The production of the polymeric nanocomposite was divided into two stages: i) homogenization of solids and ii) conformation by RAM extrusion, as shown in Figure 1.

i. A mass of polymeric powder (388 g for Pilot 1 and 436.5 g for Pilot 2) was added to the suspension of the rGO in ethanol and was kept under agitation in an ultrasonic bath and mechanical mixing simultaneously at 60 °C for 1 h. The suspension was heated in an oven at 70 °C for 8 h to remove the solvent. The solid material was homogenized via a solid mixture in a ball mill (Servitech) with a rotation speed of 80 rpm for 8 h. Thus, a masterbatch of UHMWPE-rGO was obtained at a nanofiller concentration of 3 wt%. Ten kilograms and 150 kg of masterbatch were produced for the Pilot 1 and Pilot 2 stages, respectively.

ii. The production of the UHMWPE-rGO nanocomposites was conducted with the dilution of the masterbatch to concentrations of 0.10 wt% (Pilot 1) and 0.25 wt% (Pilot 1 and Pilot 2) in a paddle mixer (Baron) in 30 kg batches with a mixing time of 40 min. The plates were shaped via RAM extrusion (Baron) in an industrial environment on a pilot scale. For Pilot 1, 30 kg of nanocomposite containing 0.10 wt% rGO and 90 kg of nanocomposite containing 0.25 wt% nanofiller were produced. For Pilot 2, 1,500 kg of nanocomposite containing 0.25 wt% rGO was produced. The extrusion process consists of accommodating the nanoadditivated polymeric powder in silos (mixed with a specific lubricant for this extrusion process), which it directs to a cavity at the beginning of the extruder die for sintering. Then, the piston maintains a constant pressure until the polymer melts under a controlled temperature (150 °C). The piston hydraulic system keeps the mass under a constant working pressure close to 42 bar for 80 s. After this cycle, the piston returns to fill the initial cavity of the extruder die. The material remains in the extruder die for 150 min with controlled cooling, resulting in plates with a thickness of 10 mm and a width of 1.25 m being formed for Pilot 1. In the case of the plates produced in Pilot 2, the thickness was 40 mm, and the width was 1.25 m. The same extrusion process was performed for the neat UHMWPE to produce samples without the nanoadditive. The quantity of masterbatches and the rGO contents for Pilot 1 and Pilot 2 are summarized in Table 1.

2.4 Characterization techniques

Fourier transform infrared spectroscopy–FTIR was performed with a Frontier spectrophotometer (Perkin Elmer) in ATR (Total Attenuated Reflection) mode, scanned from 650 to 4,000 cm^{-1}, resolution of 4 cm^{-1}, with 64 total scans and force of 115 N. Raman spectroscopy was carried out in a spectrometer with a confocal microscope (Witec Alpha 300R), and a 457 nm (1 mV) laser energy was used. Raman spectroscopy measurements were carried out for 23 aliquots collected during the carbon nanomaterial dispersion process. For each sample collected, analyses were carried out at 5 different points. Some Raman spectra are shown in Supplementary Figure S1.

Thermogravimetric analysis (TG) was carried out in TA Instruments equipment with a heating rate of 10 °C min^{-1} and a temperature range of 25°C–700 °C in a platinum crucible and synthetic air environment. Differential scanning calorimetry (DSC) was performed using TA instrument equipment under a helium atmosphere at a flow rate of 100 mL $min^{-1,}$ a mass of approximately 6 mg, and a temperature range of 0°C–200 C at 10 C.min^{-1}. The crystallinity of the samples was calculated according to Eq. (1), where ΔHm is the total heat energy per unit mass and ΔHc is the fusion enthalpy for the 100% crystalline sample (ΔHc = 293 J g^{-1}) (Kanaga Karuppiah et al., 2008)

$$X_c\,(\%) = \frac{\Delta H_m}{\Delta H_C} \times 100 \quad (1)$$

The filler and morphological structures of the polymeric nanocomposites and pure UHMWPE polymer were investigated by scanning electron microscopy (SEM) in an FEG scanning electron microscope with an FIB nanofabrication system (Quanta FEG 3D FEI) with an acceleration voltage of 5 kV. The surfaces of

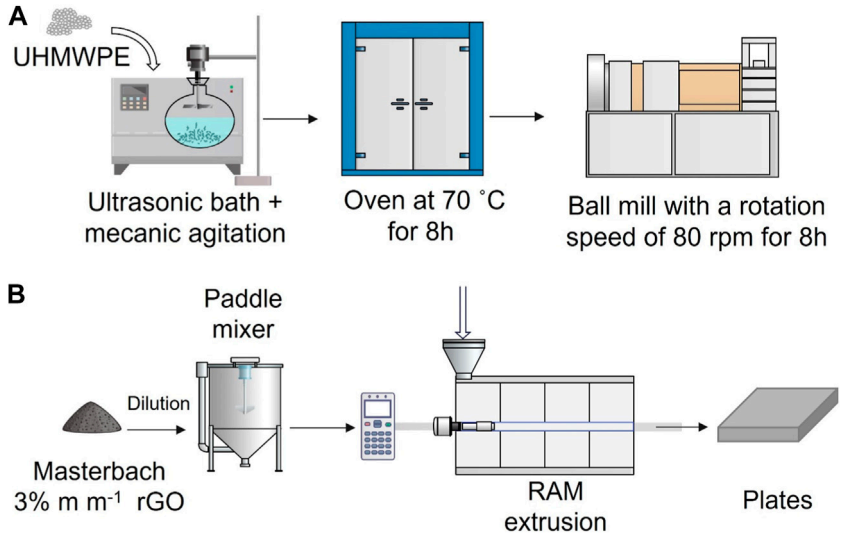

FIGURE 1
Scheme of the processing steps **(A)** Homogenization of solids; **(B)** Conformation by RAM extrusion.

TABLE 1 Samples, quantities of masterbatch produced and rGO content.

Sample	Quantity of masterbatch produced (kg)	rGO content (%wt.)
UHMWPE	-	0
Nanocomposite - Pilot 1	10	0.10 and 0.25
Nanocomposite - Pilot 2	150	0.25

the polymeric materials were metallized with a Au/Pd film with a thickness of 15 nm. Transmission electron microscopy (TEM) was conducted with a Tecnai G2-20–FEI SuperTwin 200 kV microscope. Atomic force microscopy (AFM) was performed with an Asylum Research MFP-3D-AS in contact mode; aliquots from the 5 g L^{-1} suspension of rGO were previously prepared with a 2.5x dilution and subsequently deposited on a mica substrate.

The tensile tests were conducted according to the ASTM D638 standard (ASTM D638-14, 2022) in universal EMIC equipment with a load cell of 5 kN and test speed of 10 mm min^{-1}. Twenty specimens were prepared for analysis of the mechanical behavior of the pure polymer (UHMWPE) and the nanocomposites at concentrations of 0.10 wt% and 0.25 wt% rGO. The impact resistance test was performed with the samples subjected to a 50 J pendulum in the impact hammer of the XJ series impact equipment in Charpy mode, and the results refer to an average of 90 measurements across multiple regions. Two-body abrasive wear resistance (rotating pin-on-drum) was conducted according to ISO 4649, in which twenty specimens were tested (ISO 4649:2017, 2017). The equipment consists of a rotating drum coated with specific sandpaper for abrasion with 60# grain, certified by VSM, supplied by the company Abrasfran. The abrasive wear resistance of the UHMWPE and nanocomposite samples was evaluated by covering 40 m of sliding distance with rotation of 40 rpm in the drum with a normal applied force of 10 N. The results were calculated according to Eq. (2), which determines the relative volume loss (ΔV_{rel}) due to the average mass loss of the tested material (Δm_t) and the average mass loss of the reference material ($\Delta m_{const.}$), due to the density of the tested material (ρ_t) and constant mass loss of the reference material (Δm_r).

$$c\Delta V_{rel.}\left(cm^3\right) = \frac{\Delta m_t\left(g\right) \times \Delta m_{const.}\left(g\right)}{\rho_t\left(g\,cm^{-3}\right) \times \Delta m_r\left(g\right)} \tag{2}$$

The three-body abrasive wear test is based on the ASTM G65 standard (ASTM G65-162021, 2021) and makes use of the rubber wheel type tribometer. Method B of Standard ASTM G65 was used with high abrasion severity, using a normal force of 130 N on the specimen surface and a rubber wheel speed of 200 rpm for 10 min. The abrasive agent used was a typical Brazilian sand with a granulometry of 50# (ABNT NBR 7214:2015) (ABNT NBR 7214: 2015, 2015). The data obtained allow the calculation of the volume lost in wear (Eq. (3)), which considered V_p as the volume lost in wear, Δ_m as the loss of mass in wear, and ρ as the density of the material worn.

$$V_p\left(mm^3\right) = \frac{\Delta m\left(g\right)}{\rho\left(g\,cm^{-3}\right)} \times 1000 \tag{3}$$

The surface topographies were investigated with two- and three-body wear tests using a Hommelwerke LV-100 profilometer with a 90° angle probe and a 5 μm radius. Five hundred one-dimensional scans of 5 mm length, 1 μm distance and 0.5 mm s^{-1} speed were performed. The results were collected through Turbo Wave software

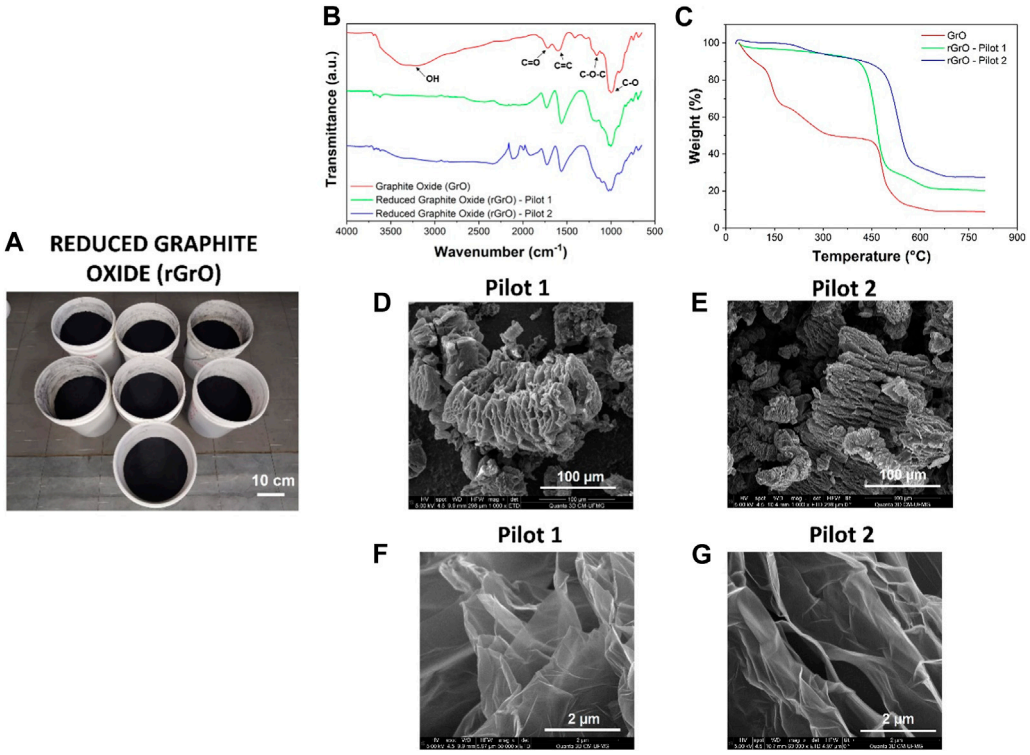

FIGURE 2
(A) 5.0 kg of reduced graphite oxide. Characterization of the reduced graphite oxide (rGrO) **(B)** FTIR spectra; **(C)** TG curves; **(D) (F)** SEM image–Pilot 1; **(E) (G)** SEM image–Pilot 2.

and treated by HommelMap Expert software, resulting in topographic maps.

The surface wettability was characterized through contact angle measurements. The sessile drop method was used in which a drop of deionized water was deposited on the surface before and after the abrasive wear tests. The test was carried out in a goniometer (Data Physics OCA 15EC) operated at 20°C, and the profile of the drop obtained was collected by SCA20 software. The reported values were the average of thirty measurements for each sample, as described in Supplementary Table S1.

3 Results and discussion

The main challenges faced in this work were to design a feasible process on a large scale that guarantees the quality of the results obtained for the nanocomposite on a laboratory scale, as described in our previous work (Amurin et al., 2022). The main differences in the overall scale-up routes with respect to the laboratory-scale methodologies were the use of a rotary furnace to reduce the graphite oxide; the increase of one order of magnitude in the concentration of the rGO suspension for exfoliation from 0.5 g L^{-1} in the laboratory scale to 5 g L^{-1} in pilot scales; the RAM extrusion rather than the compression molding conducted to produce the nanocomposite plates in the pilot scales; and a difference between the thickness of the plates produced in the stages of scale-up, 10 mm for Pilot 1 plates and 40 mm for Pilot 2 plates. Therefore, it was necessary to monitor in Pilot 1 and Pilot 2 how all these important changes in the overall process would impact the properties of the nanocomposites to guarantee the final production of the 1,500 kg that were used to make available 500 plates of UHMWPE-rGO to be applied in a prototype with strict property control in a Brazilian mining company.

The first stage was to produce well exfoliated rGO to be dispersed in the masterbatch of UHMWPE. Starting from graphite oxide (GrO) produced with approximately 40% oxygenated groups, as can be observed in Figure 2B,C in the FTIR spectra and TG plots of rGrO. To obtain reduced graphite oxide, reduction was conducted in a rotary furnace. The use of the rotary furnace rather than microwave reduction (Amurin et al., 2022) was necessary to obtain the 5 kg necessary for the targeted scale-up with a reproducible quality. The FTIR and TG results (Figures 2B,C) indicate that the process of reduction and simultaneous thermal expansion via a rotary furnace result in fillers with characteristics similar to those produced by the reduction process via microwave irradiation (Amurin et al., 2022), leading to a filler with approximately 3% oxygenated functions. One of the main desirable characteristics of the material is the expansion of the graphitic layers, as it facilitates the subsequent exfoliation of the carbon material in a solvent medium and under ultrasonic and mechanical agitation. It can be seen in the SEM images of Figures 2D,E that in both cases (Pilot 1 and Pilot 2), there are fillers with expanded multilayers, a morphology that can facilitate nanofiller exfoliation in liquid medium. Furthermore, it can be seen that the thin layers of

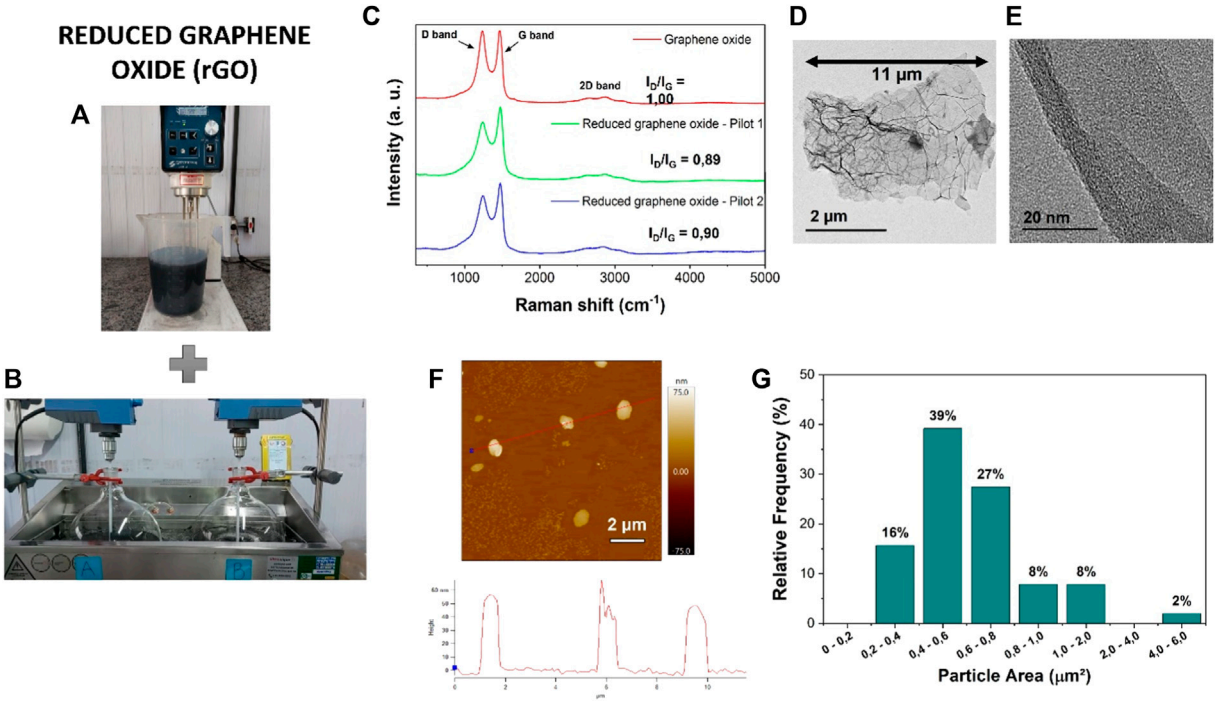

FIGURE 3
Production process of the nanofiller (rGO): **(A)** high shear exfoliation process; **(B)** ultrasonic bath and mechanical agitation exfoliation. Characterization of reduced graphene oxide: **(C)** Average Raman spectra with 457 nm laser energy; **(D)** TEM image; **(E)** High-resolution TEM image; **(F)** AFM image; **(G)** Nanofiller relative area distribution from AFM images.

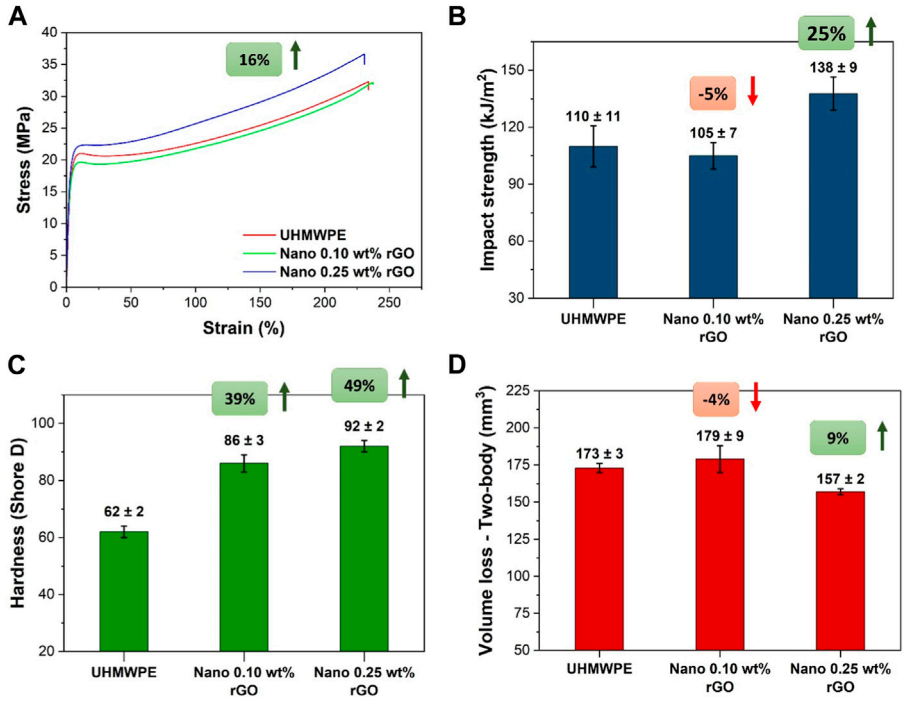

FIGURE 4
Characterization of the UHMWPE and nanocomposite plates at 0.10 wt% and 0.25 wt% of rGO content produced in the Pilot 1 step: **(A)** Average curve of stress as a function of strain; **(B)** impact strength; **(C)** hardness and **(D)** volume loss (two-body mode).

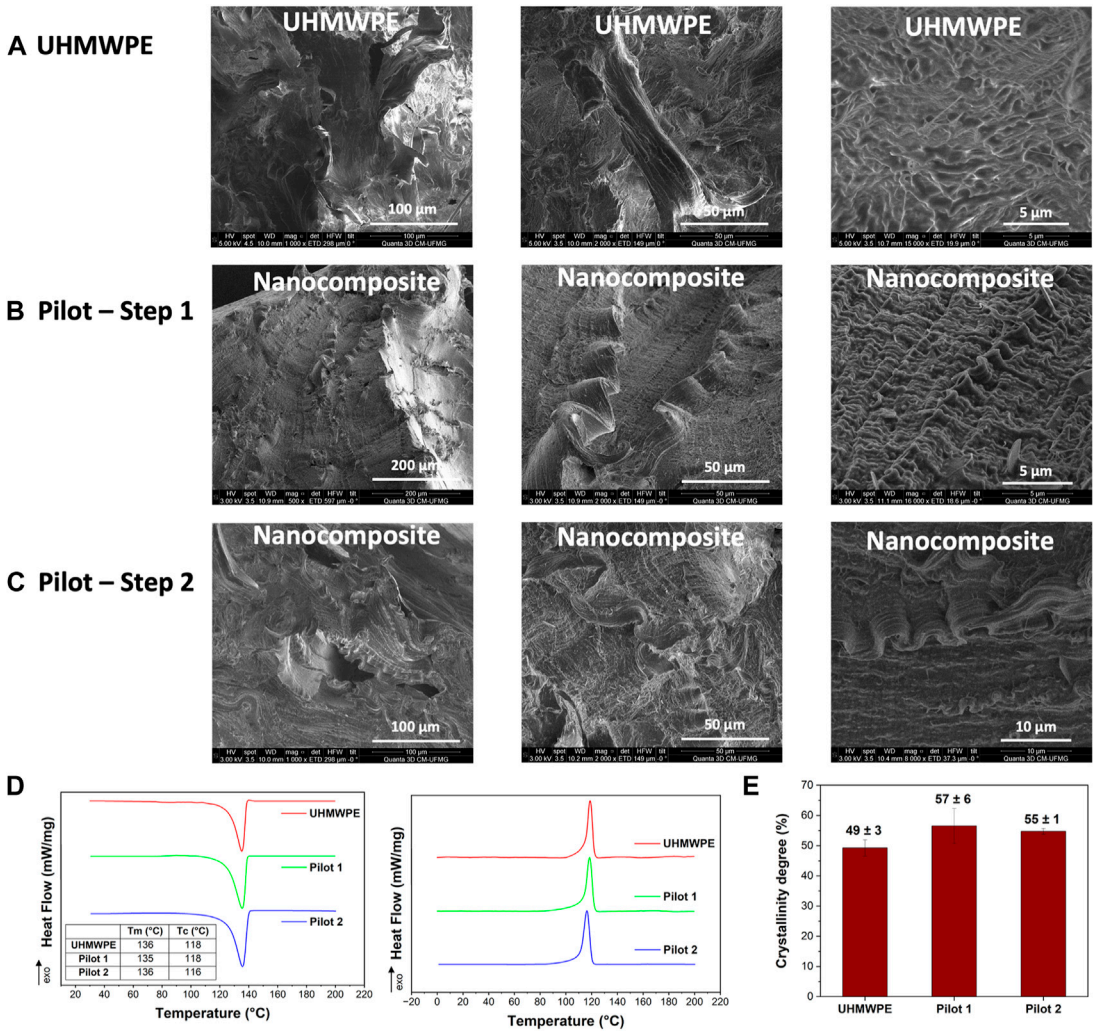

FIGURE 5
Morphological comparison between the nanocomposite plates at 0.25 wt% rGO content in the two stages of scale-up. SEM images of **(A)** UHMWPE **(B)** Pilot 1; **(C)** Pilot 2; **(D)** DSC curves in heating and cooling scan; **(E)** Crystallinity degree.

graphene tend to form a stable expanded three-dimensional network, as observed in Figures 2F,G. Therefore, the process route adopted is highly effective for the production of rGrO on a large scale, with quality and reproducibility.

The results presented in Figure 3 refer to the characteristics of the nanofiller after the exfoliation process of the starting filler rGrO (exfoliation in solvent medium by mechanical mixing in high shear, followed by ultrasonic bath and mechanical agitation) producing rGO. It must be considered that the concentration of the suspension is approximately 5 g L^{-1} (1 order of magnitude higher compared to laboratory-scale production (Amurin et al., 2022)). The Raman spectra in Figure 3C are the average of an ensemble of measurements, as explained in the Supplementary Material. *The ratio of intensities of the D band and G band of carbonaceous materials allows the evaluation of the degree of defects present in their structures* (Ferrari et al., 2006). The ID/IG results indicate that graphene oxide has a more defective structure than the reduced graphite oxide and graphene oxide in our work, as expected.

The exfoliated rGO nanofillers consist of a nanomaterial with few layers and some folded regions, as seen in Figures 3D,E. In addition, it has a lateral size of approximately 11 µm (Figure 3D). The high-resolution TEM images clearly show the layers of graphene, indicating the acquisition of two-dimensional carbon nanomaterials, as the Raman spectrum confirms (Figure 3A). The AFM results (Figure 3F) indicate that the nanofiller has a thickness of less than 60 nm after drying the samples for the measurement. In addition, the average areas of the side of the two-dimensional nanomaterials are on the micrometric order (Figure 3G), which is an important parameter to promote physical interaction with the polymeric chain of UHMWPE. It is important to consider that the process of exfoliation continues in the presence of the polymer in the solid-state mixing in the ball mill and further in the extrusion stage. Therefore, we propose that the final nanocomposites will have rGO dispersed in the polymeric matrix.

Three compositions were tested during the study performed on a laboratory scale, i.e., 0.10 wt%, 0.25 wt% and 0.50 wt% of rGO. The nanocomposite containing 0.50 wt% rGO was not produced in this

TABLE 2 Results of mechanical characterization for the plates of neat polymer and nanocomposites with 0.25 wt% rGO in the two stages of scale-up.

Properties	UHMWPE	Pilot 1	Pilot 2
Tensile strength (MPa)	32 ± 1	37 ± 2	32 ± 1
Rupture Strain (%)	234 ± 11	231 ± 6	202 ± 8
Young's Modulus (MPa)	727 ± 144	1,059 ± 128	904 ± 52
Impact strength (kJ/m^2)	110 ± 11	138 ± 11	123 ± 11
Hardness (Shore D)	62 ± 2	92 ± 2	90 ± 5

scale-up investigation due to inferior performance at the laboratory scale with respect to the other compositions (Amurin et al., 2022). The agglomeration of the nanofiller at this concentration is considered to start to influence negatively.

The masterbatch containing 3 wt% of nanofiller was diluted in the pure polymer to obtain nanocomposites with final concentrations of 0.10 wt% and 0.25 wt% of rGO in the Pilot 1 step, making it possible to evaluate the material with the best performance after all changes applied to the process to allow scale up. The set of results in Figure 4 shows that the nanocomposite containing 0.10 wt% rGO presented inferior performance with respect to the neat polymer in terms of impact resistance, Figure 4B, and abrasive wear, Figure 4D. In the case of tensile strength, Figure 4A shows that the curves of the nanocomposite with 0.10 wt% rGO and UHMWPE are similar. The nanocomposite containing 0.25 wt% rGO showed gains in properties with respect to UHMWPE for all evaluated properties. Therefore, the production of the nanocomposite containing 0.25 wt% rGO in pilot scale 2 was defined.

Figure 5 shows the comparison between the nanocomposites produced with 0.25 wt% rGO in the two steps of scale-up. These nanocomposites were obtained from the dilution of the masterbatch 3 wt%, and an important difference characterized the final plates that were produced. In the Pilot 1 test, the thickness of the plates was 10 mm, and in the Pilot 2 step, they were 40 mm. Thicker plates were produced in the Pilot 2 stage because of the need for specific dimensions for application as a prototype. However, the specimen for characterization obtained from the thicker plates was extracted from the bulk, whereas the specimen in the Pilot 1 plates came from the surface.

Figure 5A displays the SEM images of the plates produced from UHMWPE in an industrial environment. Note that the lamellar morphology tends to be less ordered than expected for this kind of polyolefin (Barron and Birkinshaw, 2008); however, microfibers are present in specific regions. Figure 5B shows the images for the nanocomposite plate produced in Pilot 1, where the lamellar crystalline region is long-range and well-ordered, which may be due to the influence of the rGO. In the case of the nanocomposite produced on the Pilot 2 scale (Figure 5C), typical UHMWPE morphologies (lamellae, microfibers and nodulus) with superior characteristics compared to UHMWPE can be identified. Large thicknesses and aligned lamellae are formed with a high degree of ordering in both stages of scaling up, probably due to the nanofiller presence. The increase in the degree of crystallinity (Figure 5E) presents a response that corroborates the SEM images.

Table 2 summarizes the mechanical results obtained for the neat polymer and nanocomposite plates with 0.25 wt% rGO produced in this work. The UHMWPE was processed under similar conditions as the nanocomposites to allow comparison. The tensile strength and rupture strain did not show significant changes for the nanocomposites with respect to UHMWPE. Otherwise, rigidity, hardness and impact strength exhibited important gains by the addition of the nanofiller. Figure 6 shows the results of the properties that were improved by the addition of the nanofiller. Scanning electron microscopy images of the tensile and impact strength fracture surfaces are shown in Supplementary Figure S3, S4,

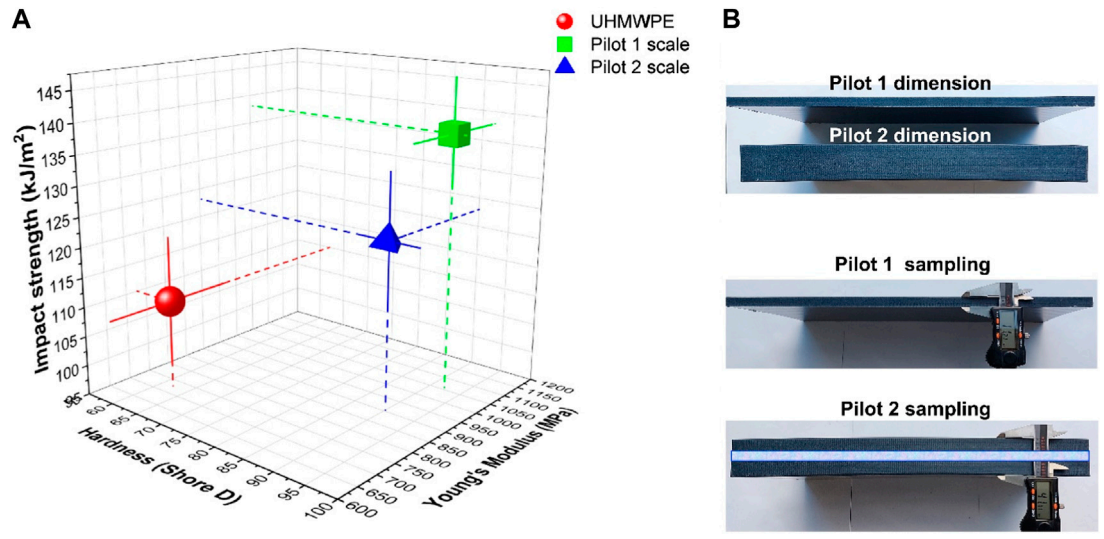

FIGURE 6
(A) Comparison of impact strength, hardness and Young's modulus among the plates of UHMWPE and nanocomposites of Pilot 1 and Pilot 2 with 0.25 wt% of rGO; **(B)** Dimensions of the plates from Pilot 1 and Pilot 2 scale up. In the case of pilot 2, the analysis was performed on the plate bulk.

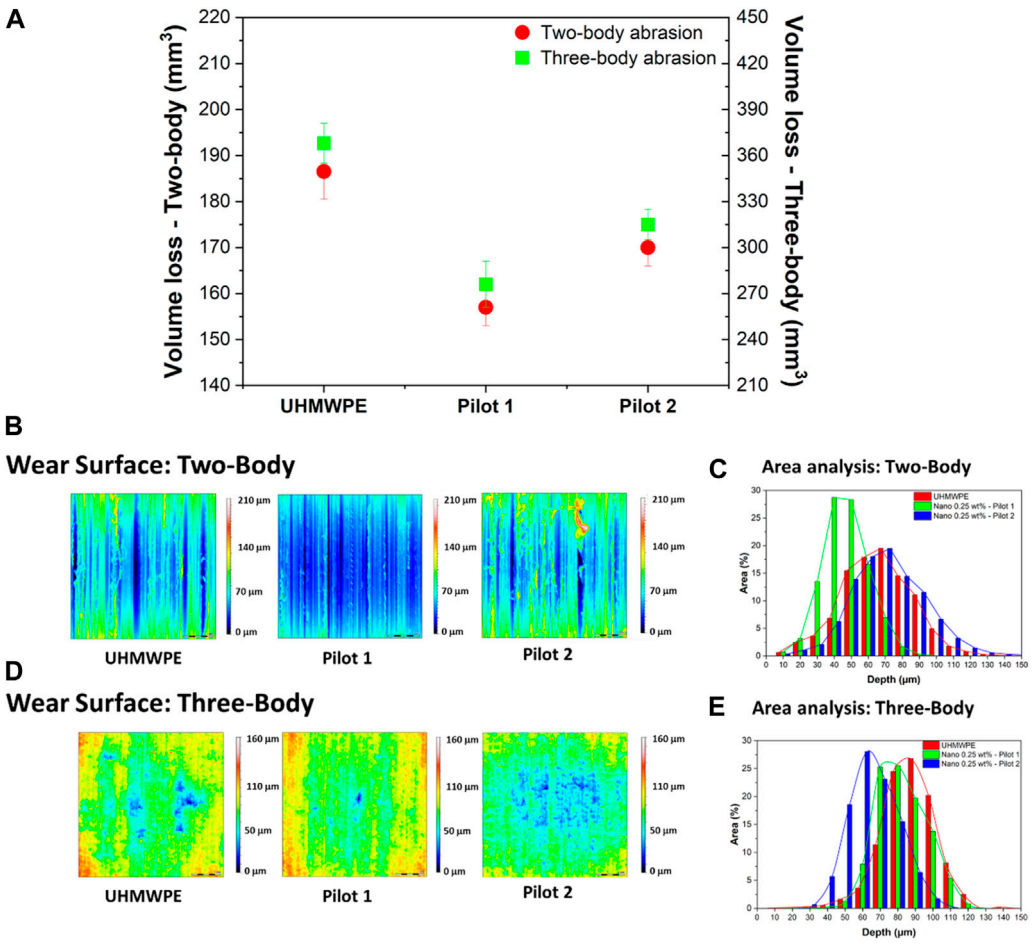

FIGURE 7
Wear results for the UHMWPE and nanocomposite plates at 0.25 wt% rGO from Pilot 1 and Pilot 2 scale up. **(A)** Volume loss–two- and three-body abrasion; **(B)** 2D–image of wear surface in two-body abrasion mode; **(C)** Analysis of area x depth obtained from the profilometry of wear surface in two-body abrasion mode; **(D)** 2D–image of wear surface in three-body abrasion mode; **(E)** Analysis of area x depth obtained from the profilometry of wear surface in three-body abrasion mode.

respectively. These images support the conclusion that the microfibers present between the amorphous/crystalline phases naturally reinforce the nanocomposite. Furthermore, the two-dimensional carbon nanofiller network tends to prevent crack propagation due to a high level of nanofiller dispersion and the absence of clusters.

The nanocomposite plates resulting from the dilution of the masterbatch containing 3 wt% rGO exhibit positive results and corroborate the analyses of the nanocomposite produced at the laboratory scale (Amurin et al., 2022), even considering all the changes made to the process to allow scale up. The Pilot 1 nanocomposite stood out in terms of impact resistance and rigidity, as seen in Figure 6, in which considerable gains are observed with respect to the neat polymer plate. Pilot 2 is a scale-up of 3,000 times with respect to the laboratory, and the resulting nanocomposite plate still shows superior performance compared to the neat polymer. However, Table 2 and Figure 6 show that the properties of impact resistance and rigidity are lower compared to the Pilot 1 nanocomposite. As mentioned above for the discussion of the structural and morphological characterization, we hypothesized that the lower performance of the specimen produced in Pilot 2 is because they were obtained from thicker plates that demand longer processing times and show a lower degree of crystallinity than the Pilot 1 samples.

The comparison of our results with the literature is possible by considering other authors' production on a small scale. Suñer et al. (Suñer et al., 2015) presented an increase of approximately 15% in the modulus of elasticity for UHMWPE containing between 0.1 and 2.0 wt% graphene oxide compared to pure UHMWPE. A 5% increase in Shore D hardness was reported by Aliyu *et al.* (Aliyu et al., 2019) with the addition of 0.5 wt% graphene nanoplatelets (GnPs). Other works reported an increase in the microhardness of UHMWPE for nanocomposites with 0.1–2.0 wt% GO (Suñer et al., 2015; Pang et al., 2015) and 0.7 and 3.0 wt% rGO (Çolak et al., 2020) added to the polymer. Pang *et al.* (Pang et al., 2015) showed significant increases in impact Izod, more than 3 times for the addition of 1.0 wt% GO to UHMWPE. Our data indicate an increase for the best cases of 35% in elastic modulus, 50% for hardness and 25% in impact strength in Charpy mode with the addition of

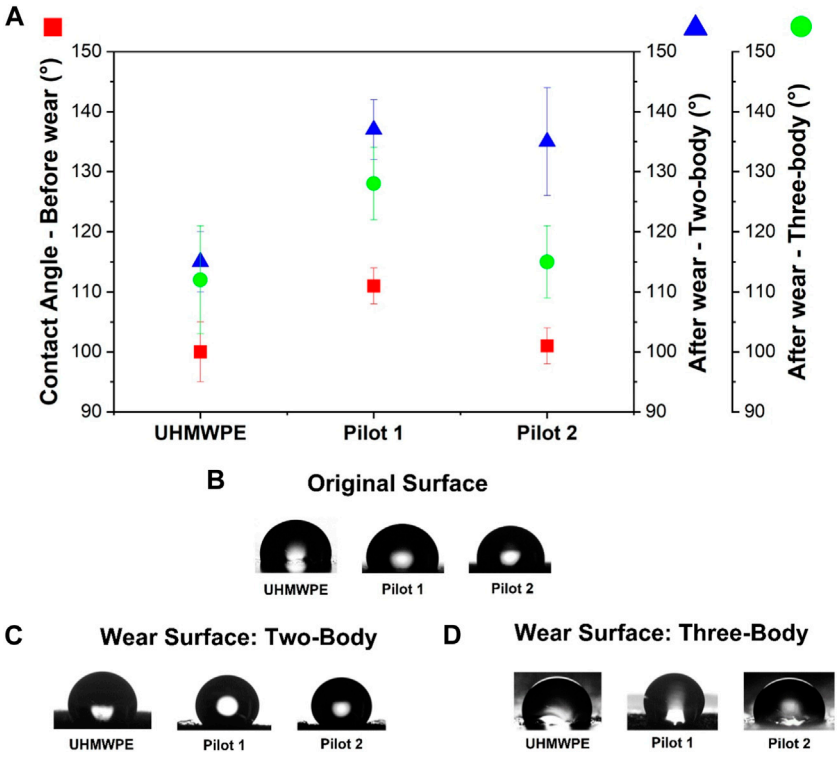

FIGURE 8
Wettability results for the UHMWPE and nanocomposite plates with 0.25 wt% of rGO from Pilot 1 and Pilot 2 scale up. **(A)** Contact angle; **(B)** Drop–original surface; **(C)** Drop on wear surface from two-body test; **(D)** Drop on wear surface from three-body test.

0.25 wt% of rGO, all associated with nanocomposite plates produced in pilot scales. Therefore, one can affirm that this work reports superior performance related to the literature with respect to rigidity and hardness.

Two- and three-body abrasive wear resistances were evaluated using pin-drum and rubber wheel tests, respectively. For both nanocomposite plates–Pilot 1 and Pilot 2–the volume losses are lower than the neat UHMWPE, as can be observed in Figure 7, indicating that there was a significant increase in resistance to abrasive wear with the addition of rGO. Tribological behavior is extremely influenced by the severity of the test, granulometry, shape and hardness of the abrasive agents, but both types of tests show the same tendency of gains with rGO. However, we must consider that the hardness is vital to enable low wear when subjected to abrasive wear. When comparing neat polymer to nanocomposites (Pilot 1 and Pilot 2), abrasion wear performance follows a clear trend with hardness (Somberg et al., 2023).

The two-body abrasive wear mode works with fixed abrasive agents and provides high severity to the softer phase body wear. The volume loss decreases for the nanocomposite plates, showing an improvement of 15% and 9% for the Pilot 1 and Pilot 2 nanocomposites, respectively, with respect to the neat UHMWPE. In the abrasive wear tests on three bodies (rubber wheel), in which the abrasive agents are free to roll on the surface that will be worn, the parameters used for the tests followed the standard for testing metallic materials (steel), which is quite a challenge for a polymeric plate. The three-body abrasive wear resistance shows an improvement of 24% and 16% for the Pilot 1 and Pilot 2 nanocomposites, respectively, when compared to the neat UHMWPE, as shown in Figure 7.

Worn surface topographies for nanocomposite plates (Pilot 1 and Pilot 2) were analyzed by profilometry, as shown in Figures 7B,C, to identify the pattern created during abrasive wear. Uniform wear marks, deep grooves and total material removal occur in the case of the two-body wear test for the surface of the neat UHMWPE. In the case of the nanocomposite plate of Pilot 1, the wear grooves became less deep. Moreover, the polymeric material is not completely removed by the passage of the abrasive agent, which is more evident for the nanocomposite plate of Pilot 2.

The rubber wheel results show deeper marks, as can be observed in Figure 7C, mainly for the neat polymer plate. In the case of the nanocomposite plates, the wear of the surface is less pronounced. In general, the roughness profiles for the different wear test configurations are very different from each other. However, the comparison between the damage caused to the surface of the nanocomposite and neat polymer plates indicates that the incorporation of rGO contributes to the increase in resistance to abrasive wear, regardless of the severity and mode of wear.

Tribological tests and topography analyses of UHMWPE nanocomposites, or even of the pure polymer, after being subjected to pin-on-drum and rubber wheel abrasive tests are not reported in the literature to the best of our knowledge. However, some authors present results of a decrease in the polymer wear rate through pin-on-disk sliding tests with the addition of carbon nanomaterials such as graphene nanoplatelets and GO (Aliyu

et al., 2019; Bahrami et al., 2016). Our group also reported in a recent work for laboratory-scale UHMWPE nanocomposites containing 0.1, 0.25 and 0.50 wt% rGO gains in tribological results with pin-on-disk sliding tests (Soares et al., 2022).

The contact angle results are shown in Figure 8 and Supplementary Table S1. These measurements were performed on the surfaces before wear tests and after the two types of wear tests conducted in this work. Two important features influence the contact angle: the hydrophobicity and the roughness of the surfaces (Law and Zhao, 2015). The original surface results before wear tests, Figure 8B, show an increase in the contact angle for the nanocomposite plate produced in Pilot 1, whereas in Pilot 2, the wettability seems similar to that of the neat polymer.

The contact angle data for the wear surfaces show, in both types of wear tests, significant increases from close to 115° (neat polymer) to close to 130° or more for the Pilot 1 plates. The Pilot 2 plates show a different behavior from the two-body test, producing wear surfaces that show a decrease in wettability and a contact angle of 135°, whereas the wear surfaces originating from the three-body test show a contact angle similar to that of the neat polymer plate. This result can be interpreted as being associated with the different degrees of severity of the two wear tests and the different thicknesses of the plates from Pilot 1 and Pilot 2. The thicker plate of Pilot 2 is probably being tested on a surface where the concentration of rGO is not the same as the surface of Pilot 1.

4 Conclusion

Significant changes in the processing to advance from the laboratory scale to the pilot scale were necessary in all operations, i.e., graphite oxidation, rGrO exfoliation, masterbatch production, and RAM extrusion to conform plates. The Pilot 1 stage was carried out with a scale approximately 200x higher than the laboratory study, and Pilot 2 concerned a scale approximately 3,000x higher with respect to the laboratory study. The systematic characterization of the structure, morphology, and properties of the filler, nanofiller and nanocomposite at all stages guarantees the best choices for the production of nanocomposite plates with multifunctionality, which means simultaneous gains in mechanical and tribological properties. The content of 0.25 wt% rGO was validated as the one showing the best performance. The plates produced in Pilot 2 were 4x thicker than the plates originating from Pilot 1 processing. The effect of the thickness of the plates on the mechanical and tribological properties was noticeable. Herein, the successful scale-up of the nanocomposite UHMWPE/rGO was demonstrated, which indicates the possibility of advancing industrial production, considering the specific characteristics of both the polymer and nanofiller tested in this work.

Data availability statement

The original contributions presented in the study are included in the article/Supplementary Material, further inquiries can be directed to the corresponding author.

Author contributions

LA: Conceptualization, Investigation, Methodology, Project administration, Supervision, Validation, Writing–original draft, Writing–review and editing, Data curation, Formal Analysis. PO: Formal Analysis, Investigation, Methodology, Writing–original draft. AS: Investigation, Methodology, Writing–original draft, Data curation. NR: Data curation, Investigation, Methodology, Writing–original draft. DR: Investigation, Methodology, Writing–original draft, Conceptualization, Formal Analysis, Project administration, Supervision, Validation, Writing–review and editing. GS: Conceptualization, Investigation, Methodology, Project administration, Supervision, Validation, Writing–original draft, Funding acquisition, Resources, Visualization, Writing–review and editing

Funding

The author(s) declare financial support was received for the research, authorship, and/or publication of this article. University support.

Acknowledgments

The authors thank the companies Vale S.A. and Baron S.A. CNPq and Microscopy Center of UFMG are also acknowledged. This manuscript is available at the preprint server SSRN at https://papers.ssrn.com/sol3/papers.cfm?abstract_id=4511644 (Amurin et al., 2018).

Conflict of interest

The author(s) declare financial support was received for the research, authorship, and/or publication of this article.

The authors declare that the research was conducted in the absence of any commercial or financial relationships that could be construed as a potential conflict of interest.

Publisher's note

All claims expressed in this article are solely those of the authors and do not necessarily represent those of their affiliated organizations, or those of the publisher, the editors and the reviewers. Any product that may be evaluated in this article, or claim that may be made by its manufacturer, is not guaranteed or endorsed by the publisher.

Supplementary material

The Supplementary Material for this article can be found online at: https://www.frontiersin.org/articles/10.3389/frcrb.2023.1291283/full#supplementary-material

References

ABNT NBR 7214:2015 (2015). *Areia normal para ensaio de cimento - especificação*, 1–4.

Aliyu, I. K., Mohammed, A. S., and Al-Qutub, A. (2019). Tribological performance of ultra high molecular weight polyethylene nanocomposites reinforced with graphene nanoplatelets. *Polym. Compos.* 40 (S2), E1301–E1311. doi:10.1002/pc.24975

Amurin, L., Oliveira, P. N., Pereira Ana Flávia, T. S., Ribeiro, N. C., Rezende, D. B., and Silva, G. G. 2018 Ultrahigh molecular weight polyethylene-reduced graphene oxide scaling up to produce wear resistant plates. Available at: https://ssrn.com/abstract=4511644.

Amurin, L. G., Felisberto, M. D., Ferreira, F. L., Soraes, P. H., Oliveira, P. N., Santos, B. F., et al. (2022). Multifunctionality in ultra high molecular weight polyethylene nanocomposites with reduced graphene oxide: hardness, impact and tribological properties. *Polym. Guildf.* 240, 124475. doi:10.1016/j.polymer.2021.124475

ASTM D638-14 (2022). *Standard test method for tensile properties of plastics*. doi:10.1520/D0638-14

ASTM G65-16(2021) (2021). *Standard test method for measuring abrasion using the dry sand/rubber wheel apparatus*. doi:10.1520/G0065-16R21

Bahrami, H., Ramazani S A, A., Shafiee, M., and Kheradmand, A. (2016). Preparation and investigation of tribological properties of ultra-high molecular weight polyethylene (UHMWPE)/graphene oxide. *Polym. Adv. Technol.* 27 (9), 1172–1178. doi:10.1002/pat.3779

Barron, D., and Birkinshaw, C. (2008). Ultra-high molecular weight polyethylene - evidence for a three-phase morphology. *Polym. Guildf.* 49 (13–14), 3111–3115. doi:10.1016/J.POLYMER.2008.05.004

Celanese (2022). *Gur 4152 - PE-UHMWCelanese*, 1–3.

Çolak, A., Göktaş, M., and Mindivan, F. (2020). Effect of reduced graphene oxide amount on the tribological properties of UHMWPE biocomposites under water-lubricated conditions. *SN Appl. Sci.* 2 (3), 375–377. doi:10.1007/s42452-020-2179-4

de Grafite, N. (2023) Grafine 72140. Available at: https://www.grafite.com/grafine (Accessed March 21, 2023).

dos Reis, T. M. C., Assis, A. L. S., de Castro, V. G., and Silva, G. G. (2020). Processo de obtenção de óxido de grafeno e produto.

dos Reis, T. M. C., de Castro, V. G., Amurin, L. G., and Silva, G. G. (2023). Graphene oxide dispersion in epoxy resin prepared by direct phase transfer from ethanol: rheology and aging. *Compos. Part C. Open Access* 10, 100340. doi:10.1016/j.jcomc.2022.100340

Dreyer, D. R., Park, S., Bielawski, C. W., and Ruoff, R. S. (2010). The chemistry of graphene oxide. *Chem. Soc. Rev.* 39 (1), 228–240. doi:10.1039/B917103G

Ferrari, A. C., Meyer, J. C., Scardaci, V., Casiraghi, C., Lazzeri, M., Mauri, F., et al. (2006). Raman spectrum of graphene and graphene layers. *Phys. Rev. Lett.* 97 (18), 187401–187404. doi:10.1103/PhysRevLett.97.187401

Friedrich, K. (2018). Polymer composites for tribological applications. *Adv. Industrial Eng. Polym. Res.* 1 (1), 3–39. doi:10.1016/j.aiepr.2018.05.001

Gao, Q., Liu, S., Hou, K., Li, Z., and Wang, J. (2022). Graphene-based nanomaterials as lubricant additives: a review. *Lubricants* 10, 273–310. doi:10.3390/lubricants10100273

Greenfeld, I., and Wagner, H. D. (2015). Nanocomposite toughness, strength and stiffness: role of filler geometry. *Nanocomposites* 1 (1), 3–17. doi:10.1179/2055033214Y.0000000002

Herrera-Ramírez, L. C., Castell, P., Castillo-Rodríguez, M., Fernández, Á., and Guzman de Villoria, R. (2017). The effect of a semi-industrial masterbatch process on the carbon nanotube agglomerates and its influence in the properties of thermoplastic carbon nanotube composites. *J. Polym. Sci. B Polym. Phys.* 55 (2), 189–197. doi:10.1002/polb.24258

Hummers, W. S., and Offeman, R. E. (1958). Preparation of graphitic oxide. *J. Am. Chem. Soc.* 80 (6), 1339. doi:10.1021/ja01539a017

ISO 4649:2017 (2017). *Rubber, vulcanized or thermoplastic — determination of abrasion resistance using a rotating cylindrical drum device*.

Johnson, D. W., Dobson, B. P., and Coleman, K. S. (2015). A manufacturing perspective on graphene dispersions. *Curr. Opin. Colloid & Interface Sci.* 20 (5–6), 367–382. doi:10.1016/j.cocis.2015.11.004

Kanaga Karuppiah, K. S., Bruck, A. L., Sundararajan, S., Wang, J., Lin, Z., Xu, Z. H., et al. (2008). Friction and wear behavior of ultra-high molecular weight polyethylene as a function of polymer crystallinity. *Acta Biomater.* 4 (5), 1401–1410. doi:10.1016/j.actbio.2008.02.022

Law, K. Y., and Zhao, H. (2015). Surface wetting: characterization, contact angle, and fundamentals. *Surf. Wetting Charact. Contact Angle, Fundam.*, 1–162. doi:10.1007/978-3-319-25214-8

Li, Y., He, H., Huang, B., Zhou, L., Yu, P., and Lv, Z. (2018). *In situ* fabrication of cellulose nanocrystal-silica hybrids and its application in UHMWPE: rheological, thermal, and wear resistance properties. *Polym. Compos.* 39 (S3), E1701–E1713. doi:10.1002/PC.24690

Li, Y., Wu, D., and Chen, G. (2007). Preparation and characterization of high-density polyethylene/expanded graphite conducting masterbatch. *J. Appl. Polym. Sci.* 106 (5), 3119–3124. doi:10.1002/APP.25842

Pang, W., Ni, Z., Chen, G., Huang, G., Huang, H., and Zhao, Y. (2015). Mechanical and thermal properties of graphene oxide/ultrahigh molecular weight polyethylene nanocomposites. *RSC Adv.* 5 (77), 63063–63072. doi:10.1039/c5ra11826c

Park, M. V. D. Z., Bleeker, E. A., Brand, W., Cassee, F. R., van Elk, M., Gosens, I., et al. (2017). Considerations for safe innovation: the case of graphene. *ACS Nano* 11 (10), 9574–9593. doi:10.1021/acsnano.7b04120

Potts, J. R., Dreyer, D. R., Bielawski, C. W., and Ruoff, R. S. (2011). Graphene-based polymer nanocomposites. *Polym. Guildf.* 52 (1), 5–25. doi:10.1016/j.polymer.2010.11.042

Shirvanimoghaddam, K., Balaji, K., Ahmadi, M., Ajdari Nazarloo, H., Yadav, R., Zabihi, O., et al. (2023). Strategies to resolve intrinsic conflicts between strength and toughness in polyethylene composites. *Adv. Industrial Eng. Polym. Res.* doi:10.1016/j.aiepr.2023.03.004

Soares, P. H. V., de Oliveira, P. N., Viáfara, C. C., Silva, G. G., Amurin, L. G., and da Silva, A. B. (2022). Effect of the reduced graphene oxide on the tribological behavior of UHMWPE/rGO nanocomposites under sliding contact conditions. *Polym. Eng. Sci.* 62 (8), 2641–2656. doi:10.1002/pen.26047

Somberg, J., Gonçalves, G., and Emami, N. (2023). Graphene oxide versus graphite and chemically expanded graphite as solid lubricant in ultrahigh molecular weight polyethylene composites. *Tribol. Int.* 187, 108643. doi:10.1016/j.triboint.2023.108643

Spitalsky, Z., Tasis, D., Papagelis, K., and Galiotis, C. (2010). Carbon nanotube–polymer composites: chemistry, processing, mechanical and electrical properties. *Prog. Polym. Sci.* 35 (3), 357–401. doi:10.1016/j.progpolymsci.2009.09.003

Suñer, S., Joffe, R., Tipper, J. L. L., and Emami, N. (2015). Ultra high molecular weight polyethylene/graphene oxide nanocomposites: thermal, mechanical and wettability characterisation. *Compos. Part B Eng.* 78, 185–191. doi:10.1016/j.compositesb.2015.03.075

Visco, A., Yousef, S., Galtieri, G., Nocita, D., Pistone, A., and Njuguna, J. (2016). Thermal, mechanical and rheological behaviors of nanocomposites based on UHMWPE/paraffin oil/carbon nanofiller obtained by using different dispersion techniques. *JOM* 68 (4), 1078–1089. doi:10.1007/s11837-016-1845-x

Zhang, Z., Luo, J., Zhao, S., Ge, S., Carrillo, J. M. Y., Keum, J. K., et al. (2022). Surpassing the stiffness-extensibility trade-off of elastomers via mastering the hydrogen-bonding clusters. *Matter* 5 (1), 237–252. doi:10.1016/j.matt.2021.11.007

frontiers | Frontiers in Carbon

TYPE Original Research
PUBLISHED 13 December 2023
DOI 10.3389/frcrb.2023.1300811

OPEN ACCESS

EDITED BY
Marinella Striccoli,
Consiglio Nazionale delle Ricerche—CNR, Italy

REVIEWED BY
Octavian Buiu,
National R&D Institute for Microtechnologies-IMT Bucharest, Romania
Gianluca Minervini,
Politecnico di Bari, Italy

*CORRESPONDENCE
Cintya. D. A. E. S. Barbosa,
cintya.barbosa@iqb.ufal.br

RECEIVED 23 September 2023
ACCEPTED 22 November 2023
PUBLISHED 13 December 2023

CITATION
Da Silva LE, Araujo APdL, Almeida JH, de Vasconcelos LBOD, Silva MdO, Lima DJP, Viana RdS, Ferro JNdS, Goulart MOF, Xavier JA and Barbosa CDAES (2023), Carbon dots-based fluorescent films to act as a potential antioxidant agent and pH ratiometric sensor for skin applications.
Front. Carbon 2:1300811.
doi: 10.3389/frcrb.2023.1300811

Carbon dots-based fluorescent films to act as a potential antioxidant agent and pH ratiometric sensor for skin applications

Livia E. Da Silva[1], Anna Paula de L. Araujo[1], James Henrique Almeida[2], Ledja. B. O. D. de Vasconcelos[1], Messias de O. Silva[1], Dimas. J. P. Lima[1], Rodrigo da S. Viana[3], Jamylle N. de S. Ferro[2], Marília O. F. Goulart[1], Jadriane A. Xavier[1] and Cintya. D. A. E. S. Barbosa[1]*

[1]Institute of Chemistry and Biotechnology, Federal University of Alagoas, Maceió, Alagoas, Brazil, [2]Institute of Biological Sciences and Health, Federal University of Alagoas, Maceió, Alagoas, Brazil, [3]Technology Center, Federal University of Alagoas, Maceió, Alagoas, Brazil

The wound healing process is accompanied by changes in pH values. Monitoring this physicochemical parameter can indicate the effectiveness of the applied treatment and act as early identification of wound infection. This study focuses on the development of a fluorescent film-based polyvinyl alcohol (PVA) and carbon dots (CDs) derived from lemon bagasse (CD-L) and *ortho*-phenylenediamine (CD-oPD) named to act as antioxidants and potential ratiometric fluorescent pH sensors, in wound applications. The I_{460}/I_{550} intensity ratio, as a function of pH value for the dual-system CDs prepared from the mixture of CD-L and CD-oPD, named CD-L/oPD, was investigated. The fit corresponded to a sigmoidal function in the pH range of 5–10, with a relationship having a r^2 = 0.992. The variation in the values of the I_{460}/I_{550} ratio allows for the visualization of the color change from yellowish-green to green with increasing pH. Through a simulated *ex vivo* pig skin model, it was possible to note that the films prepared from mixed of the CD-L and CD-oPD carbon dots incorporated in a matrix PVA named CD-L/oPD-F was more efficient at visually discriminating color in relation to changes in pH than the films prepared from both individual CD-L (CD-L-F) and CD-oPD (CD-oPD-F) carbon dots. CD-L and CD-oPD demonstrated antioxidant capacity against reactive oxygen species (ROS). The IC_{50} values for CD-L and CD-oPD were 56.7 and 39.5 μg mL^{-1} in the DPPH$^{\bullet}$ inhibition assay, and 25.1 and 63.4 μg mL^{-1} in the HOCl scavenging one, respectively. MTT viability assays using human non-tumoral skin fibroblast (HFF-1) cell showed a cell survival rate of over 80% for both CDs up to a concentration of 1,000 μg mL^{-1}. Finally, the developed films can act in a bifunctional way, by monitoring healing through pH changes and by acting as an antioxidant agent in the treatment of wounds.

KEYWORDS

carbon dots, wound healing, ROS scavenger, polyvinyl alcohol, PH sensor film, dual emission

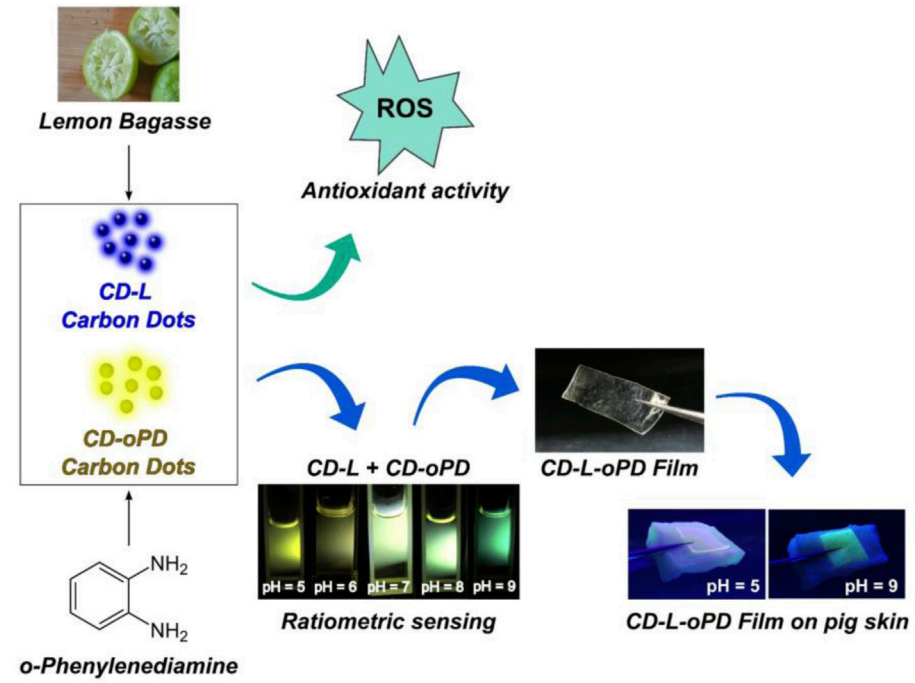

GRAPHICAL ABSTRACT

1 Introduction

Carbon dots are luminescent carbon nanoparticles (CNP) with sizes smaller than 10 nm and a spherical morphology (He et al., 2022; Wang et al., 2022). A graphitic structure forms the core, while the surface contains functional groups characteristic of the materials used during synthesis, mainly from the precursor (Ding et al., 2020; He et al., 2022; Davi, L. B. O. et al., 2021). CDs exhibit excellent optical properties, such as fluorescence in the visible spectrum, good dispersion in water, biocompatibility, photo-stability, low toxicity, antimicrobial activity, and low-cost synthesis (Mary et al., 2022). These properties associated with their non-invasiveness and good sensitivity have contributed to the development of various biological fluorescent sensors (Omidi et al., 2017; Yang et al., 2019).

The pH in biological systems plays a critical role in maintaining homeostasis and regulating vital processes (Mei et al., 2022). In this sense, a number of diseases are associated with disrupted pH values, and monitoring their changes is important to aid treatment. (Xia et al., 2019; Macairan et al., 2020). The exudates (liquids) released in the wounds during the healing process are capable of responding to pH, since the pH value influences physiological processes, such as the inflammatory response, collagen formation and angiogenesis (Zhu et al., 2020). The skin surface has a typical pH value ranging from 4 to 6, providing resistance against microbial invasion (Zhu et al., 2020; Sharma et al., 2023). However, chronic wounds have a more alkaline pH, between 7 and 9, and are more vulnerable to bacterial infections, while acute wounds have a pH similar to that of the skin under normal conditions, around 4 to 6, due to the activity of neutrophils which prevent the colonization of bacteria (Kadam et al., 2019; Zhu et al., 2020; Pang et al., 2023). In this sense, pH can help monitoring wound healing by enabling previous information to be provided which can contribute to effective treatment (Tang et al., 2021).

CDs have emerged as versatile and promising materials in the field of pH sensing. When exposed to different pH environments, CDs exhibit alterations in their emission spectra, resulting in changes in the wavelength of the emission or intensity (Yang et al., 2019; Zhang et al., 2019; Ehtesabi et al., 2020; Liu et al., 2021). pH-responsive property has positioned them as valuable tools for pH-sensing applications in various systems (Wang et al., 2020; Cui et al., 2021). Although studies on the treatment of wounds using CDs are in progress, the use of these nanoparticles in the detection of pH in wounds is rare (Omidi et al., 2017; Kasouni et al., 2021; Wu et al., 2022; Farshidfar et al., 2023). Omidi et al. (2017) synthesized single-channel CDs with blue emission derived from ammonium citrate to fabricate CD/chitosan nanocomposite films for application in wound healing. The results had shown that they were able to detect pH variation, during *in vivo* stages of wound healing (rat model). Yang et al. (2019) also prepared orange-emitting CDs using 1, 2, 4-triaminobenzene and urea (O-CDs), applied in the monitoring of wound healing, through the detection of pH values variation. Medical cotton cloth (MCC) was used as a support for the O-CDs and the combined (O-CDs/MCC) system was responsive to a pH range of 5 up 9.

However, the presence of only one emission band and/or gradation of wavelength of the maximum emission changes with low clarity, and difficulties to be visualized challenged the pH detection. In light of the limitations of single-channel nanoparticles, researchers are developing ratiometric sensors to improve the sensitivity of CDs to pH. (Song et al., 2017; Lei et al., 2020; Xu et al., 2020; Li et al., 2021; Silva et al., 2022). Ratiometric fluorescent sensors typically exhibit dual emission

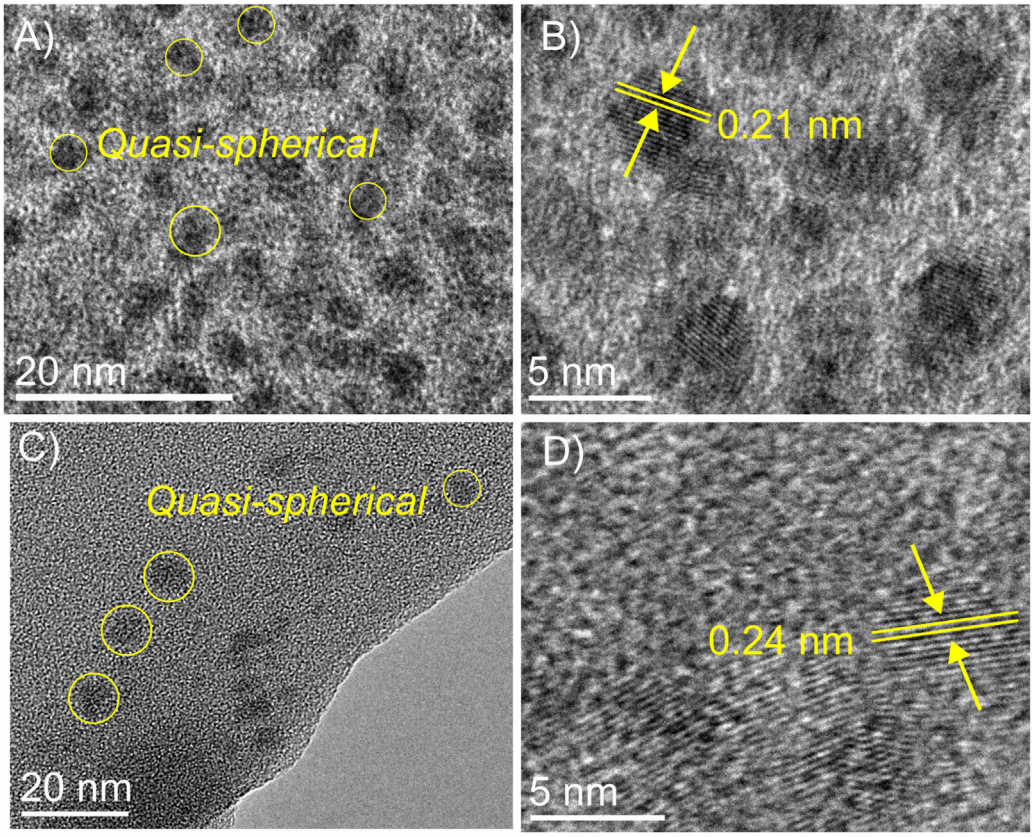

FIGURE 1
TEM micrographs for CD-L **(A,B)** and CD-oPD **(C,D)**.

bands at different wavelengths (Silva et al., 2022). A correlation is provided from the ratios of the fluorescence intensities of the different wavelengths of the sample, which minimizes background interferences, improving the sensitivity, precision and detection of the material (Li et al., 2021). In addition, ratiometric sensors enable rapid detection due to the response of the sample, which can also be seen with the naked eye. From this perspective, they can be applied to the detection of ions, pH, temperature, diseases, etc (Lei et al., 2020; Xu et al., 2020; Li et al., 2021). The advantages of these sensors, combined with the unique properties of CDs, allow the development of new platforms for *in situ* pH detection in biological systems with high efficiency. In this regard, the obtained results are highly promising for early diagnosis, and treatment's monitoring of diseases, such as chronic wounds (Yang et al., 2019; Farshidfar et al., 2023; Sharma et al., 2023).

Additionally, the use of CDs as antioxidant agents for therapeutic applications has been widely explored, however, in wounds, are still not common (Huangfu et al., 2021; Moniruzzaman et al., 2022; Roy et al., 2022; Varillas et al., 2022). In this sense, Qu et al. (2023) synthesized positively charged CDs from *p*-phenylenediamine and polyethyleneimine and studied their ability to reduce radicals as $DPPH^{\bullet}$, $^{\bullet}OH$ and $O_2^{\bullet-}$ in wounds, and results indicated that CDs effectively eliminated excess of these radicals, and relieved excessive inflammatory responses (Qu et al., 2023). Reactive oxygen species (ROS) are formed during normal cellular respiration, but studies have shown that in excess they can contribute to the development and progression of diseases resulting from oxidative stress (Juan et al., 2021; Dong et al., 2022). According to the intensity scale, we have the so-called physiological oxidative stress (eustress), essential for redox signaling and excessive and toxic oxidative stress, which causes damage to biomolecules (distress) (Sies et al., 2017). In general, wounds healing experiences three phases: inflammation, proliferation and maturation. In the inflammatory phase, an excess of ROS is produced, which is considered to be the main factor hindering skin regeneration (Bankoti et al., 2017). Thus, distress occurs, causing oxidative structural modifications in lipids, DNA, and proteins, leading to necrosis at the wound site (Bankoti et al., 2017; Juan et al., 2021).

The immobilization of CDs-based colorimetric/fluorescent pH sensors, and antioxidant agents in polymeric matrices is a good strategy for their use as bioactive dressings (Liu et al., 2021). In this sense, due to its properties of biocompatibility, hydrophilicity, low cost, and known benefits in wound healing, the synthetic polyvinyl alcohol (PVA) has been explored in the manufacture of dressings, usually associated with other organic and inorganic compounds (Moghaddam et al., 2021; Jin, 2022; Qu et al., 2023).

As such, this study aims to develop biocompatible, antioxidant fluorescent pH sensors using dual-system CDs prepared from lemon peel bagasse (CD-L) and *o*-phenylenediamine (CD-oPD) to offer a

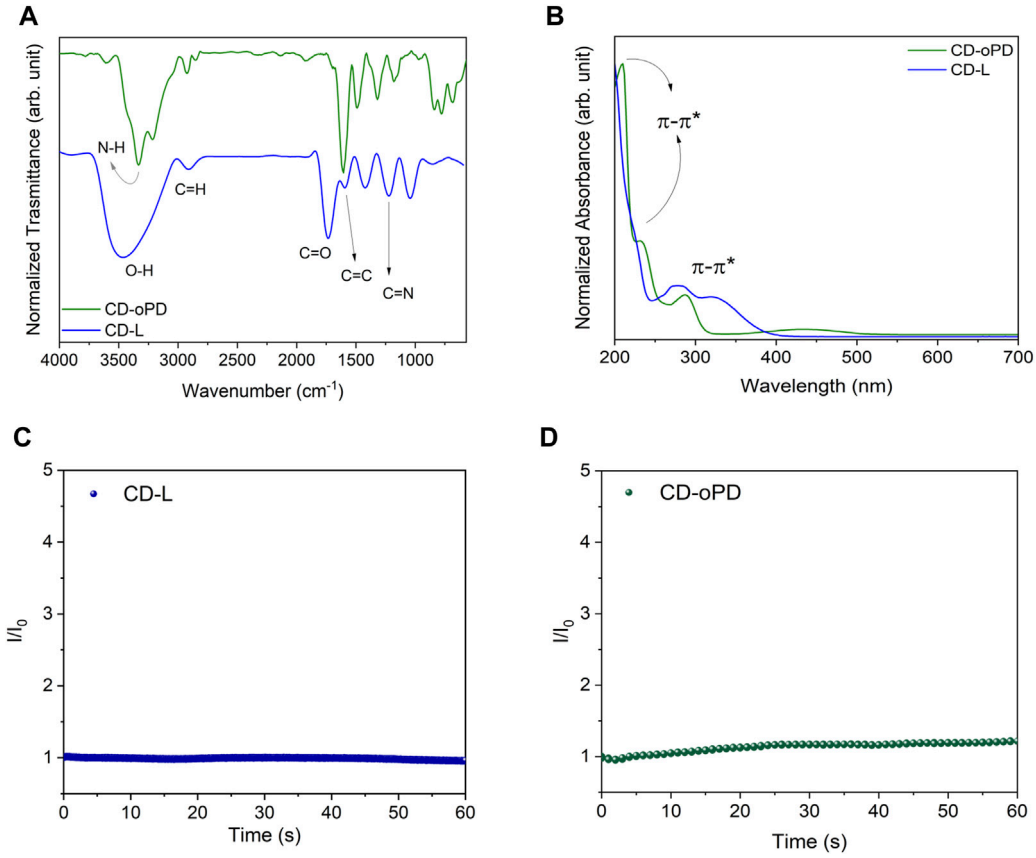

FIGURE 2
(A) FT-IR spectra for CD-L (blue line) and CD-oPD (green line), **(B)** UV-Vis absorption spectra for CD-L (blue line) and CD-oPD (green line), **(C)** Photostability under UV light (365 nm) for CD-L and **(D)** under UV light (350 nm) for CD-oPD.

real-time, *in situ* measurement of pH value and redox status in wounds.

2 Experimental

2.1 Chemicals

Tahiti lemons (Citrus latifolia) were obtained from local markets (SisGen access number: A4098F3). The chemicals o-phenylenediamine, boric acid, acetic acid, phosphoric acid, MTT [3-(4,5-dimethylthiazol-2-yl)-2,5-diphenyltetrazolium bromide], polyvinyl alcohol (PVA-average mol wt 89,000–98,000) and glycerol were acquired from Sigma-Aldrich (St. Louis, United States). Deionized water (18.2 MΩ cm) obtained from the Master System MS 2000 (Gehaka, Brazil) was used. Pig belly skin was purchased freshly from a local butcher.

2.2 Synthesis of lemon waste-derived carbon dots (CD-L)

The CD-L was synthesized according to the methodology reported by Silva et al., 2023. Briefly, the aqueous extract of Tahiti lemon was obtained using 60 g of the bagasse in 130 mL of deionized water, stirred for 60 min at 100°C. After heating, the mixture containing lemon bagasse was separated from the aqueous extract by filtration through a filtered through the fluted paper in a glass funnel. Fifty (50) mL of this resulting solution was heated using a domestic microwave (5 min, 720 W). Subsequently, 50 mL of deionized water was added to the solids resulting to obtain a suspension containing the CDs, since the solvent was completely evaporated during the reaction. The purification was carried by centrifugation of suspension at high speed (15,000 rpm), and filtration, using membranes of cellulose acetate (0.22 μm). The concentration of CD-L in the aqueous solution was ≈20 mg mL^{-1}. Finally, they were stored in a refrigerator at 4°C.

2.3 Synthesis of *o*-phenylenediamine-derived carbon dots (CD-oPD)

The CD-oPD was obtained by a simple hydrothermal reaction adapted from Davi et al. (2021). The reaction consisted of a mixture of 20 mg of *o*-phenylenediamine and 10 mL of deionized water in a stainless steel reactor, which was heated for 4 h at 200°C. The purification and storage of the

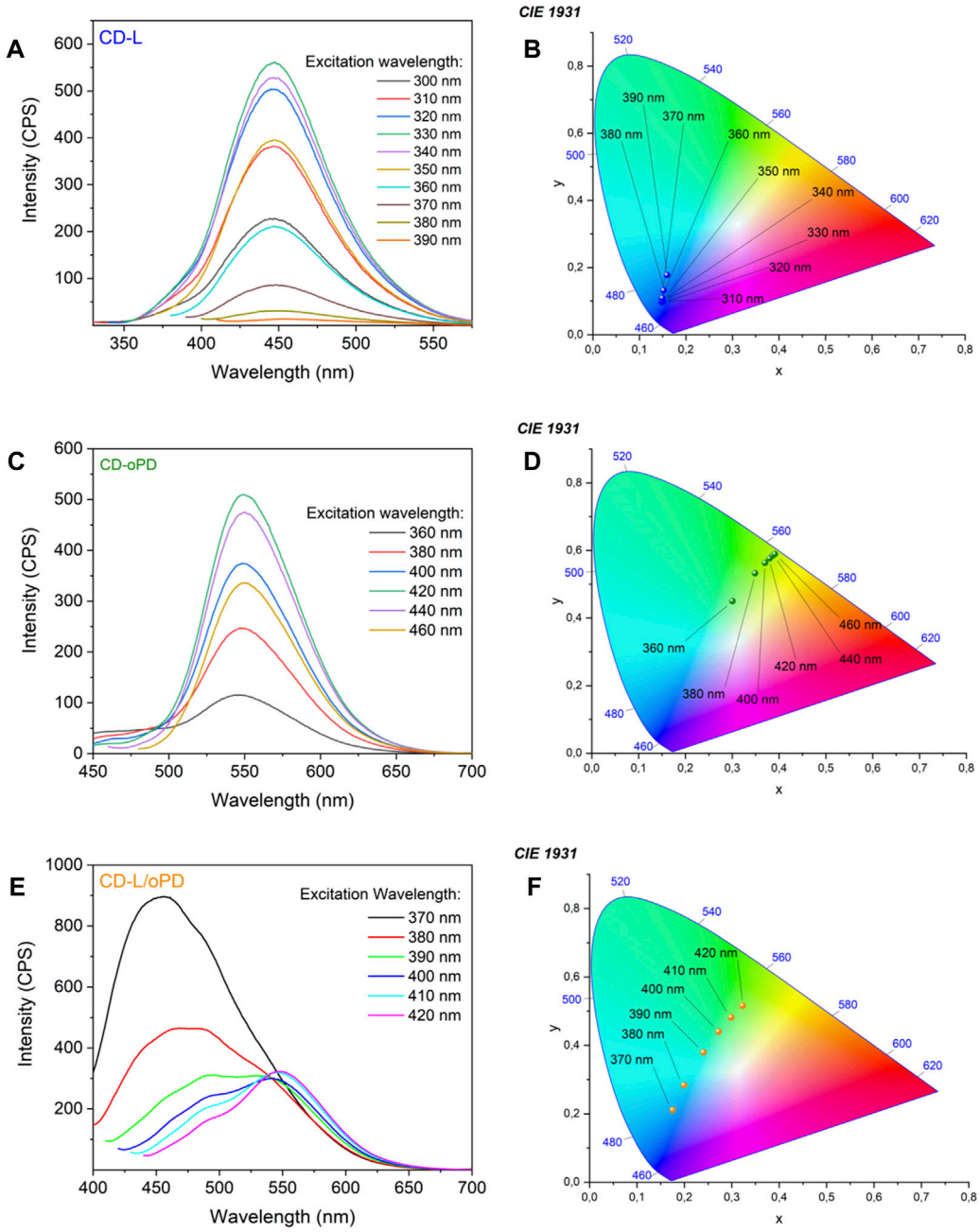

FIGURE 3
Photoluminescence spectra for **(A)** CD-L, **(B)** CD-oPD and **(C)** CD-L/oPD and CIE chromaticity diagram for **(D)** CD-L, **(E)** CD-oPD, and **(F)** CD-L/oPD.

CD-oPD was carried out according to the established protocol for CD-L.

2.4 Film of CD-L-F, CD-oPD -F and CD-L/oPD-F

The synthesis of the film CD-L/oPD-F was based on reported data (Elias et al., 2023). Briefly, 150 mg of PVA dissolved in 5 mL of deionized water under stirring at 80°C for 5 min. After cooling, 250, 125, and 60 µL of CD-L, CD-oPD, and glycerol were added to the solution, respectively. The mixture was stirred, deposited onto a plastic Petri dish (35 mm x 10 mm), and placed in an oven at 50°C for 48 h. The same procedure was used to synthesize film CD-L/CD-oPD-F, adding 250 µL of CD-L and 125 µL of CD-oPD.

2.5 *Ex-vivo* pH ratiometric sensor model

The pH ratiometric sensor assay using the CD-L/oPD-F film was carried out on pig belly skin samples *ex vivo*. Pieces of pig skin were cut uniformly in a 2 cm × 1.5 cm size and sprayed with different pH solutions ranging from 5 to 9 for 15 min according to previous studies (Tamayol et al., 2016). The CD-L-F or CD-oPD-F film was cut

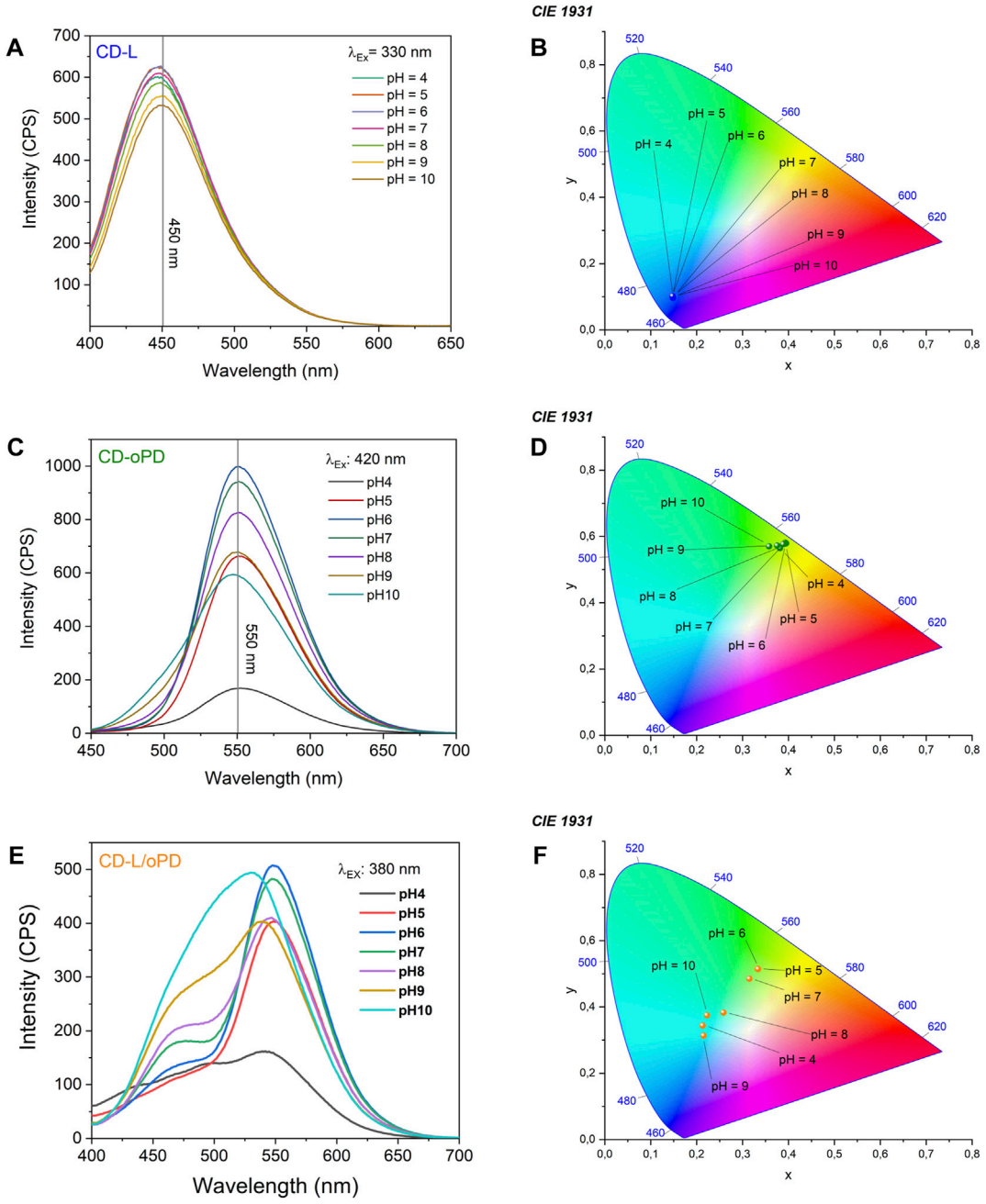

FIGURE 4
Photoluminescence spectra under different pH values for **(A)** CD-L, **(B)** CD-oPD and **(C)** CD-L/oPD and CIE chromaticity diagram for **(D)** CD-L, **(E)** CD-oPD and **(F)** CD-L/oPD.

in 1 cm × 1 cm and supported on the skin. After 30 min, the emission colors of the films were visualized through an ultraviolet lamp (360 nm).

2.6 Swelling test of the CD-L-F, CDs-oPD -F and CD-L/oPD-F films

The swelling assay was performed to evaluate the absorption and solubility of CD-L-F, CD-oPD-F and CD-L/oPD-F films in Britton-Robinson buffer solution at different pH. The films were cut into squares of 1.0 cm × 0.5 cm and immersed at intervals of time up to 90 min in a buffer solution at pH 5, 7 and 9 (≈37°C). Afterward, the films were removed from the solution and the excess buffer solution on the surface of the films was removed by blotting the surface with tissue paper (this procedure was carried out in triplicate). The swelling degree (%SW) was calculated according to Eq. 1, where M_t represents the mass of the film at intervals of time and M_0 represents the mass of the dry film at the initial time.

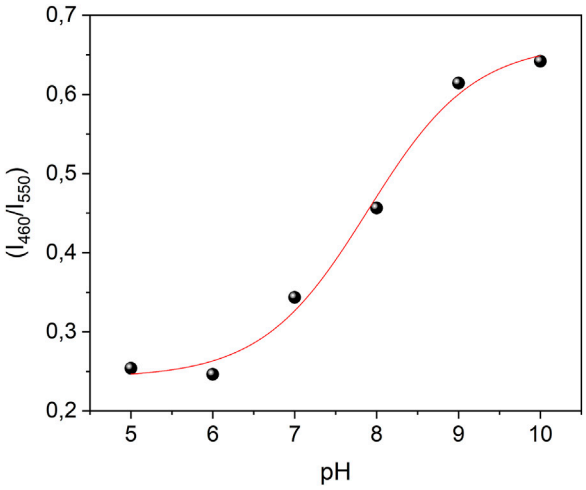

FIGURE 5
Sigmoidal fitting of the ratiometric fluorescent (I_{460}/I_{550}) CD-L/oPD in different pH.

$$\%SW = \frac{M_t\text{-}M_0}{M_0} \text{x } 100 \quad (1)$$

2.7 Characterization of materials

For Transmission Electron Microscopy (TEM) images, a JEM-2100 (JEOL, Japan) with a 200-kV accelerating voltage was used. The CDs for TEM measurements were prepared by diluting them 10-fold with ultrapure water, followed by dispersion in an ultrasonic bath, for 5 min and the resulting materials were deposited on 400-mesh carbon-coated Cu grids. To process our TEM microscopy images, we used ImageJ software for particle characterization. One hundred (100) particles were counted, and, based on this count, the average particle size for each CD synthesized was calculated. Fourier transform infrared spectroscopy (FTIR) spectra analysis of the CDs was carried out using Nicolet iS05 FTIR Spectrometer (Thermo Fisher Scientific, United States) and potassium bromide (KBr) pelleting method. To obtain the KBr pellets of the CDs, approximately 50 µL of the concentrated solution of CD-L and CD-oPD was dropped onto 20 mg of KBr. The sample was dried in an oven at 100°C for 24 h. The spectral range used for analysis was 4,000 to 400 cm^{-1}. The ultraviolet-visible (UV-Vis) absorption spectra of the CDs were acquired via Shimadzu UV/Vis/NIR Spectrometer UV-3600. The UV-Vis measurements of the films were carried on the aforementioned equipment using the solid-state system, in which the films were previously cut into a rectangular shape of 2 cm × 1.25 cm. Fluorescence spectroscopy analysis of the CDs in solution was carried out using a Shimadzu RF-5301PC Fluorescence Spectrophotometer. Solid-state measurements of the films were recorded using the Horiba-Jobin Yvon Fluorolog-3 spectrofluorometer. The emission modulation of CD-L and CD-*o*PD to obtain the ratiometric system was performed based on the photoluminescence spectrum of the sample and analyzed while varying the quantity of CDs. Thus, the obtained CD-L and CD-oPD were mixed in a ratio of 2:1 to produce the ratiometric system CD-L/oPD. The FL of the CDs (CD-L, CD-oPD and CD-L/oPD) as a function of pH was then measured using a Shimadzu RF-5301PC spectrofluorimeter. For this purpose, 50 and 25 µL of CD-L and CD-oPD, respectively, were added to 2 mL of pH solution (4–10). CD-L/oPD was measured by mixing 50 and 100 µL of CD-L and CD-oPD, respectively, in 2 mL of pH solution (4–10). The pH 4 to 10 solutions were prepared using Britton Robinson buffer (BR buffer) (0.1 mol/L), which was prepared using acetic, boric and phosphoric acids, all at a concentration of 0.4 mol/L. The acids were mixed and analyzed in a pHmeter to obtain the required pH value. Solutions of hydrochloric acid and sodium hydroxide (1 mol/L) were used to calibrate the solutions from pH 4 to 10. The photostability of the CDs was evaluated using photoluminescence spectroscopy. 50 and 25 µL of CD-L and CD-oPD, respectively, were added separately to 2 mL of water in a quartz cuvette. The fluorescence intensity (FI) of CD-L and CD-oPD was recorded under UV lamp excitation at 365 and 350 nm with emission monitored at 450 and 550 nm, respectively. Analyses were carried out for 60 min continuously, with the sample partially irradiated. The CIE 1931 chromaticity color coordinates diagram were obtained using the emission spectra of the all materials from the software Origin Pro.

2.8 Viable cells assay

To determine the biocompatibility of CD-oPD, MTT assay was used as previously reported (Mosmann, 1983; Silva et al., 2023). Human skin fibroblast lineage (HFF-1) cells were grown in 96-well plates, treated with different concentrations (0–1,000 µg mL^{-1}) and incubated for 24 h at 37°C, in a CO_2 incubator. After that, the optical density (OD) of the cells was measured at 540 nm using a spectrophotometer leading to viability (%), according to Eq. 2:

$$\text{Viability (\%)} = (\text{OD of treated cells}/\text{OD of untreated cells}) \times 100 \quad (2)$$

For statistical analysis of viable cell results, the ANOVA one-way test was used and data were compared using Tukey's method. The statistically significant difference accepted was $p < 0.05$.

2.9 Hypochlorous acid (HOCl) scavenging activity

The HOCl scavenging activity was performed according to Lucas et al. (2021). An HOCl solution was prepared at the time of analysis by adjusting the pH value of a 1% (v/v) NaOCl solution to 6.2 with H_2SO_4 addition. The reaction system consisted of the addition of phosphate buffer (100 mM, pH 7.4), CD-L or CD-oPD (3–100 µg mL^{-1}) solution, dihydrorodamine solution (DHR, 5 µM), and HOCl (5 µM). Fluorescence measurements were performed in a microplate reader (Infinite® 200 PRO, TECAN, Männedorf, Switzerland), at 310 K, at wavelengths of 505 ± 10 nm and 530 ± 10 nm, for excitation and emission,

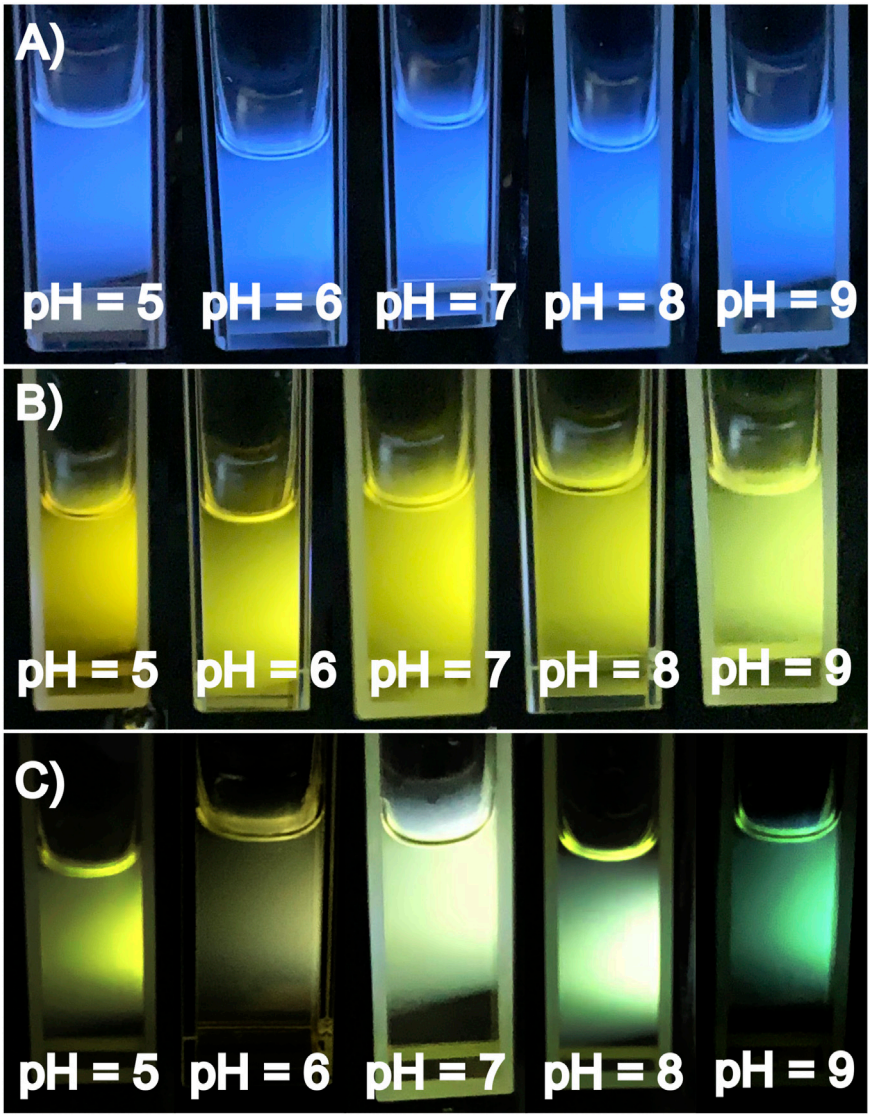

FIGURE 6
(A) Photographs of CD-L, **(B)** CD-oPD and **(C)** CD-L/oPD under different pH variations (pH = 5–9) under 360 nm UV lamp.

respectively. The results were expressed as the half-maximal inhibitory concentration (IC_{50}) in μg mL^{-1}.

2.10 Radical superoxide anion scavenging activity

The radical superoxide anion scavenging activity was determined according to Lucas et al. (2021). In a 96-well plate, the following solutions were added to the indicated final concentrations: CD-L (3–800 μg mL^{-1}) or CD-oPD (3–1,000 μg mL^{-1}), NADH (166 μM), NBT (43.3 μM) and PMS (2.7 μM). Potassium phosphate buffer (19 mM, pH 7.4) was used to dissolve CD-L, NADH, NBT, and PMS. Quercetin was used as a standard for comparison purposes. The experiment was conducted at 310 K in a microplate reader, and the absorbance was measured at 560 nm. The results were expressed as IC_{50} in μg mL^{-1}.

2.11 DPPH• scavenging assay

The evaluation of the reducing capacity of DPPH$^{\bullet}$ was conducted as previously described (Xavier et al., 2017). Briefly, aliquots of CD-L or CD-oPD (5–100 μg mL^{-1}) were added to a DPPH$^{\bullet}$ solution (40 μg mL^{-1} in methanol). Measurements were taken at 516 nm after 30 min of incubation in the dark, using a UV-Vis spectrophotometer (Agilent Technologies, Santa Clara, CA, United States). The results were expressed as IC_{50} in μg mL^{-1}.

3 Results and discussion

CD-L and CD-oPD were obtained by a simple and rapid method via microwave and hydrothermal procedures, respectively (Davi et al., 2021; Silva et al., 2023). TEM was used to provide information about the CDs morphology and size. In this regard, the TEM images

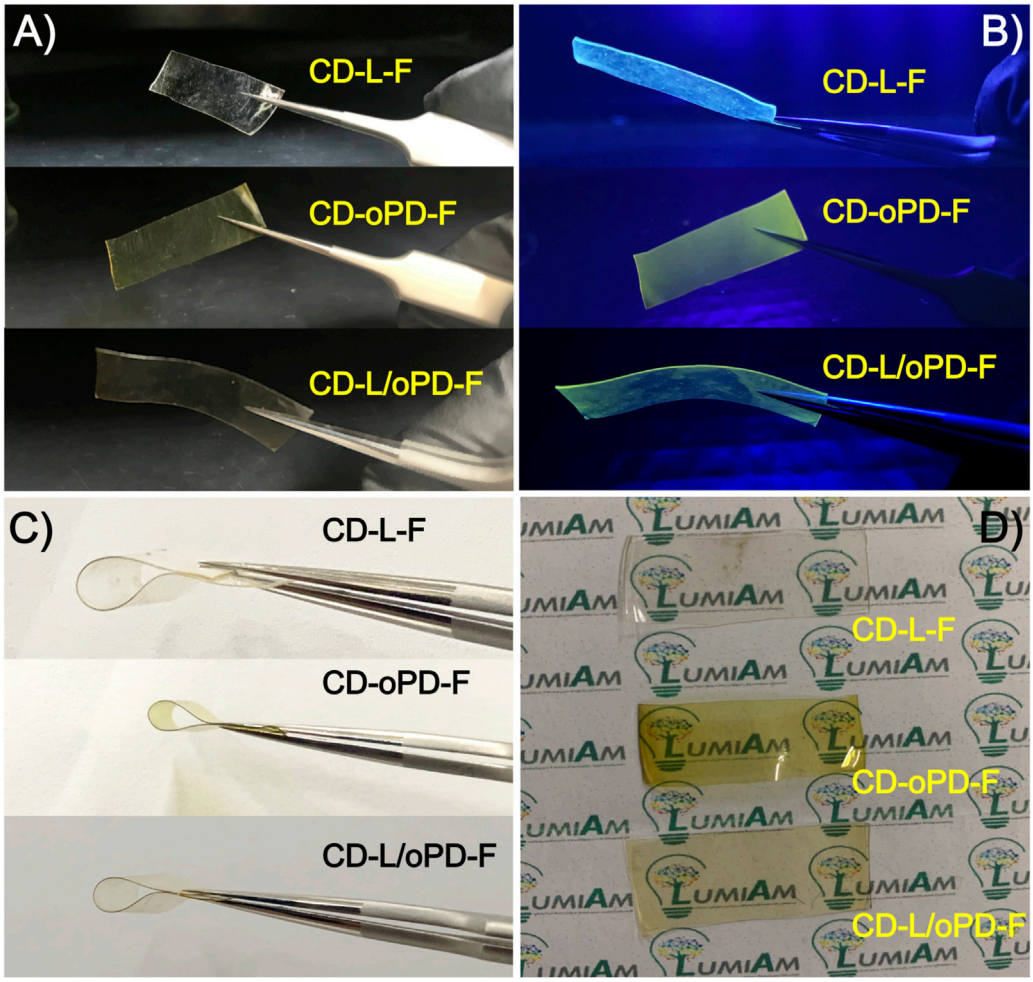

FIGURE 7
(A,B) Image before and after exposure to ultraviolet light, **(C)** flexibility tests and **(D)** transparency for CD-L-F, CD-oPD-F and CD-L/oPD-F.

showed that both CD-L and CD-oPD exhibited spherical graphitic morphology with uniform size dispersion, and average values of 2.54 ± 0.44 nm and 2.64 ± 0.60 nm, respectively (Figures 1A–C). In the magnified image displayed in Figures 1B–D, the interplanar distances typical of the graphitic structure can be observed for both carbon dots, which exhibited values of 0.21 and 0.24 nm corresponding to the diffraction plane (100) for CD-L and CD-oPD, respectively (Nascimento et al., 2023).

Fourier transform infrared spectroscopy (FTIR) was used to identify, in the CDs, the absorption peaks of the main functional groups (Figure 2A). The FTIR spectra revealed a broad and intense band attributed to the vibration of O-H stretching at around 3,445 and 3,330 cm^{-1} for CD-L and CD-oPD, respectively (He et al., 2022; Wang et al., 2022; Venugopalan and Vidya, 2023). In addition, for the CD-oPD this region includes the N-H axial deformation vibration at 3,220 cm^{-1} (Yang et al., 2019). For both CDs, it is also possible to observe C-H (sp^3) vibrations between 2,970 and 2,700 cm^{-1} (Döring et al., 2022; Jing et al., 2023). CD-L shows broad bands centered at 1722, 1,398 and 1,205 cm^{-1} suggestive of the presence C=O, C=C and C-N, associated with oxygenated groups, polyaromatic in its graphitic core and surface-functionalizing nitrogen groups, respectively (Ding et al., 2017; Ding et al., 2019). For CD-oPD, FTIR reveals peaks characteristic of aromatic C-N and N-H angular deformation associated with aromatic chain bonds observed at 1,330 and 780 cm^{-1}, respectively (Yang et al., 2019).

UV-Vis absorption spectroscopy revealed the π-π* electronic transitions of C=C bonds in the CD-L and CD-oPD graphitic nucleus, with bands centered at 225, 210 and 230 nm, respectively (Figure 2B) (Tadesse et al., 2018; Hui, 2023). In contrast, the n-π* transitions from C=O and C-N bonds can be observed in 278 e 320 nm for CD-L, and 290 e 430 nm for CD-oPD, respectively (Lu et al., 2021; Gedda et al., 2023). The photostability of the CDs was assessed using photoluminescence spectroscopy, with the fluorescence intensity (FI) recorded under UV lamp excitation for 60 min continuously (Figures 2C, D). The FI results for CD-L and CD-oPD remained practically unchanged during the analyzed period, with variations in the fluorescence signal of less than 10% (El-Shafey and Asma, 2021; Javed and O'Carroll, 2021).

Photoluminescence spectroscopy (PL) was used to investigate the luminescent properties of the CDs. CD-L and CD-oPD exhibit excitation-independent emission and the fluorescence spectrum.

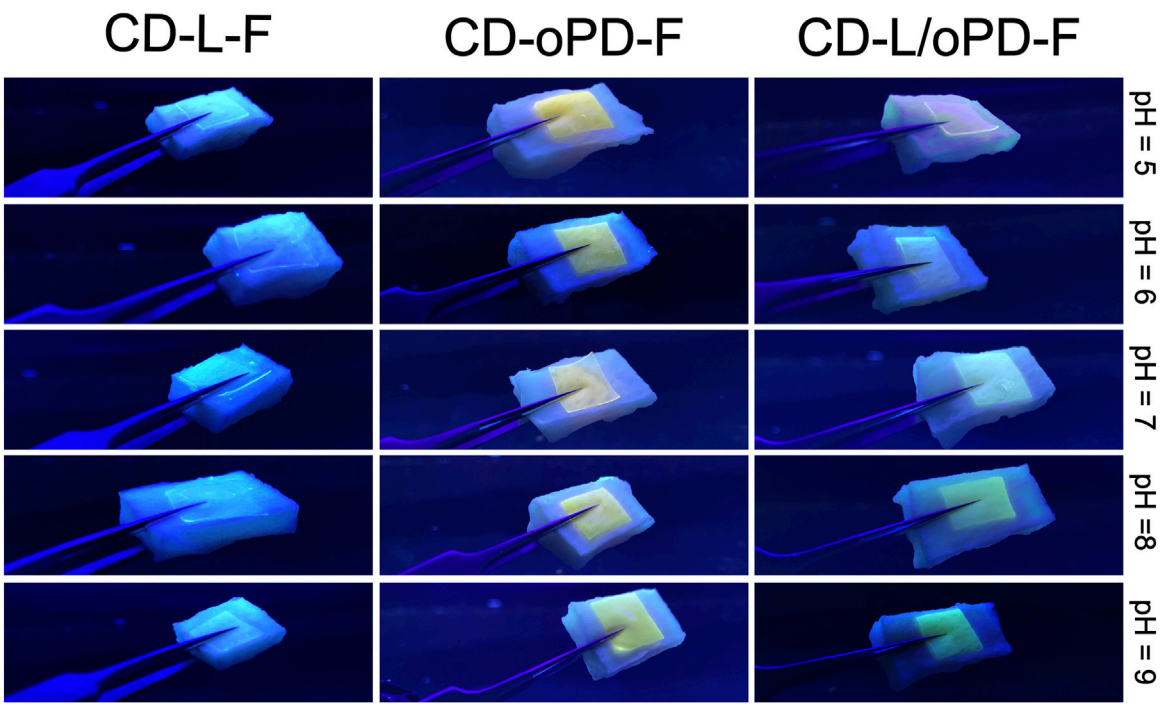

FIGURE 8
CD-L-F, CD-oPD-F, CD-L/oPD-F films supported on pieces of pig skin with different pH values.

CD-L revealed an emission band maximum centered in the blue region, at 450 nm (λ_{exc} = 330 nm) (Figure 3A). CD-oPD exhibits emission in the yellowish-green region with a maximum centered at 550 nm (λ_{exc} = 420 nm) (Figure 3C). The CDs behaviors clearly followed the chromaticity diagram, formulated by the Commission Internationale de L'Eclairage (CIE) (Figure 3B–D). Researchers have associated the independent emission of excitation wavelength (λ_{exc}) to some features of CDs, such as their uniform sizes, the presence of molecular states and/or similar groups on the surface with passivated defects (Li et al., 2014; Singh et al., 2022; Wei et al., 2023).

Under optimized conditions, solutions of CD-L and CD-oPD were mixed and it was possible to observe a fluorescence dual emission with bands centered on 450 nm and 550 nm (Figure 3E), which are consistent with the individual spectra of CD-L and CD-oPD, respectively. CD-L/oPD color coordinate points obtained from the CIE chromaticity diagram showed a clear distinction between blue and yellowish-green when the excitation wavelength increased from 370 to 420 nm (Figure 3F).

The analytical CDs response to pH variation was investigated using PL. CD-L results demonstrate that the fluorescence intensity rises with the pH increase from 4 to 5. On the other hand, fluorescence intensity decreases from pH 6 to 10 (Figure 4A). This behavior can be explained by the protonation/deprotonation mechanism, in which, after pH 7, the oxygenated groups present on the surface of CD-L are deprotonated, causing a decrease in their fluorescence intensity (Ehtesabi et al., 2020; Liu et al., 2021). In addition, the emission region did not change, remaining blue, as shown in the images of the CIE chromaticity diagram (Figure 4B).

The emission of CD-oPD was also monitored as a function of pH variation. Figure 4C shows that the fluorescence intensity gradually increased up to pH 6, after which it gradually decreased up to pH 10. This profile is similar to that of CD-L and can be explained by the same protonation/deprotonation mechanism. It can also be seen from the CIE chromaticity diagram that the emission region of CD-oPD remained in the green region (Figure 4D). Therefore, from these results, it was shown that individual CDs are unable to monitor wound healing efficiently, due to the difficult detection of color and/or fluorescence variations (Song et al., 2017; Lei et al., 2020; Xu et al., 2020; Li et al., 2021).

In this sense, a ratiometric system CD-L/oPD was developed using an optimized mixture of CD-L and CD-oPD, where the modulated resulting solutions show an excellent ratiometric colorimetric response as a function of pH (Figure 4E). From the CIE chromaticity diagram it was possible observing that the emission of CD-L/oPD aqueous solution, even with naked eyes, varied from yellowish-green to green (Figure 4F). The ratiometric system showed a high sensitivity for detecting pH in the range of 5–10. This interval, as mentioned previously, is suitable for monitoring the wound healing process. The pH response as a function of the intensity ratio (I_{460}/I_{550}) fits well to a sigmoidal curve (Figure 5), as shown in Equation 3, with an r^2 = 0.992.

$$y = 0.24 + \frac{0.66 - 0.24}{1 + 10^{0.67x\,(log\,(0-x))}} \quad (3)$$

On the other hand, CD-L and CD-oPD show a linear function in the pH range from 6 to 10. The linear fitting equation was y = 763.0–22.8x with r^2 = 0.991 and y =1,666.8–107.5x with r^2 = 0.983 for CD-L and CD-oPD, respectively (Supplementary Figures S1, S2).

10.3389/frcrb.2023.1300811

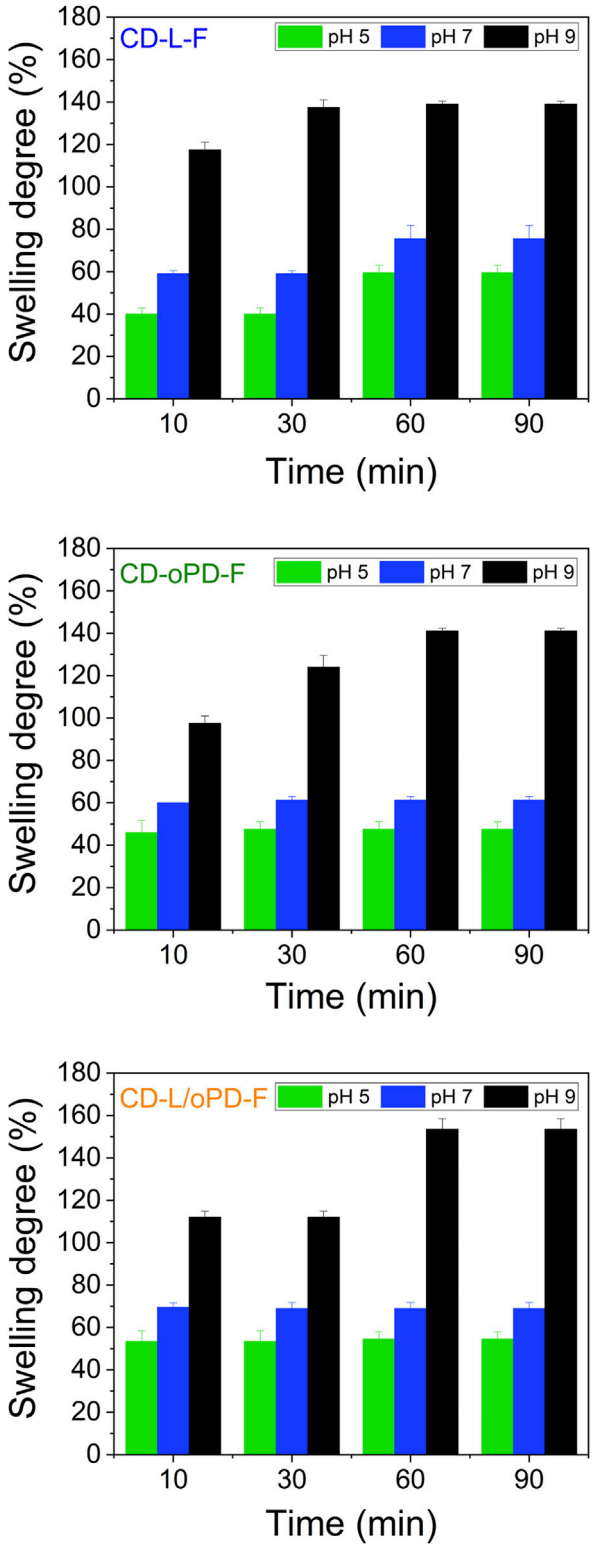

FIGURE 9
Swelling kinetics for CD-L-F, CD-oPD-F and CD-L/oPD-L in different pH values.

The data presented in Figures 4A–C, related to the influence of pH for CD-L, CD-oPD and CD-L/oPD, together with the photographs of the solutions (Figures 6A–C), indicate their corresponding trends, as expected. Hence, the CD-L results demonstrate a blue emission with no perceptible change to the naked eye. Similarly, the CD-oPD results reveal a consistent yellow emission, except at pH 9, where a pale yellowish-green color was observed. In contrast, the CD-L/oPD ratiometric system exhibits a gradient of emission color changes from yellowish-green to green with the pH varying from 5 to 9.

Both the individual nanocompounds, the CD-L and CD-oPD, and the combined one, the CD-L/oPD, were incorporated into PVA to obtain fluorescent polymeric films able to detect pH variation. Under natural light, the films obtained were colorless for CD-L-F and yellowish for CD-oPD-F and CD-L/oPD-F (Figure 7A). On the other hand, under UV light, the characteristic blue emission of CD-L was observed for CD-L-F, and yellow and yellowish-green for CD-oPD and CD-L/oPD films, respectively (Figure 7B). In addition, the fluorescent films exhibited flexibility and transparency, which can be seen in Figures 7C, D). The maximum emission wavelength of CD-L-F and CD-oPD-F shifted towards blue compared to CDs in solution. The maximum emission intensity of the CD-L-F film is at 425 nm (λ_{Exc} = 320 nm) (Supplementary Figure S3A), while CD-L in solution exhibits the maximum emission at 450 nm (λexc = 330 nm) (Figure 3A). Similarly, the maximum emission of the CD-oPD-F film occurred at 525 nm (λ_{Exc} = 410 nm) (Supplementary Figure S3B), compared to CD-oPD in solution with a maximum emission intensity of 550 nm (λ_{Exc} = 420 nm) (Figure 3B). Furthermore, when comparing CD-L/oPD solution and CD-L/oPD-F film, it can be observed that although they exhibit a similar profile in terms of the emission spectrum in the 400–650 nm range, the relative intensities of the emission bands at 450 and 550 nm have changed. In this context, it is suggested that these changes in the emission maximum or intensity ratio of the CDs in solution and in the PVA films occur due to the formation of hydrogen bonds between the PVA and the surface functional groups of the CDs when the nanoparticles are stabilized in the polymer (Bandi et al., 2018; Taspika et al., 2019). Despite the reported changes, the emission color of the films demonstrated similar behavior to those presented in solution.

For the simulation test, pork skin was exposed to solutions with different pH values in the range of 5–9, Figure 8. The prepared films were placed on the pork skin previously sprayed with different pH solutions and after 30 min they were exposed to UV radiation and a behavior similar to that previously found in the solution was clearly observed. As the pH increased from 5 to 9, a color change was observed to CD-L/oPD-F from greenish-yellow to green, respectively.

The values of the swelling degree (%SW) at different pH values of the films produced are shown in Figure 9. Overall, the degree of swelling of the films increased with pH and time reached equilibrium in 60 min. The minimum and maximum %SW values of the films at pH 5, 7 and 9 were 47.5–59.5, 59.0–75.5 and 97.5–153.5, respectively. These values were suitable to maintain the shape and uniform edges of the films, after the swelling tests (Supplementary Figures S4–S6). The swelling response as a function of pH can be attributed to ionizable functional groups of the PVA (OH) and CDs (OH and COOH), which promote an electrostatic repulsion and

TABLE 1 DPPH$^{\bullet}$, $O_2^{\bullet-}$ and HOCl scavenging potential (IC_{50}, mean ± SD) of CD-L and CD-oPD.

Sample	$O_2^{\bullet-}$ IC_{50} (μg mL^{-1})	HOCl IC_{50} (μg mL^{-1})	DPPH$^{\bullet}$ IC_{50} (μg mL^{-1})
CD-L	272.8 ± 3.3	25.1 ± 0.5	56.7 ± 0.2
CD-oPD	[a]	63.4 ± 3.8	39.5 ± 0.4
Quercetin	26.6 ± 3.7	5.6 ± 1.0	2.8 ± 0.2

[a]Inactive until the concentration of 1,000 μg mL−1.

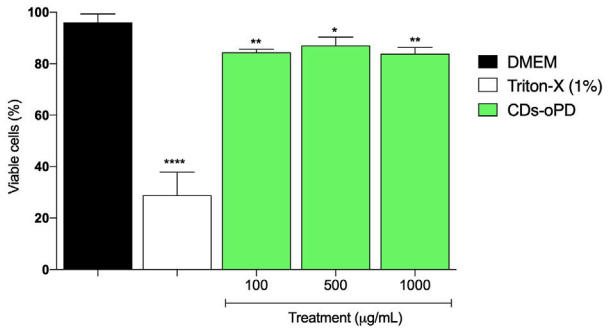

FIGURE 10
MTT assay results of the treatment of the HFF-1 cells with CD-oPD (100–1,000 μg mL^{-1}). Bars represent the mean ± standard error of the mean (SEM) of triplicates performed in the assay. Data are expressed as % viable cells compared to the control group (DMEM). Results were analyzed using GraphPad Prism software using ANOVA followed by Tukey's post-test, *p <0.05 and **p <0.01 (DMEM vs. treatment).

increase interactions with water in the function of the increase of pH (Naeem et al., 2017; Kalantari et al., 2020; Sabzi et al., 2020; Akhlaq et al., 2021; Suhail et al., 2021). As a result, an expansion of the film is observed creates a greater surface area available for the diffusion of water molecules, which leads to a significant increase in the degree of absorption of the medium. (Zafar et al., 2023).

The antioxidant capacity of CDs has been extensively examined and is attributed to the functional groups present on their surface that can stabilize reactive species through mechanisms of electron transfer or hydrogen atom transfer. The DPPH$^{\bullet}$ assay is the most commonly employed method because it is fast, easy, and economically viable; however, it is not a physiologically relevant reactive species. In this study, in addition to evaluating the antioxidant capacity of CD-oPD and CD-L against DPPH$^{\bullet}$, we also examined their potential to eliminate two biologically relevant reactive species: $O_2^{\bullet-}$ and HOCl (Table 1).

CD-L exhibited higher antioxidant capacity against physiological reactive species such as $O_2^{\bullet-}$ and HOCl. CD-oPD showed no elimination capacity against $O_2^{\bullet-}$, however, it demonstrated a greater potential for capturing the DPPH radical, with a lower IC_{50}. CDs derived from Beta vulgaris (beet juice) exhibited an IC_{50} of 231.7 μg mL^{-1} (Smrithi et al., 2022), value higher than those obtained in this study, indicating greater potential for reducing DPPH$^{\bullet}$ by CD-oPD and CD-L (Table 1). CDs derived from cloves exhibited an IC_{50} value (57 μg mL^{-1}) (Pandey et al., 2022) similar to that obtained for CD-L and higher than that obtained for CD-oPD (Table 1). Clove-derived CDs were also assessed against $O_2^{\bullet-}$ and showed an IC_{50} of 53 μg mL^{-1} (Pandey et al., 2022), indicating greater activity against this reactive species, compared to CD-L.

The samples were evaluated for their biocompatibility (absence of cytotoxicity) by the MTT method. As shown in Figure 10, cells exposed to CD-oPD showed viability greater than 80% at all concentrations tested, similar to cells treated with CD-L (Silva et al., 2023), corroborating the relatively negligible cytotoxicity of the CDs in non-transformed human fibroblasts HFF-1 cells. Cells treated with triton-X (1%) were used as a control for reduced cell viability (28% of viable cells) (Arechabala et al., 1999; Goiato et al., 2023). In comparison with other CDs and nanomaterials reported in the literature, the cell viability of CD-oPD in human fibroblasts (HFF-1 cells) exhibited more prominent cell viability (Supplementary Table S1).

Although carbon dots have been explored as fluorescent pH sensors, there are still few studies on their use for monitoring pH in wounds, since this parameter changes during the healing process. In addition, systematic studies aimed at combining different properties to offer both monitoring and treatment of wound healing are still rare (Omidi et al., 2017; Yang et al., 2019; Liu et al., 2021; Liu et al., 2021). In this sense, this work seeks to combine the use of CDs in the form of films to act as an antioxidant agent, protective barrier and colorimetric pH sensor in wounds with a view to their use as bioactive dressings.

4 Conclusion

Carbon dots (CD) derived from lemon peel bagasse (L) and *o*-phenylenediamine (*o*-PD) were prepared via simple microwave and hydrothermal methods, respectively. The blue fluorescence of CD-L and the yellow-green of CD-oDP were successfully explored in the preparation of a highly efficient dual-emissive system CD-L/oPD for pH detection. Polymeric films based on PVA and a mixture of CD-L and CD-oPD were prepared and when applied on pig skin, they displayed a significant change in the wavelength of the emission line from greenish-yellow to green with the increase of the pH values from 5 to 9. In addition, the CDs exhibited low cytotoxicity in human fibroblasts HFF-1 cells and relevant antioxidant capacity. Finally, the fluorescent film based on a CD ratiometric system may have potential for monitoring the *in-situ* pH of wounds.

Data availability statement

The original contributions presented in the study are included in the article/Supplementary Material, further inquiries can be directed to the corresponding author.

Author contributions

LS: Conceptualization, Investigation, Methodology, Visualization, Writing–original draft, Writing–review and editing. AA: Investigation, Methodology, Visualization, Writing–review and editing. JA: Investigation, Methodology, Visualization, Writing–review and editing. LD: Investigation, Methodology, Writing–review and editing, Visualization. MS: Investigation, Methodology, Visualization, Writing–review and editing. DL: Investigation, Visualization, Writing–review and editing, Resources. RV: Conceptualization, Investigation, Visualization, Writing–review and editing. JF: Investigation, Methodology, Resources, Visualization, Writing–review and editing. MG: Investigation, Resources, Visualization, Writing–review and editing. JX: Investigation, Methodology, Resources, Visualization, Writing–review and editing. CB: Conceptualization, Investigation, Project administration, Resources, Supervision, Writing–original draft, Writing–review and editing, Visualization.

Funding

The author(s) declare that financial support was received for the research, authorship, and/or publication of this article. The authors gratefully acknowledge the financial support of the Brazilian research funding agencies CAPES (Coordination for the Improvement of Higher Education Personnel) for fellowships (88887.636268/2021-00) and FAPEAL (N°: 60030.0000002294/2022) for financial support.

Acknowledgments

The authors thank the Universidade Federal de Alagoas (UFAL). RV expressed their appreciation for fellowships granted by FAPEAL/CNPq (Grant No. DCR2022051000008). The authors would like to thank Tatiane Oliveira dos Santos and Laboratório Multiusuário de Microscopia de Alta Resolução (LabMic) of the University of Goiás, Brazil, for HRTEM measurements. Optics and Nanoscopy Group (GON) for providing the infrastructure to perform the characterizations optical of CDs.

Conflict of interest

The authors declare that the research was conducted in the absence of any commercial or financial relationships that could be construed as a potential conflict of interest.

Publisher's note

Supplementary material

The Supplementary Material for this article can be found online at: https://www.frontiersin.org/articles/10.3389/frcrb.2023.1300811/full#supplementary-material

References

Akhlaq, M., Azad, A. K., Ullah, I., Nawaz, A., Safdar, M., Bhattacharya, T., et al. (2021). Methotrexate-Loaded gelatin and polyvinyl alcohol (gel/PVA) hydrogel as a pH-sensitive matrix. *polymers* 13 (14), 2300. doi:10.3390/polym13142300

Arechabala, B., Coiffard, C., Rivalland, P., Coiffard, L. J. M., and Roeck-Holtzhauer, Y. D. (1999). Comparison of cytotoxicity of various surfactants tested on normal human fibroblast cultures using the neutral red test, MTT assay and LDH release. *J. Appl. Toxicol.* 19 (3), 163–165. doi:10.1002/(SICI)1099-1263(199905/06)19:3<163::AID-JAT561>3.0.CO;2-H

Bandi, R., Devulapalli, N. P., Dadigala, R., Gangapuram, B. R., and Guttena, V. (2018). Facile conversion of toxic cigarette butts to N,S-codoped carbon dots and their application in fluorescent film, security ink, bioimaging, sensing and logic gate operation. *ACS Omega* 3 (10), 13454–13466. doi:10.1021/acsomega.8b01743

Bankoti, K., Rameshbabu, A. P., Datta, S., Das, B., Mitra, A., and Dhara, S. (2017). Onion derived carbon nanodots for live cell imaging and accelerated skin wound healing. *J. Mater. Chem. B* 5 (32), 6579–6592. doi:10.1039/c7tb00869d

Cui, F., Sun, J., Ji, J., Yang, X., Wei, K., Xu, H., et al. (2021). Carbon dots-releasing hydrogels with antibacterial activity, high biocompatibility, and fluorescence performance as candidate materials for wound healing. *J. Hazard. Mater.* 406, 124330. doi:10.1016/j.jhazmat.2020.124330

da Silva, K. R. M., Calado, C. M. S., dos Santos, T. V., Sales, T. O., Viana, R. S., Silva, U. R., et al. (2022). Plate-like CDots/EuBDC nanocomposite for ratiometric luminescence thermometry. *J. Mater. Chem. C* 10 (32), 11614–11624. doi:10.1039/d2tc01587k

da Silva, L. E., Calado, O. L. L., de Oliveira Silva, S. F., da Silva, K. R. M., Henrique Almeida, J., de Oliveira Silva, M., et al. (2023). Lemon-derived carbon dots as antioxidant and light emitter in fluorescent films applied to nanothermometry. *J. Colloid Interface Sci.* 651, 678–685. doi:10.1016/j.jcis.2023.07.124

Davi, L. B. D. O., Lima, DJDP, and Barbosa, CDDES (2021a). SÍNTESE DE CARBON DOTS A PARTIR DE DERIVADOS DE ANILINA A FIM DE AVALIAR O EFEITO DOS SUBSTITUINTES NAS PROPRIEDADES FOTOFÍSICAS E ESTRUTURAIS/SYNTHESIS OF CARBON DOTS FROM ANILINE DERIVATIVES IN ORDER TO EVALUATE THE EFFECT OF SUBSTITUENTS ON PHOTOPHYSICAL AND STRUCTURAL PROPERTIES. *Braz. J. Dev.* 7 (1), 2732–2743. doi:10.34117/bjdv7n1-186

Davi, L. B. O., Lima, D., and Barbosa, C. (2021b). Synthesis and modulation of multicolor fluorescent carbon dots from p-phenylenediamine and dansyl derivative for white light emitting diodes. *Opt. Mater.* 121, 111502. doi:10.1016/j.optmat.2021.111502

Ding, H., Ji, Y., Wei, J. S., Gao, Q. Y., Zhou, Z. Y., and Xiong, H. M. (2017). Facile synthesis of red-emitting carbon dots from pulp-free lemon juice for bioimaging. *J. Mater. Chem. B* 5 (26), 5272–5277. doi:10.1039/c7tb01130j

Ding, H., Li, X. H., Chen, X. B., Wei, J. S., Li, X. B., and Xiong, H. M. (2020). Surface states of carbon dots and their influences on luminescence. *J. Appl. Phys.* 127 (23), 231101. doi:10.1063/1.5143819

Ding, H., Zhou, X., Qin, B., Zhou, Z., and Zhao, Y. (2019). Highly fluorescent near-infrared emitting carbon dots derived from lemon juice and its bioimaging application. *J. Luminescence* 211, 298–304. doi:10.1016/j.jlumin.2019.03.064

Dong, C., Ma, X., Huang, Y., Zhang, Y., and Gao, X. (2022). Carbon dots nanozyme for anti-inflammatory therapy via scavenging intracellular reactive oxygen species. *Front. Bioeng. Biotechnol.* 10, 1–8. doi:10.3389/fbioe.2022.943399

Döring, A., Ushakova, E., and Rogach, A. L. (2022). Chiral carbon dots: synthesis, optical properties, and emerging applications. *Light Sci. Appl.* 11 (1), 75–23. doi:10.1038/s41377-022-00764-1

Ehtesabi, H., Hallaji, Z., Najafi Nobar, S., and Bagheri, Z. (2020). Carbon dots with pH-responsive fluorescence: a review on synthesis and cell biological applications. *Microchim. Acta* 187 (2), 150. doi:10.1007/s00604-019-4091-4

Elias, L., Orlando Lucas de L. Calado, and Cintya D. A. do E. S. Barbosa, (2023). Study of the photophysical properties of carbon dots derived from banana peels from different cities used to produce ink and film fluorescence. *J. Bioeng. Technol. health* 5, 250–256. doi:10.34178/jbth.v5i4.247

El-Shafey, A. M., and Asma, M. (2021). Carbon dots: discovery, structure, fluorescent properties, and applications. *Green Process. Synthesis* 10, 134–156. doi:10.1515/gps-2021-0006

Farshidfar, N., Fooladi, S., Nematollahi, M. H., and Iravani, S. (2023). Carbon dots with tissue engineering and regenerative medicine applications. *RSC Adv.* 13 (21), 14517–14529. doi:10.1039/d3ra02336b

Gedda, G., Sankaranarayanan, S. A., Putta, C. L., Gudimella, K. K., Rengan, A. K., and Girma, W. M. (2023). Green synthesis of multi-functional carbon dots from medicinal plant leaves for antimicrobial, antioxidant, and bioimaging applications. *Sci. Rep.* 13 (1), 6371–6379. doi:10.1038/s41598-023-33652-8

Goiato, M., Marobo, A., Caxias, F., da Silva, E., Gonçalves, L., Oliveira, S., et al. (2023). Cytotoxicity of cleaning agents for ocular prostheses. *Polym. Med.* 53 (1), 37–46. doi:10.17219/pim/163118

He, C., Xu, P., Zhang, X., and Long, W. (2022). The synthetic strategies, photoluminescence mechanisms and promising applications of carbon dots: current state and future perspective. *Carbon* 186, 91–127. doi:10.1016/j.carbon.2021.10.002

Huangfu, S., Jin, G., Sun, Q., Li, L., Yu, P., Wang, R., et al. (2021). The use of crude carbon dots as novel antioxidants for natural rubber. *Polym. Degrad. Stab.* 186, 109506. doi:10.1016/j.polymdegradstab.2021.109506

Hui, S. (2023). Carbon dots (CDs): basics, recent potential biomedical applications, challenges, and future perspectives. *J. Nanoparticle Res.* 25, 68. doi:10.1007/s11051-023-05701-w

Javed, N., and O'Carroll, D. M. (2021). Carbon dots and stability of their optical properties. *Part. Part. Syst. Charact.* 38 (4), 1–12. doi:10.1002/ppsc.202000271

Jin, S. G. (2022). Production and application of biomaterials based on polyvinyl alcohol (PVA) as wound dressing. *Chem. Asian J.* 17 (21), 2022005955–e202200613. doi:10.1002/asia.202200595

Jing, H. H., Bardakci, F., Akgöl, S., Kusat, K., Adnan, M., Alam, M., et al. (2023). Green carbon dots: synthesis, characterization, properties and biomedical applications. *J. Funct. Biomaterials* 14 (1), 27–32. doi:10.3390/jfb14010027

Juan, C., Pérez de la Lastra, J. M., Plou, F. J., and Pérez-Lebeña, E. (2021). The chemistry of reactive oxygen species (ROS) revisited: outlining their role in biological macromolecules (DNA, lipids and proteins) and induced pathologies. *Int. J. Mol. Sci.* 22, 4642. doi:10.3390/ijms22094642

Kadam, S., Nadkarni, S., Lele, J., Sakhalkar, S., Mokashi, P., and Kaushik, K. S. (2019). Bioengineered platforms for chronic wound infection studies: how can we make them more human-relevant? *Front. Bioeng. Biotechnol.* 7, 418. doi:10.3389/fbioe.2019.00418

Kalantari, K., Mostafavi, E., Saleh, B., Soltantabar, P., and Webster, T. J. (2020). Chitosan/PVA hydrogels incorporated with green synthesized cerium oxide nanoparticles for wound healing applications. *Eur. Polym. J.* 134, 109853. doi:10.1016/j.eurpolymj.2020.109853

Kasouni, A. I., Chatzimitakos, T. G., Troganis, A. N., and Stalikas, C. D. (2021). Citric acid-based carbon dots: from revealing new insights into their biological properties to demonstrating their enhanced wound healing potential by *in vitro* and *in vivo* experiments. *Mater. Today Commun.* 26, 102019. doi:10.1016/j.mtcomm.2021.102019

Lei, X., Fu, Y., Wu, Y., Chen, L., and Liang, J. (2020). A ratiometric fluorescent probe for pH detection based on Ag 2 S quantum dots-carbon dots nanohybrids: ratiometric fluorescent pH probe. *R. Soc. Open Sci.* 7, 200482. doi:10.1098/rsos.200482

Li, S., Song, X., Hu, Z., and Feng, G. (2021). A carbon dots-based ratiometric fluorescence probe for monitoring intracellular pH and bioimaging. *J. Photochem. Photobiol. A Chem.* 409, 113129. doi:10.1016/j.jphotochem.2021.113129

Li, X., Zhang, S., Kulinich, S. A., Liu, Y., and Zeng, H. (2014). Engineering surface states of carbon dots to achieve controllable luminescence for solid-luminescent composites and sensitive Be2+ detection. *Sci. Rep.* 4, 4976–4978. doi:10.1038/srep04976

Liu, C., Zhang, F., Hu, J., Gao, W., and Zhang, M. (2021a). A mini review on pH-sensitive photoluminescence in carbon nanodots. *Front. Chem.* 8, 1–9. doi:10.3389/fchem.2020.605028

Liu, X., Xu, H., Zhang, M., and Yu, D. G. (2021b). Electrospun medicated nanofibers for wound healing: review. *Membranes* 11 (10), 770. doi:10.3390/membranes11100770

Lu, S., Li, Z., Fu, X., Xie, Z., and Zheng, M. (2021). Carbon dots-based fluorescence and UV–vis absorption dual-modal sensors for Ag+ and L-cysteine detection. *Dyes Pigments* 187, 109126. doi:10.1016/j.dyepig.2020.109126

Lucas, M., Freitas, M., Xavier, J. A., Moura, F. A., Goulart, M. O. F., Ribeiro, D., et al. (2021). The scavenging effect of curcumin, piperine and their combination against physiological relevant reactive pro-oxidant species using *in vitro* non-cellular and cellular models. *Chem. Pap.* 75 (10), 5269–5277. doi:10.1007/s11696-021-01710-y

Macairan, J. R., Zhang, I., Clermont-Paquette, A., Naccache, R., and Maysinger, D. (2020). Ratiometric pH sensing in living cells using carbon dots. *Part. Part. Syst. Charact.* 37 (1), 1–7. doi:10.1002/ppsc.201900430

Mary, S. K., Koshy, R. R., Arunima, R., Thomas, S., and Pothen, L. A. (2022). A review of recent advances in starch-based materials: bionanocomposites, pH sensitive films, aerogels and carbon dots. *Carbohydr. Polym. Technol. Appl.* 3, 100190. doi:10.1016/j.carpta.2022.100190

Mei, H., Gu, X., Wang, M., Chen, J., Yang, X., Liu, X., et al. (2022). A tri-response colorimetric-fluorescent probe for pH and lysosomal imaging. *Sensors Actuators B Chem.* 370, 132425. doi:10.1016/j.snb.2022.132425

Moghaddam, M. A., Martino, A. D., and Šopík, T. (2021). Polylactide/polyvinylalcohol-based porous bioscaffold loaded with gentamicin for wound dressing applications. *Polymers* 13 (6), 7–9. doi:10.3390/polym13060921

Moniruzzaman, M., Dutta, S. D., Lim, K. T., and Kim, J. (2022). Perylene-derived hydrophilic carbon dots with polychromatic emissions as superior bioimaging and NIR-responsive photothermal bactericidal agent. *ACS Omega* 7 (42), 37388–37400. doi:10.1021/acsomega.2c04130

Mosmann, T. (1983). Rapid colorimetric assay for cellular growth and survival: application to proliferation and cytotoxicity assays. *J. Immunol. Methods* 65, 55–63. doi:10.1016/0022-1759(83)90303-4

Naeem, F., Khan, S., Jalil, A., Ranjha, N. M., Riaz, A., Haider, M. S., et al. (2017). pH responsive cross-linked polymeric matrices based on natural polymers: effect of process variables on swelling characterization and drug delivery Properties. *Bioimpacts* 7 (3), 177–192. doi:10.15171/bi.2017.21

Nascimento, S. M. S. D., Sonsin, A. F., Barbosa, C. D. A., and Fonseca, E. J. S. (2023). Study of the pH effect on the optical and morphological properties of S, N self-doped carbon dots applied as fluorescent anti-counterfeiting ink and pH sensor. *Nanotechnology* 34 (36), 365708. doi:10.1088/1361-6528/acdc30

Omidi, M., Yadegari, A., and Tayebi, L. (2017). Wound dressing application of pH-sensitive carbon dots/chitosan hydrogel. *RSC Adv.* 7 (18), 10638–10649. doi:10.1039/c6ra25340g

Pandey, A. K., Bankoti, K., Nath, T. K., and Dhara, S. (2022). Hydrothermal synthesis of PVP-passivated clove bud-derived carbon dots for antioxidant, catalysis, and cellular imaging applications. *Colloids Surfaces B Biointerfaces* 220, 112926. doi:10.1016/j.colsurfb.2022.112926

Pang, Q., Yang, F., Jiang, Z., Wu, K., Hou, R., and Zhu, Y. (2023). Smart wound dressing for advanced wound management: real-time monitoring and on-demand treatment. *Mater. Des.* 229, 111917. doi:10.1016/j.matdes.2023.111917

Qu, X., Gao, C., Fu, L., Chu, Y., Wang, J. H., Qiu, H., et al. (2023). Positively charged carbon dots with antibacterial and antioxidant dual activities for promoting infected wound healing. *ACS Appl. Mater. Interfaces* 15 (15), 18608–18619. doi:10.1021/acsami.2c21839

Rodríguez-Varillas, S., Fontanil, T., Obaya, Á. J., Fernández-González, A., Murru, C., and Badía-Laíño, R. (2022). Biocompatibility and antioxidant capabilities of carbon dots obtained from tomato (Solanum lycopersicum). *Appl. Sci.* 12, 773. doi:10.3390/app12020773

Roy, S., Ezati, P., Rhim, J. W., and Molaei, R. (2022). Preparation of turmeric-derived sulfur-functionalized carbon dots: antibacterial and antioxidant activity. *J. Mater. Sci.* 57 (4), 2941–2952. doi:10.1007/s10853-021-06804-2

Sabzi, M., Afshari, M. J., Babaahmadi, M., and Shafagh, N. (2020). pH-dependent swelling and antibiotic release from citric acid crosslinked poly(vinyl alcohol) (PVA)/nano silver hydrogels. *Colloids Surfaces B Biointerfaces* 188, 110757. doi:10.1016/j.colsurfb.2019.110757

Sharma, S., Mohler, J., Mahajan, S. D., Schwartz, S. A., Bruggemann, L., and Aalinkeel, R. (2023). Microbial biofilm: a review on formation, infection, antibiotic resistance, control measures, and innovative treatment. *Microorganisms* 11 (6), 1614. doi:10.3390/microorganisms11061614

Sies, H., Berndt, C., and Jones, D. P. (2017). Oxidative stress. *Annu. Rev. Biochem.* 86, 715–748. doi:10.1146/annurev-biochem061516-045037

Singh, A., Qu, Z., Sharma, A., Singh, M., Tse, B., Ostrikov, K., et al. (2022). Ultra-bright green carbon dots with excitation-independent fluorescence for bioimaging. *J. Nanostructure Chem.* 13 (3), 377–387. doi:10.1007/s40097-022-00501-5

Smrithi, S. P., Kottam, N., Muktha, H., Mahule, A. M., Chamarti, K., Vismaya, V., et al. (2022). Carbon dots derived from Beta vulgaris: evaluation of its potential as antioxidant and anticancer agent. *Nanotechnology* 33 (4), 045403. doi:10.1088/1361-6528/ac30f1

Song, W., Duan, W., Liu, Y., Ye, Z., Chen, Y., Chen, H., et al. (2017). Ratiometric detection of intracellular lysine and pH with one-pot synthesized dual emissive carbon dots. *Anal. Chem.* 89 (24), 13626–13633. doi:10.1021/acs.analchem.7b04211

Suhail, M., Fang, C. W., Khan, A., Minhas, M. U., and Wu, P. C. (2021). Fabrication and *in vitro* evaluation of pH-sensitive polymeric hydrogels as controlled release carriers. *Gels* 7 (3), 110. doi:10.3390/gels7030110

Tadesse, A., Devi, D. R., and Hagos, M. (2018). Facile green synthesis of fluorescent carbon quantum dots from citrus lemon juice for live cell imaging. *Asian J. Nanosci. Mater.* 1 (1), 36–46. doi:10.26655/ajnanomat.2018.1.5

Tamayol, A., Akbari, M., Zilberman, Y., Comotto, M., Lesha, E., Serex, L., et al. (2016). Flexible pH-sensing hydrogel fibers for epidermal applications. *Adv. Healthc. Mater.* 5 (6), 711–719. doi:10.1002/adhm.201500553

Tang, N., Zheng, Y., Jiang, X., Zhou, C., Jin, H., Jin, K., et al. (2021). Wearable sensors and systems for wound healing-related ph and temperature detection. *Micromachines* 12 (4), 430–515. doi:10.3390/mi12040430

Taspika, M., Permatasari, F. A., Nuryadin, B. W., Mayangsari, T. R., Aimon, A. H., and Iskandar, F. (2019). Simultaneous ultraviolet and first near-infrared window absorption of luminescent carbon dots/PVA composite film. *RSC Adv.* 9 (13), 7375–7381. doi:10.1039/c8ra09742a

Venugopalan, P., and Vidya, N. (2023). Microwave-assisted green synthesis of carbon dots derived from wild lemon (Citrus pennivesiculata) leaves as a fluorescent probe for tetracycline sensing in water. *Spectrochimica Acta - Part A Mol. Biomol. Spectrosc.* 286, 122024. doi:10.1016/j.saa.2022.122024

Wang, B., Cai, H., Waterhouse, G. I. N., Qu, X., Yang, B., and Lu, S. (2022). Carbon dots in bioimaging, biosensing and therapeutics: a comprehensive review. *Small Sci.* 2 (6), 2200012. doi:10.1002/smsc.202200012

Wang, Z., Liu, L., Bu, W., Zheng, M., Jin, N., Zhang, K., et al. (2020). Carbon dots induce epithelial-mesenchymal transition for promoting cutaneous wound healing via activation of TGF-β/p38/snail pathway. *Adv. Funct. Mater.* 30 (43), 2004886. doi:10.1002/adfm.202004886

Wei, X. L., Shi, Q. L., Jiang, L., and Qin, Y. (2023). Multicolour carbon dots with excitation-independent emission by microwave solvothermal reaction. *Carbon Lett.* 33 (1), 191–201. doi:10.1007/s42823-022-00416-9

Wu, X., Abbas, K., Yang, Y., Li, Z., Tedesco, A. C., and Bi, H. (2022). Photodynamic anti-bacteria by carbon dots and their nano-composites. *Pharmaceuticals* 15 (4), 487–521. doi:10.3390/ph15040487

Xavier, J., Valentim, I. B., Camatari, F. O. S., de Almeida, A. M. M., Goulart, H. F., Ferro, J. N. S., et al. (2017). Polyphenol profile by uhplc-ms/ms, anti-glycation, antioxidant and cytotoxic activities of several samples of propolis from the northeastern semi-arid region of Brazil. *Pharm. Biol.* 55 (1), 1884–1893. doi:10.1080/13880209.2017.1340962

Xia, C., Cao, M., Xia, J., Zhou, G., Jiang, D., Zhang, D., et al. (2019). An ultrafast responsive and sensitive ratiometric fluorescent pH nanoprobe based on label-free dual-emission carbon dots. *J. Mater. Chem. C* 7 (9), 2563–2569. doi:10.1039/c8tc05693e

Xu, S., He, X., Huang, Y., Liu, X., Zhao, L., Wang, X., et al. (2020). Lysosome-targeted ratiometric fluorescent sensor for monitoring pH in living cells based on one-pot-synthesized carbon dots. *Microchim. Acta* 187 (8), 478–516. doi:10.1007/s00604-020-04462-w

Yang, P., Zhu, Z., Zhang, T., Zhang, W., Chen, W., Cao, Y., et al. (2019). Orange-emissive carbon quantum dots: toward application in wound pH monitoring based on colorimetric and fluorescent changing. *Small* 15 (44), 1–11. doi:10.1002/smll.201902823

Zafar, N., Mahmood, A., Ilyas, S., Ijaz, H., Muhammad Sarfraz, R., Mahdi, W. A., et al. (2023). Novel Natrosol/Pectin-co-poly acrylate based pH-responsive polymeric carrier system for controlled delivery of Tapentadol Hydrochloride. *Saudi Pharm. J.* 31 (8), 101671. doi:10.1016/j.jsps.2023.06.004

Zhang, T., Dong, S., Zhao, F., Deng, M., Fu, Y., and Lü, C. (2019). Tricolor emissive carbon dots for ultra-wide range pH test papers and bioimaging. *Sensors Actuators, B Chem.* 298, 126869. doi:10.1016/j.snb.2019.126869

Zhu, Y., Zhang, J., Song, J., Yang, J., Du, Z., Zhao, W., et al. (2020). A multifunctional pro-healing zwitterionic hydrogel for simultaneous optical monitoring of pH and glucose in diabetic wound treatment. *Adv. Funct. Mater.* 30 (6), 1–9. doi:10.1002/adfm.201905493

frontiers | Frontiers in Carbon

TYPE Original Research
PUBLISHED 15 December 2023
DOI 10.3389/frcrb.2023.1305515

OPEN ACCESS

EDITED BY
Lei Shi,
Sun Yat-sen University, China

REVIEWED BY
Ricardo Wagner Nunes,
Departamento de Física—ICEx—Universidade Federal de Minas Gerais, Brazil
Rami Ahmad El-Nabulsi,
Chiang Mai University, Thailand

*CORRESPONDENCE
A. Latgé,
alatge@id.uff.br

RECEIVED 01 October 2023
ACCEPTED 28 November 2023
PUBLISHED 15 December 2023

CITATION
Lage LL and Latgé A (2023), Quasi-one-dimensional carbon-based fractal lattices.
Front. Carbon 2:1305515.
doi: 10.3389/frcrb.2023.1305515

Quasi-one-dimensional carbon-based fractal lattices

L. L. Lage and A. Latgé*

Instituto de Física, Universidade Federal Fluminense, Niterói, Rio de Janeiro, Brazil

Fractal systems are now considered alternative routes for engineering physical properties on the nanoscale. In particular, stable annular quantum corrals have been demonstrated in distinct synthesis procedures and can provide interesting localized and resonant states. We here present a theoretical description of effective fractal lattices, mainly composed of annular Koch geometries based on carbon atoms, and of more complex organic molecules described by triangular Sierpinski geometries. A single band tight-binding approach is considered to derive electronic and transport properties. Fractal molecular linear chains composed of fractal Koch quantum corrals are proposed, and their electronic transport is discussed based on the complexity of the neighboring hopping. The spatial charge distributions at different energies highlight the contribution of the composing metallic and carbons atoms in the quantum corral features, serving as a guide to new functionalization applications based on the symmetry and fractal peculiarities of the proposed nanostructured lattices.

KEYWORDS

fractals, molecular chains, electronic and transport properties, Koch fractals, tight-binding models

1 Introduction

A crucial size parameter for determining the physical properties of a system is its dimensions. For example, in quasi-1D nanostructured systems such as extensively studied graphene nanoribbons (Castro Neto et al., 2009; Wakabayashi et al., 2010; Berdonces-Layunta et al., 2022), the electron confinement is characterized by 1D-like Van Hove singularities in the density of states (DOS). Quantum corrals are also important nanosystems for studying localized states and have been explored since their first synthesis in 1993 (Crommie et al., 1993). More recently, covalently linked large-sized organic quantum corrals were made possible through bottom-up growth processes with atomic precision, revealing a high degree of controlling localization and resonant states (Peng et al., 2021). Usually, the localized states are highly degenerated and exhibit a set of flat bands of increasing interest to condensed matter physics (Freeney et al., 2022; Kempkes et al., 2019).

On the other hand, fractals are fascinating natural objects and have been extensively investigated within mathematical and theoretical frameworks, taking into account the different focuses for discussing fractal geometries. Advances and future challenges of fractal materials have been discussed recently by Gowrisankar and Banerjee (2021), with advanced research proposing the application of fractal features to the dynamics of highly nonlinear complex systems. A very good overview of fractal origins and applications is also available in the classical book by Mandelbot (1983). The advance of experimental techniques in synthesizing finite fractal molecules, such as self-assembly (Shang et al., 2015), electrostatic attraction (Dai et al., 2023), have allowed a better comprehension of the particles interacting within fractal lattices; this lies in non-integer dimensions known as "Hausdorff dimensions". Carbon-nanotube-based networks have been successfully designed

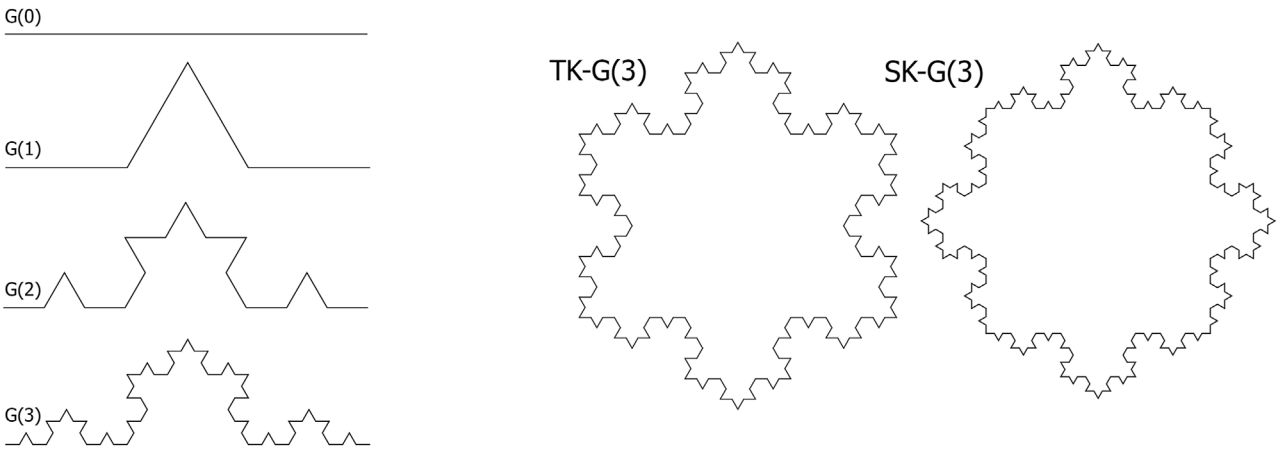

FIGURE 1
Left chart: Koch lines generations 0, 1, 2, and 3 from top to bottom, respectively. Right chart: triangular Koch TK-G (3) and square Koch SK-G (3).

to work as neural sensor devices (Browning et al., 2021), among other interesting fractal hierarchical investigations of single-walled carbon nanotube films (De Nicola et al., 2015) and other graphite systems (Zhou et al., 2016). Electrons and photons (Xu et al., 2021) moving through such lattices undergo the fractional dimension of the structures, revealing self-similar patterns on the corresponding band structures, density of states (DOS), and electronic conductance. Molecular chains based on carbon Sierpinski triangle architectures have been recently reported (Zhang Y., et al. 2020; Lage and Latgé,2022), exhibiting the manifestation of different spatial charge distribution which may be explored in functional nanodevices (de Laissardie're et al., 2010).

Here, we present a fractal version of a Koch snowflake-like quantum corral in two symmetries: the triangular and square Koch corrals. A topological description of the systems is depicted in Figure 1: triangular and square Koch rings, named "TK-G (n)" and "SK-G (n)", respectively. The decorated rings are obtained by particular rotations in the Koch lines, resulting in C_{3v} and C_{4v} symmetries, respectively. The Koch chain dimension is calculated from $D = log(N)/log(L)$, with N being the number of lines between each corner and L the proportional length-fraction of each line compared with the first order G (0), giving $D = log(4)/log(3) = log(16)/log(9) = log(64)/log(27) \approx 1.26$, respectively, for the 1^{st}, 2^{nd}, and 3^{th} generations. As expected, this dimension applies also for the TK and SK snowflakes.

Such quasi-one-dimensional fractal geometries with triangular, square, pentagonal, and hexagonal symmetries were experimentally probed through chemical routes, in which nitrogen bases are connected between metallic atoms (Ru, Fe, and Co) to construct quantum-corral molecular architectures with trapped electrons (Wang et al., 2018; Jiang et al., 2017; Zhang Z. et al., 2020.) With the actual engineering facilities of varying molecular geometries mainly assembled by carbon based composites (Peng et al., 2021), quantum corrals have become ideal systems for studying electronic wave resonances, electronic confinement, and other rich quantum responses. In this work, we explore a variety of localized states in annular geometries, considering both triangular and square Koch symmetries. We investigate electronic properties such as transmission, band structure, and the spatial distributions of the electronic states through density of states on molecular chains that may be compared with STM images. The systems are described within a tight binding framework in which the lattice is included in a microscopy point of view, and not following continuum models (El-Nabulsi and Anukool, 2021; El-Nabulsi and Anukool, 2023). The theoretical approach is used to describe synthesized chemical molecules and to prescribe possible smart routes for application in selective transport nanodevices.

2 Theoretical model

A single-orbital tight-binding (TB) Hamiltonian is used to describe the proposed Koch systems, given by:

$$H = \sum_i \varepsilon_i c_i^\dagger c_i + \sum_{\langle ij \rangle} t_{ij} c_i^\dagger c_j + \sum_{\langle\langle ij \rangle\rangle} t'_{ij} c_i^\dagger c_j + h.c. \quad (1)$$

with ε_i being the on-site energy for an atom located at site i, $c_i^\dagger$ (c_i) being the creation (annihilation) operator of an electron on site i, and $t_{i,j}$ and $t'_{i,j}$ being the hopping energies for nearest neighbors (1N) and second-nearest neighboring (2NN) atoms, respectively. We discuss below the effects of considering both first and second neighboring atoms in the Hamiltonian. For the corral lattices, we discuss here, via fractal Koch curves, the urgency of including second and/or further neighboring interactions which will be dictated by the real system to be described, and by a proper comparison with the experimental data, if available (STM images and dI/dV curves, for instance), and with first principle calculations.

The electronic properties of the studied corrals are derived via the eigenfunctions ψ_n and eigenenergies λ_n determination, with n being the number of sites. The local density of states (LDOS) is obtained using a Lorentzian function to better adjust the electronic states as following:

$$LDOS(E, r_0) = \frac{1}{2\pi} \sum_n |\psi_n(r_0)|^2 \frac{\Gamma}{(E - \lambda_n)^2 + 0.25\Gamma^2}, \quad (2)$$

where r_0 are the site positions. The total density of states (DOS) is calculated by summing $LDOS(E, r_0)$ over all sites.

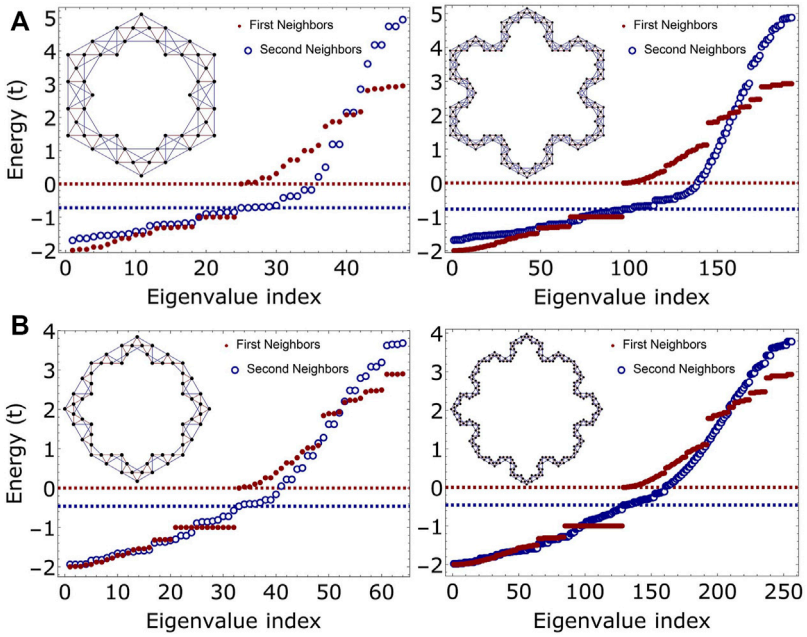

FIGURE 2
Comparison between the energy spectra of **(A)** triangular and **(B)** square Koch corrals of second (left) and third (right) generations, G (2) and G (3), respectively. Fermi levels are marked by dashed lines.

Transport properties are calculated using the Landauer approach (Data, 1995), in which the system is decoupled into three parts: central conductor, and right and left leads (Felix et al., 2022; Santos et al., 2020; Chico et al., 2015). We consider semi-infinite Koch chains as leads, perfectly matching the central scattering region. Following the Green function formalism, we can also obtain local DOS. The central advanced (a) and retarded (r) Green functions are given as

$$G_c^{a,r}(E) = \left[\omega - H_c - \Sigma_L^{a,r}(E) - \Sigma_R^{a,r}(E)\right]^{-1}, \quad (3)$$

with $\omega = E \pm i\eta$, η being an infinitesimal energy value and H_c being the Hamiltonian of the central part. $\Sigma_{L,R}^{a,r}(E)$ correspond to left and right self-energies, given by the related surface Green functions, from which the coupling matrices are obtained via $\Gamma^{L,R}(E) = i(\Sigma_{L,R}^{r}(E) - \Sigma_{L,R}^{a}(E))$. Finally, to derive the electronic conductance in Koch chains, G (E)=$2e^2/h\mathcal{T}(E)$, we calculate the energy-dependent transmission given by

$$\mathcal{T}(E) = \mathrm{Tr}\left[\mathbf{\Gamma}^L \boldsymbol{G}_c^r \mathbf{\Gamma}^R \boldsymbol{G}_c^a\right]. \quad (4)$$

3 Results and discussions

3.1 Koch quantum corrals

We now explore square and triangular geometries, using the Koch fractal, as basic units that comprise molecular systems. Figures 2A, B presents a comparison between the eigenenergies of TK and SK-second generation corrals, respectively, considering first (red curves) and second (blue curves) neighbors, with the second hopping given by $t' = 0.5t$. This particular value of hopping energy may be overestimated compared to the smaller intensity parameter usually adopted for graphene-based lattices ($t' = 0.1t$). It was chosen considering an inverse linear dependence with atomic distance. Smaller values that should also be considered reduce the changes on the electronic features compared to the single first-neighbor model. However, as we want to highlight how changes may be induced by considering the NN2, we consider stronger coupling limits. It is clear from the results in Figure 2 that the two fractal arrangements (triangular and square) have similar energy spectra for both first and second neighbor models, although they have different numbers of atoms. The corresponding Fermi energies are depicted for both cases in blue and red horizontal dashed lines. While there are available energy states crossing the Fermi level for the 2NN model, the Fermi level is marked by an energy gap $E_{gap} = t$ for the 1N description, revealing a semiconducting-like feature for that model. A simple comparison between the G (2)-TK and SK eigenvalue results for first neighbors shows a 6- and 12-order degeneracy for the state $E = -t$, respectively, which is responsible for the sharp peak in the corresponding electronic density of states (red curve) in the bottom of Figure 3A.

By comparing the LDOS for both first- and second-neighbor results at $E = -t$ (Figure 3B), we note that the electronic density is localized in a dimer-like charge distribution or displayed mostly around all the corral sites, respectively. This difference occurs due to the degeneracy lift and the subsequent formation of a bounding state, caused by the inclusion of second-neighbor interactions that are responsible for spreading the charges through the annular corral. At $E = -1.64t$, the dimmer-like feature is preserved for the case of the 1N model, although rotated spatially relative to the $E = -t$ example, and preferring the external ST positions. In contrast, the charge for

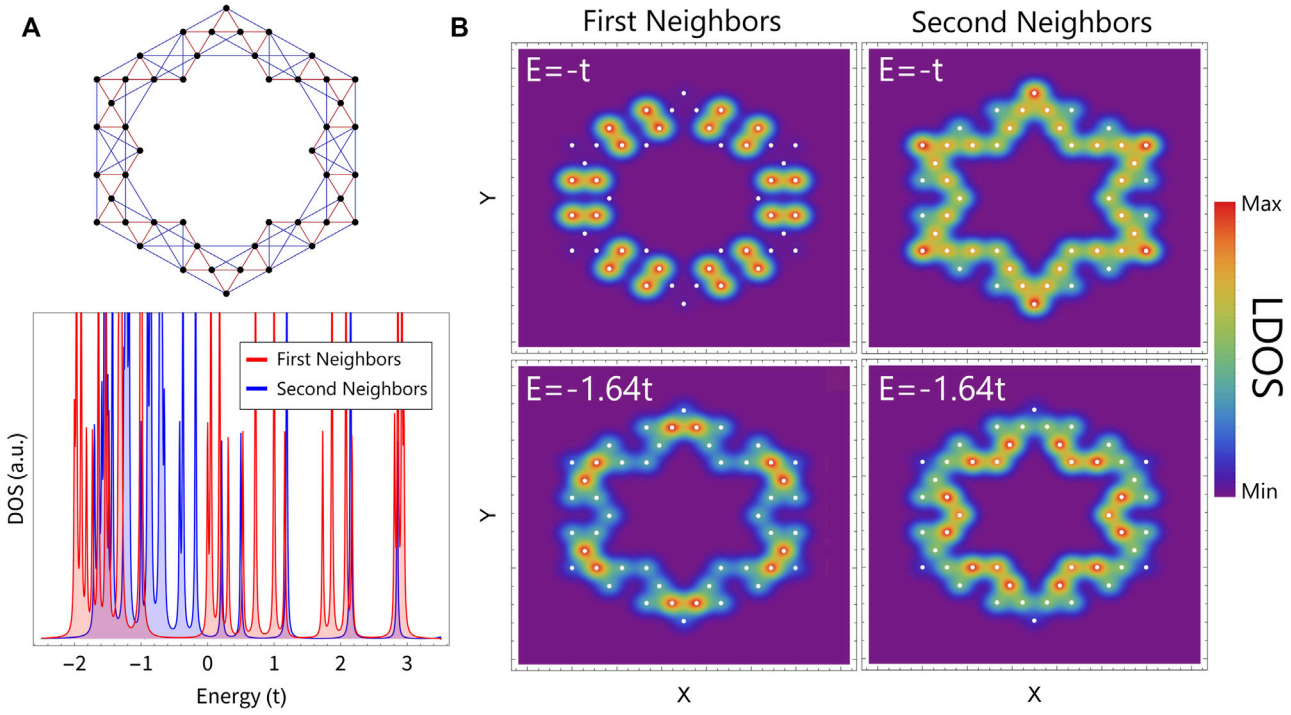

FIGURE 3
Results for a G (2)-TK using first (red curve) and second neighbors (blue curve) TB models. **(A)** Schematic view of the triangular corral (top) and DOS (bottom). **(B)** LDOS comparison at energy values equal to $E = -t$ and $E = -1.64t$, available for both cases. Parameters: $t' = 0.5t$ and $\varepsilon = 0$.

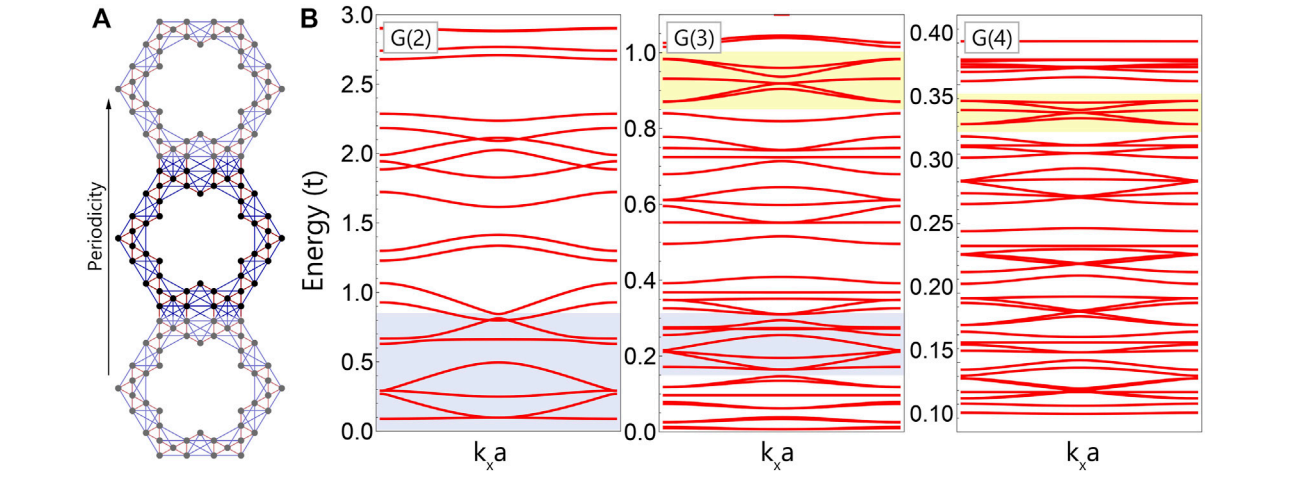

FIGURE 4
(A) G (2)-TK chain illustration with first (red lines) and second (blue lines) neighbors; **(B)** Corresponding G (2), G (3), and G (3)-TK electronic bands considering only first neighbors and $\varepsilon = 0$.

the 2NN case is more pronounced at the internal sites of the corral (see bottom part of Figure 3B). It is important to emphasize that, although triangular and square Koch corrals exhibit similar eigenspectra, as shown in 2, the charges are distributed as expected around the sites according to each symmetry. The charge distribution effects are also preserved in molecular Koch-corral chains, as discussed next.

3.2 Molecular Koch-corral chains

As previously reported (Zhang Z. et al., 2020), the synthesized corrals are usually displayed in lines very close to each other, or sometimes physically connected (Dai et al., 2023). Therefore, in this section we propose a TB model connecting the Koch corrals in order to create a kind of molecular chain with periodic boundary

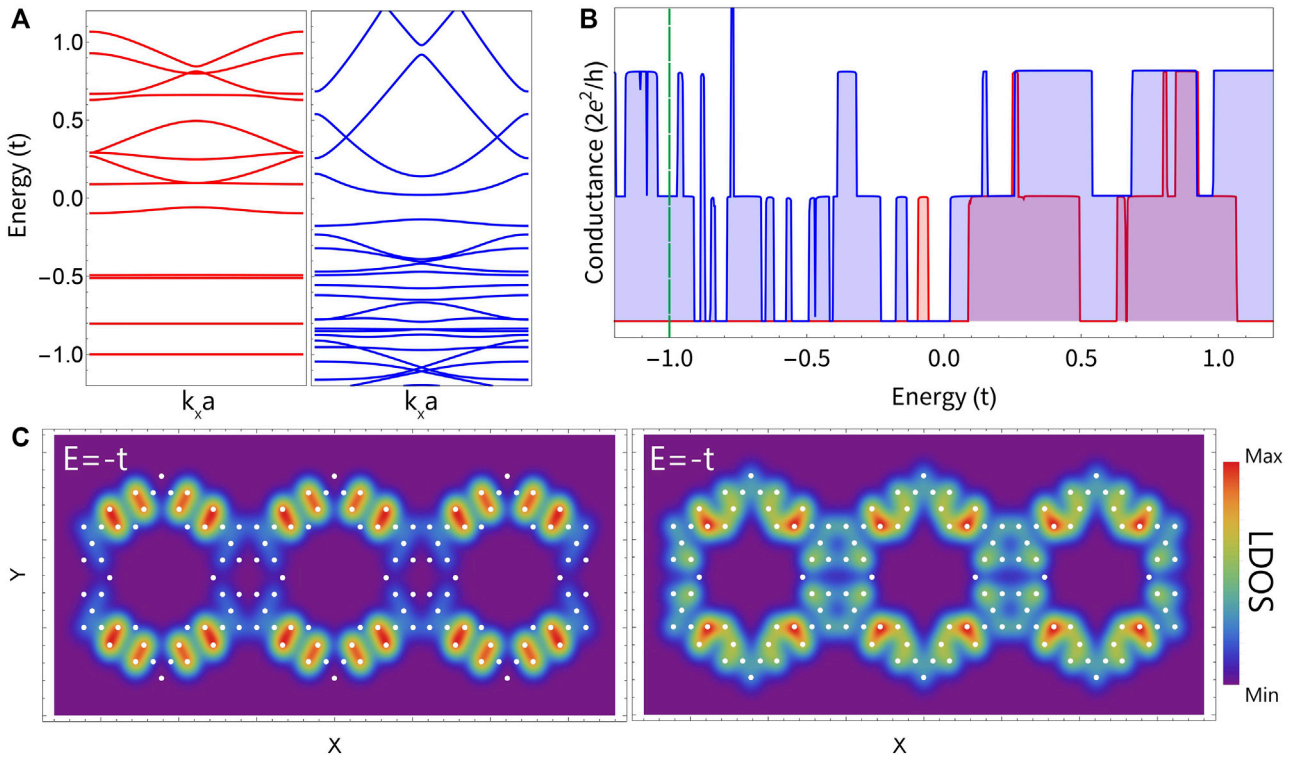

FIGURE 5
TK-G2 chain results considering first (red) and up to second (blue) neighbors, respectively. **(A)** Electronic bands, **(B)** electronic conductance, and **(C)** local density of states at $E = -t$.

conditions along one single direction. Usually, the fractal dimension in a perfectly symmetrical system promotes energy spectra with fractal characteristics and exhibiting infinite band gaps in the thermodynamic limit. Such characteristic features are verified by comparing electronic band structures or the density of electronic states of different fractal generations revealing the self-similar aspects in energies (Lage and Latgé,2022; Pedersen, 2020). The results for the electronic structures for three successive generations G (2), G (3), and G (4) are shown in Figure 4 using the 1N model. It is possible to see the occurrence of self-similarity allusions between the band structures, highlighted by the shadow regions (blue and yellow) in the figure, at narrower energy ranges as we move to higher orders of Koch-corral structures. This is a fundamental aspect of the fractal nature emerging from the electronic properties of such systems. It is important to note that real self-similarity patterns should require perfect fractal geometries, as presented, for instance, in triangular Sierpinski lattices (Domany et al., 1983; Wang, 1995; Pedersen, 2020). In the construction of the proposed TK chains, the presence of the interfaces between the fractal units breaks the ideal fractal symmetry of the single flakes. In the absence of such perfect self-similarity features, we have not explored the localization nature of the involved wavefunctions.

Figure 5A compares the electronic structure of the TK-G2 discussed in Figure 4, considering 1N (red curves) and 2NN (blue curves) models. Remarkably, the negative energy spectrum for the 1N model exhibits almost flat bands—that is, without dispersion, a manifestation of high localized states. For the 2NN approach, however, the spectrum is more dispersed. The electronic conductance results for TK-G (2) chains described by both models are shown in Figure 5B. As expected from the electronic bands relative to the 1N model, the transport response is mostly null for the considered negative energy range. In a more realistic model, up to second neighborhood, the number of available channels increases—marked by the blue conductance in the same energy range—due to the non-zero electronic group velocities in the energy interval from $-1.2t$ to zero.

Concerning to the charge distribution at $E = -t$ (Figure 5C), it is clear that, for the 1N model, the charges are concentrated around particular sites that resemble the localized states for the same geometry in the single corral (Figure 3). The wavefunction of such states does not spread along the neighboring unit cells of the molecular chain (Koch corrals), resulting in high localized states and suppression of the transport response at this energy. The situation is completely different within the 2NN model, as shown in the results of the corresponding LDOS (right panel in Figure 3C), highlighting the delocalization of the state through the chain.

3.3 Effective molecular quantum corrals

As mentioned in the introduction, with recent experimental advances in the synthesis and fabrication of carbon nanocomposites, new possible geometries can be explored that take into account the interplay between fractal structures and regular geometries. Here, we propose a quantum corral based on hexagonal symmetries similar to the previously reported hexagram (Zhang Z. et al., 2020) and

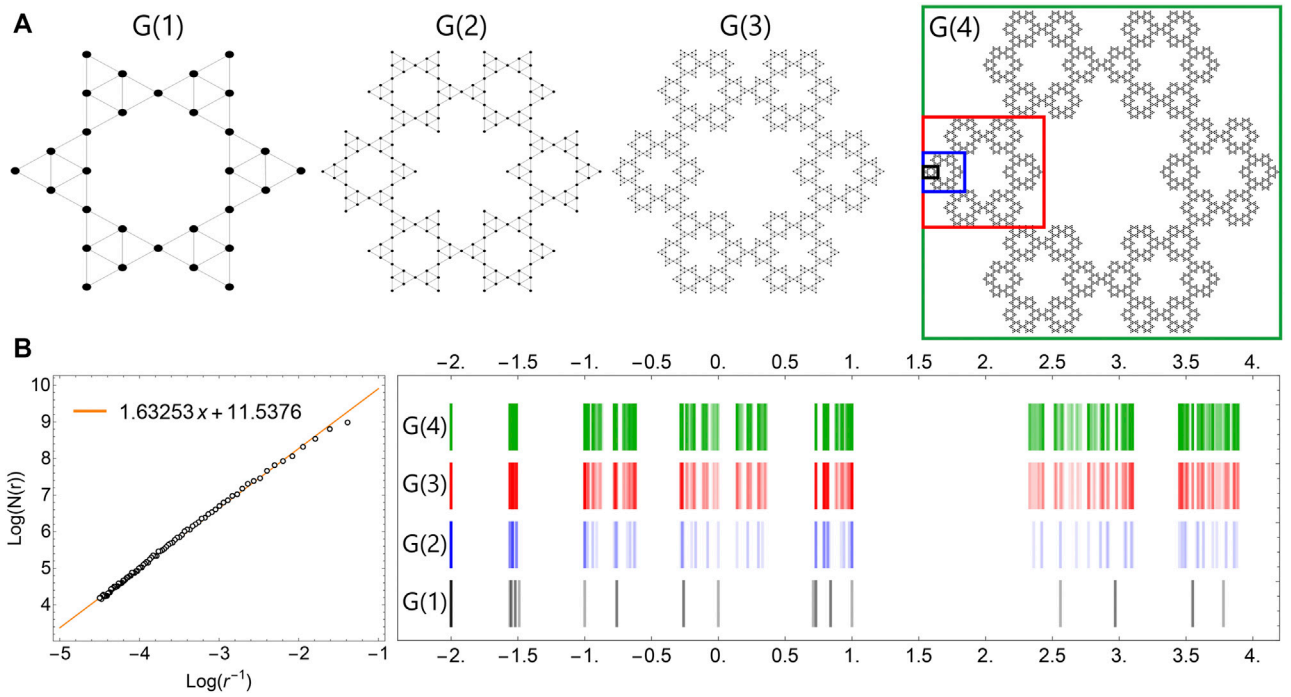

FIGURE 6
(A) From left to right: schematic view of G (1–4) fractal corral structures. For G (4), the colored squares distinguish G (1–4) generations. **(B)** Left: numerical results for energy spectra in G (1–4); colored bar bright is directly proportional to the degeneracy order of states. Right: box counting linear fit result.

hexagonal gasket (Newkome et al., 2006). However, in our suggested TB framework, the systems can be considered hexagonal triangular Sierpinski corrals of different orders (HTS). They are generated by repeating Sierpinski triangles connected to form self-similar objects like Koch corrals, as depicted in the G (1–4) sequence (Figure 6A). For the sake of simplicity, we first consider the nanostructures composed of equal atoms, represented by the black dot in all the 4^{th} first generations G (1–4). In particular, we have taken all on-site energies in the Hamiltonian $\epsilon_i = 0$ representing the carbon lattices. The fractal dimension D of the proposed system can be calculated through the relation (Foroutan-pour et al., 1999):

$$D = \lim_{r \to 0} \frac{Log[N(r)]}{Log[r^{-1}]} \tag{5}$$

with $N^{®}$ being the number of squares as a function of the size r delimited by the image size. The box counting method (Kaurov, 2012) was used to estimate the fractal dimension, where it can be obtained by the linear regression of the values as illustrated in the right-hand chart in Figure 6B. The dimension estimated for the nanostructured system proposed here is $D \approx 1.63$, which is consistent with the reported version with hexagonal units instead of Sierpinski triangles (Devaney, 2004), where $D = log(6)/log(3) \approx 1.63$.The energy spectrum for the first G (1–4) generations is depicted in the diagram shown in the right-hand panel of Figure 6B. The corresponding degeneracy of the states is coded by the brightness of the colored bars in a direct correspondence. For example, at $E = -2t$ there are 6, 42, 258, and 1,554 degenerate states in the sequence of G (1–4), respectively, and also at $E = -t$ for G (2–4).

Returning to the molecular synthesized structures, due to the presence of chemical elements in the systems other than carbon atoms, we have chosen different on-site energies in the numerical calculations: $\varepsilon_C = 0.25t$, $\varepsilon_{Fe} = -0.25t$, and $\varepsilon_{Ru} = -0.35t$.We have also investigated (not shown here) cases in which $\varepsilon_{Ru} > \varepsilon_{Fe}$, which did not produce significantly changes in the present results. The set of different atomic site symmetries in the effective lattice is denoted by circles of different colors, as illustrated in the right-hand chart in Figure 7A. Note that other non-equivalent sites are also marked in the figure with dashed black circles that represent sites very similar to those marked by purple and red circles. The LDOS corresponding to the four non-equivalent colored sites are shown in Figure 7B. The total density of states (averaged over the total number of atoms) is also displayed in shaded grey curves. Special charge densities over the quantum corral sites are depicted in Figure 7C for different states marked in the eigenenergy spectrum diagram. The spatial LDOS for the energies $E = -0.3t$ and 0, next to the Fermi level ($E_F = -0.3t$), and also for $E = 1.1t$, show that the main contributions comes from Fe and C sites located in the internal hexagonal. On the other hand, for $E = -1.3t$, the highest LDOS values come from the Ru atom positions. The charge density panels are consistent with the previous results of the LDOS versus energy presented in Figure 7B, which highlight the charge distribution weight at the individual atomic corral sites. The construction of higher generation lattices would help to identify possible self-similarity manifestations on the electronic properties. Also important is the incorporation of spin-orbit coupling, mainly at the metallic sites, and hybridized-orbital models to allow more realistic description of the metal organic fractal structures (Canellas Núnez et al., 2023). Such

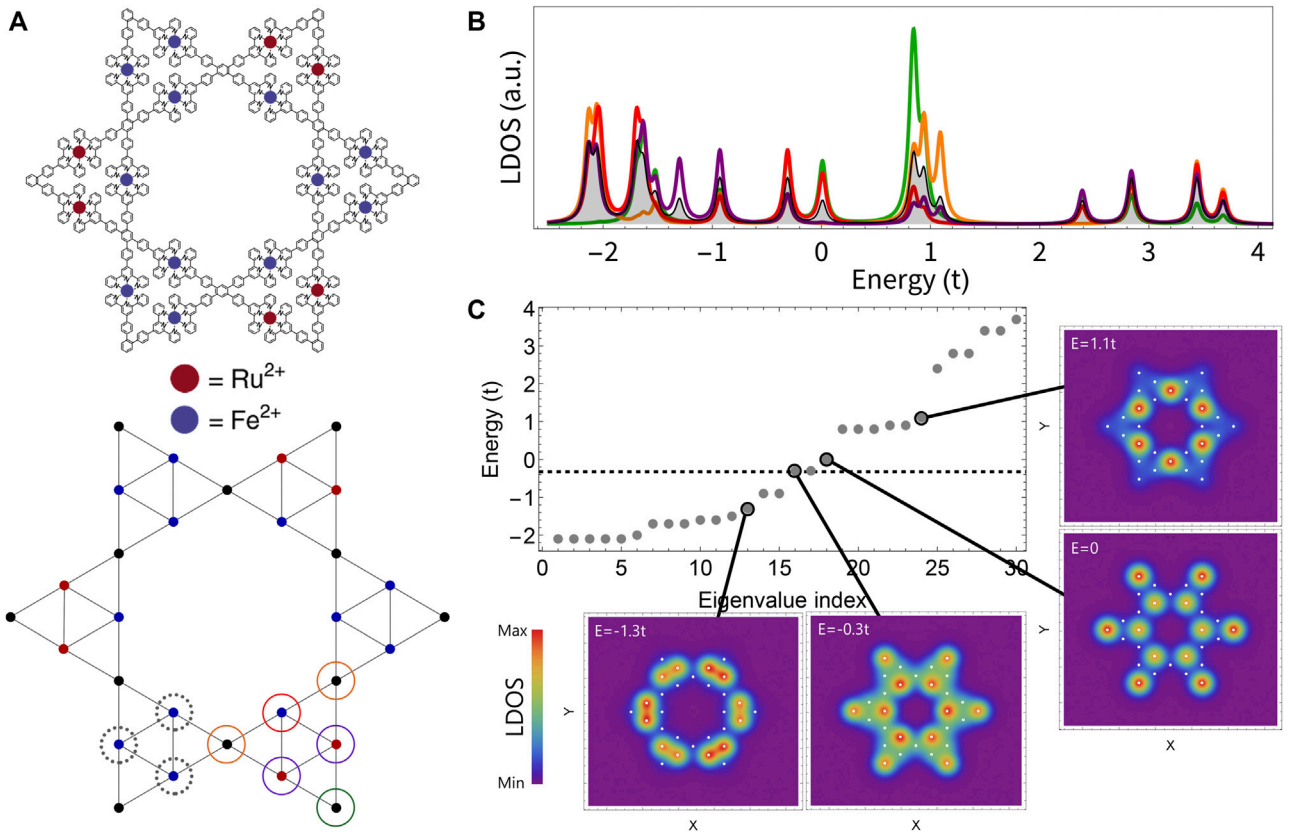

FIGURE 7
(A) Top: chemical molecule illustration synthesized experimentally (adapted from Zhang Z. et al. 2020)). Bottom: proposed tight-binding effective quantum corral, with colored dots denoting C (black), Fe (blue), and Ru (red) atoms. **(B)** LDOS of the corresponding sites marked by colored circles in the TB corral and total averaged DOS (gray curve). **(C)** Energy spectrum with the electronic charge distribution for $E = -1.3t$, $-0.3t$, 0, and $1.1t$. TB parameters: $\varepsilon_C = 0.25t$, $\varepsilon_I = -0.25t$, and $\varepsilon_{Ru} = -0.35t$.

analysis can help in engineering the electronic responses of the quantum Triangle Sierpinski corrals and propose appropriate functionalization of the molecules.

4 Conclusion

This research has explored the nature of localized states in quantum corrals created by fractal structures, based on C atoms, such as Koch lines and Sierpinski triangles. Annular triangular and square Koch structures were proposed within a first- and up to second-neighbor tight-binding framework. Comparison between the two approaches reveals the existence of spreading electronic states around the corrals, favoring the 2NN description for possible transport applications. The emergence of conducting channels is revealed for the proposed corral chains, similar to what had been previously verified for other organic molecular fractal chains (Lage and Latgé,2022). Furthermore, quantum corral architectures based on triangular Sierpinski units were proposed to effectively describe synthesized organic molecular corrals. The results revealed rich features on the electronic properties and good agreement with STM images of the experimental data (Zhang Y. et al., 2020). Higher order fractal structures can be envisaged that allow investigation of self-similarity responses. Also, more sophisticated descriptions within the same tight-binding approach, incorporating many-body correlation terms (spin-orbit couplings at the metallic sites and electron-electron correlations), may be extended to better describe complex molecular systems with transition metals. We believe that the present research can be used to guide the synthesis of a variety of real fractal molecular nanostructures, highlighting the particular symmetries and possibilities of new functionalization procedures.

Data availability statement

The raw data supporting the conclusions of this article will be made available by the authors, without undue reservation.

Author contributions

LLL: conceptualization, investigation, methodology, software, visualization, writing–original draft, writing–review and editing. AL: conceptualization, funding acquisition, investigation, methodology, project administration, supervision, validation, visualization, writing–original draft, writing–review and editing.

Funding

The author(s) declare that financial support was received for the research, authorship, and/or publication of this article. This work was financed by Brazilian Agencies CNPq and FAPERJ within grant E-26/200.569/2023.

Acknowledgments

The authors would like to thank the INCT de Nanomateriais de Carbono for providing support on the computational infrastructure. LLL thanks the CNPq scholarship.

Conflict of interest

The authors declare that the research was conducted in the absence of any commercial or financial relationships that could be construed as a potential conflict of interest.

Publisher's note

References

Berdonces-Layunta, A., Schulz, F., Aguilar-Galindo, F., Lawrence, J., Mohammed, M. S. G., Muntwiler, M., et al. (2021). Order from a mess: the growth of 5-armchairgraphene nanoribbons. *ACS Nano* 15, 16552–16561. doi:10.1021/acsnano.1c06226

Browning, L. A., Watterson, W., Happe, E., Silva, S., Abril Valenzuela, R., Smith, J., et al. (2021). Investigation of fractal carbon nanotube networks for biophilic neural sensing applications. *Nanomaterials* 11, 636. doi:10.3390/nano11030636

Canellas Núnez, R., Liu, C., Arouca, R., Eek, L., and Yin, Y. (2023). *Topological edge and corner states in bi fractals on insb*. arxiv-2309.09860.

Castro Neto, A., Guinea, F., Peres, N. M. R., Novoselov, K. S., and Geim, A. (2009). The electronic properties of graphene. *Rev. Mod. Phys.* 81, 109–162. doi:10.1103/RevModPhys.81.109

Chico, L., Latgé, A., and Brey, L. (2015). Symmetries of quantum transport with rashba spin–orbit: graphene spintronics. *Phys. Chem. Chem. Phys.* 17, 16469–16475. doi:10.1039/C5CP01637A

Crommie, M. F., Lutz, C. P., and Eigler, D. M. (1993). Confinement of electrons to quantum corrals on a metal surface. *Science* 262, 218–220. doi:10.1126/science.262.5131.218

Dai, J., Zhao, X., Peng, Z., Li, J., Lin, Y., Wen, X., et al. (2023). Assembling surface molecular sierpiński triangle fractals via K^+-Invoked electrostatic interaction. *J. Am. Chem. Soc.* 145 (25), 13531–13536. doi:10.1021/jacs.3c03691

Data, S. (1995). *Electronic transport in mesoscopic sysytems*. United Kindgom: Cambridge University Press.

De Nicola, F., Castrucci, P., Scarselli, M., Nanni, F., Cacciotti, I., and De Crescenzi, M. (2015). Multi-fractal hierarchy of single-walled carbon nanotube hydrophobic coatings. *Sci. Rep.* 5, 8583. doi:10.1038/srep08583

Devaney, R. L. (2004). Chaos rules!. *Math. Horizons* 12(2), 11–13. doi:10.1080/10724117.2004.12023675

Domany, E., Alexander, S., Bensimon, D., and Kadanoff, L. P. (1983). Solutions to the Schrödinger equation on some fractal lattices. *Phys. Rev. B* 28, 3110–3123. doi:10.1103/PhysRevB.28.3110

El-Nabulsi, R. A., and Anukool, W. (2021). Quantum dots and cuboid quantum wells in fractal dimensions with position-dependent masses. *Appl. Phys. A* 127, 856. doi:10.1007/s00339-021-04989-6

El-Nabulsi, R. A., and Anukool, W. (2023). Analysis of quantum effects in metal oxide semiconductor field effect transistor in fractal dimensions. *MRS Commun.* 13, 233–239. doi:10.1557/s43579-023-00334-5

Felix, A. B., Pacheco, M., Orellana, P., and Latgé, A. (2022). Vertical and in-plane electronic transport of graphene nanoribbon/nanotube heterostructures. *Nanomaterials* 12, 3475–34759. doi:10.3390/nano12193475

Foroutan-pour, K., Dutilleul, P., and Smith, D. (1999). Advances in the implementation of the box-counting method of fractal dimension estimation. *Appl. Math. Comput.* 105, 195–210. doi:10.1016/S0096-3003(98)10096-6

Freeney, S. E., Slot, M. R., Gardenier, T. S., Swart, I., and Vanmaekelbergh, D. (2022). Electronic quantum materials simulated with artificial model lattices. *ACS Nanosci. Au* 2, 198–224. doi:10.1021/acsnanoscienceau.1c00054

Gowrisankar, A., and Banerjee, S. (2021). Frontiers of fractals for complex systems: recent advances and future challenges. *Eur. Phys. J. Special Top.* 230, 3743–3745. doi:10.1140/epjs/s11734-021-00376-7

Jiang, Z., Li, Y., Wang, M., Song, B., Wang, K., Sun, M., et al. (2017). Self-assembly of a supramolecular hexagram and a supramolecular pentagram. *Nat. Commun.* 8, 15476–154788. doi:10.1038/ncomms15476

Kaurov, V. (2012). Measuring fractal dimension of natural object from digital images. *Math. Stack Exch.* 2012.

Kempkes, S. N., Slot, M. R., Freeney, S. E., Zevenhuizen, S. J. M., Vanmaekelbergh, D., Swart, I., et al. (2019). Design and characterization of electrons in a fractal geometry. *Nat. Phys.* 15, 127–131. doi:10.1038/s41567-018-0328-0

L Lage, L., and Latgé, A. (2022). Electronic fractal patterns in building Sierpinski-triangle molecular systems. *Phys. Chem. Chem. Phys.* 24, 19576–19583. doi:10.1039/d2cp02426h

Mandelbot, B. B. (1983). *The fractal geometry of nature*. 3 edn. New York: Henry Holt and Company.

Newkome, G. R., Wang, P., Moorefield, C. N., Cho, T. J., Mohapatra, P. P., Li, S., et al. (2006). Nanoassembly of a fractal polymer: a molecular "Sierpinski hexagonal gasket ". *Science* 312, 1782–1785. doi:10.1126/science.1125894

Pedersen, T. G. (2020). Graphene fractals: energy gap and spin polarization. *Phys. Rev. B* 101, 235427. doi:10.1103/PhysRevB.101.235427

Peng, X., Mahalingam, H., Dong, S., Mutombo, P., Su, J., Telychko, M., et al. (2021). Visualizing designer quantum states in stable macrocycle quantum corrals. *Nat. Commun.* 12, 5895. doi:10.1038/s41467-021-26198-8

Santos, H., Latgé, A., Brey, L., and Chico, L. (2020). Spin-polarized currents in corrugated graphene nanoribbons. *Carbon* 168, 1–11. doi:10.1016/j.carbon.2020.05.054

Shang, J., Wang, Y., Chen, M., Dai, J., Zhou, X., Kuttner, J., et al. (2015). Assembling molecular Sierpiński triangle fractals. *Nat. Chem.* 7 (5), 389–393. doi:10.1038/nchem.2211

Trambly de Laissardière, G., Mayou, D., and Magaud, L. (2010). Localization of Dirac electrons in rotated graphene bilayers. *Nano Lett.* 10, 804–808. doi:10.1021/nl902948m

Wakabayashi, K., Sasaki, K. I., Nakanishi, T., and Enoki, T. (2010). Electronic states of graphene nanoribbons and analytical solutions. *Sci. Technol. Adv. Mater.* 11, 054504. doi:10.1088/1468-6996/11/5/054504

Wang, L., Liu, R., Gu, J., Song, B., Wang, H., Jiang, X., et al. (2018). Self-assembly of supramolecular fractals from generation 1 to 5. *J. Am. Chem. Soc.* 140, 14087–14096. doi:10.1021/jacs.8b05530

Wang, X. R. (1995). Localization in fractal spaces: exact results on the Sierpinski gasket. *Phys. Rev. B* 51, 9310–9313. doi:10.1103/PhysRevB.51.9310

Xu, X. Y., Wang, X. W., Chen, D. Y., Smith, C. M., and Jin, X. M. (2021). Quantum transport in fractal networks. *Nat. Phot.* 15, 703–710. doi:10.1038/s41566-021-00845-4

Zhang, Y., Zhang, X., Li, Y., Zhao, S., Hou, S., Wu, K., et al. (2020a). Packing sierpiński triangles into two-dimensional crystals. *J. Am. Chem. Soc.* 142, 17928–17932. doi:10.1021/jacs.0c08979

Zhang, Z., Li, Y., Song, B., Zhang, Y., Jiang, X., Wang, M., et al. (2020b). Intra- and intermolecular self-assembly of a 20-nm-wide supramolecular hexagonal grid. *Nat. Chem.* 12, 468–474. doi:10.1038/s41557-020-0454-z

Zhou, Z., Bouwman, W. G., Schut, H., Desert, S., Jestin, J., Hartmann, S., et al. (2016). From nanopores to macropores: fractal morphology of graphite. *Carbon* 96, 541–547. doi:10.1016/j.carbon.2015.09.069

frontiers | Frontiers in Carbon

TYPE Original Research
PUBLISHED 02 February 2024
DOI 10.3389/frcrb.2024.1352122

OPEN ACCESS

EDITED BY
Anthony B. Dichiara,
University of Washington, United States

REVIEWED BY
Chi-Hsien Huang,
Ming Chi University of Technology, Taiwan
Octavian Buiu,
National R&D Institute for Microtechnologies-IMT Bucharest, Romania

*CORRESPONDENCE
Matheus F. F. das Neves,
matheusfneves@gmail.com
Lucimara S. Roman,
lucimara.roman@ufpr.br

RECEIVED 07 December 2023
ACCEPTED 17 January 2024
PUBLISHED 02 February 2024

CITATION
das Neves MFF, Mukim S, Ferreira MS and Roman LS (2024), Mechanisms of methanol detection in graphene oxide and conductive polymer active layers for gas sensing devices. *Front. Carbon* 3:1352122.
doi: 10.3389/frcrb.2024.1352122

Mechanisms of methanol detection in graphene oxide and conductive polymer active layers for gas sensing devices

Matheus F. F. das Neves[1]*, Shardul Mukim[2], Mauro S. Ferreira[2,3] and Lucimara S. Roman[1]*

[1]Department of Physics, Federal University of Paraná, Curitiba, Paraná, Brazil, [2]School of Physics, Trinity College Dublin, Dublin, Ireland, [3]Centre for Research on Adaptive Nanostructures and Nanodevices (CRANN) and Advanced Materials and Bioengineering Research (AMBER) Centre, Trinity College Dublin, Dublin, Ireland

The admixture of PEDOT:PSS with Graphene Oxide (GO) in precise proportions achieves a substantial reduction in electrical resistivity, thereby augmenting its suitability as an electrode in organic devices. This study explores the electrical and morphological attributes of commercial PEDOT:PSS and chemically synthesized aqueous PEDOT ink when both are combined with GO. The investigation extends to the application of these conductive inks as active layers in flexible methanol sensing devices. Notably, a resistivity minimum is observed in the case of GO: PEDOT:PSS 78%, while the highest response to methanol is attained with GO: PEDOT:PSS 68%. To establish a theoretical underpinning for these findings, and to understand the interaction between gas/vapors with nanostructured materials, a model rooted in Kirchhoff's Circuit approach is developed, with the aim of elucidating the factors behind the resistivity minimum and response maximum at distinct specific mass ratios between PEDOT and GO. Calculating the equivalent resistivity and response of the systems, the positions of minimum and maximum points are in agreement with the experimental data. Furthermore, the influence of PSS in the samples is examined, unveiling diverse interaction mechanisms between methanol molecules and the active layer, resulting in varying signals during the exposure to alcoholic vapor. The theoretical model is subsequently applied to these systems, demonstrating qualitative and quantitative agreement with the experimental results.

KEYWORDS

PEDOT, graphene oxide, gas sensor, nodal analysis, organic electronics

1 Introduction

Poly (3,4-ethylenedioxythiophene), commonly referred to as PEDOT, stands out as one of the most widely utilized conductive polymers in the realm of organic electronics. Its prevalence owes itself to its inherent attributes of high electrical conductivity, partial transparency and flexibility Anand et al. (2021); das Neves et al. (2019); Nie et al. (2023). However, the hydrophobic nature of this polymer necessitates its processing in polar solvents, including water. This requirement leads to the blending of PEDOT with soluble molecules and necessitates the use of additional additives to stabilize dispersion. Notably, the most prevalent combination involves polystyrene sulfonate, denoted as PSS, resulting in the composite PEDOT:PSS. The addition of an excess of PSS serves to increase the PEDOT

concentration in water, facilitating dispersion and enabling the commercialization of conductive inks in varying concentrations. Numerous studies in the literature highlight the utility of PEDOT:PSS in the domain of organic electronic devices.

In the context of Organic Photovoltaics (OPVs), PEDOT:PSS has found application both as a semi-transparent electrode Lee et al. (2020) and as a hole transport layer Miranda et al. (2021); Chang et al. (2023); de Jesus Bassi et al. (2021). This polymeric conductive ink has also found relevance in other devices, including batteries del Olmo et al. (2022), supercapacitors Yoonessi et al. (2019), and Organic Light Emitting Diodes (OLED) Cinquino et al. (2022); Gu et al. (2019). Moreover, in organic gas sensing devices, this material serves as an active layer, enabling interactions with specific gases or vapors. For instance, Pasupuleti et al. (2021) have proposed the combination of these materials to detect Nitrogen Dioxide (NO_2). Similarly, Alves et al. (2022) have demonstrated the use of PEDOT:PSS and graphene oxide for monitoring methanol in confined spaces and, unlike the present study, it showed how a nanostructuring process affects the devices' efficiency.

Particularly in recent years, advancements in deposition techniques have allowed for the fabrication of flexible devices. Conductive polymers and their derivatives play a pivotal role in this regard, as their application as inks enables deposition methods such as casting, spin coating, and slot-die coating. The inherent flexibility of these materials facilitates large-scale production through techniques like roll-to-roll, an industrial method that demands robust and flexible substrates. Consequently, these devices exhibit eco-friendliness and versatility, thanks to their plastic properties, lightweight nature, processability, and recyclability Carneiro et al. (2023). These properties motivates the use of acetate as a flexible substrate for sensor fabrication in this study.

Despite the advantages that PSS imparts in terms of water dispersibility and ink stabilization, it's important to note that PSS is an insulating polymer that can potentially compromise the full electrical properties of PEDOT. Numerous studies have demonstrated that additional treatments can significantly enhance electrical conductivity, often by orders of magnitude. One common approach involves the incorporation of carbon nano-materials, such as Graphene Oxide (GO). For instance, Borges et al. (2019) have shown that there exists an optimal mass ratio between GO and PEDOT where conductivity improves significantly, attributed to chain polymer alignment and additional doping facilitated by GO. Another strategy to augment PEDOT properties involves the use of polar solvents to remove PSS from samples, thereby improving the organization of polymeric films das Neves et al. (2019).

So it would be interesting to propose new fabrication routes that do not require further treatments. PEDOT, being inherently hydrophobic, presents challenges in achieving water dispersibility, although not insurmountable ones. das Neves et al. (2021) have demonstrated the production of substantial quantities of PEDOT aqueous dispersion through monomer polymerization in acetonitrile, employing Iron (III) chloride without additional surfactants or insulating polymers, and utilizing Cl^- as a counter-ion. This opens up the possibility of producing a PEDOT conductive ink without the need for PSS and the subsequent steps required to remove the insulating polymer. In this study, it is replicated an established method for polymerizing PEDOT aqueous conductive ink das Neves et al. (2021) and introduce a novel approach that substitutes GO for PSS, investigating the effect of PSS in PEDOT-based samples.

The developed conductive inks composed of PEDOT and GO are applied in this study as active layers for flexible devices to monitor alcohol in a confined set up environment. Furthermore, this study reveals the interaction differences between active layers using PSS (commercial inks) and without this insulating polymer (polymerized samples). The methanol sensor devices employed in this study rely on an active layer that adsorbs chemical species, yielding a real-time amplified electrical response. A significant advantage of organic sensing devices lies in their operation at room temperature, in contrast to inorganic counterparts, which often require much higher temperatures exceeding 100°C Alves et al. (2022); Afzal (2019). The use of room temperature devices holds particular appeal, especially in confined space environments, as it demands less energy and reduces the risk of accidents, and the sensors presented in this study are characterized at 21°C.

Many contaminants in such environments consist of volatile compounds, and these can be effectively detected using composites like PEDOT-based thin films Vigna et al. (2021); Fujita et al. (2022). GO dispersions can enhance these composites' electrical conductivity das Neves et al. (2019), transconductance, and response by increasing surface area and organizing polymer chains Alves et al. (2022). Alcoholic vapors such as methanol are frequently encountered in confined spaces like grain silos and fuel tanks Alves et al. (2022); Wu et al. (2022) and the presence of this toxic and flammable compound at specific concentrations or during extended exposures poses hazards to human health Hashemi et al. (2022).

This paper aims to investigate the interaction between alcoholic vapors and nanostructured materials, as the response varies depending on the constituents of the active layer. Additionally, the impact of PSS in the inks is examined by comparing commercial PEDOT:PSS with chemically synthesized PEDOT and their blends with GO. These thin films find application in organic and flexible sensor devices designed for monitoring methanol levels in confined spaces. This exploration provides a deeper understanding of the roles played by PSS and GO as dopants for PEDOT, both from experimental and theoretical perspectives.

2 Methodology

2.1 Materials

A commercial aqueous solution of PEDOT:PSS was procured from Sigma-Aldrich with a concentration of 1.3 wt% of polymer in water, containing 500 μg L^{-1} of PEDOT and 800 μg L^{-1} of PSS. Graphite was obtained from Nacional de Grafite (Graflake 99580, 99.8% carbon). Additionally, 3,4-ethylenedioxythiophene (EDOT) (99%), acetonitrile (HPLC, 99%), and anhydrous iron (III) chloride ($FeCl_3$, 97%) were sourced from Sigma-Aldrich. Deionized water (18 MΩ) was obtained using Elga Purelab Flex equipment. Flexible substrates were produced from conventional acetate transparency sheets.

2.2 Preparation of PEDOT, GO: PEDOT and GO: PEDOT: PSS

The PEDOT aqueous dispersion was obtained through the oxidative polymerization of EDOT using $FeCl_3$ in acetonitrile, followed by a series of washing steps with acetonitrile and deionized water, as detailed in das Neves et al. (2021). Additional information regarding the synthesis of PEDOT can be found in the Supplementary Information. An aqueous PEDOT ink was prepared by isolating the wet solid from the aforementioned synthesis procedure described in the Supplementary Information. Specifically, 1.25 g of wet solid PEDOT was placed in a 100 mL round-bottom glass flask, along with 50 mL of deionized water, and subjected to 1 h of bath sonication, with cooling facilitated by the addition of small ice portions. The GO aqueous dispersion was generated through the oxidation of graphite, followed by liquid exfoliation and centrifugation, ultimately resulting in the desired graphene oxide dispersion. The graphite oxidation procedure was carried out following Hummers' modified method established in the literature Mehl et al. (2014). Further details regarding the preparation of the GO aqueous dispersion can be found in the Supplementary Information. Additional information regarding the properties of GO can be found in the cited literature Mehl et al. (2014); Borges et al. (2019); das Neves et al. (2019).

To create the GO:PEDOT aqueous dispersion, 1.25 g of wet polymerized solid PEDOT was combined with 37 mL of GO aqueous dispersion (0.05 mg mL^{-1}) and 13 mL of deionized water in a 100 mL round-bottom glass flask. The mixture was subjected to 1 h of ultrasound bath sonication, with cooling aided by small ice portions. Following ultrasound sonication, the PEDOT and GO: PEDOT inks were stored in glass vials.

The GO:PEDOT:PSS conductive inks were formulated by adding varying volumes (30, 60, 90, 120, 150, and 300 μL) of commercial PEDOT:PSS to 3 mL of GO aqueous dispersion. The mixture underwent 24 h of vigorous magnetic stirring, as previously described in Borges et al. (2019); das Neves et al. (2019); Holakoei et al. (2020). These samples were denoted as GO:PEDOT:PSS, followed by the respective percentage, corresponding to the concentration of PEDOT relative to GO. This concentration was calculated based on the molar mass and mass ratio established in prior studies, resulting in the following percentages: GO:PEDOT: PSS 40%, 59%, 68%, 74%, 78%, and 88%. The 100% sample represents pure PEDOT:PSS. Notably, GO:PEDOT:PSS 78% exhibits a mass ratio of 5.8×10^{-2} of GO/PEDOT, which is reported as the optimal proportion concerning electrical conductivity and optical transmittance on glass substrates Borges et al. (2019); das Neves et al. (2019).

2.3 Preparation of substrates and deposition of thin films

Interdigitated electrodes were meticulously prepared on commercial flexible acetate substrates using standard photolithography techniques, following the methodology outlined in Eising et al. (2017); Alves et al. (2022). These electrodes consisted of sputtered chromium followed by gold thin films, featuring an active area of 10 mm^2 and a band spacing of 100 μm. The configuration of the interdigitated electrodes is visually depicted in Figure 1. Electrical contacts were securely attached to the electrodes using silver conductive epoxy adhesive (model 8331S-14G by MG Chemicals) and subsequently dried on a hot plate at 65°C for a duration of 3 h.

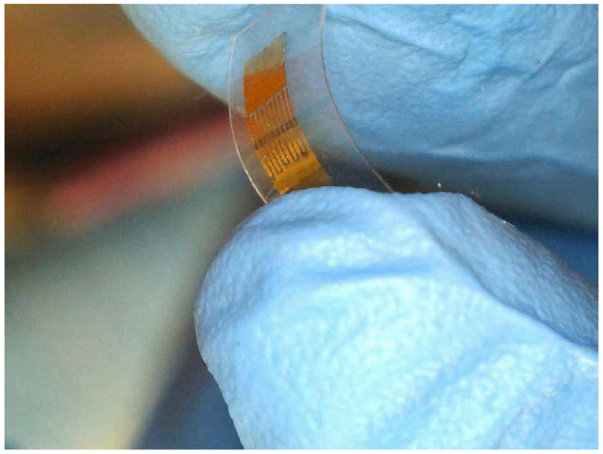

FIGURE 1
Interdigitated electrode in acetate, prepared using photolithography, to be used as substrate for the sensing device.

To create various gas sensors, a drop-casting approach was employed, depositing 10 μL of PEDOT, GO:PEDOT, GO:PEDOT: PSS, and neat PEDOT:PSS on the electrodes. The deposited thin films were left to dry at room temperature for a period of 24 h. Following the drying process, the thin films underwent thermal annealing at 40°C, utilizing a heating plate (IKA, model C-MAG HS 7), for 5 min. All of these procedures were carried out under standard room atmospheric conditions.

For thin films intended for morphological and electrical characterization, the same steps were followed. However, these films were deposited on 1 cm^2 acetate substrates without interdigitated electrodes.

2.4 Samples and sensors characterization

Morphological characterization was conducted utilizing Scanning Electron Microscopy (SEM) images, acquired with a TESCAN MIRA 3 FEG-SEM microscope operating at 10 kV and a working distance of 5 mm. Stubs with carbon paper were employed, ensuring electrical contact through copper adhesive ribbon.

Sheet resistance values were determined through four-probe measurements performed on acetate substrates utilizing Jandel Universal probe equipment. For each sample, these measurements were carried out 10 times, employing both forward and reverse electrical currents bias for each measurement. Subsequently, electrical conductivity was calculated using the relation $\sigma = \frac{1}{R_s \times t}$, where R_s represents the sheet resistance, and t denotes the thickness of the thin films. Thickness values were obtained through profilometry using a Veeco Dektak 150 instrument.

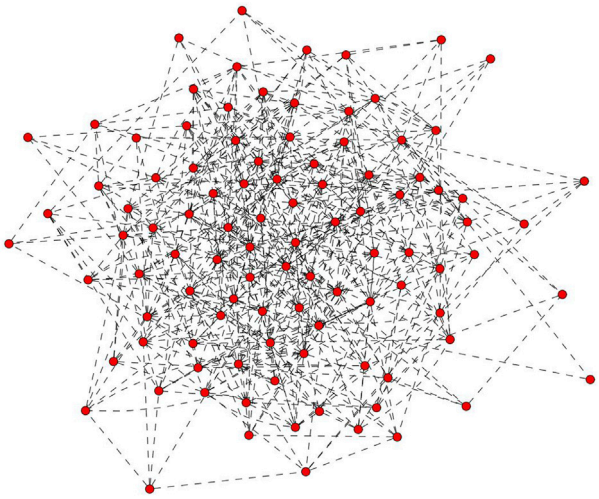

FIGURE 2
Random network (RNW) to depict a GO:PEDOT:PSS system.

Dynamic Light Scattering (DLS) measurements were conducted using a Malvern Zetasizer Nano Zs, model ZEN 3600, operating at 25°C with a 633 nm laser. A total of 20 measurements were performed for 10 s each, with an equilibrium time of 30 s. Particle sizes were calculated using the Mark-Houwink model. Zeta potential was determined using a Malvern Zetasizer Nano S at 25°C, involving 3 measurements for each sample, with 20 acquisitions each and an equilibrium time of 30 s.

The sensor response, represented as the change in electrical resistance, was characterized by calculating the absolute value of the difference between the electrical resistance of the device when exposed to the analyzed gas (R) and the electrical resistance under dry air conditions (R0). This value was then divided by R0 and presented as a percentage. To assess the response of the sensors to methanol (CH_3OH) in dry air, a setup consisting of a sensor probe within a tubular system was employed. Gas intake was controlled using a flowmeter and solenoid valves, as previously described in other studies Eising et al. (2017); Alves et al. (2022). All sensors were tested five times over a span of 2 weeks. The established methanol concentration was maintained at 1,000 ppm.

Using a multimeter (Agilent 34401A), the electrical resistance of the device and its changes during gas flow were continuously monitored in a controlled environment with 0% air humidity and a temperature of 21°C. The set up maintains air humidity through rotameters and dry air flowing through sample environment, while room temperature is controlled by an air conditioner and monitored using an LM35 connected to the system. Previous studies showed that 21°C is the optimum temperature that these sensors present a higher response. The same for air humidity, where if water is present, it can hinder methanol influence by swelling effect Alves et al. (2022). The samples were subjected to cycles of dry air for 3 min, followed by air containing the defined methanol concentration for 2 min. The device's measurements and gas intake were simultaneously controlled using a non-commercial software application.

2.5 Theoretical approach

There are very few theoretical descriptions based on real-world networks in which their physical characteristics are accounted for. Figure 2 depicts an example of a random network that resembles the connectivity of the PEDOT:PSS system. The problem of modelling such systems begins with the lack of information one can derive about connectivity. Most of these techniques are computationally very demanding as the physical characteristics depend on not just connectivity but material properties, and density to say a few.

O'Callaghan et al. (2016) showed that an effective medium approach provides a simple, but equivalent, way to evaluate properties of disordered networks with the help of an ordered square lattice network. In this study, it is considered a square lattice of dimensions 100 × 100. Every node is labeled as GO, PEDOT or PSS, and the weight of links, *i.e.*, resistance encodes the interactions between those constituents.

The equivalent resistance between the two points on the network can be calculated as Eq. 1

$$R_{x,y} = \left(M^{-1}_{x,x} + M^{-1}_{y,y} - M^{-1}_{x,y} - M^{-1}_{y,x}\right) \quad (1)$$

Here, $R_{x,y}$ is the equivalent resistance between the electrodes placed at site x and y. M is Kirchoff's matrix that encodes the connectivity and interaction between the entities contributing to electronic transport.

To begin with, it is considered a system where each node was assigned to be GO, and as a result, all the links present in the network are identical to one another. Due to the insulating behavior of the Graphene Oxide the resistivity of such system is high. Adding PEDOT and/or PSS to the network reduces the concentration of GO nodes as it is introduced low-resistance links in the system. The resistivity associated with a purely GO network is significantly higher than the PEDOT:PSS doped system. As the concentration of PEDOT:PSS increases the resistivity of the network drops due to the highly conductive PEDOT-GO behavior. The addition of PEDOT:PSS to the GO system creates a competition of resistances that dominates the equivalent resistivity of the network. A minimum is identified when the resistance distribution of both GO and PEDOT dominates the equivalent resistance. This perfectly resembles the resistivity minimum position determined in the experiments.

The simplicity of the model facilitates the integration of methanol for assessing the sensing behavior. Interaction with methanol can be modeled in the form of changes in the resistance of the links between neighboring nodes. The specific values assigned to each link are based on experimental data, reflecting the differences in resistance during exposure to methanol.

3 Results and discussions

3.1 Optimized samples—resistivity and response

The conductive inks containing commercial PEDOT:PSS were prepared by incorporating varying amounts of the polymeric compound into an aqueous Graphene Oxide (GO) dispersion.

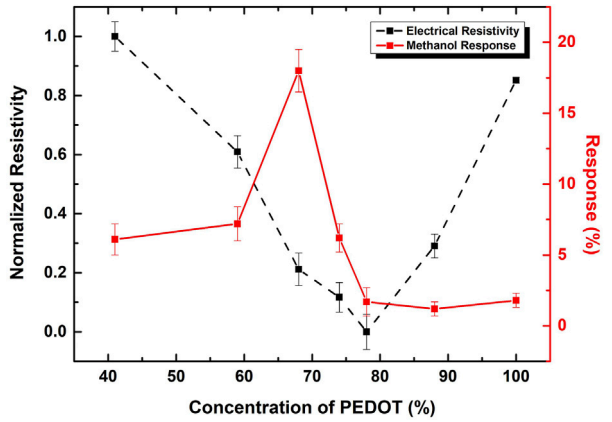

FIGURE 3
Black and dashed line shows the normalized resistivity values and Red and straight line shows the sensor response, both for GO:PEDOT: PSS 40, 59, 68, 74, 78, 88% and neat PEDOT:PSS deposited on acetate substrates. The response values corresponds to flexible sensor devices fabricated on interdigitated electrodes on top of acetate substrates.

The resulting materials were deposited on flexible acetate substrates for subsequent electrical and morphological characterization.

Previous studies have established that achieving a specific mass ratio of 5.8×10^{-2} between GO and PEDOT:PSS results in a minimum electrical resistivity. While this material has been used in Organic Photovoltaics Lima et al. (2016), the behavior was initially explored by Borges et al. (2019). They found that the sample with this precise mass ratio exhibited improved orientation of the thiophene groups within the PEDOT structure compared to lower and higher concentrations of PEDOT:PSS. This observation partially elucidates why the addition of a small amount of PEDOT:PSS to a GO aqueous dispersion, which inherently possesses insulator properties, leads to a more conductive compound than the conductor itself.

Figure 3 illustrates the normalized electrical resistivity values, represented by the black-dashed line, calculated using the sheet resistance, obtained from four-probe measurement, and the thicknesses of the thin films, that are around 250 nm. The results indicate that the lowest electrical resistivity is achieved with GO: PEDOT:PSS 78%. This concentration corresponds to the previously mentioned sample in the literature that aligns with the assigned mass ratio.

das Neves et al. (2019) conducted a study characterizing this optimized compound, investigating its morphological, optical, and electrical properties. In their research, they introduced a treatment that selectively removed a controlled amount of PSS, resulting in a more conductive thin film. Furthermore, both studies delved into charge transfer times, employing Resonant Auger Spectroscopy. Remarkably, the same sample that exhibited the minimum electrical resistivity also displayed a significantly reduced charge transfer time, determined using the Core Hole Clock method. This consistency aligns with the electrical measurements, reinforcing the pattern seen in the optimized sample.

The present study includes an additional characterization by replicating the ethyleneglycol treatment developed by das Neves and coauthors das Neves et al. (2019). The treatment involves dip-casting the dried thin films in ethyleneglycol followed by water, effectively removing PSS. Interestingly, the treatment reaffirmed that the minimum concentration remains consistent at GO:PEDOT: PSS 78%, as depicted in Supplementary Figure S1. The persistent occurrence of the minimum concentration is a topic of investigation in this present study and will be further discussed using the theoretical approach.

Methanol devices were fabricated using the interdigitated electrodes described in the experimental section. The electrode surfaces were coated by depositing 10 μL of each conductive ink, which included PEDOT, GO:PEDOT, PEDOT:PSS, and GO: PEDOT:PSS, with varying ratios between the components. In brief, the monitoring process commenced after the active layer was dried, and the devices were exposed to a controlled flow of the monitored vapor, all while maintaining a constant electrical current of 1 mA. The response was then determined by analyzing the variation in electrical resistance over time.

In the study conducted Alves et al. (2022), it was reported that the most favorable response to methanol vapor occurred with a mass ratio of 68% for GO:PEDOT:PSS, even though the highest electrical conductivity was observed at 78%. These findings, derived from sensors fabricated on glass substrates, aimed to explore a nanostructuring procedure to enhance sensing activity. In the current investigation, flexible methanol sensors are presented, employing the same method to produce GO:PEDOT:PSS inks, including the identical mass ratios previously published. The response rate results achieved with flexible devices, represented by the red-solid line in Figure 3, align with those reported by Alves et al. (2022). While there are slight variations in the response values compared to the previously cited study that employed the same inks, these differences, although less efficient, fall within the same order of magnitude. These variations can be attributed to the flexible nature of the devices, where surface interactions between the inks and the substrates contribute to differences in thin film morphology, including thickness and exposed active area. These factors directly influence the interaction between methanol and the active layers. Nonetheless, it is crucial to note that the qualitative behavior remains consistent.

The composite GO:PEDOT: PSS at a mass ratio of 68%, demonstrates the most favorable response, achieving a response of approximately 18%. Owing to this heightened response, subsequent experimental results involving GO and PEDOT:PSS will reference this specific percentage and the numerical value in the sample name will be omitted. Upon comparing the two curves, it becomes evident that beyond the concentration of 80%, the response remains independent of resistivity.

PEDOT:PSS represents an established commercial conductive ink that has found application in organic electronics for several decades. PEDOT, being hydrophobic, requires additives like stabilizers, surfactants, or negatively charged polyelectrolytes, such as PSS, to enable its dispersion in water. However, the electrical insulating properties of PSS can limit the full potential of PEDOT. Numerous published studies Lo et al. (2022); Saxena et al. (2019); Ouyang (2013) have explored the impact of PSS on PEDOT-based samples, highlighting its doping effect on PEDOT polymeric chains. Certain studies, such as the one conducted by das Neves et al. (2021), have introduced a synthesis route resulting in a

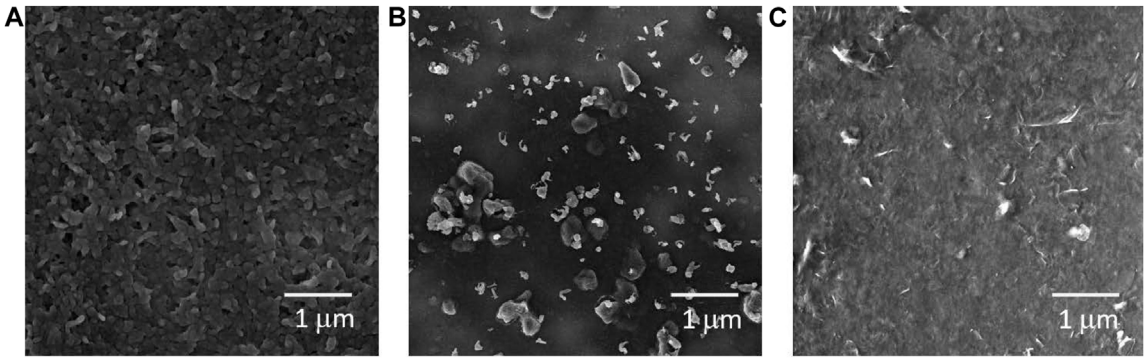

FIGURE 4
Scanning Electron Microscopy images for **(A)** PEDOT, **(B)** GO:PEDOT, and **(C)** GO:PEDOT:PSS 68% deposited on acetate substrates by drop casting.

pure PEDOT sample in water, utilizing electrostatic repulsion to stabilize the dispersion. This process yields electrical conductivity levels approaching that of commercial PEDOT:PSS. This study replicate both the aforementioned PEDOT synthesis route and introduce a new method incorporating GO. The aim is not only to compare morphology and electrical properties but also to investigate the mechanism of gas sensing devices. This comparison encompasses commercial PEDOT:PSS and the polymerized aqueous conductive ink PEDOT, both of which include GO in their composition.

3.2 Coloidal and morphological properties

GO:PEDOT samples exhibit an average particle size of approximately 480 nm, which is 300 nm larger than the reported size of PEDOT das Neves et al. (2021) and the DLS graph is depicted in Supplementary Figure S2. The ζ potential for this ink is +45.8 mV, indicating a metastable state, similar to the equilibrium state of the aqueous PEDOT ink. GO:PEDOT samples can be stored in glass flasks at low temperatures (4°C) for up to 4 months without coagulation, providing ample usability. The electrical resistivity of GO:PEDOT samples is approximately 0.35 Ωcm^{-1}, whereas for PEDOT samples, it stands at 0.45 Ωcm^{-1}. These resistivity values were calculated for samples with thicknesses of 290 nm and 230 nm, respectively. These results are within the same order of magnitude as previous characterizations presented in the literature for PEDOT aqueous ink deposited on glass substrates das Neves et al. (2021). Notably, the difference lies in the present study, where the thin films are deposited via drop casting on flexible acetate substrates. These electrical measurements indicate that the resistivity of the polymerized compounds remains competitive with the commercial PEDOT:PSS.

SEM images are displayed in Figure 4. Thin films of PEDOT (a) and GO:PEDOT:PSS 68% (c) exhibit homogeneity and even distribution on the substrates. In contrast, Figure 4B presents the GO:PEDOT sample, characterized by numerous clusters that may have formed during the polymerization process. These clusters appear to be comprised of GO sheets covered by a polymeric mass of PEDOT. These results align with previously published findings das Neves et al. (2021); Borges et al. (2019); das Neves et al. (2019); Alves et al. (2022). Figure 4A illustrates the polymeric mass of PEDOT nanoparticles, while Figure 4C highlights the polymeric appearance of the sample with exposed GO sheets spanning the substrate. Supplementary Figure S3 provides additional images for various concentrations of GO:PEDOT:PSS and includes PEDOT and GO:PEDOT comparison in a 500 nm scale.

3.3 Response over time

Figure 5 presents the percentage values, representing the sensor response, over time, comparing inks with and without PSS. The cycles denote exposure to methanol followed by dry air, each at a concentration of 1,000 ppm, complemented by additional cycles following the same pattern. In a previous study Alves et al. (2022) varied the methanol concentration from 1×10^3 to 450×10^3 ppm in order to calculate Freundlich Isotherm. It was concluded that GO:PEDOT:PSS exhibited a higher affinity than the commercial active layer, corroborating the reported results in this work. As expected, higher methanol concentrations presented higher response as the atmosphere is much more saturated. Moreover, it was demonstrated that below this minimum concentration, neat PEDOT:PSS active layer shows no response. Based on this prior characterization, the methanol concentration of 1,000 ppm was chosen to conduct the present analyzes.

The calculated percentage efficiency varies among the tested materials, with GO:PEDOT:PSS exhibiting the highest efficiency at 18%, followed by the PEDOT:PSS sample at around 4%, and both PEDOT and GO:PEDOT at approximately 2% and 1.5%, respectively. These results emphasize the increase in efficiency achieved by incorporating GO only in samples containing PSS, as previously predicted, reaffirming the necessity of this insulating component to enhance the doping effect by GO. This significant improvement can still be attributed to the larger surface area offered by GO sheets, facilitating enhanced adsorption of methanol molecules and, consequently, resulting in higher efficiency compared to active layers composed only of PEDOT:PSS or PEDOT.

Despite the presence of functional groups in GO, which may impede its electrical conductivity, several studies have demonstrated the interaction between PEDOT and GO, resulting in polymer chain

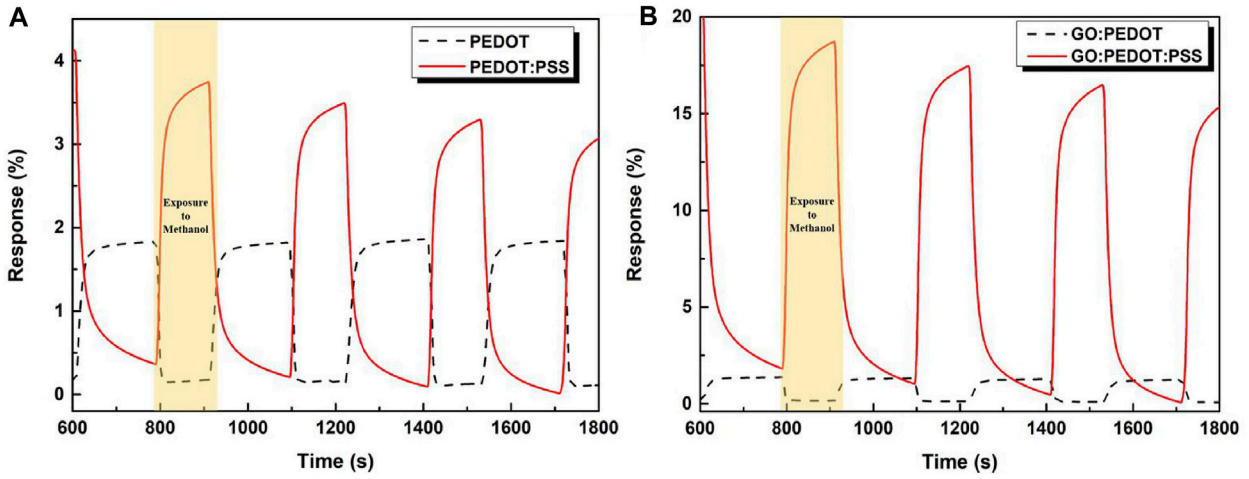

FIGURE 5
Response rate of the different devices in function of time and exposure to methanol for samples **(A)** Commercial ink PEDOT:PSS and chemically synthesized PEDOT and **(B)** Commercial ink PEDOT:PSS and chemically synthesized PEDOT, both with GO in its composition.

alignment and improved electrical conductivity Holakoei et al. (2020); das Neves et al. (2019); Borges et al. (2019); Alves et al. (2022). Additionally, these studies have revealed that GO effectively separates the PEDOT and PSS components, exposing PEDOT on the surface of the thin film. This exposure promotes a more intense interaction with methanol, consequently increasing sensor activity.

Furthermore, Alves et al. (2022) elucidated an additional doping effect engendered by the interaction between GO and PEDOT, facilitating the movement of more free charges that can interact with the monitored gas or vapor. An examination of SEM images reveals that the GO:PEDOT:PSS sample exposes GO sheets on the thin film's surface, correlating the heightened efficiency with the expanded surface area enabled by GO Hasani et al. (2015). Conversely, in GO:PEDOT samples, clusters of GO coated with PEDOT are observable. While GO:PEDOT exhibits a similar efficiency percentage when compared to polymerized samples, this can be attributed to the presence of clusters hinders even with the increased availability of charges. However, the response value does not approach that of GO:PEDOT:PSS due to inadequate cluster connectivity. Eising et al. (2021) demonstrated that cluster size and connectivity impact the response to exposed gas/vapor. In cases where clusters are large and well-connected, the electrical inner resistance increases while the electrical contact resistance decreases in relation to the contact area between clusters. The cluster sizes in this study are comparable; however, the distribution does not permit proper interconnection, resulting in a transduction mechanism reliant on the bulky polymeric mass. Consequently, the efficiency remains akin to that of a pure PEDOT sensor, despite the supplementary doping effect on the polymer chains.

Despite the superior performance of the commercial ink containing GO, it is noteworthy that, in the absence of GO, the polymerized PEDOT ink exhibits a comparable level of efficiency to that of the commercial PEDOT:PSS. The production of the polymerized aqueous PEDOT ink exclusively relies on water as a solvent, eliminating the need for stabilizers and surfactants. This characteristic not only enhances its ecological appeal but also contributes significantly to reduce production costs das Neves et al. (2021). Furthermore, the sensors manufactured using the internally produced PEDOT exhibit enhanced stability compared to their commercial counterparts, with faster saturation times. This stability is evident in the absence of any observable drift in the resistance curves. The efficiency values of active layers using the commercial polymers slightly drops over time in addition to the observed drift aspect. Eising et al. (2021) observed the same behavior for polyaniline and carbon nanotubes and suggested that it can be associated to local heating due to the current flow during the measurement procedure. Since PSS presents insulator properties, this effect can be pronounced in the samples containing this polymer.

Furthermore, it is worth noting that in the case of commercial samples containing PSS, their resistance increases upon exposure to methanol. Conversely, for the polymerized samples without PSS, the resistance decreases during exposure. This contrasting behavior can be attributed to various factors, including the swelling effect observed in samples containing PSS. Polar solvents like methanol and water can infiltrate the active layer due to interactions with PSS, which is a hygroscopic material. This infiltration leads to a separation of the polymeric chains, resulting in reduced connectivity and electrical conductivity Zeng et al. (2010); Yoon and Khang (2016). Additionally, the consumption of free charges plays a crucial role due to the reduction in methanol molecules, which increases the resistance of the devices Alves et al. (2022). In opposite, the absence of PSS may mitigate the swelling effect, and the decrease in resistance can be associated with the reorganization of charges, facilitated by the polymer being in a doped and conductive state das Neves et al. (2021). These phenomena will be further examined through theoretical modeling.

3.4 Theoretical modeling

The systems incorporating a graphene oxide network along with PEDOT and PSS can be analyzed using a theoretical framework to elucidate the observed outcomes. In this investigation, a GO network

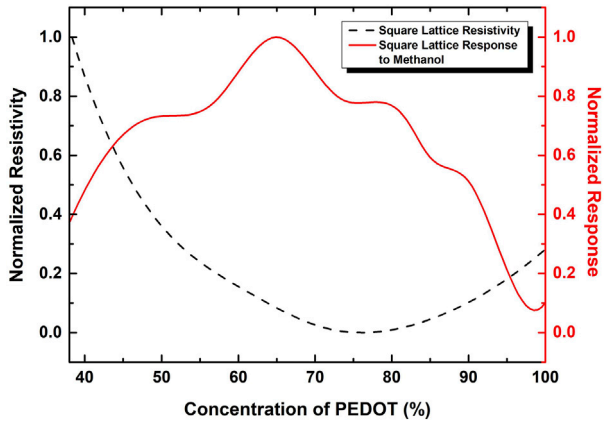

FIGURE 6
Normalized Resistivity values for the square lattice network representation of GO:PEDOT:PSS systems, indicated by the black-dashed line, showing the minimum in a determined concentration of PEDOT. Red-solid line represents the results for the Normalized Response Rate for methanol exposure, revealing the behaviour for different concentrations of PEDOT in GO network.

was employed to calculate the resistance or resistivity of the samples through the utilization of the Kirchoff matrix. The number of PEDOT and PSS entities was systematically altered to study their influence on the electrical properties of the network. It is important to note that the number of PEDOT and PSS components was maintained at the levels specified by the manufacturer, amounting to 0.5% for PEDOT and 0.8% for PSS, except when considering isolated PEDOT.

This simple model reveals the existence of an optimal concentration of PEDOT and GO, leading to the minimum resistivity. The graph in Figure 6 illustrates the outcomes obtained from a square lattice representation.

This result is consistent with the experimental data reported in this study and referenced in prior literature throughout the text. Despite the addition of PEDOT:PSS to the GO aqueous dispersion, and its corresponding lower volume fraction in the blend, the calculated ratios between the components, in terms of molar concentration, suggest that the optimal ratio is approximately 78% of PEDOT, a value remarkably close to the minimum value determined using the theoretical model, and it is showed by the black-dashed line.

The graph in Supplementary Figure S4 indicates a slightly different result for a random network. As expected, the minimum spot has changed to a lower value, approximately 65%, owing to the enhanced connectivity between the components compared to the square lattice. Nevertheless, these results are promising, considering the simplicity of this model and the proximity of the findings to those obtained with the square lattice representation, where connectivity is constrained to a maximum of 4.

These outcomes suggest a competition among the resistivities of the components within the network. Both GO and PSS are electrical insulators, with PEDOT being the conductive constituent in this blend. This competition in resistivities results in a global minimum. Prior to this optimal concentration, there isn't enough PEDOT to significantly enhance electrical conductivity, and both GO and PSS act as insulator pathways for charge carriers. Beyond this optimum concentration, the electrical conductivity of the sample approaches that of pure PEDOT. This conclusion aligns with the findings of Alves et al. (2022) and das Neves et al. (2019), where it is explicitly demonstrated that GO dopes PEDOT, increasing the number of free charges and, consequently, the electrical conductivity for this specific mass ratio. Furthermore, both sets of authors discuss the morphological changes induced by GO in the polymeric chains, contributing to improved electrical conductivity due to the synergistic effects of induced charge, polymer orientation, and morphology enhancement.

The identical network representation can also be employed to illustrate the sensor's response in the presence of methanol molecules. Figure 6 displays the response of the modeled sensors by the red-solid line, wherein the resistance links between the nodes are altered to signify methanol exposure, ensuring that the alcohol is distributed throughout every component, as per the saturated atmosphere during the experimental measurements.

The response reaches its maximum value at a concentration of approximately 65%, with both the Resistivity and Response curves following the pattern shown in Figure 3. It closely aligns with the performance of the GO:PEDOT:PSS 68% sample, and the findings are consistent with the research conducted by Alves et al. (2022). This behavior mirrors the pattern observed for the resistivity minimum. Despite both GO and PSS interact with methanol, the sensor's active layer must conduct the signal to the external circuit, and both GO and PSS are considered electrical insulators. PEDOT, being the conductive polymer, also interacts with the alcoholic vapor and efficiently carries the signals for monitoring. Alves et al. (2022) demonstrated that GO, by increasing the number of free charges, enhances the sensing activity, especially in specific concentrations. With a higher quantity of available charges, methanol molecules can consume these polarons, leading to an increase in the electrical resistance of the device and consequently enhancing the sensing activity.

Using this model improved to investigate the sensing activity, it was compared the samples with and without PSS. As depicted in Figure 5, when exposed to methanol molecules, the GO:PEDOT and PEDOT samples exhibit a decrease in electrical resistance, indicating sensor activity. However, in the presence of PSS within the system, the resistance increases, as indicated in both Figures 5A, B.

Alves et al. (2022) employed Density Functional Theory (DFT) to investigate the behavior of samples containing PSS when exposed to methanol. PSS is an insulating polymer often added to enhance the dispersibility of PEDOT in water while also doping PEDOT, increasing the number of empty states and facilitating hole mobility. However, polar molecules present in the surrounding atmosphere have the capacity to diminish this doping effect and, consequently, the electrical conductivity of the PEDOT chain.

In addition to these findings, the DFT data indicated a more pronounced doping effect when GO is introduced into the system, contributing to the increased efficiency with a favorable average adsorption energy. The authors suggested that GO enhances the availability of polarons. Consequently, the higher efficiency was attributed to GO:PEDOT:PSS samples due to the presence of GO, which amplifies the disruption of PEDOT doping caused by methanol molecules. Furthermore, the DFT results also revealed

interactions between GO, PEDOT, and PSS with methanol molecules through oxygenated groups. The mechanism, therefore, involves a process of PEDOT dedoping as a result of the consumption of available polarons by methanol molecules. In this case, methanol functions as a reducing agent, consistent with its chemical structure Saaedi et al. (2019); Singh and Sharma (2022).

In the current study, the application of the same model presented in the discussed results above is proposed. Supplementary Figure S5 illustrates the results for samples both with and without PSS. These findings demonstrate a qualitative alignment between the experimental data and the theoretical approach. While a comprehensive explanation for these results remains elusive and requires further investigation, certain observations can be made. Notably, the presence of PSS influences the resistance of the network. Both GO and PSS exhibit high electrical resistances, but PSS is an insulator polymer, whereas GO contains specific functional groups with insulating properties. Consequently, GO represents a component with high electrical resistance but also features regions that can conduct electricity, thereby engendering the desired interplay between resistances within the network, resulting in the observed contrasting behavior. Furthermore, the model posits that all components interact with methanol molecules, thereby giving rise to the step functions observed during exposure to the alcoholic vapor.

Methanol is recognized as a reducing agent, and changes in resistance within gas sensing devices are often associated with either doping or dedoping processes. Typically, an increase in resistance corresponds to a dedoping process, while a decrease implies doping. In this context, for methanol to reduce the electrical resistance, it should contribute charge carriers to PEDOT, effectively acting as an oxidizing agent. However, this is an unusual scenario, as it typically demands a substantial amount of energy to facilitate such a process. Additionally, catalytic reactions, which involve oxidizing agents for alcohols, do not apply in this case. Lin and Fan (2020) have discussed analogous behavior, where a decrease in resistance occurs in chemiresistive Carbon Dioxide (CO_2) gas sensors. In their study, CO_2 donates free electrons to the device, thereby increasing the number of free charges and subsequently enhancing electrical conductivity. Another aspect relevant to this specific case of charge flow in PEDOT samples relates to the redistribution of charges on the thin film's surface. The polymerized PEDOT in question exists in a doped state with polaron and bipolaron structures, as observed by das Neves et al. (2021). This rebalancing of charges can delocalize charge carriers and create new pathways, temporarily increasing the electrical conductivity of PEDOT samples. This reorganization results in the decrease of resistance during the exposure to methanol vapors instead of charge exchange as proposed for PEDOT:PSS-based samples.

4 Conclusion

This study investigated the utility of conductive inks composed of GO, PEDOT, and PEDOT:PSS, which were applied to flexible acetate substrates as active layers for methanol sensor devices. Electrical measurements revealed a minimum resistivity point corresponding to GO:PED-OT:PSS 78%, while the highest response to methanol, reaching up to 18%, was observed with GO:PEDOT:PSS 68%. Although the greatest values for both conductivity and response were associated with a commercial ink containing PSS, sensors crafted from the synthesized aqueous conductive ink consisting of pure PEDOT and GO:PEDOT demonstrated stability with sensitivities up to 2%. Furthermore, sensors with and without PSS exhibited different interaction mechanisms with the active layers. Flexible devices produced using commercial PEDOT:PSS experienced an increase in resistance upon exposure to methanol molecules, while pure PEDOT demonstrated a decrease in resistance values. Additionally, a model was developed to explore the aforementioned challenges, offering explanations for the global minimum in electrical resistivity and the maximum response. This approach employed a Kirchoff matrix within a square lattice representation and supported both qualitative and quantitative interpretations of the experimental data. The model illustrated the competition between the resistances of PEDOT, PSS, and GO, given that PEDOT is conductive while the latter two are insulators. Moreover, the model qualitatively represented the behavior of sensors with and without PSS, accounting for both resistance increase and decrease, respectively. This simple model effectively addressed the three research questions posed in this study, with the square lattice representation serving as a simplified yet powerful method for studying such systems, yielding results consistent with larger systems.

Data availability statement

The original contributions presented in the study are included in the article/Supplementary Material, further inquiries can be directed to the corresponding authors.

Author contributions

MdN: Conceptualization, Data curation, Investigation, Methodology, Writing–original draft, Writing–review and editing, Formal Analysis, Software. SM: Conceptualization, Formal Analysis, Methodology, Software, Writing–review and editing. MF: Conceptualization, Formal Analysis, Resources, Supervision, Validation, Writing–review and editing. LR: Formal Analysis, Funding acquisition, Methodology, Supervision, Writing–review and editing.

Funding

The author(s) declare financial support was received for the research, authorship, and/or publication of this article. MdN acknowledges CAPES—PRINT for the scholarship with process number 88887.694786/2022-00 and CNPq for the scholarship with process number 140712/2020-8.

Acknowledgments

The authors acknowledge CNPq, CAPES, Fundação Araucária and INCT Nanocarbono for funding. We thank Centro de Microscopia Eletrônica (CME) for SEM images. MdN thanks CNPq and CAPES—PRINT for the fellowship.

Conflict of interest

The authors declare that the research was conducted in the absence of any commercial or financial relationships that could be construed as a potential conflict of interest.

Publisher's note

All claims expressed in this article are solely those of the authors and do not necessarily represent those of their affiliated organizations, or those of the publisher, the editors and the reviewers. Any product that may be evaluated in this article, or claim that may be made by its manufacturer, is not guaranteed or endorsed by the publisher.

Supplementary material

The Supplementary Material for this article can be found online at: https://www.frontiersin.org/articles/10.3389/frcrb.2024.1352122/full#supplementary-material

References

Afzal, A. (2019). β-Ga2O3 nanowires and thin films for metal oxide semiconductor gas sensors: sensing mechanisms and performance enhancement strategies. *J. Materiomics* 5, 542–557. doi:10.1016/j.jmat.2019.08.003

Alves, L. S., Neves, M. F. F. d., Benatto, L., Ramos, M. K., Eising, M., de Oliveira, C. K. B., et al. (2023). Influence of nanostructuring sensors based on graphene oxide and pedot: pss for methanol detection. *IEEE Sensors J.* 23, 1845–1853. doi:10.1109/jsen.2022.3228954

Anand, A., Madalaimuthu, J. P., Schaal, M., Otto, F., Gruenewald, M., Alam, S., et al. (2021). Why organic electronic devices comprising pedot: pss electrodes should be fabricated on metal free substrates. *ACS Appl. Electron. Mater.* 3, 929–943. doi:10.1021/acsaelm.0c01043

Bassi, M. d. J., Wouk, L., Renzi, W., Oliveira, C. K., Duarte, J. L., Heisler, I. A., et al. (2021). Non-radiative energy transfer in aqueously dispersed polymeric nanoparticles for photovoltaic applications. *Synth. Met.* 275, 116740. doi:10.1016/j.synthmet.2021.116740

Borges, B. G. A. L., Holakoei, S., F das Neves, M. F., W de Menezes, L. C., de Matos, C. F., Zarbin, A. J., et al. (2019). Molecular orientation and femtosecond charge transfer dynamics in transparent and conductive electrodes based on graphene oxide and pedot: pss composites. *Phys. Chem. Chem. Phys.* 21, 736–743. doi:10.1039/c8cp05382k

Carneiro, M., das Neves, M. F., de Muniz, G. I., Filho, M. A. S. C., Oliveira, C. K., and Roman, L. S. (2023). Ecological, flexible and transparent cellulose-based substrates without post-production treatment for organic electronic devices. *J. Mater. Sci. Mater. Electron.* 34, 186–219. doi:10.1007/s10854-022-09667-8

Chang, Y.-M., Li, W.-L., Tsai, C.-H., and Teng, N.-W. (2023). Mitigating the efficiency loss of organic photovoltaic cells using phosphomolybdic acid-doped pedot: pss as hole transporting layer. *Adv. Energy Sustain. Res.* 4, 2300006. doi:10.1002/aesr.202300006

Cinquino, M., Prontera, C. T., Zizzari, A., Giuri, A., Pugliese, M., Giannuzzi, R., et al. (2022). Effect of surface tension and drying time on inkjet-printed pedot: pss for ito-free oled devices. *J. Sci. Adv. Mater. Devices* 7, 100394. doi:10.1016/j.jsamd.2021.09.001

das Neves, M. F., Damasceno, J. P. V., Junior, O. D., Zarbin, A. J., and Roman, L. S. (2021). Conductive ink based on pedot nanoparticles dispersed in water without organic solvents, passivant agents or metallic residues. *Synth. Met.* 272, 116657. doi:10.1016/j.synthmet.2020.116657

das Neves, M. F. F., Damasceno, J. P. V., Holakoei, S., Rocco, M. L. M., Zarbin, A. J. G., De Oliveira, C. K. B. Q. M., et al. (2019). Enhancement of conductivity and transmittance of graphene oxide/pedot: pss electrodes and the evaluation of charge transfer dynamics. *J. Appl. Phys.* 126, 215107. doi:10.1063/1.5124619

del Olmo, R., Mendes, T. C., Forsyth, M., and Casado, N. (2022). Mixed ionic and electronic conducting binders containing pedot: pss and organic ionic plastic crystals toward carbon-free solid-state battery cathodes. *J. Mater. Chem. A* 10, 19777–19786. doi:10.1039/d1ta09628a

Eising, M., Cava, C. E., Salvatierra, R. V., Zarbin, A. J. G., and Roman, L. S. (2017). Doping effect on self-assembled films of polyaniline and carbon nanotube applied as ammonia gas sensor. *Sensors Actuators B Chem.* 245, 25–33. doi:10.1016/j.snb.2017.01.132

Eising, M., O'Callaghan, C., Eduardo Cava, C., Schmidt, A., Gorgatti Zarbin, A. J., Ferreira, M. S., et al. (2021). The role of carbon nanotubes on the sensitivity of composites with polyaniline for ammonia sensors. *Carbon Trends* 3, 100026. doi:10.1016/j.cartre.2021.100026

Fujita, H., Hao, M., Takeoka, S., Miyahara, Y., Goda, T., and Fujie, T. (2022). Paper-based wearable ammonia gas sensor using organic–inorganic composite pedot: pss with iron (iii) compounds. *Adv. Mater. Technol.* 7, 2101486. doi:10.1002/admt.202101486

Gu, Z.-Z., Tian, Y., Geng, H.-Z., Rhen, D. S., Ethiraj, A. S., Zhang, X., et al. (2019). Highly conductive sandwich-structured cnt/pedot: pss/cnt transparent conductive films for oled electrodes. *Appl. Nanosci.* 9, 1971–1979. doi:10.1007/s13204-019-01006-4

Hasani, A., Dehsari, H. S., Gavgani, J. N., Shalamzari, E. K., Salehi, A., Afshar Taromi, F., et al. (2015). Sensor for volatile organic compounds using an interdigitated gold electrode modified with a nanocomposite made from poly (3, 4-ethylenedioxythiophene)-poly (styrenesulfonate) and ultra-large graphene oxide. *Microchim. Acta* 182, 1551–1559. doi:10.1007/s00604-015-1487-7

Hashemi, S. A., Bahrani, S., Mousavi, S. M., Omidifar, N., Arjmand, M., Lankarani, K. B., et al. (2022). Differentiable detection of ethanol/methanol in biological fluids using prompt graphene-based electrochemical nanosensor coupled with catalytic complex of nickel oxide/8-hydroxyquinoline. *Anal. Chim. Acta* 1194, 339407. doi:10.1016/j.aca.2021.339407

Holakoei, S., Veiga, A. G., Turci, C. C., das Neves, M. F. F., Wouk, L., V Damasceno, J. P., et al. (2020). Conformational and electron dynamics changes induced by cooling treatment on go: pedot: Pss transparent electrodes. *J. Phys. Chem. C* 124, 26640–26647. doi:10.1021/acs.jpcc.0c07827

Kim, D. H., Lee, D. J., Kim, B., Yun, C., and Kang, M. H. (2020). Tailoring pedot: pss polymer electrode for solution-processed inverted organic solar cells. *Solid-State Electron.* 169, 107808. doi:10.1016/j.sse.2020.107808

Lima, L., Matos, C., Gonçalves, L., Salvatierra, R., Cava, C., Zarbin, A., et al. (2016). Water based, solution-processable, transparent and flexible graphene oxide composite as electrodes in organic solar cell application. *J. Phys. D Appl. Phys.* 49, 105106. doi:10.1088/0022-3727/49/10/105106

Lin, Y., and Fan, Z. (2020). Compositing strategies to enhance the performance of chemiresistive co2 gas sensors. *Mater. Sci. Semicond. Process.* 107, 104820. doi:10.1016/j.mssp.2019.104820

Lo, C.-Y., Wu, Y., Awuyah, E., Meli, D., Nguyen, D. M., Wu, R., et al. (2022). Influence of the molecular weight and size distribution of pss on mixed ionic-electronic transport in pedot: pss. *Polym. Chem.* 13, 2764–2775. doi:10.1039/d2py00271j

Mehl, H., Matos, C. F., Neiva, E., Domingues, S., and Zarbin, A. (2014). The effect of variation of reactional parameters in the preparation of graphene by oxidation and reduction of graphite. *Quím. Nova* 37. doi:10.5935/0100-4042.20140252

Miranda, B. H., Corrêa, L. d. Q., Soares, G. A., Martins, J. L., Lopes, P. L., Vilela, M. L., et al. (2021). Efficient fully roll-to-roll coated encapsulated organic solar module for indoor applications. *Sol. Energy* 220, 343–353. doi:10.1016/j.solener.2021.03.025

Nie, S., Qin, F., Liu, Y., Qiu, C., Jin, Y., Wang, H., et al. (2023). High conductivity, semiconducting, and metallic pedot: pss electrode for all-plastic solar cells. *Molecules* 28, 2836. doi:10.3390/molecules28062836

O'Callaghan, C., Gomes da Rocha, C., Manning, H. G., Boland, J. J., and Ferreira, M. S. (2016). Effective medium theory for the conductivity of disordered metallic nanowire networks. *Phys. Chem. Chem. Phys.* 18, 27564–27571. doi:10.1039/c6cp05187a

Ouyang, J. (2013). "secondary doping" methods to significantly enhance the conductivity of pedot: pss for its application as transparent electrode of optoelectronic devices. *Displays* 34, 423–436. doi:10.1016/j.displa.2013.08.007

Pasupuleti, K. S., Reddeppa, M., Nam, D.-J., Bak, N.-H., Peta, K. R., Cho, H. D., et al. (2021). Boosting of no2 gas sensing performances using go-pedot: pss nanocomposite chemical interface coated on langasite-based surface acoustic wave sensor. *Sensors Actuators B Chem.* 344, 130267. doi:10.1016/j.snb.2021.130267

Saaedi, A., Shabani, P., and Yousefi, R. (2019). High performance of methanol gas sensing of zno/pani nanocomposites synthesized under different magnetic field. *J. Alloys Compd.* 802, 335–344. doi:10.1016/j.jallcom.2019.06.088

Saxena, N., Pretzl, B., Lamprecht, X., Bießmann, L., Yang, D., Li, N., et al. (2019). Ionic liquids as post-treatment agents for simultaneous improvement of seebeck coefficient and electrical conductivity in pedot: pss films. *ACS Appl. Mater. interfaces* 11, 8060–8071. doi:10.1021/acsami.8b21709

Singh, S., and Sharma, S. (2022). Temperature dependent selective detection of ethanol and methanol using mos2/tio2 composite. *Sensors Actuators B Chem.* 350, 130798. doi:10.1016/j.snb.2021.130798

Vigna, L., Verna, A., Marasso, S., Sangermano, M., D'Angelo, P., Pirri, F., et al. (2021). The effects of secondary doping on ink-jet printed pedot: pss gas sensors for vocs and no2 detection. *Sensors Actuators B Chem.* 345, 130381. doi:10.1016/j.snb.2021.130381

Wu, F., Pan, X., Wang, H., Hua, M., Yu, H., Zang, X., et al. (2022). Experimental study on the explosion characteristic and flame propagation of methanol spray at different injection pressures. *Fuel* 325, 124746. doi:10.1016/j.fuel.2022.124746

Yoon, S.-S., and Khang, D.-Y. (2016). Roles of nonionic surfactant additives in pedot: pss thin films. *J. Phys. Chem. C* 120, 29525–29532. doi:10.1021/acs.jpcc.6b12043

Yoonessi, M., Borenstein, A., El-Kady, M. F., Turner, C. L., Wang, H., Stieg, A. Z., et al. (2019). Hybrid transparent pedot: pss molybdenum oxide battery-like supercapacitors. *ACS Appl. Energy Mater.* 2, 4629–4639. doi:10.1021/acsaem.8b02258

Zeng, F.-W., Liu, X.-X., Diamond, D., and Lau, K. T. (2010). Humidity sensors based on polyaniline nanofibres. *Sensors Actuators B Chem.* 143, 530–534. doi:10.1016/j.snb.2009.09.050

frontiers | Frontiers in Carbon

TYPE Original Research
PUBLISHED 05 February 2024
DOI 10.3389/frcrb.2024.1305183

OPEN ACCESS

EDITED BY
Duncan John Mowbray,
Yachay Tech University, Ecuador

REVIEWED BY
Sadegh Sadeghzadeh,
Iran University of Science and Technology, Iran
Pilgyu Kang,
George Mason University, United States

*CORRESPONDENCE
Solange B. Fagan,
solange.fagan@gmail.com

RECEIVED 30 September 2023
ACCEPTED 03 January 2024
PUBLISHED 05 February 2024

CITATION
de Matos CF, Leão MB, Vendrame LFO, Jauris IM, Zanella I and Fagan SB (2024), Unlocking the paracetamol adsorption mechanism in graphene tridimensional-based materials: an experimental-theoretical approach.
Front. Carbon 3:1305183.
doi: 10.3389/frcrb.2024.1305183

Unlocking the paracetamol adsorption mechanism in graphene tridimensional-based materials: an experimental-theoretical approach

Carolina F. de Matos[1,2], Mayara B. Leão[1], Laura F. O. Vendrame[3], Iuri M. Jauris[4], Ivana Zanella[3] and Solange B. Fagan[3]*

[1]Environmental Science and Technology Center, Campus Caçapava do Sul, Federal University of Pampa, Caçapava do Sul, Brazil, [2]Chemistry Department, Federal University of Santa Maria, Santa Maria, Brazil, [3]Physics Department, Franciscan University, Santa Maria, Brazil, [4]School of Sciences, Pontifical Catholic University of Rio Grande do Sul, Porto Alegre, Brazil

The omnipresence of emerging contaminants in the aquatic environment is indisputable. These contaminants include chemical substances not removed in traditional water and sewage treatment processes. To ensure the quality of water and healthy aquatic ecosystems, new treatment technologies and materials are essential to effectively control the presence of these contaminants in the aquatic environment. More than that, it is important to know how molecules interact with these new materials. A low-cost alternative currently available is adsorption. Despite this method being widely studied, describing the interaction mechanisms between the materials and the analytes is not usual, limiting the obtainment of more efficient materials. Thus, the objective of this work was to understand, in a theoretical-experimental way, the forms of interaction in the adsorption of the drug paracetamol, widely used worldwide, in materials based on graphene with different chemical and structural properties. For this, kinetic and isothermal experimental studies were carried out using four materials that contemplated different dimensions, pore sizes, and oxidation degrees. In theoretical studies, density functional theory (DFT) simulations were performed to cover quantum details, revealing how paracetamol interacts with different graphene structures. According to theoretical studies, binding energies, binding distances, and charge transfer between oxidized graphene and paracetamol drug are compatible with physical adsorption, strongly dependent on the type and number of functional groups on the graphene surface. These results agree with the experimental data where the highest adsorptions were observed precisely for materials containing a higher proportion of functional groups and where these groups are more available (more porous), with adsorptive capacities reaching 235.7 mg/g. Our findings

contribute to scientific knowledge about using graphene structures as an adsorbent material, providing a solid basis for future studies and developing more efficient and advanced water treatment technologies.

KEYWORDS

contaminants, density functional theory, functional groups, oxidized graphene, simulation

1 Introduction

Graphene, graphene oxide (GO), and reduced graphene oxide (2D-rGO) have been widely used as adsorbents to remove different classes of contaminants from water (Ersan et al., 2017; Bolisetty et al., 2019; Liu et al., 2019; Yousefi et al., 2019; Alves et al., 2021). This application is highlighted for this type of material due to its unique properties, such as high specific surface area and amphiphilic structure, in materials with polar groups (Alves et al., 2021; Huang et al., 2021). Pristine graphene, besides its limitations in obtaining (Wang et al., 2020), has limited applications due to its hydrophobicity and its unique π-π interactions. GO and rGO, on the other hand, improve the accessibility of contaminants in aqueous systems and extend material-analyte interactions through hydrogen bonding and electrostatic interactions (Deshwal et al., 2023; Fan et al., 2023). Despite the range of these materials in removing contaminants, their applications are limited by agglomeration or re-stacking of graphene sheets through strong π-π and van der Waals interactions between the sheets. This process results in a reduction in surface area, poor dispersion in aqueous media, and a consequent reduction in adsorption efficiency (Shan et al., 2017; Alves et al., 2021; Lin et al., 2021; Wong et al., 2022). In addition, due to their two-dimensional structure, these materials can be easily leached into water bodies, being affected by a difficult recovery process.

An alternative to solve these problems is using three-dimensional materials of reduced graphene oxide (3D-rGO). These materials have interconnected pores formed by the disorderly bonding of two-dimensional reduced graphene oxide sheets (Shan et al., 2017). These materials are a solution to the problems mentioned above and have excellent mechanical properties, specific surface areas, and high porosity (Torabi Fard et al., 2022). Based on their structures and properties, these materials have been applied in different contaminant removal methods, such as photocatalysis, advanced Fenton oxidation, capacitive deionization (Jung et al., 2018; Wang et al., 2019; Yang et al., 2020; Yu et al., 2022), and especially adsorption (Bruckmann et al., 2022; Leão et al., 2022; Leão et al., 2023). This water treatment method is widely used due to its simplicity and high efficiency (Hiew et al., 2019). In the case of three-dimensional graphene materials and their derivatives, relevant and desirable adsorptive capacities have been found for different contaminants (Torabi Fard et al., 2022), such as metals, dyes (Liu and Qiu, 2020; Lin et al., 2021; Sun et al., 2021), organic solvents, oils (Liu and Qiu, 2020; Wong et al., 2022), pesticides (Guo et al., 2021), and drugs. In the case of drugs, different classes have been removed through the adsorption process, using three-dimensional materials based on graphene, decorated or not. Recent studies show, for example, the use of three-dimensional reduced graphene oxide functionalized with caffeic acid in the removal of norfloxacin (220.99 mg g^{-1}) and ketoprofen (125.37 mg g^{-1}) (Lu et al., 2020); when functionalized with chitosan, a similar material was able to remove up to 14.4 mg g^{-1} of sulfamethazine (Hamed et al., 2022). The synergistic effects of 3D-rGO/MnO_2 were evaluated in removing and degrading tetracycline from water, which can remove up to 91% of this drug (Song et al., 2019). The 3D-rGO has also been applied to efficiently remove ibuprofen, diclofenac and naproxen with efficiencies of up to 526 mg g^{-1} (Umbreen et al., 2018).

Pharmaceutical products are not fully eliminated in conventional water and sewage treatments and are destined for water resources. There, they can impact the organisms that live in that ecosystem and humans (Villaescusa et al., 2011; Hamed et al., 2022). A drug that has attracted attention due to its characteristics is paracetamol (PCM), also known as acetaminophen, the most widely used analgesic worldwide (Villaescusa et al., 2011; van den Driesche et al., 2015; Hiew et al., 2022). When ingested, paracetamol cannot be completely metabolized, and approximately 20% of the drug is excreted into the environment as metabolites, ending up in water bodies and effluent treatment plants. During the disinfection process of water or effluents, paracetamol may be reactive with hypochlorite, generating significantly toxic compounds (Bedner and MacCrehan, 2006). In addition, several studies suggest that paracetamol may have endocrine-disrupting effects at all stages of human development, being able to act as an anti-androgenic substance and causing male reproductive disorders (van den Driesche et al., 2015; Albert et al., 2013; Kristensen et al., 2016; Kristensen et al., 2011; Kristensen et al., 2012). In addition to the wide use and risks attributed to this drug, there is also a low number of studies evaluating its removal using adsorption since conventional water treatment techniques (Villaescusa et al., 2011; Hamed et al., 2022). Paracetamol adsorption has been described on silica, alumina (Lorphensri et al., 2006), aquifer sand (Hamed et al., 2022), and carbon materials such as coconut activated carbon (Fernandez et al., 2015), rice husk (Paredes-Laverde et al., 2019), and tea leaves (Wong et al., 2018), grape stalk, yohimbe bark and cork bark (Villaescusa et al., 2011), multi-walled carbon nanotubes (Yanyan et al., 2018) and graphene oxide (Moussavi et al., 2016). At the same time, no studies report the use of graphene-based three-dimensional materials, which had their previously mentioned advantages.

Simultaneously, to find new materials capable of efficiently removing this drug, it is necessary to determine the interaction mechanisms between the material and the analyte. These determinations can be carried out using computer simulations, where one can simulate the interaction with materials that present different degrees of oxidation or pore sizes, for example,. In this sense, the objective of this work was to experimentally evaluate the efficiency of 3D-rGO materials with different degrees of oxidation of the structure and a two-dimensional graphene oxide material (2D-rGO) in the adsorption of the analgesic paracetamol.

Furthermore, the experimental results were compared with *ab initio* computer simulations to elucidate the mechanisms involved in the material-analyte interaction.

2 Experimental

2.1 Experimental setup and details

2.1.1 Obtaining 2D graphene-based material

Two-dimensional reduced graphene oxide was obtained from the chemical oxidation of graphite, followed by exfoliation to obtain graphene oxide. The reducing agent ascorbic acid was used at a concentration of 25 mmol L^{-1} 150 mL of GO dispersion (1 mg mL^{-1}) and the corresponding amount of reducing agent were added to a round bottom flask and kept at reflux for 3 h. At the end of the process, the material obtained was washed several times with distilled water.

2.1.2 Obtaining 3D graphene-based materials

The three-dimensional materials of reduced graphene oxide (3D-rGO) were obtained as described by Leão et al. (Leão et al., 2022), from the chemical oxidation of graphite followed by exfoliation in an ultrasound bath (SP Labor, model SP-UL, frequency 50 kHz) to obtain graphene oxide. A dispersion of this graphene oxide at a concentration of 1 mg mL^{-1} was used to obtain 3D-rGO. This was obtained from a thermochemical process using the ascorbic acid-reducing agent at different concentrations (0, 5, and 25 mmol L^{-1}). The corresponding amount of reducing agent and 50 mL of GO dispersion were added to 100 mL beakers, mixed, and taken to an autoclave (Stermax Digital Super Top, 21 L) at 120 C for 90 min. At the end of the process, the monoliths were removed and washed with distilled water, ready for use as a hydrogel. The entire synthesis process takes about 2 h.

The abbreviations for reference to the samples in this work are 3D-rGO for three-dimensional reduced graphene oxide. The second part of the acronym refers to different concentrations of reducing agent (0, 5 and 25 mmol L^{-1}); for example, 3D-rGO0 is used for 3D reduced material without ascorbic acid, and so on.

2.1.3 Materials characterization

The complete characterization of these materials is better described in our previous work (Leão et al., 2022). In this previously published work, the characterizations of X-ray Diffraction (XRD), Fourier Transform Infrared Spectroscopy (FTIR), Raman Spectroscopy, Thermogravimetry (TGA) and zero charge point pH (pH_{ZCP}) are presented. To avoid repetitions, in this work, the characterization of 3D-rGO0, 3D-rGO5, 3D-rGO25 and 2D-rGO was performed using Scanning Electron Microscopy (SEM), Brunauer–Emmett–Teller (BET) specific surface area values, and indirect potentiometric titration.

For Scanning Electron Microscopy, a MIRA 3 FEG-SEM microscope was used. The samples were placed on double-sided copper tapes previously glued on the sample holder. All samples were metalized with chromium; the source voltage was 15 kV. The BET method obtained the surface area using a Quantachrome Instrument, NOVA 4200e, United States. The indirect potentiometric titration was performed according to Hanelt et al. (2011) (Hanelt et al., 2011). The materials were kept in a NaOH 0.0025 mol L^{-1} solution, standardized with potassium biphthalate, for 24 h. At the end of this time, the solution was filtered and titrated with HCl 0.001 mol L^{-1}, using KCl 0.01 mol L^{-1} as a supporting electrolyte.

2.1.4 Adsorption experimental studies

The kinetic study used 8 mg of each material, left in contact with 5 mL of PCM 50 mg L^{-1}. At predetermined time intervals and until equilibrium, the concentration of PCM in the solution was determined. From the data obtained, the adsorptive capacity of the materials was calculated using Equation (1) (Thue et al., 2018), where Qe, is the adsorptive capacity in mg g^{-1}, Ce and Cf are the initial and final concentrations of the solution (mg L^{-1}), V is the volume of solution (L) and m is the mass of the adsorbent (g). The obtained results were fitted to non-linear kinetic models of general order, pseudo-first order and pseudo-second order.

$$Qe = \frac{(Ce - Cf) \times V}{m} \quad (1)$$

As for the equilibrium isotherms, 8 mg of adsorbent was kept in contact with 5 mL of PCM at 50, 100, 250, 500, 1,000, 1,500 and 2000 mg L^{-1} concentrations. After 5 h, the final drug concentration in the solution was determined. The adsorptive capacity was determined from Equation (1), and the data were fitted to the non-linear isothermal models of Langmuir, Freundlich and Sips.

All experiments were conducted at an ambient temperature of approximately 25 C, with constant stirring at 150 rpm. Solution concentrations were determined using a Kasuaki IL-593-S UV-Vis spectrophotometer at a wavelength of 242 nm. All experiments were performed in triplicates.

3 Computational model and details

3.1 *Ab initio* simulations

The *ab initio* simulation was performed using SIESTA code (Soler et al., 2002). They were evaluated through first-principles calculations based on DFT (Hohenberg and Kohn, 1964; Kohn and Sham, 1965) to obtain electronic, structural, and energetic properties. In all calculations, we used the local density approximation (LDA) parameterized by Perdew and Zunger to describe the exchange–correlation potential. LDA is more suitable than the Generalized Gradient Approximation (GGA) to study weakly interacting systems and also the presence of π-stacking interactions on sp^2-like materials. It is also important to outline that similar LDA calculations have been employed successfully in our group to describe the most diverse types of systems related to Gr-molecule interactions, resulting in an excellent tool for the connection between theory and experiments. Additionally, the present methodology used in this work allowed us for a feasible comparison with previously published work by our team, where the LDA results for binding energy and bond distance are very close to the experimental one (Jauris et al., 2017; de Oliveira et al., 2021; Bruckmann et al., 2022; Leão et al., 2023).

The interactions between the core and the valence electrons were employed through Troullier–Martins pseudopotentials (Troullier and Martins, 1991), whereas the molecular orbitals made use of a localized double zeta plus polarization (DZP) (Sankey and Niklewski, 1989) basis

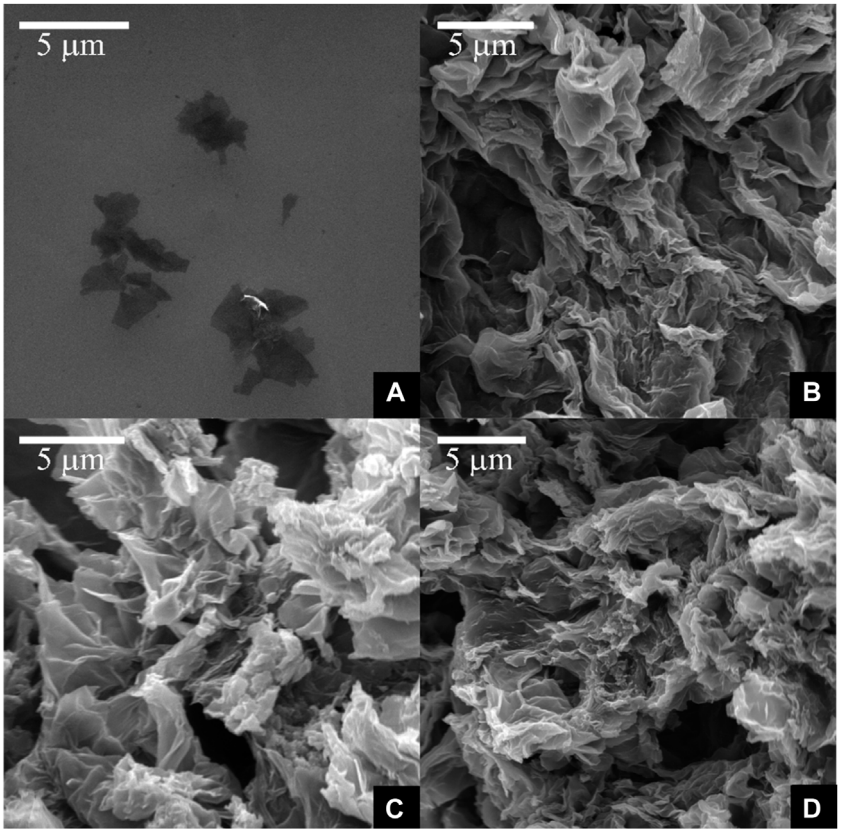

FIGURE 1
Scanning Electron Microscopy of 2D-rGO **(A)**, 3D-rGO0 **(B)**, 3D-rGO5 **(C)**, and 3D-rGO25 **(D)** materials.

TABLE 1 Properties of the materials obtained according to the characterizations performed (Leão et al., 2022).

Material	Concentration of COOH (mmol g^{-1})	Specific surface area (m^2 g^{-1})
2D-rGO	-	91.6
3D-rGO0	10.62 ± 1.84	172.274
3D-rGO5	3.08 ± 0.12	163.198
3D-rGO25	2.52 ± 1.34	62.807

set through a limited energy shift of 0.05 eV. The cutoff of 200 Ry in the grid integration represents the charge density for all interactions. Mulliken population analysis evaluated the electronic charge transfer between paracetamol (PCM) and graphene (Gr).

The structural optimization was performed by a conjugate gradient method. All atomic coordinates were allowed to move until the residual forces were less than 0.05 eV/Å. The computational method and simulation parameters were similar to those used in our previous work (de Oliveira et al., 2021; Bruckmann et al., 2022; Leão et al., 2023). These structures can describe qualitatively the results by combining simulations and experimental data for molecule adsorption.

Thus, the structures studied were graphene functionalized with one epoxy/two epoxy groups (Gr[O]/Gr[2O]), one hydroxyl/two hydroxyl groups (Gr[OH]/Gr[2OH]), and one carboxyl/two carboxyl groups (Gr[COOH]/Gr[2COOH]), where each of them interacts with PCM (CAS 103-90-2; $C_8H_9NO_2$). Three different pairs Gr[O]/Gr[2O], Gr[OH]/Gr[2OH], and Gr[COOH]/Gr[2COOH], were used in the simulation and represent the type and quantity of functional groups in the graphene model used. They reflect possible functional groups present in reduced graphene oxide structures. We do not use the same functional groups simultaneously, so it would be possible to evaluate their individual collaboration. These models were chosen to explain the effect of the type and quantity of functional groups on the PCM adsorption mechanism on three-dimensional materials based on graphene, whose structural differences are mainly due to the amount and kind of oxygenated groups.

The optimized structures can be seen in Supplementary Figure S1. We use several different configurations for every system associated with PCM. Notably, only the most stable configurations are presented in this work. The final binding energies (EB) were calculated according to Equation 2, which is based on the Basis Set Superposition Error (BSSE) (Boys and Bernardi, 1970),

$$EB = -\left[E(Gr + PCM) - E(Grghost + PCM) - E(Gr + PCMghost)\right] \quad (2)$$

where EB is the binding energy, EB(Gr + PCM) is the total energy of the Gr plus PCM molecule. The subscript "ghost" corresponds to the additional basis wave functions centered at the position of the Gr or at the PCM molecule but without any atomic potential. The minimum distance (DB) values between the PCM and the Gr

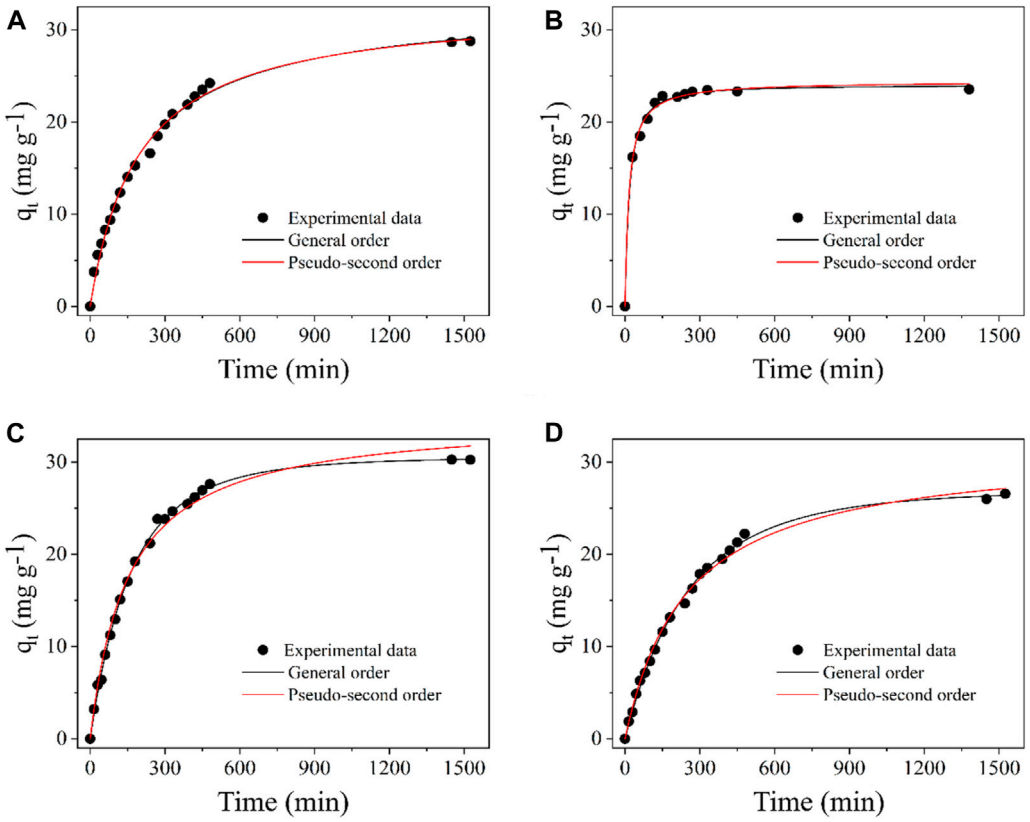

FIGURE 2
Adsorption kinetics of paracetamol in 2D-rGO **(A)**, 3D-rGO0 **(B)**; 3D-rGO5 **(C)**, and 3D-rGO25 **(D)**.

TABLE 2 The kinetic parameters for paracetamol adsorption by 2D-rGO, 3D-rGO0, 3D-rGO5, and 3D-rGO25.

	2D-rGO	3D-rGO0	3D-rGO5	3D-rGO25
General-order				
k_N(min^{-1}.(g.mg^{-1})$^{n-1}$)	9.46 × 10^{-5}	0.005	0.003	0.002
q_e (mg.g^{-1})	33.529	23,998	30,517	26,938
n	2.140	1,770	1,233	1,213
$t_{1/2}$ (min)	203,829	16,693	123,602	188,380
R^2_{adj}	0.9925	0.9949	0.9978	0.9973
SD	0.719	0.476	0.447	0.420
Pseudo-second order				
k_2(g.mg^{-1}.min^{-1})	1.590 × 10^{-4}	0.003	1,886 × 10^{-4}	1,282 × 10^{-4}
q_e (mg.g^{-1})	32.634	24,417	34,902	31,544
$t_{1/2}$ (min)	192,728	15,910	151,871	247,299
R^2_{adj}	0.9930	0.9950	0.9911	0.9937
SD	0.7013	0.474	0.8956	0.642

were obtained from the nearest atoms. The bond distance (DB) values between PCM and Gr are obtained from the minimum interatomic distance between the systems. In this paper, to quantify an interaction such as physical or chemical adsorption, we considered parameters such as charge transfer, bond distance, and detailed analysis from the electronic energy levels of the systems, similar to those used in previous works (Vendrame et al., 2019; Concu et al., 2020; Leão et al., 2022; Leão et al., 2023).

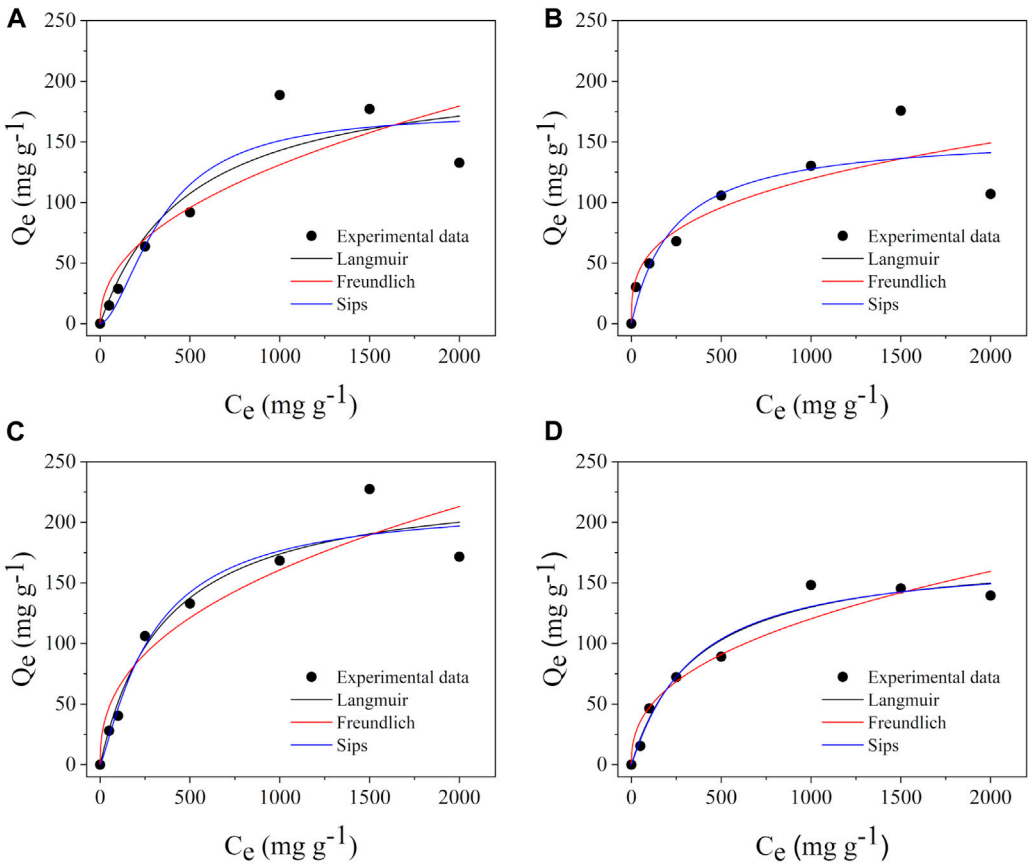

FIGURE 3
Adsorption isotherms of paracetamol in 2D-rGO **(A)**, 3D-rGO0 **(B)**; 3D-rGO5 **(C)**, and 3D-rGO25 **(D)**.

4 Results and discussion

4.1 Material characterization

As already mentioned, a detailed version of the characterization of these materials can be found in the article that describes the process of synthesis and characterization of these materials (Leão et al., 2022). The SEM images of the four studied materials are shown in Figure 1. The structural difference between 2D-rGO (Figure 1A) and 3D materials can be observed. While the first one appears as small sheets, the others have these sheets interconnected disorderly, forming a three-dimensional porous network. It is also possible to observe significant differences among the 3D materials (Figure 1B–D). The greater the amount of reducing agent added, the greater the compaction of the structure, which has smaller cavities. Thus, it can be expected that different behaviors are found for the materials due to their morphology. Self-assembling graphene oxide sheets form 3D graphene network structures through hydrogen bonding, electrostatic interaction, or π-π interactions. Wang et al. (2019) Considering the self-assembly mechanism of graphene hydrogels via hydrothermal routes, the pore size results from the size of the bubbles formed during the process. It must be considered that a greater degree of oxygen functionalization promotes greater interaction with the polar solvent, leaving larger hydrate pores. However, when the reduction process removes the hydrophilic groups, the water in the pore decreases, consequently allowing for higher structure compaction.

The results of the concentration of functional groups (Table 1) show that the greater the amount of reducing agent added, the smaller the number of oxygenated groups. These results are corroborated by the FTIR spectra available in (Leão et al., 2022). Likewise, for 3D materials, the greater the amount of reducing agent, the smaller the material-specific surface areas; the 2D-rGO material has an intermediate surface, closer to the 3D-rGO25 material–which is the 3D version closest to it. The combination of these results shows that the variation in the amount of reducing agent used interferes with the chemical structure and the morphology of the materials.

4.2 Experimental adsorption results

From the experimental adsorption studies, it was possible to compare the efficiencies of the materials as follows. The kinetic study, shown in Figure 2, and detailed data in Table 2, show that the behavior of the adsorption rate is influenced by the synthesis method and the concentration of the reducing agent, that is, the presence of functional groups. Reaching adsorption equilibrium was approximately 5 h for 3D-rGO0, 12 h for 3D-rGO5, 20 h for 3D-rGO25 and 24 h for 2D-rGO. Respectively, for the four materials, $t_{1/2}$ was 15.9, 123.6, 188.4 and 192.7 min. This last value represents the

10.3389/frcrb.2024.1305183

TABLE 3 Isotherm parameters for paracetamol adsorption using 2D-rGO, 3D-rGO0, 3D-rGO5 and 3D-rGO25 adsorbent.

	2D-rGO	3D-rGO0	3D-rGO5	3D-rGO25
Langmuir				
Q_{max} ($mg.g^{-1}$)	213,48	157,647	235,692	176,765
K_L ($L.mg^{-1}$)	0.0020	0.0043	0.0028	0.0028
R^2_{adj}	0,8677	0,8404	0,9372	0,9647
SD	26,531	22,869	20,140	11,067
Freundlich				
K_F ($mg.g^{-1}(mg.L^{-1})^{-1/n_F}$)	5,703	13,148	9,685	7,291
n_F	2,204	3,130	2,459	2,463
R^2_{adj}	0.7937	0.8095	0.8850	0.9226
SD	33,136	24,986	27,244	16,394
Sips				
Q_{max} ($mg.g^{-1}$)	175,098	157,647	215,902	172,335
K_s ($L.mg^{-1}$)	$4,431 \times 10^{-5}$	0.004	0.001	0.002
n_s	0.583	1	0.827	0.953
R^2_{adj}	0.8678	0.8085	0.9280	0.9579
SD	26,528	25,051	21,562	12,091

TABLE 4 Binding distance (DB), charge transfer [△q (e–)], Highest Occupied Molecular Orbital (HOMO), Lowest Unoccupied Molecular Orbital (LUMO) difference (△HL), and binding Q21 energy (EB). The positive signal in the charge transfer indicates that the Gr is a charge donor. The bold values correspond to the most stable structures.

Configuration	DB (Å)	Δq (e–)	ΔHL (eV)	EB (eV)
Gr[O]+PCM-I	2.33 (OGr-HPCM)	0.21	1.34	0.38
Gr[O]+PCM-II	**1.88 (OGr-HPCM)**	**0.29**	**1.25**	**0.60**
Gr[O]+PCM-III	2.29 (OGr-HPCM)	0.16	1.50	0.23
Gr[2O]+PCM-I	2.16 (OGr-HPCM)	0.13	1.56	0.27
Gr[2O]+PCM-II	**2.00 (OGr-HPCM)**	**0.35**	**1.31**	**0.49**
Gr[2O]+PCM-III	2.13 (OGr-HPCM)	0.05	1.55	0.24

time required for 50% of the analyte to be adsorbed and is used to compare the different materials (Thue et al., 2018).

From these results, we can infer that the 3D-rGO0 material can adsorb PCM faster, followed by the 3D-rGO5, 3D-rGO25, and 2D-rGO materials. Similar behavior has been described previously in our articles (Vijayaraghavan et al., 2006; Leão et al., 2022) in the adsorption of safranin and methylene blue dyes. We verified, then, that the behavior obtained for the dyes can be extended to the drug PCM. As in previous works, adsorption takes place more quickly in materials where there is a greater amount of oxygenated functional groups and the presence of larger cavities and/or pores. Additionally, the 3D-rGO0 material presents different behavior due to its granular structure. This structural configuration allows a larger material area to interact with the PCM, accelerating the adsorptive process. In the case of other materials, the intra-particle diffusion process must be responsible for the increased velocity in materials with larger pore sizes. As seen previously, the greater the amount of reducing agent added during synthesis, the smaller the cavities/pores, and the more compact the structure. At the same time, smaller amounts of oxygenated functional groups are available for interaction with the analytes. Such conditions guarantee the order of adsorption speed in the studied materials.

Adsorption isotherms were constructed to determine the adsorptive capacity of the materials for the drug PCM (Figure 3). The adsorptive capacities of 235.7, 176.8, 175.1 and 157.6 mg g^{-1} were determined for 3D-rGO5, 3D-rGO25, 2D-rGO, and 3D-rGO0 materials, respectively (Table 3). An important observation point is the isothermal models that best fit each result. While all three three-dimensional materials showed a better fit to the Langmuir isothermal model, only 2D-rGO showed a better fit to the Sips isothermal model. This result indicates that their dimensionality influences the adsorptive behavior of the materials. While the Langmuir model

10.3389/frcrb.2024.1305183

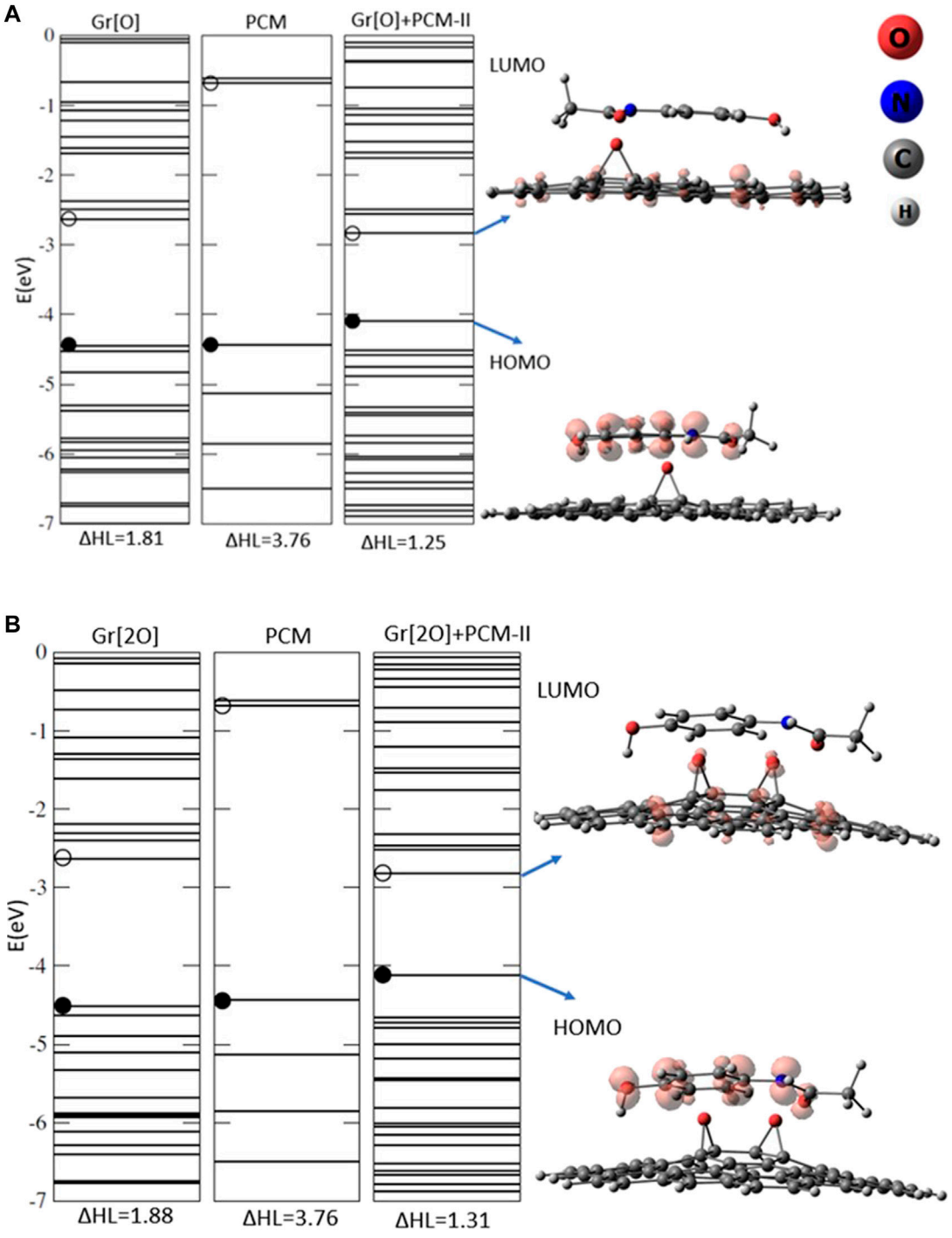

FIGURE 4
Electronic levels and LDOS for the most stable configuration: **(A)** Gr[O] +PCM-II and **(B)** Gr[2O]+PCM-II configurations with orbital charge density isosurfaces 0.0093 e−/(Å)^3.

describes monolayer adsorption, the Sips model, also called Langmuir-Freundlich, has two behaviors: at low adsorbate concentrations, it reduces to the Freundlich isotherm (Vijayaraghavan et al., 2006), and at high concentrations, predicts monolayer adsorption, with a limited number of sites on the surface of the adsorbent, characteristic of the Langmuir isotherm (Lima et al., 2015; Soltani et al., 2019).

Another important point in the adsorption study concerns the differences in adsorption capacities. Differently from the kinetic study, there is a highlight for the 3D-rGO5 material, which can absorb 235.7 mg g^{-1}. Next, we observed that the 3D-rGO25 and 2D-rGO materials have similar adsorptive capacities. In common, both materials have the highest addition of reducing agent (25 mmol L^{-1}), presenting a similar degree of reduction. Finally, the 3D-rGO0

10.3389/frcrb.2024.1305183

TABLE 5 Relevant data for minimum distance (DB), charge transfer (Δq (e–)), HOMO and LUMO difference (ΔHL), and binding energy (EB). The positive signal in the charge transfer indicates that the oxidized graphene is a charge donor.

Configuration	DB (Å)	Δq (e–)	ΔHL (eV)	EB(eV)
Gr[OH]+PCM-I	2.37 (CGr-HPCM)	0.17	1.72	0.30
Gr[OH]+PCM-II	2.37 (CGr-HPCM)	0.19	1.64	0.35
Gr[OH]+PCM-III	**1.75 (HGr-OPCM)**	0	**1.80**	**0.60**
Gr[2OH]+PCM-I	1.92 (OGr-HPCM)	0.13	1.12	0.47
Gr[2OH]+PCM-II	1.76 (OGr-HPCM)	0.35	0.66	0.69
Gr[2OH]+PCM-III	**1.52 (HGr-OPCM)**	**0.05**	**1.13**	**1.28**

material, which has excellent kinetic performance, has the lowest adsorptive capacity. From these results, we can infer some considerations. First, material morphology appears to be dominant in the adsorptive process. This can be observed mainly for the 3D-rGO0 material, which can adsorb PCM quickly but not in large quantities due to its loose granular structure. Secondly, due to similar synthesis, 3D-rGO25 and 2D-rGO materials have identical amounts of oxygenated groups. Thus, it can be deduced that smaller amounts of oxygenated functional groups result in smaller quantities of PCM. The presence of oxygenated groups is a secondary factor in the adsorption. Finally, 3D-rGO5 stands out, which presents a cohesive three-dimensional structure, is porous, less compacted, and has larger cavities and an intermediate number of oxygenated groups. Such material seems ideal for the adsorption of the drug PCM, due to its morphology and presence of oxygenated groups.

4.3 Computational results

Theoretical calculations were conducted to understand the interaction mechanisms between different three-dimensional graphene materials and the drug paracetamol, focusing on the type and number of oxygenated groups in the materials. This section provides the details of the calculations.

4.3.1 Ab initio simulations - Gr[O]/Gr[2O] interacting with PCM

To gain insights into the atomistic details of the interaction, we present the main results for Gr[O] and Gr[2O], graphene with one and two oxygen atoms attached, respectively. Both interact with the PCM molecule, and the results for the most stable configurations are presented in Table 4. The optimized structures of the most stable configurations can be found in the Supplementary Figure S2.

Table 1 presents the minimum atomic distance (DB), binding energy (EB) and electronic charge transfer (Δq (e–)) of the most stable configurations for both Gr[O]+PCM and Gr[2O]+PCM systems.

All results showed that these systems interact in a physisorption regime for both Gr structures. For PCM adsorbed on Gr[O], the most stable configuration was Gr[O]+PCM-II, with a binding energy of 0.60 eV and a distance of 1.88 Å (OGr-HPCM). The same occurs to PCM adsorbed on Gr[2O]. The most stable configuration was Gr[2O] + PCM-II, where this system presents a 0.49 eV for the binding energy with a binding distance of 2.00 Å (OGr-HPCM).

In the binding distance column, the first atom always refers to a graphene (Gr) atomic structure, while the second refers to a paracetamol (PCM) molecule. Figure 4 shows the energy levels for the Gr[O]+PCM-II and Gr[2O] + PCM-II systems. The same figure also presents the local density of states (LDOS) for the HOMO and LUMO levels.

The difference between the highest occupied molecular orbital (HOMO, represented by the solid black circle) and the lowest unoccupied molecular orbital (LUMO, represented by the hollow circle) is given in electron volts (eV). The values found are 1.81 eV for isolated graphene with one oxygen atom (Gr[O]) and 1.25 eV for the most stable interacting system between these two structures (Gr[O]+PCM-II). For isolated graphene with two oxygen atoms (Gr[2O]), the difference between HOMO and LUMO is 1.88 eV, and the interacting system, Gr[2O]+PCM-II, shows a value of 1.31 eV.

The difference between HOMO and LUMO levels is similar to the isolated graphene, without significant changes. Furthermore, we observe that there is only an overlap of the paracetamol (PCM) molecule levels with the graphene but no substantial changes in the electronic properties of the resultant system compared to the pristine ones.

Regarding the local density of states (LDOS) analysis, both systems, with one or two oxygen atoms attached to graphene, show HOMO energy level contribution on the PCM molecule, while the LUMO on the graphene structure. This characteristic leads us to a physisorption mechanism since we have only one structure contribution for each energy level.

4.3.2 *Ab initio* simulations - Gr[OH]/Gr[2OH] interacting with PCM

Here, we show Gr[OH] and Gr[2OH] data. This means we now considered two different types of oxidized Gr: the first has one OH chemical group, and the second has two OH chemical groups attached to its surface.

Both Gr[OH] and Gr[2OH] interact with PCM molecules in multiple configurations, and the key data are presented in Table 5. Table 5 shows the minimum atomic distance (DB), binding energy (EB), and electronic charge transfer (Δq (e–)) of the most stable configurations for both the Gr[OH]+PCM and Gr[2OH]+PCM systems. The optimized structures of the most stable configurations can be seen in the Supplementary Figure S3.

10.3389/frcrb.2024.1305183

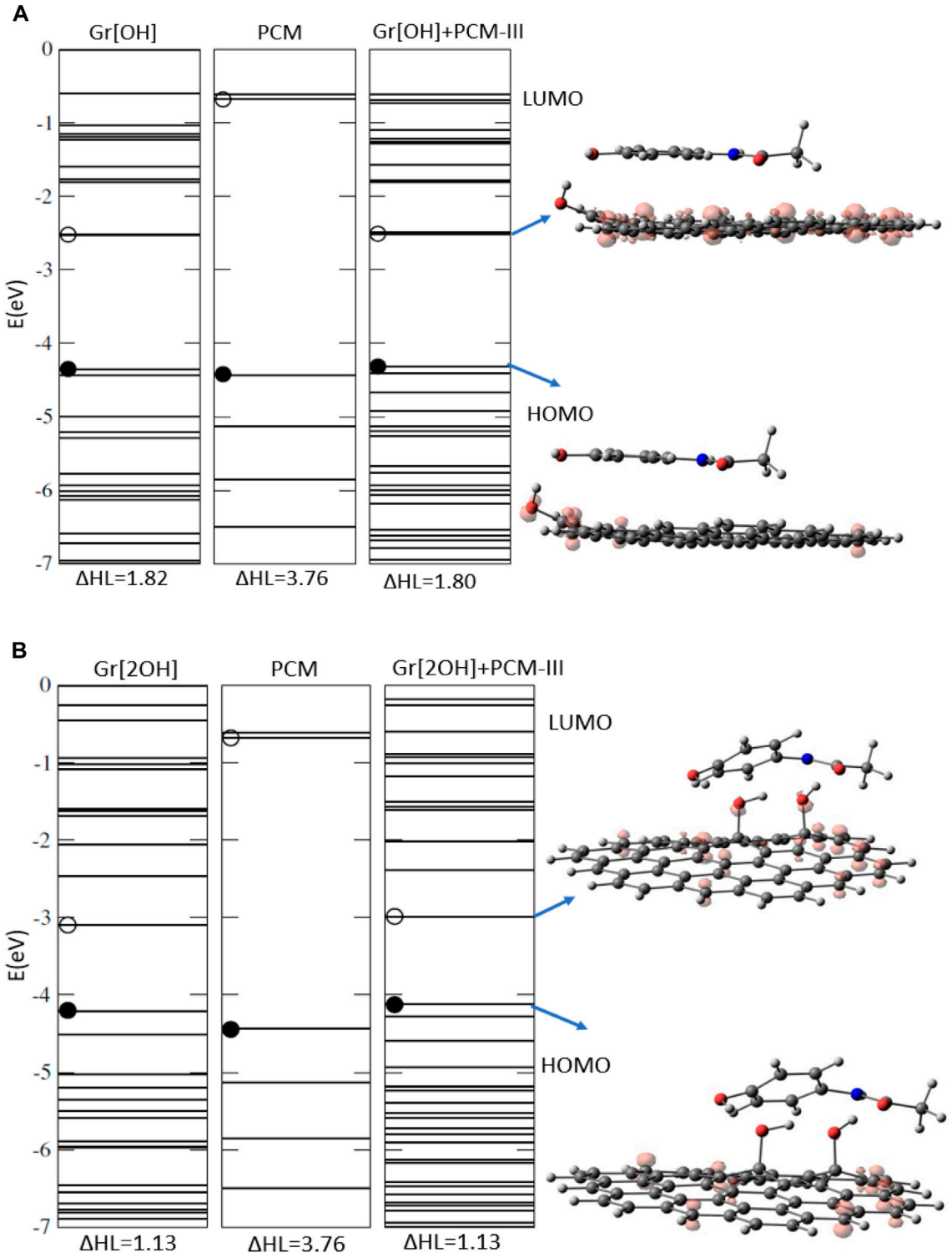

FIGURE 5
Electronic levels and LDOS for the most stable configuration: **(A)** Gr[OH] interacting with PCM (Gr[OH]+PCM-III) and **(B)** Gr[2OH] interacting with PCM molecule (Gr[2OH]+PCM-III) with orbital charge density isosurfaces 0.0093 e–/(Å)^3.

For PCM adsorbed on Gr[OH], the most stable configuration was Gr[OH]+PCM-III, with a binding energy of 0.60 eV and a distance of 1.75 Å (HGr-OPCM). For PCM adsorbed on Gr[2OH], the most stable configuration was Gr[2OH]+PCM-III, where this system presents a 1.28 eV for the binding energy with a binding distance of 1.52 Å (HGr-OPCM).

The binding energies for Gr[2OH]+PCM-III are high, suggesting the possibility of chemical interaction. However, the bond distance and

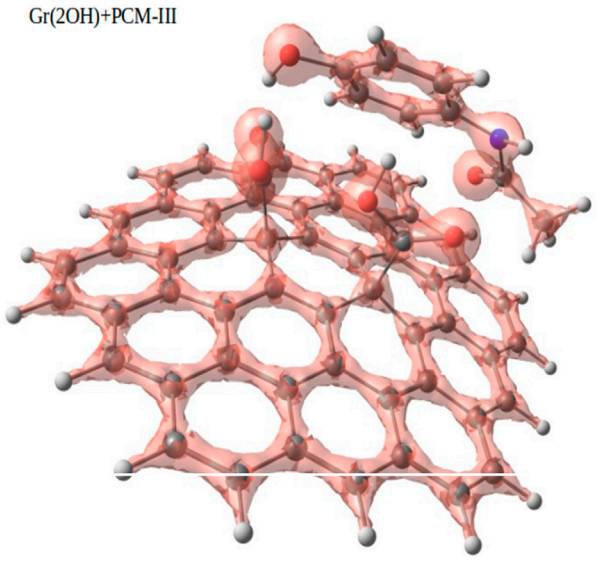

FIGURE 6
Total electronic charge density isosurface for the most stable configurations for Gr[2OH]+PCM-III using orbital charge density isosurfaces of 0.0093 e–/(Å)^3.

charge transfer values for Gr[2OH]+PCM-III are incompatible with chemisorption. Therefore, the presence of these hydrogen bonds cannot lead to significant changes in the physical adsorption regime of PCM on graphene. An electronic study of these configurations was conducted to confirm these findings, and the results are shown in Figure 5 and Figure 6.

Figure 5 shows the energy levels and the local density of states (LDOS) for both the Gr[OH]+PCM-III and Gr[2OH]+PCM-III systems. We can see that the HOMO energy level has a contribution from the graphene (Gr) structure, and the same occurs with the LUMO. This data suggests that both systems are interacting through the physisorption regime. However, the system with two OH chemical groups has a smaller binding distance and higher binding energy. For a more detailed analysis, Figure 6 shows the total charge density isosurface plots for the most stable configuration, Gr[2OH]+PCM-III, to investigate the possibility of chemisorption.

This analysis scans every single energy level of the system and shows its total electronic distribution, allowing us to confirm whether there is chemisorption between the structures (Figure 6). The image confirms no chemisorption between the -OH chemical groups and the PCM molecule. As can be seen, the charges are localized only on the Gr(2OH) and PCM molecules, with no charge lines shared between the systems. There is no electron sharing between the two structures. This result confirms that this system exhibits a physisorption interaction, as observed in previous work with graphene nanomaterials and different molecules (de Oliveira et al., 2021; Bruckmann et al., 2022; Leão et al., 2023).

4.3.3 *Ab initio* simulations - Gr[COOH]/Gr[2COOH] interacting with PCM

At last, we present the data for Gr[COOH] and Gr[2COOH]. In this case, we now have a first Gr with one COOH chemical group and a second Gr with two COOH chemical groups attached to their surface. Both Grs interact with the PCM molecule. Table 6 presents the minimum atomic distance (DB), binding energy (EB), and electronic charge transfer (Δq(e–)) of the most stable configurations for both Gr[COOH]+PCM and Gr[2COOH]+PCM systems. The optimized structures of the most stable configurations can be seen in Supplementary Figure S4.

The binding energy features the configuration Gr[COOH]+PCM-II and Gr[2COOH]+PCM-III as the most stable for Gr[COOH]+PCM and Gr[2COOH]+PCM systems, respectively. After calculating the BSSE, we found a 0.79 eV and DB of 1.61 Å (OGr-HPCM) for Gr[COOH]+PCM-II and 1.48 eV and DB of 1.49 Å (OGr-HPCM) for Gr[2COOH]+PCM-III systems. Figure 7 shows the energy levels and the LDOS for both Gr[COOH]+PCM-II and Gr[2COOH]+PCM-III systems.

We can observe that the HOMO energy level shows a contribution from the PCM molecule for the Gr[COOH]+PCM-II system and a contribution from the Gr[COOH] structure for the Gr[COOH]+PCM-III system. In the LUMO level, we can observe a contribution from Gr[2COOH] with a strong contribution from the functionalized COOH groups.

The binding energies for Gr[2COOH]+PCM-II and Gr[2COOH]+PCM-III are high, as we also observed for Gr[2OH]+PCM-II, suggesting the existence of chemical interaction. It is important to emphasize that in both cases, more than one functional group in the Gr increases the interactions with the PCM molecule. Once again, we performed the total electronic charge density isosurface analysis to check for any signs of chemisorption for the Gr[2COOH]+PCM-II and Gr[2COOH]+PCM-III systems, shown in Figure 8.

TABLE 6 Binding distance (DB), charge transfer (Δq (e–)), HOMO and LUMO difference (ΔHL), and binding energy (EB). The positive signal in the charge transfer indicates that the graphene is a charge donor.

Configurations	DB (Å)	Δq (e–)	ΔHL (eV)	EB (eV)
Gr[COOH]+PCM-I	2.22 (OGr-HPCM)	0.15	1.54	0.34
Gr[COOH]+PCM-II	**1.61 (OGr-HPCM)**	**0.32**	**1.18**	**0.79**
Gr[COOH]+PCM-III	2.81 (CGr-HPCM)	0.12	1.43	0.12
Gr[2COOH]+PCM-I	1.66 (OGr-HPCM)	0.38	1.25	0.63
Gr[2COOH]+PCM-II	1.41 (HGr-OPCM)	0.01	1.75	1.26
Gr[2COOH]+PCM-III	**1.49 (OGr-HPCM)**	**0.13**	**1.81**	**1.48**

10.3389/frcrb.2024.1305183

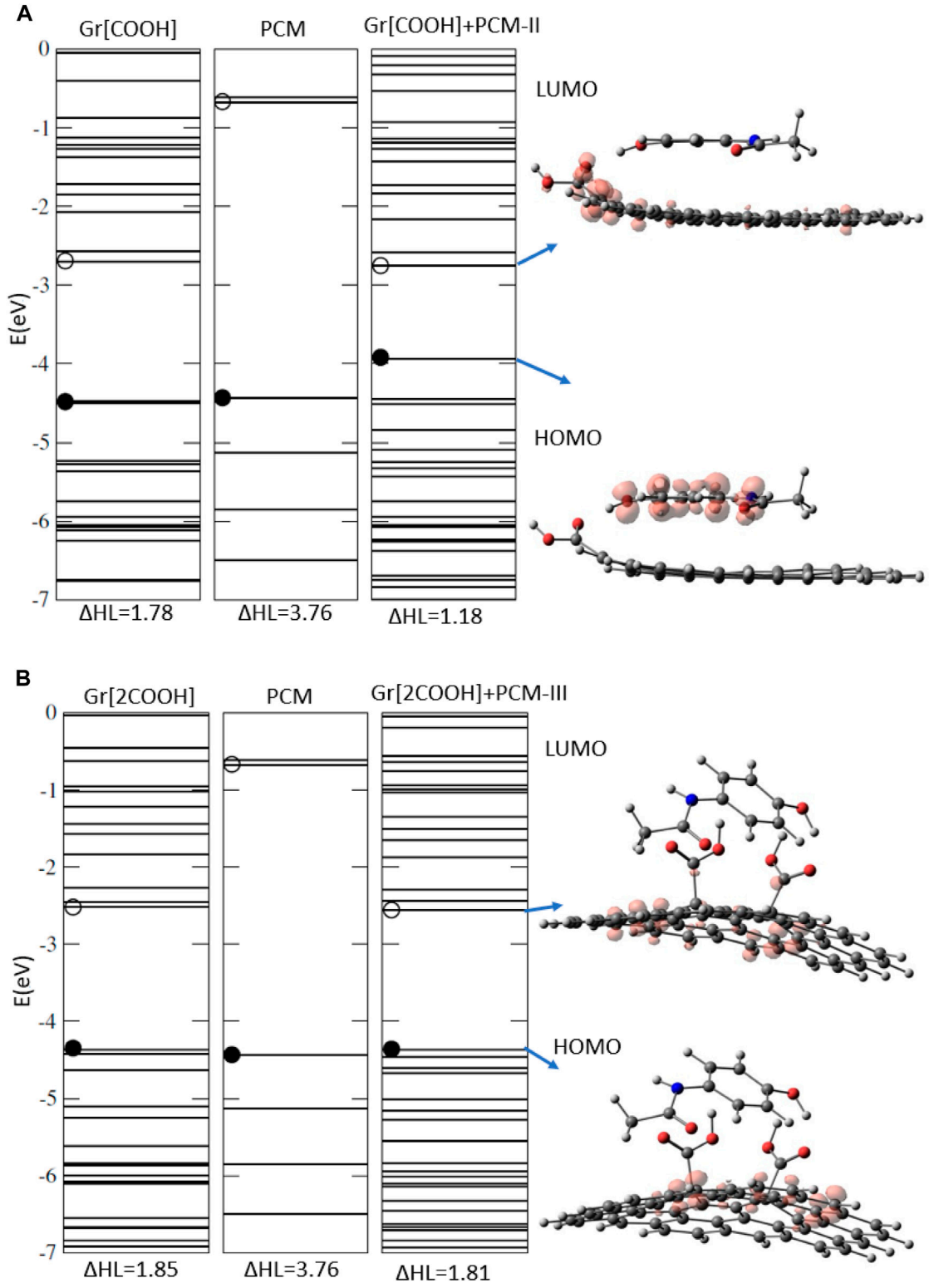

FIGURE 7
Electronic levels and LDOS for the most stable configuration of **(A)** Gr[COOH] interacting with PCM (Gr[COOH]+PCM-II), **(B)** Gr[2COOH] interacting with PCM molecule (Gr[2COOH]+PCM-III) with orbital charge density isosurfaces 0.0093 e–/(Å)^3.

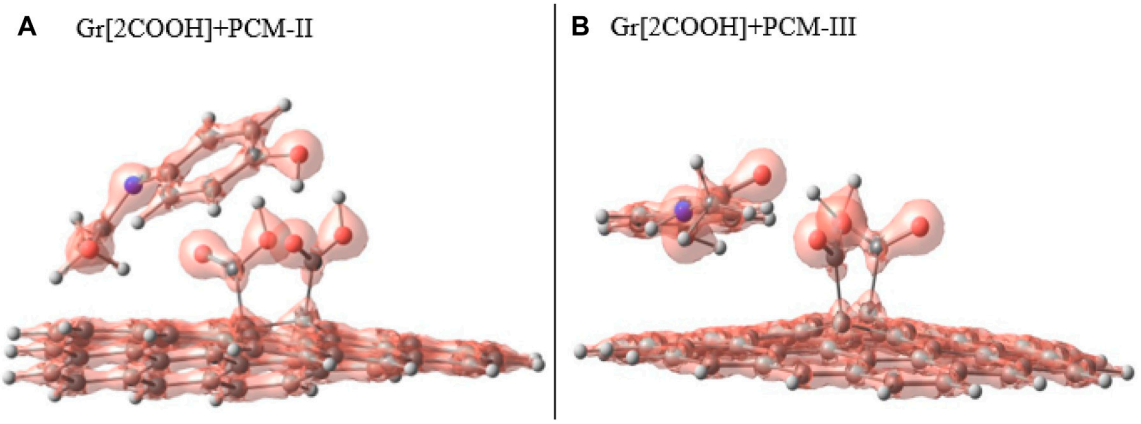

FIGURE 8
Total electronic charge density isosurface for the most stable configurations for **(A)** Gr[2COOH]+PCM-II, **(B)** Gr[2COOH]+PCM-III using orbital charge density isosurfaces of 0.0093 e−/(Å)3.

In Figure 8A, it is made clear that the PCM molecule does not share electrons with anyone close to it, and in Figure 8B, we can also confirm that the Gr structure and PCM molecule cannot share electrons with how they are arranged.

Despite the high binding energies and/or small binding distances observed for the Gr[2OH] and Gr[2COOH] systems, all systems exhibited a physisorption regime. This suggests that increasing the number of functional groups tends to increase the energies and binding of the systems.

The adsorption of PCM onto graphene, with one or two functionalizations, was simulated to provide a good understanding of the adsorption process of the PCM molecule onto the surfaces of functionalized graphene materials. The Mulliken population analysis showed that the electronic charge transfers indicate that graphene materials have an amphoteric character, depending on the position of the PCM during the adsorption process.

In addition to the binding energies, the high values of the minimum distance between the systems, the low values of charge transfer, and the total charge density between the systems indicate that the interaction occurred through a physical adsorption regime. A strong hydrogen bonding tendency was observed between the functional groups and PCM for all functional groups attached to graphene, increasing the number of epoxy, hydroxyl, and carboxyl functional groups on the graphene surface led to significant increases in the graphene+PCM binding energy. Therefore, the intensity of the binding energies depends on the presence of some types of functional groups on the graphene surface. A deformation in the Gr structure is also observed as the number of functionalized groups increases. These results agree with the experimental data, where the highest adsorptions were observed for materials containing a higher proportion of functional groups and where these groups are more available, such as the 3D-rGO5 material. Our research group also found similar results in recent works with methylene blue (Leão et al., 2023). The three different functional groups attached to the graphene surface used in the simulation reflect the 2D-rGO experimental synthesized well. The results from graphene Gr[OH]/Gr[2OH] and Gr[COOH]/Gr[2COOH] are consistent, showing that increasing the number of functional groups leads to an increase in binding energies. Greater binding energy can also be associated with a better adsorption capacity. As described in experimental results, due to similar synthesis, 3D-rGO25 and 2D-rGO materials have identical amounts of oxygenated groups. Regardless of 3D-rGO25 pursuit cavities/pores in comparison with 2D-rGO, which are more compact structures, it can be noted that the adsorption capacities were similar in both cases; thus, the number of functional groups could be responsible for these similarities. On the other hand, 3D-rGO5, which presents a structure similar to 3D-rGO25, exhibits better adsorption compacity than 3D-rGO25, revealing that more functional groups could enhance the adsorption capacity up to a threshold.

5 Conclusion

Our results showed that three-dimensional graphene-based materials exhibit interesting adsorption results with only minor changes in the material synthesis. These changes result in variations in the specific surface areas, pore sizes, and amount of oxygenated functional groups in the structure. The combination of experiments with computational studies allowed us to verify the influence of these characteristics of the materials on the adsorption of paracetamol.

Generally, it was observed that the more oxidized the material, the greater the adsorption efficiency, except for the material without adding a reducing agent, which does not form a three-dimensional porous structure. Ab initio studies revealed that the binding energies, bond distances, and charge transfer between oxidized graphene and the PCM drug are compatible with physical adsorption. The results demonstrate no chemisorption, as confirmed by the total electronic charge density measure. Moreover, the intensity of physical adsorption strongly depends on the type of oxygen group on the graphene surface, increasing as the number of functional groups increases. These results satisfactorily explain the results obtained experimentally: the larger the pores (which makes it easier for paracetamol to reach oxygenated sites), the more oxidized the material, and the better its efficiency in adsorbing paracetamol.

Data availability statement

The original contributions presented in the study are included in the article/Supplementary material, further inquiries can be directed to the corresponding author.

Author contributions

CM: Data curation, Investigation, Writing–original draft. ML: Data curation, Investigation, Writing–original draft. LV: Formal Analysis, Methodology, Software, Writing–original draft. IJ: Formal Analysis, Methodology, Software, Writing–original draft. IZ: Conceptualization, Software, Supervision, Validation, Writing–review and editing. SF: Conceptualization, Funding acquisition, Resources, Supervision, Validation, Writing–review and editing.

Funding

The author(s) declare that financial support was received for the research, authorship, and/or publication of this article. The author(s) declare that receive financial support from Brazilian National Council for Scientific and Technological Development (CNPq, proc. 424146/2018- 5 and proc. 403427/2021-5), Coordination for the Improvement of Higher Education Personnel (CAPES, financing Code 001), Research Support Foundation of the State of Rio Grande do Sul (FAPERGS, TO 21/2551-0000736-2 and TO 21/2551-0002024-5).

Conflict of interest

The authors declare that the research was conducted in the absence of any commercial or financial relationships that could be construed as a potential conflict of interest.

Publisher's note

All claims expressed in this article are solely those of the authors and do not necessarily represent those of their affiliated organizations, or those of the publisher, the editors and the reviewers. Any product that may be evaluated in this article, or claim that may be made by its manufacturer, is not guaranteed or endorsed by the publisher.

Supplementary material

The Supplementary Material for this article can be found online at: https://www.frontiersin.org/articles/10.3389/frcrb.2024.1305183/full#supplementary-material

References

Albert, O., Desdoits-Lethimonier, C., Lesné, L., Legrand, A., Guillé, F., Bensalah, K., et al. (2013). Paracetamol, aspirin and indomethacin display endocrine disrupting properties in the adult human testis *in vitro*. *Hum. Reprod.* 28, 1890–1898. doi:10.1093/humrep/det112

Alves, D. C. d.S., Healy, B., Yu, T., and Breslin, C. B. (2021). Graphene-based materials immobilized within chitosan: applications as adsorbents for the removal of aquatic pollutants. *Materials* 14, 3655. doi:10.3390/ma14133655

Bedner, M., and MacCrehan, W. A. (2006). Transformation of acetaminophen by chlorination produces the toxicants 1, 4-benzoquinone and N-acetyl-p-benzoquinone imine. *Environ. Sci. Technol.* 40, 516–522. doi:10.1021/es0509073

Bolisetty, S., Peydayesh, M., and Mezzenga, R. (2019). Sustainable technologies for water purification from heavy metals: review and analysis. *Chem. Soc. Rev.* 48, 463–487. doi:10.1039/c8cs00493e

Boys, S. F., and Bernardi, F. (1970). The calculation of small molecular interactions by the differences of separate total energies. Some procedures with reduced errors. *Mol. Phys.* 19, 553–566. doi:10.1080/00268977000101561

Bruckmann, F. d. S., Zuchetto, T., Ledur, C. M., dos Santos, C. L., da Silva, W. L., Binotto Fagan, S., et al. (2022). Methylphenidate adsorption onto graphene derivatives: theory and experiment. *New J. Chem.* 46, 4283–4291. doi:10.1039/d1nj03916d

Concu, R., González-Durruthy, M., Cordeiro, M. N. D., Zanela, I., and Cordeiro, D. (2020). Developing a multi-target model to predict the activity of monoamine oxidase A and B drugs. *Curr. Top. Med. Chem.* 20, 1593–1600. doi:10.2174/1568026620666200603121224

de Oliveira, P. V., Zanella, I., Bulhoes, L. O. S., and Fagan, S. B. (2021). Adsorption of 17 β-estradiol in graphene oxide through the competing methanol co-solvent: experimental and computational analysis. *J. Mol. Liq.* 321, 114738. doi:10.1016/j.molliq.2020.114738

Deshwal, N., Singh, M. B., Bahadur, I., Kaushik, N., Kaushik, N. K., Singh, P., et al. (2023). A review on recent advancements on removal of harmful metal/metal ions using graphene oxide: experimental and theoretical approaches. *Sci. Total Environ.* 858, 159672. doi:10.1016/j.scitotenv.2022.159672

Ersan, G., Apul, O. G., Perreault, F., and Karanfil, T. (2017). Adsorption of organic contaminants by graphene nanosheets: a review. *Water Res.* 126, 385–398. doi:10.1016/j.watres.2017.08.010

Fan, S., Yu, Z., Wang, X., Tao, Y., Shao, H., Long, M., et al. (2023). A facile graphene oxide modified approach towards membrane with prominent improved permeability and antifouling performance. *Desalination* 545, 116130. doi:10.1016/j.desal.2022.116130

Fernandez, M. E., Ledesma, B., Román, S., Bonelli, P. R., and Cukierman, A. L. (2015). Development and characterization of activated hydrochars from orange peels as potential adsorbents for emerging organic contaminants. *Bioresour. Technol.* 183, 221–228. doi:10.1016/j.biortech.2015.02.035

Guo, Z., Feng, Y., Zhang, C., Huang, G., Chi, J., Yao, Q., et al. (2021). Three dimensional graphene materials doped with heteroatoms for extraction and adsorption of environmental pollutants in wastewater. *J. Environ. Sci. Health, Part C* 39, 17–43. doi:10.1080/26896583.2020.1863725

Hamed, R., Jodeh, S., Hanbali, G., Safi, Z., Berisha, A., Xhaxhiu, K., et al. (2022). Eco-Friendly synthesis and characterization of double-crossed link 3D graphene oxide functionalized with chitosan for adsorption of sulfamethazine from aqueous solution: experimental and DFT calculations. *Front. Environ. Sci.* 10, 977. doi:10.3389/fenvs.2022.930693

Hanelt, S., Orts-Gil, G., Friedrich, J. F., and Meyer-Plath, A. (2011). Differentiation and quantification of surface acidities on MWCNTs by indirect potentiometric titration. *Carbon* 49, 2978–2988. doi:10.1016/j.carbon.2011.03.016

Hiew, B. Y. Z., Lee, L. Y., Lai, K. C., Gan, S., Thangalazhy-Gopakumar, S., Pan, G.-T., et al. (2019). Adsorptive decontamination of diclofenac by three-dimensional graphene-based adsorbent: response surface methodology, adsorption equilibrium, kinetic and thermodynamic studies. *Environ. Res.* 168, 241–253. doi:10.1016/j.envres.2018.09.030

Hiew, B. Y. Z., Tee, W. T., Loh, N. Y. L., Lai, K. C., Hanson, S., Gan, S., et al. (2022). Synthesis of a highly recoverable 3D MnO2/rGO hybrid aerogel for efficient adsorptive separation of pharmaceutical residue. *J. Environ. Sci.* 118, 194–203. doi:10.1016/j.jes.2021.12.036

Hohenberg, P., and Kohn, W. (1964). Inhomogeneous electron gas. *Phys. Rev.* 136, B864–B871. doi:10.1103/physrev.136.b864

Huang, P., Jia, H., Wang, T., Xu, Y., Zhang, L., Wei, X., et al. (2021). Effects of modification degrees on the colloidal stability of amphiphilic janus graphene oxide in aqueous solution with and without electrolytes. *Langmuir* 37, 10061–10070. doi:10.1021/acs.langmuir.1c01283

Jauris, I., Matos, C. F., Zarbin, A. J. G., Umpierres, C. S., Saucier, C., Lima, E. C., et al. (2017). Adsorption of anti-inflammatory nimesulide by graphene materials: a combined theoretical and experimental study. *Phys. Chem. Chem. Phys.* 19, 22099–22110. doi:10.1039/c7cp04272h

Jung, H., Cho, K. M., Kim, K. H., Yoo, H.-W., Al-Saggaf, A., Gereige, I., et al. (2018). Highly efficient and stable CO2 reduction photocatalyst with a hierarchical structure of mesoporous TiO2 on 3D graphene with few-layered MoS2. *ACS Sustain. Chem. Eng.* 6, 5718–5724. doi:10.1021/acssuschemeng.8b00002

Kohn, W., and Sham, L. J. (1965). Self-consistent equations including exchange and correlation effects. *Phys. Rev.* 140, A1133–A1138. doi:10.1103/physrev.140.a1133

Kristensen, D. M., Hass, U., Lesné, L., Lottrup, G., Jacobsen, P. R., Desdoits-Lethimonier, C., et al. (2011). Intrauterine exposure to mild analgesics is a risk factor for development of male reproductive disorders in human and rat. *Hum. Reprod.* 26, 235–244. doi:10.1093/humrep/deq323

Kristensen, D. M., Lesné, L., Le Fol, V., Desdoits-Lethimonier, C., Dejucq-Rainsford, N., Leffers, H., et al. (2012). Paracetamol (acetaminophen), aspirin (acetylsalicylic acid) and indomethacin are anti-androgenic in the rat foetal testis. *Int. J. Androl.* 35, 377–384. doi:10.1111/j.1365-2605.2012.01282.x

Kristensen, D. M., Mazaud-Guittot, S., Gaudriault, P., Lesné, L., Serrano, T., Main, K. M., et al. (2016). Analgesic use—prevalence, biomonitoring and endocrine and reproductive effects. *Nat. Rev. Endocrinol.* 12, 381–393. doi:10.1038/nrendo.2016.55

Leão, M. B., Rosa, P. C., Dalla Corte, C. L., and Matos, C. F. (2022). Eco-friendly, non-toxic and super adsorbent hydrogels based on graphene. *Mater. Chem. Phys.* 288, 126408. doi:10.1016/j.matchemphys.2022.126408

Leão, M. B., Vendrame, L., Fagan, S. B., Zanella, I., Jauris, I. M., Bordin, J. R., et al. (2023). Combining multi-scale simulations and experiments to unveil the adsorption of methylene blue in graphene tridimensional-based materials. *Mol. Syst. Des. Eng.* 8, 666–680. doi:10.1039/d2me00268j

Lima, É. C., Adebayo, M. A., and Machado, F. M. (2015). "Kinetic and equilibrium models of adsorption," in *Carbon nanomaterials as adsorbents for environmental and biological applications* (Berlin, Germany: Springer), 33–69.

Lin, Y., Tian, Y., Sun, H., and Hagio, T. (2021). Progress in modifications of 3D graphene-based adsorbents for environmental applications. *Chemosphere* 270, 129420. doi:10.1016/j.chemosphere.2020.129420

Liu, H., and Qiu, H. (2020). Recent advances of 3D graphene-based adsorbents for sample preparation of water pollutants: a review. *Chem. Eng. J.* 393, 124691. doi:10.1016/j.cej.2020.124691

Liu, X., Ma, R., Wang, X., Ma, Y., Yang, Y., Zhuang, L., et al. (2019). Graphene oxide-based materials for efficient removal of heavy metal ions from aqueous solution: a review. *Environ. Pollut.* 252, 62–73. doi:10.1016/j.envpol.2019.05.050

Lorphensri, O., Intravijit, J., Sabatini, D. A., Kibbey, T. C., Osathaphan, K., and Saiwan, C. (2006). Sorption of acetaminophen, 17α-ethynyl estradiol, nalidixic acid, and norfloxacin to silica, alumina, and a hydrophobic medium. *Water Res.* 40, 1481–1491. doi:10.1016/j.watres.2006.02.003

Lu, Y., Li, Y., Gao, Y., Ai, B., Gao, W., and Peng, G. (2020). Facile preparation of 3D GO with caffeic acid for efficient adsorption of norfloxacin and ketoprofen. *Water Sci. Technol.* 81, 1461–1470. doi:10.2166/wst.2020.193

Moussavi, G., Hossaini, Z., and Pourakbar, M. (2016). High-rate adsorption of acetaminophen from the contaminated water onto double-oxidized graphene oxide. *Chem. Eng. J.* 287, 665–673. doi:10.1016/j.cej.2015.11.025

Paredes-Laverde, M., Salamanca, M., Silva-Agredo, J., Manrique-Losada, L., and Torres-Palma, R. A. (2019). Selective removal of acetaminophen in urine with activated carbons from rice (Oryza sativa) and coffee (Coffea arabica) husk: effect of activating agent, activation temperature and analysis of physical-chemical interactions. *J. Environ. Chem. Eng.* 7, 103318. doi:10.1016/j.jece.2019.103318

Sankey, O. F., and Niklewski, D. J. (1989). *Ab initio* multicenter tight-binding model for molecular-dynamics simulations and other applications in covalent systems. *Phys. Rev. B* 40, 3979–3995. doi:10.1103/physrevb.40.3979

Shan, D., Deng, S., Li, J., Wang, H., He, C., Cagnetta, G., et al. (2017). Preparation of porous graphene oxide by chemically intercalating a rigid molecule for enhanced removal of typical pharmaceuticals. *Carbon* 119, 101–109. doi:10.1016/j.carbon.2017.04.021

Soler, J. M., Artacho, E., Gale, J. D., García, A., Junquera, J., Ordejón, P., et al. (2002). The SIESTA method for *ab initio* order-N materials simulation. *J. Phys. Condens. Matter* 14, 2745–2779. doi:10.1088/0953-8984/14/11/302

Soltani, R., Marjani, A., and Shirazian, S. (2019). Facile one-pot synthesis of thiol-functionalized mesoporous silica submicrospheres for Tl (I) adsorption: isotherm, kinetic and thermodynamic studies. *J. Hazard. Mater.* 371, 146–155. doi:10.1016/j.jhazmat.2019.02.076

Song, C., Guo, B.-B., Sun, X.-F., Wang, S.-G., and Li, Y.-T. (2019). Enrichment and degradation of tetracycline using three-dimensional graphene/MnO2 composites. *Chem. Eng. J.* 358, 1139–1146. doi:10.1016/j.cej.2018.10.119

Sun, H., Lin, Y., Takeshi, H., Wang, X., Wu, D., and Tian, Y. (2021). Synthesis of 3D graphene-based materials and their applications for removing dyes and heavy metals. *Environ. Sci. Pollut. Res.* 28, 52625–52650. doi:10.1007/s11356-021-15649-w

Thue, P. S., Sophia, A. C., Lima, E. C., Wamba, A. G., de Alencar, W. S., dos Reis, G. S., et al. (2018). Synthesis and characterization of a novel organic-inorganic hybrid clay adsorbent for the removal of acid red 1 and acid green 25 from aqueous solutions. *J. Clean. Prod.* 171, 30–44. doi:10.1016/j.jclepro.2017.09.278

Torabi Fard, N., Tadayon, F., Ahmad Panahi, H., and Moniri, E. (2022). Synthesize, characterization and application of a novel three-dimensional magnetic graphene oxide decorated with polyester dendrimers for detection of donepezil hydrochloride in pharmaceutical formulation and biological fluid. *Synth. Met.* 290, 117141. doi:10.1016/j.synthmet.2022.117141

Troullier, N., and Martins, J. L. (1991). Efficient pseudopotentials for plane-wave calculations. *Phys. Rev. B* 43, 1993–2006. doi:10.1103/physrevb.43.1993

Umbreen, N., Sohni, S., Ahmad, I., Khattak, N. U., and Gul, K. (2018). Self-assembled three-dimensional reduced graphene oxide-based hydrogel for highly efficient and facile removal of pharmaceutical compounds from aqueous solution. *J. colloid interface Sci.* 527, 356–367. doi:10.1016/j.jcis.2018.05.010

van den Driesche, S., Macdonald, J., Anderson, R. A., Johnston, Z. C., Chetty, T., Smith, L. B., et al. (2015). Prolonged exposure to acetaminophen reduces testosterone production by the human fetal testis in a xenograft model. *Sci. Transl. Med.* 7, 288ra80. doi:10.1126/scitranslmed.aaa4097

Vendrame, L. F., Zuchetto, T., Fagan, S. B., and Zanella, I. (2019). Nanofilter based on functionalized carbon nanostructures for the adsorption of pentachlorophenol molecules. *Comput. Theor. Chem.* 1165, 112561. doi:10.1016/j.comptc.2019.112561

Vijayaraghavan, K., Padmesh, T., Palanivelu, K., and Velan, M. (2006). Biosorption of nickel (II) ions onto Sargassum wightii: application of two-parameter and three-parameter isotherm models. *J. Hazard. Mater.* 133, 304–308. doi:10.1016/j.jhazmat.2005.10.016

Villaescusa, I., Fiol, N., Poch, J., Bianchi, A., and Bazzicalupi, C. (2011). Mechanism of paracetamol removal by vegetable wastes: the contribution of π–π interactions, hydrogen bonding and hydrophobic effect. *Desalination* 270, 135–142. doi:10.1016/j.desal.2010.11.037

Wang, J., Duan, X., Dong, Q., Meng, F., Tan, X., Liu, S., et al. (2019). Facile synthesis of N-doped 3D graphene aerogel and its excellent performance in catalytic degradation of antibiotic contaminants in water. *Carbon* 144, 781–790. doi:10.1016/j.carbon.2019.01.003

Wang, J.-b., Ren, Z., Hou, Y., Yan, X.-l., Liu, P.-z., Zhang, H., et al. (2020). A review of graphene synthesis at low temperatures by CVD methods. *New Carbon Mater.* 35, 193–208. doi:10.1016/s1872-5805(20)60484-x

Wong, L. Y., Lau, S. Y., Pan, S., and Lam, M. K. (2022). 3D graphene-based adsorbents: synthesis, proportional analysis and potential applications in oil elimination. *Chemosphere* 287, 132129. doi:10.1016/j.chemosphere.2021.132129

Wong, S., Lim, Y., Ngadi, N., Mat, R., Hassan, O., Inuwa, I. M., et al. (2018). Removal of acetaminophen by activated carbon synthesized from spent tea leaves: equilibrium, kinetics and thermodynamics studies. *Powder Technol.* 338, 878–886. doi:10.1016/j.powtec.2018.07.075

Yang, Y., Liu, Y., Fang, X., Miao, W., Chen, X., Sun, J., et al. (2020). Heterogeneous Electro-Fenton catalysis with HKUST-1-derived Cu@ C decorated in 3D graphene network. *Chemosphere* 243, 125423. doi:10.1016/j.chemosphere.2019.125423

Yanyan, L., Kurniawan, T. A., Albadarin, A. B., and Walker, G. (2018). Enhanced removal of acetaminophen from synthetic wastewater using multi-walled carbon nanotubes (MWCNTs) chemically modified with NaOH, HNO3/H2SO4, ozone, and/or chitosan. *J. Mol. Liq.* 251, 369–377. doi:10.1016/j.molliq.2017.12.051

Yousefi, N., Lu, X., Elimelech, M., and Tufenkji, N. (2019). Environmental performance of graphene-based 3D macrostructures. *Nat. Nanotechnol.* 14, 107–119. doi:10.1038/s41565-018-0325-6

Yu, Z., Wei, L., Lu, L., Shen, Y., Zhang, Y., Wang, J., et al. (2022). Structural manipulation of 3D graphene-based macrostructures for water purification. *Gels* 8, 622. doi:10.3390/gels8100622

frontiers | Frontiers in Carbon

TYPE Original Research
PUBLISHED 21 May 2024
DOI 10.3389/frcrb.2024.1402105

OPEN ACCESS

EDITED BY
Marinella Striccoli,
Consiglio Nazionale delle Ricerche-CNR, Italy

REVIEWED BY
Angsula Ghosh,
Federal University of Amazonas, Brazil
Urol Kudratovich Makhmanov,
Academy of Sciences Republic of Uzbekistan (UzAS), Uzbekistan

*CORRESPONDENCE
Ana Paula de Carvalho Teixeira,
anapct@ufmg.br

RECEIVED 16 March 2024
ACCEPTED 03 May 2024
PUBLISHED 21 May 2024

CITATION
Diogo EBT, Vieira AFP, Nascimento MA, Pinto PS, de Paula FGF, Moreira RPL and Teixeira APC (2024), Carbon nanostructures supported on Co/serpentinite for sulfentrazone removal.
Front. Carbon 3:1402105.
doi: 10.3389/frcrb.2024.1402105

Carbon nanostructures supported on Co/serpentinite for sulfentrazone removal

Emilay Baessa Teixeira Diogo[1], Angelica Fonseca Pinto Vieira[1], Mayra Aparecida Nascimento[2], Paula Sevenini Pinto[3], Fabiano Gomes Ferreira de Paula[1], Renata Pereira Lopes Moreira[4] and Ana Paula de Carvalho Teixeira[1]*

[1]Chemistry Department, Universidade Federal de Minas Gerais (UFMG), Belo Horizonte, Minas Gerais, Brazil, [2]Centro Federal de Educação Tecnológica de Minas Gerais (CEFET-MG), Belo Horizonte, Minas Gerais, Brazil, [3]Departamento de Ciências Naturais e da Terra, Universidade do Estado de Minas Gerais (UEMG), Divinópolis, Minas Gerais, Brazil, [4]Universidade Federal de Viçosa (UFV), Viçosa, Minas Gerais, Brazil

The presence of environmental contaminants is a major problem today. In this context, it is necessary to develop new sustainable materials to be used to remediate these contaminants. In this work, the serpentinite rock was impregnated with cobalt, 5%, 10% and 20% and used as a support for the synthesis of carbon nanostructures by CVD (chemical vapour deposition) process, at 900°C. This temperature was chosen due to the high thermal stability of the carbon source. The materials were characterized by X-ray diffraction, Raman spectroscopy, thermal analysis, scanning and transmission microscopy. As expect the main phases formed were forsterite, Mg_2SiO_4, graphitic carbon and metallic cobalt. All the synthesis showed the formation of carbon structures as multiwalled carbon nanostructures over cobalt cores. The carbon structures showed good thermal stability, between 470 and 600°C. The higher the cobalt content, the higher the yield of the carbon structures synthesis, i.e. 14%, 23% and 37% for Serp5, Serp10 and Serp20, respectively. The produced materials were used to removal of the environmental contaminant sulfentrazone. After CVD process, the removal of sulfentrazone increase to 17.3%, 18.4% and 25.2% for Serp5, Serp10 and Serp20, respectively, showing an increase in sulfentrazone removal with the increase in carbon content. In addition, the percentage of sulfentrazone removal by Serp20 was greater at acidic pH values, decreasing from 41.7% to 12.7% with an increase from 2 to 10 in pH. The removal capacity obtained experimentally at a sulfentrazone concentration of 50 mg L^{-1} was equal to 14.9 mg g^{-1}. According to literature and data obtained in this work, it was observed that the removal of contaminants from the aqueous medium occurred through two mechanisms: reduction of the organic compound by Co nanoparticles and adsorption carried out by carbon nanostructures.

KEYWORDS

carbon nanostructures, serpentinite, chemical vapour deposition, adsorption, sulfentrazone

1 Introduction

Serpentinite is an ultrabasic rock that can be formed by silicate minerals: chrysotile ($Mg_3(Si_2O_5)(OH)_4$), antigorite ($Mg_3(Si_2O_5)(OH)_4$, lizardite ($Mg_3(Si_2O_5)(OH)_4$), and talc ($Mg_3Si_4O_{10}(OH)_2$) (Hirth and Guillot, 2013). Althought the distribution and presence of these minerals depend on the place where this rock is present, serpentinite is basically a Si oxide tetrahedral sheet bounded to $Mg(OH)_2$ based octahedral layer (Cao et al., 2017). Natural minerals, such as those based on serpentinite, are being increasingly used in environmental applications, due to their low cost, great abundance in nature, and easily obtainability (Lemos et al., 2016).

In this work, a novel approach was developed to use this natural inorganic material in removal of environmental contaminants, improving its properties by growing carbon nanofibers/nanotubes in its surface, producing amphiphilic materials. The CVD (Chemical Vapour Deposition) process is one of the most used for carbon nanotube synthesis based on technical simplicity, relatively low cost, and high yields (Purceno et al., 2011). Developed in the 1960s and 1970s, the CVD process consists of catalytic decomposition of carbon precursors (hydrocarbons, CO, alcohol) through catalysts, e.g., Fe/Mo, Ni, Co, that can be deposited on a thermally stable and preferably large surface area of an inert substrate (Dresselhaus et al., 2001; Dupuis, 2005; O'Connell and O'Connell, 2006; Öncel and Yürüm, 2006).

Previous work in our group has shown how those amphiphilic composites have special features. The simultaneous presence of hydrophilic Si and Si–Al oxide surface and hydrophobic carbon nanotubes (CNT) and nanofibers (CNF), allow the composites to interact well with aqueous and different organic phases. Furthermore, the presence of magnetic cores on the composite enables its removal from different media by a simple magnetic separation process (Teixeira et al., 2013; 2012; Purceno et al., 2012). These characteristics make amphiphilic materials interesting adsorbents for organic pollutants in aqueous media. One important class of organic contamination in wastewater is the herbicides.

The use of agrochemicals has grown rapidly due to high demand for food. However, the indiscriminate and disorderly use of these compounds may cause environmental and human health problems, such as gastrointestinal and respiratory system damages, cancer and fetal development issues, becoming a global concern (Siqueira and Kruse, 2008; Nascimento et al., 2016). Sulfentrazone is a pre-emergent herbicide and has a high potential persistence and moderate mobility in soil, and it may contaminate surface and ground water (Martinez et al., 2008). Therefore, the development of technologies that efficiently remove such substances becomes imperative.

Undabeytia et al. used clay-vesicle complexes composed of montmorillonite and positively charged didodecyldimethylammonium bromide (DDAB) mixed with clay (1:100 w:w) in a column filter to remove a solution with several organic pollutants in 10 mg/L initial concentration (Undabeytia et al., 2008). Their results were compared with sand/activated carbon filter. The best results were for anionic pollutants such Sulfentrazone and Imazaquin, achieving 100% adsorption capacity, but even the neutral ones (Alachlor and Atrazine) the results were three-fold higher for the clay-vesicle than the activated carbon filter. These results were achieved for 1 L solution. Lelario et al. also addressed the adsorption of organic pollutants (simazine, sulfentrazone and diclofenac) using a filter filled with polymer-, micelle- and liposome-clay composite (Lelario et al., 2017). The authors found that high solubilization capacity was the major factor in sulfentrazone adsorption due to its hydrophobic nature and the best results were for the micelle-clay composite. These results show a potential for amphiphilic materials that could interact with both the aqueous solution and the hydrophobic pollutant decreasing the solubilization capacity factor.

In the literature, three publications were found on the use of serpentinite in adsorption processes. Momcilovic et al. used serpentinite for the adsorption of Cd^{2+} and anionic organic textile dyes from synthetic water. Removals above 98% were achieved for Cd^{2+} and up to 99% for anionic dyes (Momčilović et al., 2016). Drizo et al. used serpentinite for the adsorption of phosphate from aqueous effluent. The results showed that serpentinite was efficient for removing 1.0 mg P/g in column studies (Drizo et al., 2006). Petrounias et al. activated serpentinite samples in a Los Angeles machine using different revolutions. And they observed that the materials obtained can be used as filters to remove Cu^{2+} from water (Petrounias et al., 2020). Although some papers have been published demonstrating the use of serpentinite in adsorption process, none have investigated its use in sulfentrazone removal, moreover, the potential combination of serpentinite and carbon nanostructures for that purpose.

Hereon, we described the synthesis of carbon nanofibers/nanotubes supported on serpentinite to produce magnetic amphiphilic composites to further investigate the removal of sulfentrazone contaminant in aqueous media.

2 Experimental

Serpentinite materials were provided by Pedras Congonhas Extração Arte Indústria (Nova Lima, Brazil). To study the changes in this mineral structure after a thermal treatment, the samples (5 g) were calcined at 800°C for 1 h in a tubular furnace using a quartz tube, with a heating rate of 10°C min^{-1} and a flow rate of 50 mL min^{-1} for different atmospheres: air and 8% H_2/N_2 mixture. These samples were named Serp air and Serp H_2, where Serp represents serpentinite.

2.1 Synthetic procedure

Serpentinite samples (5 g) were impregnated with an aqueous solution of cobalt nitrate hexahydrated in proportions of 5, 10 and 20 wt% of metal/support. The impregnation was done using 100 mL of cobalt nitrate hexahydrated at different concentrations in a beaker over magnetic agitation.

The resulting mixture was kept at 80°C, in a heating plate, until total evaporation of water. The obtained solids were further dried at 80°C during 24 h in a drying oven. The impregnated materials were reduced in a horizontal oven at 800°C (heating rate of 10°C.min^{-1}) for 1 h in a H_2/N_2 (8%) flow rate of 50 mL min^{-1}. Then, the reduced materials were further heated at the same heating rate until 900°C for 1 h in 50 mL min^{-1} flux of methane, using an alumina boat inside a quartz tube (CVD process). This temperature was chosen due to the high thermal stability of the carbon source. The materials were denoted as Serp5, Serp10, and Serp20, according to the cobalt content, wherein "Serp" denotes the name serpentinite, while 5, 10 and 20 refers the respective cobalt amount.

2.2 Characterization

The obtained materials were characterized by X-ray diffraction (XRD) using a Rigaku Geiger 2037 equipment, CuK α = 1,54051 Å radiation, 2θ: 5°–70°, 4°.min^{-1} with a copper tube); thermogravimetric analysis, using a DTG 60H model from Shimadzu, in air flow of 50 mL min^{-1}, heating rate of 10°C.min^{-1} until 1,000°C; elemental analysis (carbon, hydrogen and nitrogen) were obtained using a Perkin Elmer 2,400 analyzer; Raman spectroscopy, using a model Senterra from Bruker, laser 633 nm, 2 mW. 10 different measurements were taken, and the result was an average. A ×50 magnification objective was used to carry out the measurements, Scanning electronic microscopy (SEM), using a Quanta FEG 3D and Quanta FEG 200 equipments. For measurements, the samples were placed under a carbon tape; Transmission electronic microscopy (TEM), using a Tecnai G2-20 FEI. For measurements, the samples were dispersed in isopropanol and placed on holey carbon grids; N_2 adsorption-desorption isotherm were obtained using a Quantachrome autosorb equipment. The isotherms were obtained at 77 K. Before the measurements, the samples were degassed at 100°C for 24 h.

2.3 Environmental applications

The prepared materials were used to remove the environmental contaminant, sulfetrazone. Initially, the adsorption equilibrium time between Serp5 and sulfentrazone was determined. For this, 0.0100 g of Serp5 were added to 20.00 mL of sulfentrazone solution at 10.0 mg .L^{-1}, under constant agitation and temperature, with aliquots removed at different time intervals. Subsequently, factors that may affect the sulfentrazone removal, such as cobalt content (5, 10% and 20%), pH (2, 4, 6, 8, and 10) and initial sulfentrazone concentration (5–50 mg. L^{-1}) were investigated. HCl and NaOH solutions, both at 0.1 mol .L^{-1}, were used to pH adjustment.

To describe the adsorption process, Langmuir and Freundlich isothermal models were used, Eqs (1), (2), respectively. The assays were performed using initial sulfentrazone concentrations of 5–50 mg L^{-1}.

$$q_e = \frac{q_{max} K_L C_e}{1 + K_L C_e} \quad (1)$$

$$q_e = K_F C_e^{1/n} \quad (2)$$

Wherein C_e (mg.L^{-1}) is the sulfentrazone concentration at equilibrium, q_e (mg.g^{-1}) is the amount of sulfentrazone adsorbed per Gram of adsorbent at equilibrium, q_{max} (mg.g^{-1}) is the maximum adsorption capacity, K_L (g.mg^{-1}) is the constant Langmuir, K_F (mg.g^{-1}) (mg.L^{-1})^n is adsorption capacity related constant and n is the constant related to adsorption intensity. In all assays, aliquots were removed from the system at pre-established times and filtered through nitrocellulose membrane (13 mm of diameter and 0.45 µm of porosity). The remaining sulfentrazone concentration was determined by High Performance Liquid Chromatography (LC 20AT Shimadzu) coupled to UV-Vis detector (SPD 20A Shimadzu) using C18 150 mm x 4.6 mm of internal diameter. The chromatographic conditions were: The mobile phase consisted of acetonitrile, ultrafiltrated water and phosphoric acid (50:49.9:1.1, v/v/v), injection volume 20 µL, flow rate 1.0 mL min^{-1} and monitored wavelength was 207 nm.

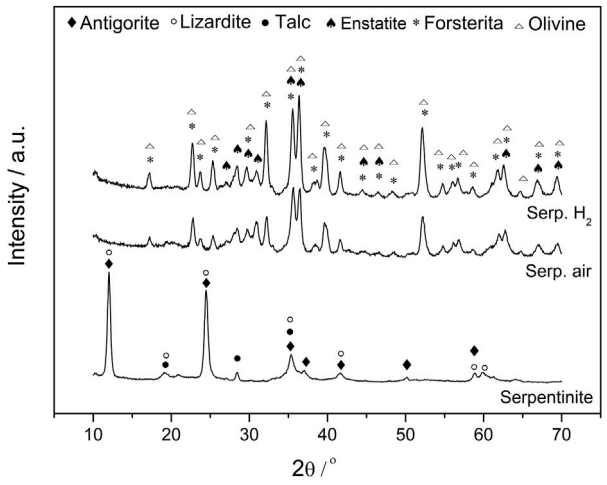

FIGURE 1
XRD patterns of serpentinite, before and after thermal treatment, in air and H_2/N_2 atmosphere at 800°C for 1 hour.

The adsorption capacity q_e (mg.g^{-1}) and removal rate (%) of sulfentrazone were calculated by Eqs (3), (4), respectively:

$$q_e = \frac{(C_0 - C_t)V}{m} \quad (3)$$

$$\% \text{ Removal} = \frac{(C_0 - C_t) \times 100}{C_0} \quad (4)$$

Wherein C_0 is the initial sulfentrazone concentration and C_t is sulfentrazone concentration at time t, V is the sulfentrazone solution volume and m is the mass of the material. All assays were performed in flasks coupled to a thermocriostatic bath (Microquímica, MQBTC 99–20) for temperature control.

3 Results and discussion

Before CVD process, the thermal stability of the serpentinite was studied at 800 °C in both oxidant (air) and reducing (H_2/N_2) atmosphere. Inert ceramic materials such as MgO and Al_2O_3 are generally used as catalyst supports for the synthesis of carbon nanomaterials via the CVD process. These matrices are stable and do not decompose or undergo modifications during the carbon deposition process at high temperatures. Serpentinite is a natural material with hydroxyl groups that undergoes phase modification during the heating process. Furthermore, serpentinite contains Fe^{2+} and Fe^{3+} ions in its structure, which is why in this work we decided to carry out a preliminary study of this rock, both in an oxidizing and reducing atmosphere. This study helped us understand which active phases are present in serpentinite at high temperatures and to understand whether any oxidation or reduction process occurs in this material during heating.

The changes in structure were observed by XRD (Figure 1). The XRD patterns for serpentinite before thermal treatment showed

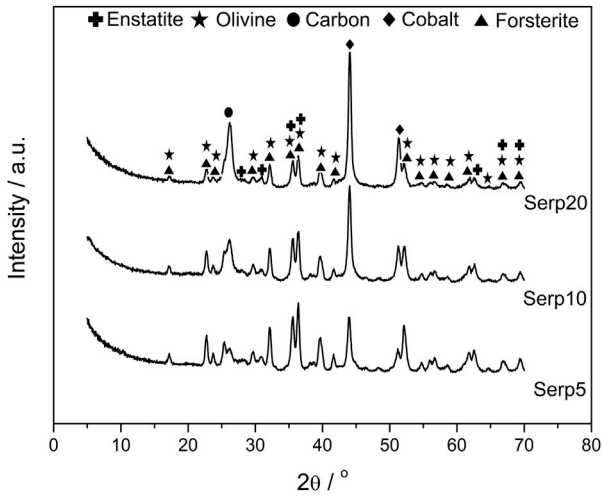

FIGURE 2
XRD patterns of serpentinite with 5, 10, and 20 %wt of Co, after CVD process.

three minerals patterns, lizardite (JCDPS 18–779), antigorite ($Mg_3Si_2O_5(OH)_4$, JCDPS 44–1,447) and talc ($Mg_3Si_4O_{10}(OH)_2$, JCDPS 3-881), as constituents. Interestingly, no crysotile phase was observed and usually this silicate mineral is very common in serpentinite samples (Teixeira et al., 2013). After 800 °C treatment in air atmosphere, it can be noticed several changes in the XRD patterns after hydrate magnesium silicate phase modifications, yielding new mineral peaks characterized as forsterite (Mg_2SiO_4, JCDPS 34-189), olivine [$(Fe,Mg)_2SiO_4$, JCDPS 2-1,343] and enstatite ($MgSiO_3$, JCDPS 2-546) (Ballotin et al., 2016). There were no differences in mineral constitution in the serpentinite samples obtained after reducing atmosphere. But it was not possible more to observe the original phases from serpentinite rock at these temperatures. Consequently, we conclude that the phases presented during CVD process were forsterite, enstatite and olivine instead of the hydrated phases lizardite, antigorite and talc.

After understanding the actual mineral phases that will behave as support in the CVD process for CNS synthesis, serpentinite was impregnated with catalyst (Co) in three different metal/support ratios, named Serp5, Serp10 and Serp15 for 5, 10% and 15 % wt of cobalt, respectively. The resultant materials were placed at 800°C in H_2/N_2 for catalyst reduction and then heated until 900°C in CH_4 for CNS growth. The temperature of 800°C was chosen for the reduction of cobalt phases because, according to the literature, this value is sufficient for the formation of cobalt nanoparticles (Lemos et al., 2016).

In this work, it was decided to use a higher temperature in the carbon deposition process due to the carbon source used. According to previous work by the group and data from the literature, more stable sources of carbon such as methane and carbon monoxide require higher temperatures for their activation and decomposition. On the other hand, for less stable sources such as acetylene and ethylene, lower temperatures can be used (Shah and Tali, 2016; Silva et al., 2020; Teixeira et al., 2013; Tessonnier and Su, 2011). Figure 2 shows the XRD patterns for all materials after CVD process.

As expected, the XRD patterns showed non-hydrate silicate phases of forsterite, olivine and enstatite (as observed in Figure 1), for all materials. In addition, it can be observed new peaks related to the metallic cobalt (JCDPS 15-806) and graphitic carbon (JCDPS 1–640). Co^0 was formed after the reduction step at 800 °C for catalyst activation, while graphitic carbon peaks indicate that carbon structures were formed in the CVD process. To elucidate the carbon structures, several techniques were used such as SEM, TEM, TG/DTG, elemental analysis, nitrogen isotherms at 77 K and Raman spectroscopy.

First, the impact of thermal treatment over the serpentinite structure was studied by SEM (Supplementary Figure S1, ESI†). Serpentinite showed a disperse structure with micrometric heterogeneous dimensions and morphology. The treatment at 800°C in H_2/N_2 atmosphere favoured the formation of some agglomerated particles, but no other significant change is observed. EDX analyses (Supplementary Figure S2, ESI†) for serpentinite showed the main presence of the elements Mg, Si, Fe and O. After heat treatments in oxidizing and reducing atmospheres, no change in the elements were observed. However, an increase in the relative intensity of the peaks referring to Mg and Si in relation to the peak of the oxygen element was noticed. This fact can be explained by the dehydroxylation of the hydrated phases of the serpentinite with loss of water molecules, which makes the phases richer in Mg and Si. After CVD process (Supplementary Figure S3, ESI†), the images show large agglomerates of carbon structures over the serpentinite support.

TEM images, Figure 3, enables a closer look at the carbon structures formed after CVD process. Most of the produced carbon is multi walled nanostructures with cobalt cores. Also, all catalytic systems were effective to grow these CNS, with no perceptive differences between the materials.

We used 12 different images of each material to carry out a statistical analysis of the diameter of the tubes and fibers formed. The results obtained were (43 ± 12) nm (46 ± 23) nm and (82 ± 38) nm to Serp5, Serp 10, and Serp20, respectively. It is possible to observe that the standard deviation of the size of the structures was high, which can be justified by the heterogeneity of the structures formed and its relation to the natural support (serpentinite) used in the CVD process. Additionally, the higher the metal content used in the synthesis of the materials, the larger the diameter of the nanostructures produced.

According to the literature, there are two most common types of nanostructure growth mechanisms using the CVD process: “tip-growth” for large catalytic particles (>>5 nm) and “base-growth” for smaller catalytic nanoparticles. From the TEM images it is possible to observe that the metallic nanoparticles inside the cavities of the carbon nanostructures have dimensions greater than 10 nm and smaller than 100 nm. Therefore, the possible mechanism for the CVD process in this work is based on tip-growth, with the formation of multiple carbon walls (Gohier et al., 2008).

The thermal stability measurements give us some information about the CNS organization structure and also about the yield of carbonaceous materials formed. The TG curves of the composites (Figure 4) showed a weight loss between 470°C and 600 °C, related to CNS oxidation. The maximum oxidation temperatures were: 548°C, 536°C and 514°C for the materials Serp5, Serp10 and Serp20, respectively. Meaning that an increase in cobalt amount

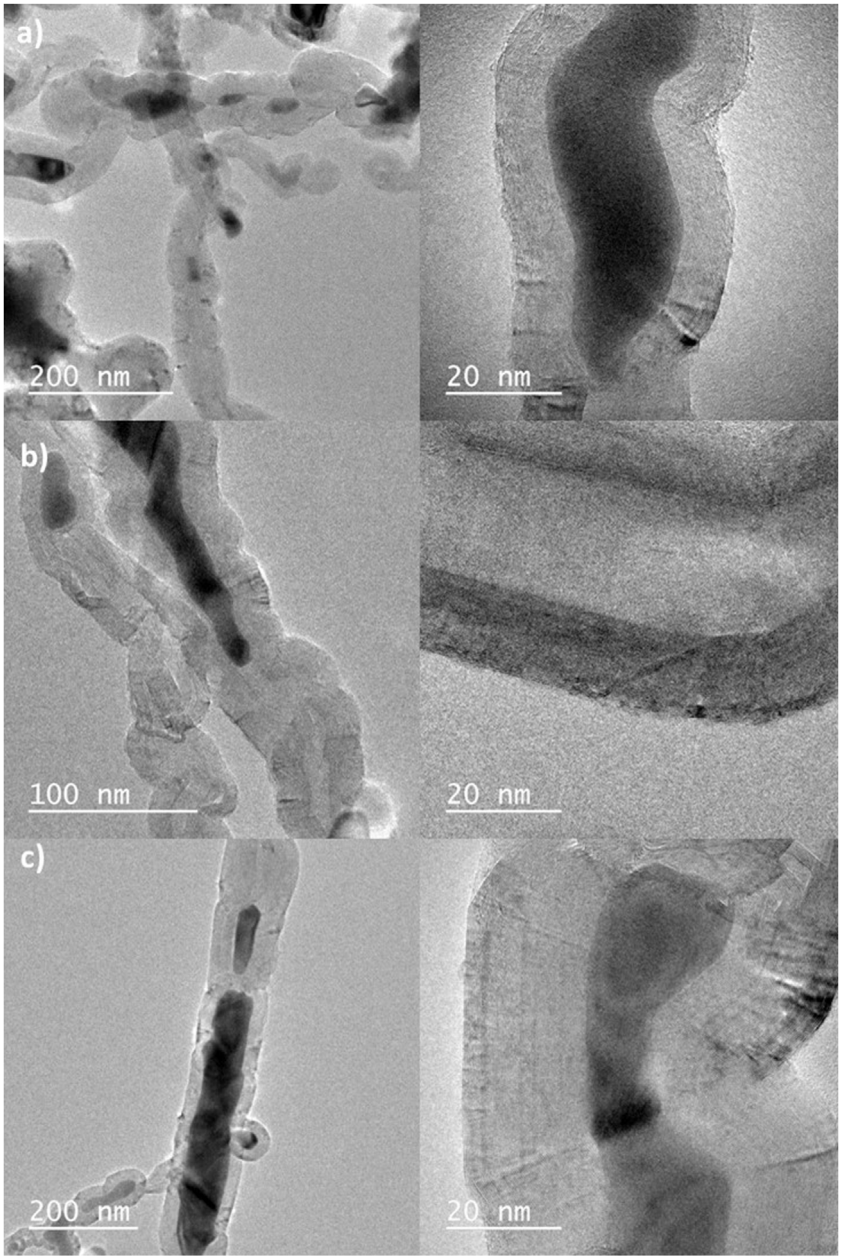

FIGURE 3
TEM images of serpentinite with 5 **(A)**, 10 **(B)** and 20 **(C)** %wt of Co, after CVD process (methane 1 h).

promotes a decrease in the maximum oxidation temperature. There are two hypotheses that may justify this fact: i) higher Co content could favor the formation of less organized structures, such as amorphous carbon or carbon nanotubes with one or a few walls that is less stable; ii) the presence of large amounts of metal particles can also catalyse carbon oxidation, decreasing the maximum oxidation temperature (McKee and Vecchio, 2006). In all curves there were no loss weight events in low temperatures, which may indicate the absence of amorphous carbon in the materials (Zhao et al., 2011; Yang et al., 2012). Considering the weight loss, it was possible to determine the approximate amount of carbon present in each sample, being 12, 23% and 35% for Serp5, Sepr10, and Serp20, respectively. So, the higher the cobalt content, the higher the yield of the carbon structures synthesis.

To confirm the carbon content of the materials, elemental analysis measurements were performed. As expected, the trend remained unchanged (14, 23% and 37 % wt, for Serp5, Serp10, and Serp20, respectively) and agreed with the obtained values by TG curves.

An important characteristic of adsorbent materials is its superficial area. Pure serpentinite, as other natural minerals, has a low superficial area, i.e. 10 $m^2 g^{-1}$ (Cao et al., 2017). After nitrogen adsorption, the materials Serp5, Serp10 and Serp20 showed no significant difference in its superficial area, i.e. 7, 9 and 14 $m^2 g^{-1}$,

10.3389/frcrb.2024.1402105

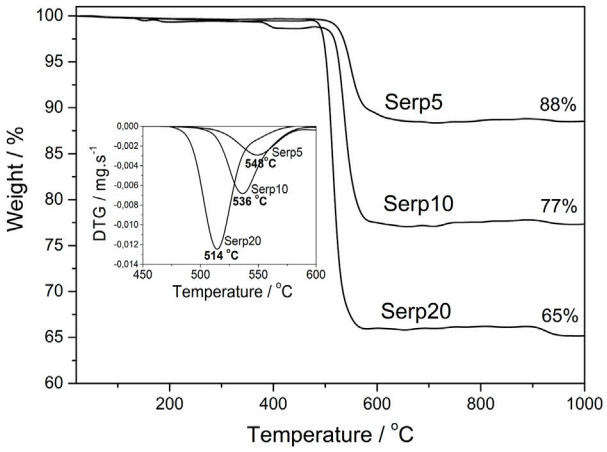

FIGURE 4
Thermogravimetric curves of serpentinite with 5, 10, and 20 %wt of Co, after CVD process, obtained in air atmosphere. In detail, DTG curves of the materials.

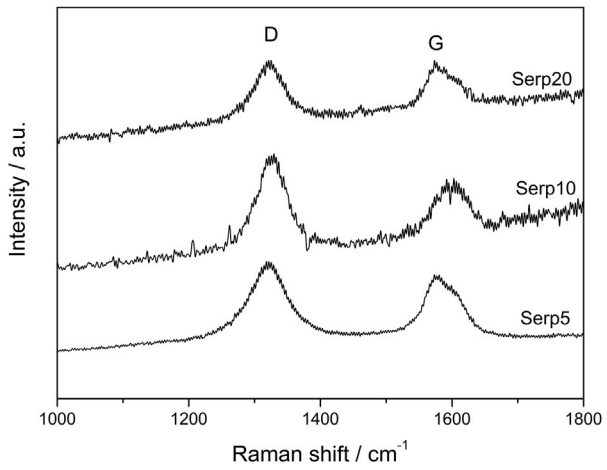

FIGURE 5
Raman spectra of serpentinite with 5, 10, and 20 %wt of Co, after CVD process.

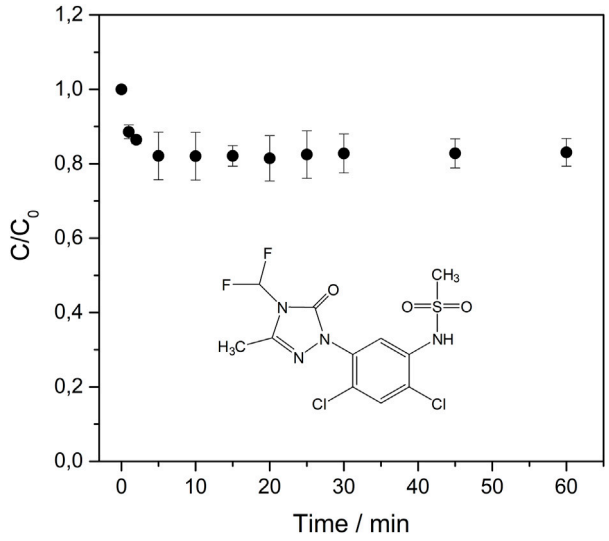

FIGURE 6
Equilibrium time of sulfentrazone adsorption by Serp5. Experimental conditions: $C_{0\ Sulfentrazone}$ = 10.0 mg L^{-1}, volume = 20.00 mL, adsorbent mass = 0.0100 g, contact time = 60 min, temperature= 25°C, $pH_{initial}$ ~ 5

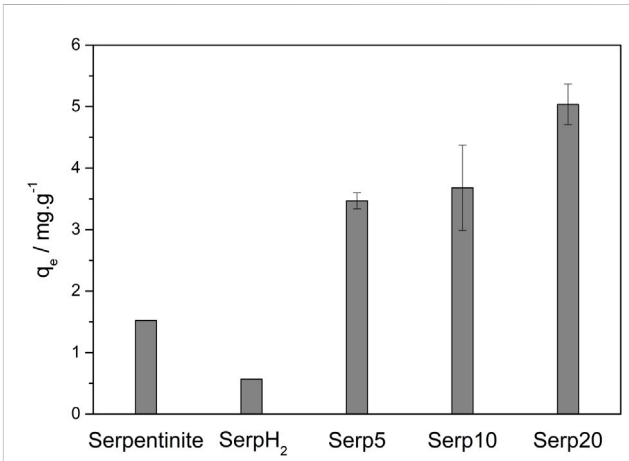

FIGURE 7
Sulfentrazone removal by serpentinite before thermal treatment, Serp5, Serp10 and Serp20. Experimental conditions: $C_{0\ Sulfentrazone}$ = 10.0 mg L^{-1}, volume = 20.00 mL, adsorbent mass = 0.0100 g, contact time = 25 min, temperature = 25°C, $pH_{initial}$ ~ 5.

respectively. It would be expected some increase, comparing to pure serpentinite, due to CNS formation, but in this case no significant change was noticed, probably due to an excess of serpentinite (matrix) in the material.

For last, for further CNS structure elucidation, Raman spectra were obtained (Figure 5). Ten different measurements were carried out for each sample and all spectra presented here represents an average result. It is possible to observe the D and G characteristics bands for carbon materials, at 1,320 and 1,580 cm^{-1} respectively (Figure 5). The D band refers to less organized carbon materials, generally defective structures, and the G-band is related to more organized carbon structures, i.e., graphite structures (Pimenta et al., 2007). The I_D/I_G ratio can be used as a parameter for the quality of carbon nanomaterials. The higher the ratio, the lower the structural organization of the material (Beyssac et al., 2003). The ratio values obtained were, 1.2; 1.1 and 1.0 to Serp5, Serp10 and Serp20. respectively. All values obtained were close to 1.0, which was expected as they were materials made from a natural support, with variable particle sizes, not favouring more organized structures. Again, no significant differences between the CNS of the three materials can be point out. Consequently, all techniques suggest that the Co content did not influenced the carbon structures, only the yield (increased when catalyst content was increased–Serp20).

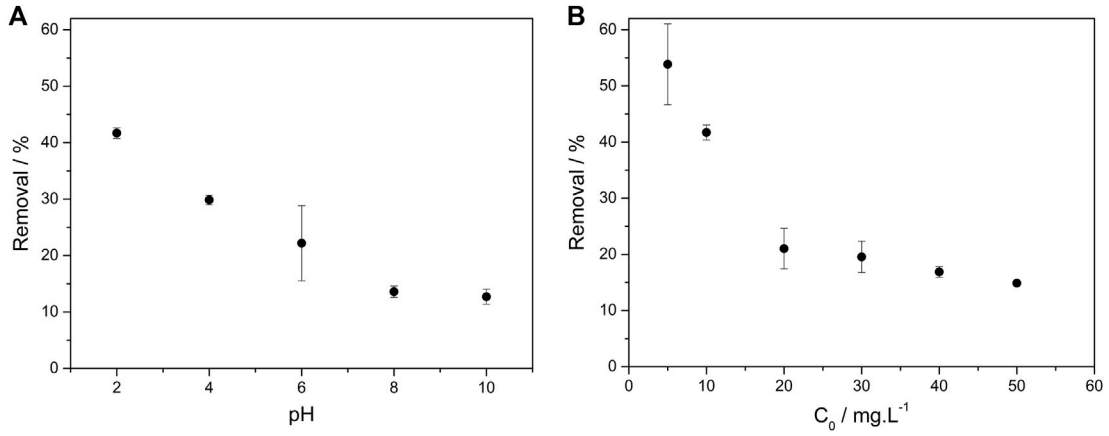

FIGURE 8
Influence of initial pH **(A)** and initial concentration **(B)** on the sulfentrazone removal by Serp20. Experimental conditions: $C_{0\ Sulfentrazone}$ = 10.0 mg L^{-1} **(A)** and 5–50 mg L^{-1} **(B)**, volume = 20.00 mL, adsorbent mass = 0.0100 g, contact time = 25 min, temperature = 25°C, $pH_{initial}$ = 2–10 **(A)**, $pH_{initial}$ = 2 **(B)**.

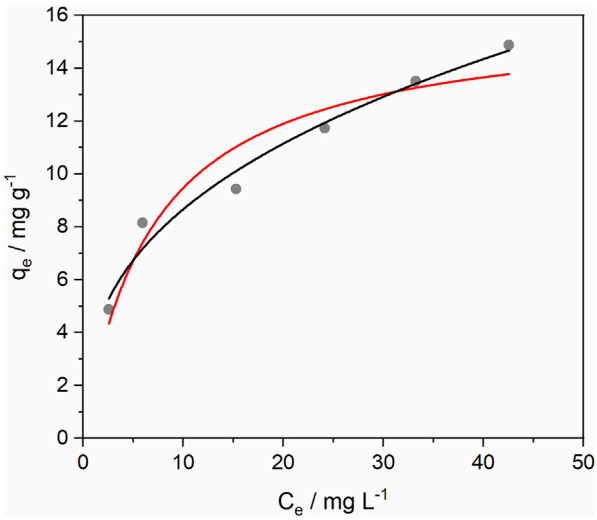

FIGURE 9
Isotherm of Langmuir (—) and Freundlich (—) for sulfentrazone adsorption by Serp 20. Experimental conditions: Initial concentration 5.0–50.0 mg.L^{-1}, solution volume 20.00 mL, adsorbent mass 0.0100 g, contact time 25 min, temperature 25°C, pH 2.

Our research group has been working on the synthesis of carbon nanostructures using natural minerals such as chrysotile (Lemos et al., 2016), vermiculite (Purceno et al., 2012) and mining waste (Silva et al., 2020) in the presence of iron or cobalt nanoparticles through the CVD process with different carbon sources and synthesis temperatures. Chrysotile, a silicate present in serpentinite rock, was impregnated with cobalt for the synthesis of carbon structures at temperatures between 600–900°C. It was observed that the best temperatures for synthesis were 800 and 900°C and the materials were efficient for adsorption of methylene blue dye (Lemos et al., 2016). Purceno and collaborators used the mineral vermiculite, a magnesium silicate, as a support for the deposition of iron and molybdenum nanoparticles. Then, it was synthesized nanostructures using methane as a carbon source at 800°C. The materials (~21% of carbon content) presented adsorption capacity between 2 and 4 mg m^{-2} for the hormone ethinyl estradiol (Purceno et al., 2012). Iron mining tailings were used for the synthesis of carbon nanomaterials using ethylene and acetonitrile as carbon sources by the CVD process at temperatures between 500–900°C. The results obtained showed that higher temperatures led to the formation of carbon nanostructures with greater yield. The materials had a capacity to remove ethinyl estradioal hormone of up to 22.3 mg. g^{-1} (Silva et al., 2020).

3.1 Removal of the sulfentrazone herbicide

The materials (Serp5, Serp10, and Serp20) were used to removal of the environmental contaminant sulfentrazone. As already discussed, this molecule is a pre-emergent herbicide and has a high potential persistence and moderate mobility in soil, which facilitates its accumulation and consequent soil and water contamination.

First, the equilibrium time required for sulfentrazone adsorption by Serp5 was determined, as shown at Figure 6. The sulfentrazone was rapidly removed by the material and 5 min were necessary for

TABLE 1 Parameters of Langmuir and Freundlich for the sulfentrazone adsorption by Serp 20.

Langmuir			Freundlich		
K_L/(L mg^{-1})	q_m/(mg g^{-1})	R^2	K_F/(mg g^{-1}) (mg L^{-1})^n	1/n	R^2
0.145 ± 0.046	16.0 ± 1.40	0.904	3.75 ± 0.424	0.364 ± 0.035	0.969

the concentration to remain constant. Initially, within the first 5 min, a larger number of active sites were available for adsorption. However, as time progressed, these active sites became progressively occupied, resulting in a deceleration of the adsorption process.

For the other experiments, it was chosen 25 min as reaction time, to obtain greater reliability that the equilibrium was reached despite any changed variable. All prepared materials and pure serpentinite were applied in the sulfentrazone removal, and the results are shown Figure 7.

The removal of sulfentrazone by serpentinite prior to thermal treatment was 7.6%. This ability to remove sulfentrazone can be attributed to the presence of minerals such as antigorite, lizardite, and talc, as evidenced in the XRD results. These minerals have amphoteric hydroxyl groups, giving them an acid-base character that enables them to acquire an electrical charge contingent upon the pH of the system. Given that the pKa of serpentinite is 4.3 and that of sulfentrazone is 6.56, during the adsorption process (at pH~5), serpentinite becomes negatively charged while sulfentrazone carries a positive charge (Alvarez-Silva et al., 2010; Rodrigues and Almeida, 2018). Consequently, an electrostatic attraction can occur, facilitating the adsorption of sulfentrazone. Similar findings were reported by Momčilović et al., who employed serpentinite for the adsorption of Cd(II) and anionic textile dyes (Momčilović et al., 2016).

After thermal treatment in reducing atmosphere, the sulfentrazone removal was only 2.8% in serpentinite. This occurred due the difference of minerals presents in the materials. Prior to thermal treatment, serpentinite presented phases of hydrated magnesium silicate, including antigorite, lizardite, and talc. However, following thermal treatment, the material exhibits phases of non-hydrated forsterite, olivine, and enstatite. These alterations in the mineral composition of serpentinite may result in a diminished electrostatic interaction between sulfentrazone and the materials, consequently leading to a reduction in adsorption capacity.

After CVD process, the removal of sulfentrazone increased to 17.3, 18.4% and 25.2% for Serp5, Serp10, and Serp20, respectively. The sulfentrazone removal increased with higher carbon content in the material. Carbonaceous materials, with sp^2 hybridization, can promote the adsorption through π-π interaction with the adsorbate aromatic ring (Chen et al., 2021). In addition, it could occur hydrogen bonding interaction between the sulfentrazone structure and the carboxyl group present in the materials. Thus, π-π interaction, hydrogen bonding and electrostatic interaction may be responsible for the adsorption of sulfentrazone, in which led to a higher contaminant removal. Duman et al. also proposed that adsorption of the herbicide diquat dibromide by oxidized multi-walled carbon nanotube occurred due to π-π interaction and electrostatic interaction (Duman et al., 2019).

Since Serp20 was more effective for sulfentrazone adsorption, this material was selected to evaluate the influence of other parameters in the process, such as initial pH and initial concentration. The results are shown in Figure 8.

As can be seen in Figure 8A, the percentage of sulfentrazone removal by Serp20 was greater at acidic pH values, decreasing from 41.7% to 12.7% with an increase in pH from 2 to 10. These results can indicate the participation of cobalt, together with the carbon structures, in the sulfentrazone removal by a degradation mechanism. Similar behavior was observed in a work with Fe/Ni nanoparticles (Nascimento et al., 2016). In an acid medium, these particles were able to degrade the sulfentrazone from the aqueous medium by the formation of atomic hydrogen and by direct electron transfer to the herbicide molecule (Nascimento et al., 2016).

To confirm the degradation of sulfentrazone by Co^0, alongside the adsorption by carbon structures, experiments were conducted at different pH, and the remaining solutions were analysed by High Performance Liquid Chromatography (Supplementary Figure S3, ESI†). At pH values 2 and 4, in addition to the sulfentrazone peak with a retention time of 4.84 min, a peak with a retention time of 3.75 min corresponding to a sulfentrazone degradation product was observed. This degradation product, as reported by Nascimento et al., can be identified as the dechlorinated sulfentrazone molecule (Nascimento et al., 2016).

Similar results were obtained in other works. Cruz et al. used Co^0/CoO nanoparticles for remazol golden yellow dye removal at pH 2 (Cruz et al., 2019). According to the authors, the electrons from the corrosion of Co^0 can be transferred directly to the dye molecules or for protons present in the system. In the last case, highly reactive hydrogen can induce the cleavage of the azo bond of the dye molecule (Cruz et al., 2019). Shao et al. used Co^0 nanoparticles embedded in nitrogen-doped mesoporous carbon nanofibers to promote the hydrogenation of levulinic acid in an H_2 atmosphere. According to the authors, the hydrogenation of levulinic acid occurs due to a reaction with atomic hydrogen, resulting from the dissociation of H_2 adsorbed in Co^0 sites (Shao et al., 2021).

At pH values above 6, the percentage of removal of sulfentrazone is lower due to the electrostatic repulsion that occurs between Serp20 and sulfentrazone. Besides that, at these pH values, the degradation of the sulfentrazone by Co^0 will not be very significant due to the passivation of the metallic cobalt surface by cobalt oxide. Metallic cobalt is not very stable in an aqueous medium, being oxidized in CoO_x, which leads to its deactivation during the reaction (Shao et al., 2021). Acidic conditions promote the removal of a passive layer of oxides and/or hydroxides that form on the metal's surface (Cruz et al., 2019).

Consequently, we believe that the removal of sulfentrazone occurred by two different mechanisms: adsorption by the carbon species produced in the CVD process and degradation through Co^0 species present in the composites.

The effect of the initial sulfentrazone concentration in the removal process was also investigated. As shown in Figure 8B, with the increase of initial concentration from 5 to 50 mg L^{-1}, the removal efficiency decreased from 53.9% to 14.9%, respectively, due to the occupation of the Serp20 adsorption sites by sulfentrazone.

Since adsorption is the principal removal process of sulfentrazone by Serp20, isotherm assays were performed. The Langmuir and Freundlich isotherm models were adjusted to the experimental data and the results are shown in Figure 9. The parameters of both models can be observed in Table 1.

As can be seen, the Freundlich model fit (R^2 = 0.969) was better compared to the Langmuir model fit (R^2 = 0.904). The removal capacity obtained experimentally at a sulfentrazone concentration of 50 mg L^{-1} was equal to 14.9 mg g^{-1}.

In other works involving the adsorption of pesticides by carbon-based materials, the Freundlich model was also the one that best fits the experimental data. Essandoh et al. obtained a maximum adsorption capacities for 2,4- dichlorophenoxyacetic acid and 2-methyl-4-chlorophenoxyacetic acid of 134 mg g^{-1} and 50 mg g^{-1}, respectively, using switchgrass biochar (Essandoh et al., 2017). Liu et al. synthesized a magnetic graphene oxide for neonicotinoid pesticide adsorption getting adsorption capacities ranging from 1.77–3.11 mg g^{-1} (Liu et al., 2017). Suo et al. used P doped biochar from corn straw for the adsorption of triazine achieved a maximum adsorption capacity for atrazine of 79.6 mg g^{-1} (Suo et al., 2019).

4 Conclusion

In this work, the serpentinite rock ($Mg_3SiO_5(OH)_4$) was used as an inorganic matrix for the synthesis of magnetic amphiphilic materials. The serpentinite was impregnated in proportions of 5, 10% and 20% by mass of cobalt/support, to obtain different amounts of carbon nanotubes, since metallic cobalt acts as a catalyst in the formation of multi-walled carbon nanotubes.]The CVD process was efficient, and it was obtained 14, 23% and 37% carbon wt, for Serp5, Serp10, and Serp20, respectively. The composites were used for sulfentrazone removal of water and variables such as inicial concentration, pH and nature of the adsorbant were studied. The results showed two main mechanisms: adorption and degradation by Co particles. The removal capacity obtained experimentally at a sulfentrazone concentration of 50 mg L^{-1} was equal to 14.9 mg g^{-1}.

Data availability statement

The original contributions presented in the study are included in the article/Supplementary Material, further inquiries can be directed to the corresponding author.

Author contributions

ED: Conceptualization, Formal Analysis, Methodology, Writing–original draft. AV: Formal Analysis, Methodology, Resources, Writing–review and editing. MN: Formal Analysis, Methodology, Writing–original draft. PP: Writing–original draft. FP: Writing–original draft. RM: Validation, Writing–review and editing. AT: Funding acquisition, Supervision, Validation, Visualization, Writing–review and editing.

Funding

The author(s) declare that financial support was received for the research, authorship, and/or publication of this article. CNPq, CAPES, FAPEMIG and INCT MIDAS for financial support UFMG Microscopy Center for the microscopy images. The company Pedras Congonhas for donating of the serpentinite samples. Programa de Produtividade em Pesquisa UEMG (PQ/UEMG 10/2022) for research grant from Paula Sevenini Pinto.

Acknowledgments

The authors gratefully acknowledge the financial support of CNPq, CAPES, FAPEMIG, INCT MIDAS, and UFMG Microscopy Center. The company Pedras Congonhas for donating of the serpentinite samples. FP thank to Programa de Produtividade em Pesquisa UEMG (PQ/UEMG 10/2022).

Conflict of interest

The authors declare that the research was conducted in the absence of any commercial or financial relationships that could be construed as a potential conflict of interest.

Publisher's note

Supplementary material

The Supplementary Material for this article can be found online at: https://www.frontiersin.org/articles/10.3389/frcrb.2024.1402105/full#supplementary-material

References

Alvarez-Silva, M., Uribe-Salas, A., Mirnezami, M., and Finch, J. A. (2010). The point of zero charge of phyllosilicate minerals using the mular–roberts titration technique. *Miner. Eng.* 23 (5), 383–389. doi:10.1016/j.mineng.2009.11.013

Arepalli, S., Nikolaev, P., Gorelik, O., Hadjiev, V. G., Holmes, W., Files, B., et al. (2004). Protocol for the characterization of single-wall carbon nanotube material quality. *Carbon* 42 (8), 1783–1791. doi:10.1016/j.carbon.2004.03.038

Ballotin, F. C., Cibaka, T. E., Ribeiro-Santos, T. A., Santos, E. M., Teixeira, A. P. d. C., and Lago, R. M. (2016). K2MgSiO4: a novel K+-Trapped biodiesel heterogeneous catalyst produced from serpentinite Mg3Si2O5(OH)4. *J. Mol. Catal. A Chem.* 422, 258–265. doi:10.1016/j.molcata.2016.02.006

Cao, C.-Y., Liang, C.-H., Yin, Y., and Du, L.-Yu (2017). Thermal activation of serpentine for adsorption of cadmium. *J. Hazard. Mater.* 329, 222–229. doi:10.1016/j.jhazmat.2017.01.042

Chen, T., Fu, C., Liu, Y., Pan, F., Wu, F., You, Z., et al. (2021). Adsorption of volatile organic compounds by mesoporous graphitized carbon: enhanced organophilicity, humidity resistance, and mass transfer. *Sep. Purif. Technol.* 264, 118464. doi:10.1016/j.seppur.2021.118464

Cruz, J. C., Nascimento, M. A., Amaral, H. A. V., Lima, D. S. D., Teixeira, A. P. C., and Lopes, R. P. (2019). Synthesis and characterization of cobalt nanoparticles for application in the removal of textile dye. *J. Environ. Manag.* 242, 220–228. doi:10.1016/j.jenvman.2019.04.059

Dresselhaus, G., Avouris, P., and Dresselhaus, M. S. (2001) *Carbon nanotubes: synthesis, structure, properties, and applications*. Berlin, Heidelberg: Springer. doi:10.1007/3-540-39947-X

Drizo, A., Forget, C., Chapuis, R. P., and Comeau, Y. (2006). Phosphorus removal by electric arc furnace steel slag and serpentinite. *Water Res.* 40, 1547–1554. doi:10.1016/j.watres.2006.02.001

Duman, O., Özcan, C., Gürkan Polat, T., and Tunç, S. (2019). Carbon nanotube-based magnetic and non-magnetic adsorbents for the high-efficiency removal of diquat dibromide herbicide from water: OMWCNT, OMWCNT-Fe3O4 and OMWCNT-κ-carrageenan-Fe3O4 nanocomposites. *Environ. Pollut.* 244, 723–732. doi:10.1016/j.envpol.2018.10.071

Dupuis, A.-C. (2005). The catalyst in the CCVD of carbon nanotubes—a review. *Prog. Mater. Sci.* 50 (8), 929–961. doi:10.1016/j.pmatsci.2005.04.003

Essandoh, M., Wolgemuth, D., Pittman, C. U., Mohan, D., and Mlsna, T. (2017). Phenoxy herbicide removal from aqueous solutions using fast pyrolysis switchgrass biochar. *Chemosphere* 174, 49–57. doi:10.1016/j.chemosphere.2017.01.105

Hirth, G., and Guillot, S. (2013). Rheology and tectonic significance of serpentinite. *Elements* 9 (2), 107–113. doi:10.2113/gselements.9.2.107

Lelario, F., Gardi, I., Mishael, Y., Dolev, N., Undabeytia, T., Nir, S., et al. (2017). Pairing micropollutants and clay-composite sorbents for efficient water treatment: filtration and modeling at a pilot scale. *Appl. Clay Sci.* 137, 225–232. doi:10.1016/j.clay.2016.12.029

Lemos, B. R. S., Soares, É. A. R., Teixeira, A. P. C., Ardisson, J. D., Fernandez-Outon, L. E., Amorim, C. C., et al. (2016). Growth of carbon structures on chrysotile surface for organic contaminants removal from wastewater. *Chemosphere* 159, 602–609. doi:10.1016/j.chemosphere.2016.06.022

Liu, G., Li, L., Xu, D., Huang, X., Xu, X., Zheng, S., et al. (2017). Metal–organic framework preparation using magnetic graphene oxide–β-cyclodextrin for neonicotinoid pesticide adsorption and removal. *Carbohydr. Polym.* 175, 584–591. doi:10.1016/j.carbpol.2017.06.074

Martinez, C. O., Silva, C. M. M. S., Fay, E. F., Nunesmaia, A., Abakerli, R. B., and Durrant, L. R. (2008). Degradation of the herbicide sulfentrazone in a Brazilian typic hapludox soil. *Soil Biol. Biochem.* 40 (4), 879–886. doi:10.1016/j.soilbio.2007.10.016

McKee, G. S. B., and Vecchio, K. S. (2006). Thermogravimetric analysis of synthesis variation effects on CVD generated multiwalled carbon nanotubes. *J. Phys. Chem. B* 110 (3), 1179–1186. doi:10.1021/jp054265h

Momčilović, M. Z., Ranđelović, M. S., Purenović, M. M., Đorđević, J. S., Onjia, A., and Matović, B. (2016). Morpho-structural, adsorption and electrochemical characteristics of serpentinite. *Sep. Purif. Technol.* 163, 72–78. doi:10.1016/j.seppur.2016.02.042

Montoro, L. A., Corio, P., and Rosolen, J. M. (2007). A comparative study of alcohols and ketones as carbon precursor for multi-walled carbon nanotube growth. *Carbon* 45 (6), 1234–1241. doi:10.1016/j.carbon.2007.01.025

Nascimento, M. A., Lopes, R. P., Cruz, J. C., Silva, A. A., and Lima, C. F. (2016). Sulfentrazone dechlorination by iron-nickel bimetallic nanoparticles. *Environ. Pollut.* 211, 406–413. doi:10.1016/j.envpol.2015.12.043

O'Connell, M. J., and O'Connell, M. J. (2006) *Carbon nanotubes: properties and applications*. Boca Raton City Taylor and Francis Group, LLC.

Öncel, Ç., and Yürüm, Y. (2006). Carbon nanotube synthesis via the catalytic CVD method: a review on the effect of reaction parameters. *Fullerenes, Nanotub. Carbon Nanostructures* 14 (1), 17–37. doi:10.1080/15363830500538441

Pimenta, M. A., Dresselhaus, G., Dresselhaus, M. S., Cancado, L. G., Jorio, A., and Saito, R. (2007). Studying disorder in graphite-based systems by Raman spectroscopy. *Phys. Chem. Chem. Phys.* 9 (11), 1276–1290. doi:10.1039/B613962K

Purceno, A. D., Barrioni, B. R., Dias, A., da Costa, G. M., Lago, R. M., and Moura, F. C. C. (2011). Carbon nanostructures-modified expanded vermiculites produced by chemical vapor deposition from ethanol. *Appl. Clay Sci.* 54 (1), 15–19. doi:10.1016/j.clay.2011.06.012

Purceno, A. D., Teixeira, A. P. C., Souza, N. J. d., Fernandez-Outon, L. E., Ardisson, J. D., and Lago, R. M. (2012). Hybrid magnetic amphiphilic composites based on carbon nanotube/nanofibers and layered silicates fragments as efficient adsorbent for ethynilestradiol. *J. Colloid Interface Sci.* 379 (1), 84–88. doi:10.1016/j.jcis.2012.04.018

Rodrigues, B. N., and Sousa de Almeida, F. (2018) *Guia de Herbicidas*. 7th ed. Viçosa city Produção Independente.

Shao, S., Yang, Y., Guo, S., Hao, S., Yang, F., Zhang, S., et al. (2021). Highly active and stable Co nanoparticles embedded in nitrogen-doped mesoporous carbon nanofibers for aqueous-phase levulinic acid hydrogenation. *Green Energy and Environ.* 6 (4), 567–577. doi:10.1016/j.gee.2020.11.005

Siqueira, S. L. de, and Kruse, M. H. L. (2008). Agrotóxicos e Saúde Humana: Contribuição Dos Profissionais Do Campo Da Saúde. *Rev. Esc. Enferm. USP* 42, 584–590. doi:10.1590/s0080-62342008000300024

Suo, F., You, X., Ma, Y., and Li, Y. (2019). Rapid removal of triazine pesticides by P doped biochar and the adsorption mechanism. *Chemosphere* 235, 918–925. doi:10.1016/j.chemosphere.2019.06.158

Teixeira, A. P. C., Purceno, A. D., Barros, A. S., Lemos, B. R. S., Ardisson, J. D., Macedo, W. A. A., et al. (2012). Amphiphilic magnetic composites based on layered vermiculite and fibrous chrysotile with carbon nanostructures: application in catalysis. *Catal. Today* 190 (1), 133–143. doi:10.1016/j.cattod.2012.01.042

Teixeira, A. P. C., Purceno, A. D., de Paula, C. C. A., da Silva, J. C. C., Ardisson, J. D., and Lago, R. M. (2013). Efficient and versatile fibrous adsorbent based on magnetic amphiphilic composites of chrysotile/carbon nanostructures for the removal of ethynilestradiol. *J. Hazard. Mater.* 248-249 (249), 295–302. doi:10.1016/j.jhazmat.2013.01.014

Undabeytia, T., Nir, S., Sánchez-Verdejo, T., Villaverde, J., Maqueda, C., and Morillo, E. (2008). A clay–vesicle system for water purification from organic pollutants. *Water Res.* 42 (4), 1211–1219. doi:10.1016/j.watres.2007.09.004

Yang, W., Sun, W. J., Chu, W., Jiang, C.Fa, and Wen, J. (2012). Synthesis of carbon nanotubes using scrap tyre rubber as carbon source. *Chin. Chem. Lett.* 23 (3), 363–366. doi:10.1016/j.cclet.2012.01.006

Zhao, W., Lee, Mi J., Kim, H. T., and Kim, Ik J. (2011). The synthesis of carbon nanotubes (CNTs) by catalytic CVD using a Fe/Co-supported zeolite template. *Electron. Mater. Lett.* 7 (2), 139–144. doi:10.1007/s13391-011-0609-6

frontiers | Frontiers in Carbon

TYPE Original Research
PUBLISHED 27 May 2024
DOI 10.3389/frcrb.2024.1400664

OPEN ACCESS

EDITED BY
Lei Shi,
Sun Yat-sen University, China

REVIEWED BY
Guillaume Perry,
Sorbonne Universités, France
Shukun Chen,
South China University of Technology, China

*CORRESPONDENCE
Silviya P. Zustiak,
silviya.zustiak@slu.edu
Irma Kuljanishvili,
irma.kuljanishvili@slu.edu

RECEIVED 14 March 2024
ACCEPTED 10 May 2024
PUBLISHED 27 May 2024

CITATION
Luc E, Aziz B, Kim Y, Lespasio M, Jombo P, Zustiak SP and Kuljanishvili I (2024), Cell spreading and viability on single-walled carbon nanotube/zinc oxide nanowire heterostructures synthesized by chemical vapor deposition.
Front. Carbon 3:1400664.
doi: 10.3389/frcrb.2024.1400664

Cell spreading and viability on single-walled carbon nanotube/zinc oxide nanowire heterostructures synthesized by chemical vapor deposition

Emily Luc[1,2], Bashar Aziz[2], Yoosuk Kim[2], Marcus Lespasio[2], Philomena Jombo[1], Silviya P. Zustiak[1]* and Irma Kuljanishvili[1,2]*

[1]Department of Biomedical Engineering, Saint Louis University, St. Louis, MO, United States, [2]Department of Physics, Saint Louis University, St. Louis, MO, United States

Recent studies have shown the wide array of biomedical applications for nanomaterials such as single-walled carbon nanotubes (SWCNTs) and zinc oxide nanowires (ZnO NWs). SWCNTs are non-cytotoxic and have a varying range of mechanical, physical, and electrical properties useful to biomedical research. ZnO NWs are biocompatible, antibacterial, and exhibit piezoelectric properties that could stimulate cell growth. While recent research has been conducted using these nanomaterials independently, our study is focused on testing cell behaviors when seeded on SWCNTs, ZnO NWs and their heterostructure assemblies. ZnO NWs/SWCNTs heterostructures prepared via chemical vapor deposition (CVD) have not been used in biomedical applications to date. Here, we describe fabrication and characterization of the two nanomaterials independently and in a heterostructure formation. The NIH 3T3 fibroblast cells and U87 glioblastoma cells were seeded on all samples, including SiO_2/Si control/reference samples, and the cell growth was studied via fluorescence microscopy and scanning electron microscopy. The focus of this study was to evaluate cell spreading, filopodia extensions, and cell viability on these nanomaterial assemblies. Results indicated that cells were able to extend filopodia on all nanostructures, however cell spreading was more pronounced on SWCNTs, and cell viability was compromised on the ZnO NWs and the ZnO NWs/SWCNTs heterostructures. In addition, soluble compounds from the nanomaterials were tested to determine their cytotoxicity towards both NIH 3T3 and U87 cells. Results indicated a significant decrease in filopodia length, cell spreading, and cell viability when cells were exposed to ZnO NWs-conditioned cell media. These findings on cellular behavior involving SWCNTs, ZnO NWs, and ZnO NWs/SWCNTs heterostructure provide valuable information on the suitability of SWCNTs and ZnO NWs for future uses in biomedical applications.

KEYWORDS

cell viability, cell spreading, chemical vapor deposition synthesis, single-walled carbon nanotubes and zinc oxide nanowires, SWCNTs-ZnO NWs heterostructures

1 Introduction

Nanomaterials have been shown useful for a wide range of biomedical applications especially as a component to be integrated into micro- and nano-sized biological systems (Wang et al., 2009; Murali et al., 2021). Among the plethora of nanomaterials, one-dimensional carbon-based materials and zinc oxide (ZnO) nanostructures, such as single-walled carbon nanotubes (SWCNTs) and ZnO nanowires (ZnO NWs), have garnered attention for biomedical applications due to their unique physical properties and relative biocompatibility. SWCNTs exhibit unparalleled mechanical strength, boasting the highest Young's modulus and tensile strength among all nanomaterials as well as having directional conductivity stemming from a unique hexagonal crystal structure of rolled-up carbon sheets (Zhou et al., 2009). On the other hand, ZnO and ZnO NWs are semiconductive, photosensitive, and biodegradable, with high exciton binding energy and antibacterial properties due to their hexagonal wurtzite crystal structure (Ciofani et al., 2012; Zhang et al., 2012). Not surprisingly, both nanomaterials have been used in a variety of biomedical applications. While concerns with the toxicity of each nanomaterial have been raised, the use of a heterostructure surface coatings combining the two nanomaterials has not been explored in detail.

SWCNTs have been used in targeted cancer therapy, in glucose biosensors, and as substrates for neural growth, owing to their ability to promote cell adhesion and growth (Imaninezhad et al., 2018) or to penetrate cells and tissues and enable drug targeting and accumulation (Dineshkumar et al., 2015; Simon et al., 2019). However, the cytotoxicity of SWCNTs is of question, specifically for powdered nanomaterials that could be endocytosed by cells. A previous study has shown that SWCNTs toxicity to U87 glioblastoma cells is related to its downregulation of CDND2, a gene that promotes cell cycle progression, and upregulation of DUSP1 and DTNA, which are apoptosis regulator genes (Minchenko et al., 2016). Moreover, another study found that while glioblastoma growth was initially inhibited when exposed to CNTs, proliferation significantly increased over time (Imaninezhad et al., 2017; Parikh et al., 2020). On the other hand, studies of CNT-coated surfaces, unlike powered nanomaterials, have shown positive effects on non-cancerous cell behaviors including an increase of filopodia, cell spreading, proliferation and migration, and increased expressions of vinculin and talin (Bacakova et al., 2007), as well as increase in cell adhesion-related gene expressions (Ryoo et al., 2010). On the other hand, low doses of SWCNTs have been shown to affect astrocyte expression of proliferation and apoptosis related genes, thus evidencing SWCNTs possible genotoxic impact (Rudnytska et al., 2021).

ZnO NWs and ZnO nanostructures have been used in various biomedical applications, including sunscreen lotions, antibacterial coatings, biosensors, cancer-targeted drug delivery, and optical imaging (Hong et al., 2011; Sharma et al., 2022). ZnO can be cytotoxic to mammalian cells in a concentration-dependent manner due to direct cellular uptake and ion-shedding upon dissolution *in vivo*, where Zn^{2+} ions can affect cellular apoptosis mechanisms (Li et al., 2008; Wahab et al., 2011). It has been suggested that ZnO nanoparticles may be selectively localized in cancer cells from enhanced permeability and retention effect and electrostatic interactions, thus showing that they may selectively target cancer cells (Bisht and Rayamajhi, 2016). However, ZnO NWs appear to be biocompatible when used as coatings and/or presented extracellularly. For example, Cui et al. found that cells grown on ZnO NWs-covered polydimethylsiloxane (PDMS) microchips had better biocompatibility than those grown on hydrophobic PDMS alone (Cui et al., 2020).

One way to diversify functionalities and applications of individual nanomaterials and to achieve improved biocompatibility and enhanced properties is to form heterostructures of such nanomaterials. Various heterostructures have been extensively studied in nanoscience but less work has been done on determining their effect on cells for biomedical applications. One notable example of incorporating heterostructures *in vivo* has been titanium and strontium nanoparticle-nanotube heterostructures. These were made to use titanium's osseointegration property with strontium's ability to decrease osteoresorption and it was suggested that such heterostructures may be used in bone implants in clinical settings (Yin et al., 2017). CNTs and ZnO NWs heterostructures have been used previously in high performance electrodes for superconductor applications (Al-Asadi et al., 2017), as chemical sensors (Shooshtari et al., 2022), and as photocatalysts (Dai et al., 2012), but their effect on cells has not been explored in detail.

When combining ZnO and CNTs, the ZnO/CNTs hybrid materials can provide a new platform for utilizing a spectrum of properties, which can be used simultaneously in multimodal environments in the biomedical field. Still, the development of ZnO/CNTs nanocomposites for biomedical applications is in its infancy, possibly due to toxicity concerns for both ZnO and CNT-nanopowders. In contrast, one-dimensional nanowire heterostructures, such as ZnO NWs/SWCNTs when grown directly on the substrates can offer a new testing environment for the evaluation of cell behaviors. To the best of our knowledge, ZnO NWs/SWCNTs heterostructures in pristine highly crystalline formations grown directly on top of each other have not been used in biological applications, thus further emphasizing the need and the purpose of this study. The preparation of ZnO NWs/SWCNTs heterostructures directly grown on a substrate, a departure from conventional studies utilizing dispersed or powdered forms, was made possible using a novel chemical vapor deposition (CVD) method recently developed by our team (Schaper et al., 2021). This study aims to investigate the impact of the heterostructures on cells by analyzing the morphology, frequency of filopodia, and viability of NIH 3T3 mouse fibroblast and U87 glioblastoma cell lines. We hypothesized that the heterostructure of ZnO NWs/SWCNTs could work in synergy where SWCNTs could promote non-cancerous cell growth, and ZnO NWs could suppress cancerous cell growth, thus utilizing uniqueness of both nanomaterials to interact with cells in a specific and/or selective way. Our studies indicated that cells were able to adhere to the heterostructures as well as to both SWCNTs and ZnO NWs individually but, at the same time, also indicated to the possible toxicity of Zn^{2+} ions released from the ZnO NWs towards both normal and cancer cell types. Our work did not show selective ZnO NWs toxicity towards cancer cells, when used

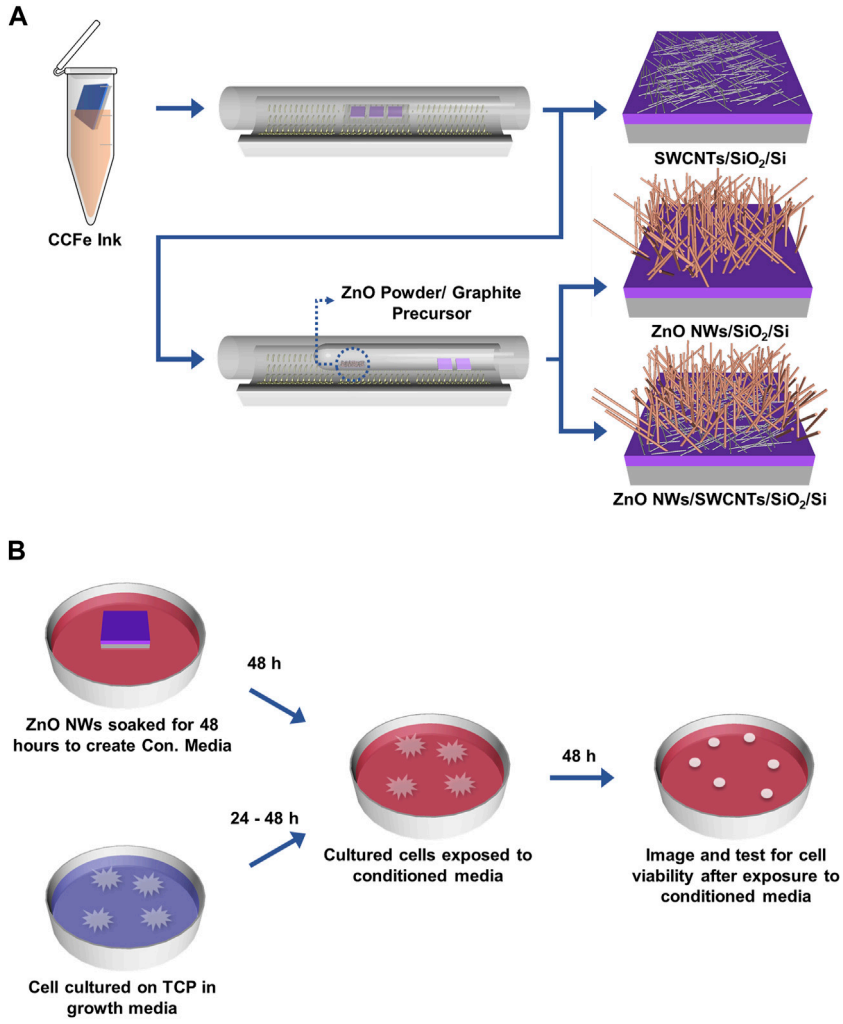

FIGURE 1
Schematic of CNTs and ZnO NWs and heterostructure synthesis on SiO_2/Si and ZnO NWs conditioned media preparation. **(A)** CVD synthesis of SWCNTs, ZnO NWs, and ZnO NWs/SWCNTs. **(B)** ZnO NWs are soaked for 48 h in complete cell medium to prepare ZnO NWs conditioned media (Con. Media). Cells cultured on TCP for 24 h were exposed to Con. Media for 48 h.

alone or in the heterostructure, underscoring the need for further research.

2 Materials and methods

2.1 Chemical vapor deposition synthesis of SWCNTs

SWCNTs were synthesized following a protocol previously established by our team (Figure 1A) (Kuljanishvili et al., 2009; Schaper et al., 2021). Briefly, SiO_2/Si chips of 5 x 5 mm were cut from SiO_2/Si wafers (UniversityWafer, South Boston, MA, P/B, (100), resistivity: 1–5 mΩ.cm, 300 nm of Thermal Oxide) and cleaned in order of acetone, isopropanol, and deionized (DI) water via sonication (BRANSON, Model #2800, 40 kHz) for 3 min in each solvent. Chips were then placed in an ultraviolet (UV) ozone system (Novascan PSD Pro Series Digital UV Ozone System, Boone, IA, United States) for 3 min to render optimal hydrophilicity. Each chip was dipped into custom composite Fe-based (CCFe) precursor ink for 10 s to ensure the entire surface was properly coated. The precursor ink consisted of 6 parts master solution (Iron (III) nitrate nonahydrate ($Fe(NO_3)_3{\cdot}9H_2O$) (Sigma-Aldrich, St. Louis, MO, United States, 99.99% purity): 3 parts DI water: 2 parts N,N-dimethylformamide (Sigma-Aldrich, St. Louis, MO, United States, ≥99% purity): 1 part Glycerol (Sigma-Aldrich, St. Louis, MO, United States, ≥99.0% purity). The chips were gently dried with the nitrogen gas and placed onto a quartz holder/boat, which was subsequently inserted into a quartz tube (Technical Glass Products, Painesville, OH, United States) inside a CVD three-zone furnace (Thermo Fisher Scientific Lindberg/Blue M, Waltham, MA, United States). The home-built CVD system is equipped with a mass flow controller (Sierra Instrument, Monterey, CA. United States) to manage the precise gas flow. The CVD growth process involved preconditioning of the catalysts at 365°C under argon (Ar) and hydrogen (H_2) gas mixture at a 1:0.5 gas ratio for 67 min followed by the growth at 900°C with methane (CH_4) precursor gas for 18 min and allowed to cool down under protection of Ar/H_2 gas mix with 1:

0.5 gas ratio. During the growth stage the mixture of $CH_4/H_2/Ar$ gas with the flow rates of 900/60/140 (sccm), respectively, was used in the CVD chamber.

2.2 CVD synthesis of ZnO NWs and ZnO NWs/SWCNTs

ZnO NWs and ZnO NWs/SWCNTs heterostructures were synthesized following a protocol previously established in our lab (Figure 1A) (Alameri et al., 2017a; Schaper et al., 2021). Briefly, to make ZnO NWs and ZnO NWs/SWCNTs, graphite (Alfa Aesar, Haverhill, MA, United States, 99.999%) and ZnO powder (Alfa Aesar, Haverhill, MA, United States, 99.999% purity) were used as precursors. 35 mg of each reagent mixed and placed into a small quartz boat (Technical Glass Products, Painesville, OH, United States). This boat was further placed into a quartz tube with one closed end, along with SiO_2/Si samples placed near the opening on the closed-end tube. ZnO NWs were grown at 930°C under Ar gas protection inside the CVD chamber. The synthesis of ZnO NWs/SWCNTs heterostructures involved growing the SWCNTs on the SiO_2/Si chips first, as described above, and subsequently growing the ZnO NWs directly on the SWCNTs, with no additional precursor catalyst thus creating seamless interface between the materials. All samples were used "as-grown" for all experiments without post-processing or surface treatments.

2.3 Nanomaterial characterization

Scanning electron microscopy (SEM; FEI Inspect F50, Lausanne, Switzerland) was used to visualize and evaluate nanomaterials. SWCNTs were imaged at 1.5 kV and ZnO NWs were imaged at 10 kV. Raman spectral measurements and analyses were also performed (Renishaw, InVia, Wotton-under-Edge, Gloucestershire, England) to determine the quality and crystallinity of the synthesized nanomaterials. Atomic force microscope (AFM; Park NX 10, Suwon, South Korea) in non-contact mode was used for carbon nanotube topographic imaging and to determine diameter of SWCNTs. Average length of SWCNTs and ZnO NWs were evaluated using ImageJ software (free download from the NIH at imagej.nih.gov). A home-built system assembled with trinocular stereo microscope equipped with a digital camera was used to take images of the sample surfaces for subsequent contact angle measurements. Briefly, 2 µL of DI water was dispensed on each sample, where samples were in ambient conditions during all measurements (with temperature and humidity maintained at 23°C and 20%, respectively). ImageJ software was used to measure the contact angle from the acquired images.

2.4 Cell maintenance

NIH 3T3 Cells (ATCC-CRL-1658™, ATCC, Manassas, VA) were maintained in Dulbecco's Modified Eagle's Medium (DMEM; Gibco ®, Bristol, RI). DMEM was supplemented with 10% heat-inactivated fetal bovine serum (FBS, Sigma-Aldrich ®, St Louis, MO), 100 units/mL Penicillin and 100 µg/mL Streptomycin (1% pen/strep). Cells were utilized between passages 7 to 18 and kept in a 37 °C and 5% CO_2 incubator. U87 MG glioblastoma cells (ATCC-HTB-14™) were maintained in Roswell Park Memorial Institute (RPMI) 1,640 medium supplemented with 10% FBS and 1% pen/strep. For both cell types, medium was refreshed every 2–3 days and cells were passaged when 80% confluence was reached by exposure to 0.05% trypsin/0.02% ethylenediamine triacetic acid (EDTA).

2.5 Cell seeding on nanomaterials

To prevent non-specific cell attachment, 1% bovine serum albumin (BSA, Thermo Fisher Scientific, Waltham, MA) in phosphate buffered saline (PBS) buffer was pipetted onto the wells of 48-well plates (100 µL/well) and incubated for 30 min, then carefully rinsed with PBS. SiO_2/Si chips with or without grown nanomaterials were sterilized by a dip in 200 proof ethanol for 1 min, dried completely in a tissue culture hood. And then placed inside the wells of the pre-treated 48-well plates (one chip per well). U87 and NIH 3T3 cells were then seeded on top of the chips at ~5,000 cells per well with 200 µL of cell medium supplemented with 10% FBS and 1% pen/strep. Cells were cultured for 24 h on top of each chip in a humidified incubator at 37°C and 5% CO_2.

2.6 Cell imaging via SEM and analysis of cell filopodia

For SEM imaging, U87 and NIH 3T3 cells on chips with and without nanomaterials were first fixed with 2.5% glutaraldehyde in 0.1 M sodium cacodylate buffer with 2% sucrose and 2 mM $CaCl_2$ (pH 7.25) and then with 1% osmium tetroxide (Electron Microscopy Sciences, Hatfield, PA) in 0.1 M sodium cacodylate buffer with 2% sucrose to preserve membrane structures. After fixation, the cells were consecutively dehydrated in 30%, 50%, 75%, 95%, and 100% ethanol. SEM (FEI Inspect F50, Lausanne, Switzerland) images were taken at 1.5 kV high voltage, and ×750 magnification. SEM images were used to observe cell filopodia with respect to nanomaterials to give qualitative data on cell interactions with the nanomaterials.

2.7 Cell imaging via microscopy and analysis of cell viability and morphology

For microscopy imaging, U87 and NIH 3T3 cells on chips with and without nanomaterials were either imaged live or fixed with 2.5% glutaraldehyde in 0.1 M sodium cacodylate buffer with 2% sucrose and 2 mM $CaCl_2$ (pH 7.25). For fluorescence imaging, live cells were stained with Cell Tracker (CellTracker™ Green CMFDA dye, Thermo Fisher, Scientific) following the manufacturer's procedure. Microscopy images were taken with a reflected light microscope (Nikon, Optiphot 66, Minato City, Tokyo, Japan) at ×20 magnification. Microscopy images were analyzed in ImageJ and used to measure cell area and calculate cell shape

factor (Eq. 1), where a shape factor value of 1 represents cells of a circular shape, while values approaching 0 indicate elongated cells.

$$Shape\ Factor = \frac{4\pi(Area)}{Perimeter^2} \quad (1)$$

Cell viability was measured with a LIVE/DEAD™ Viability/Cytotoxicity Kit, for mammalian cells (Thermo Fisher Scientific), where live cells were stained green with Calcein AM and dead cells were stained red with ethidium homodimer-1 (EthD-1). The stains were applied at concentrations of 4 μM for EthD-1 and 2 μM Calcein AM added directly to the cell media, and cells were incubated at 37°C for 30 min before imaging. In certain cases, CellTracker was used instead of Calcein AM to allow for better visualization of the whole cell while still staining all cells green. For live/dead staining, care was taken to rinse the cells gently as to cause minimal detachment of dead cells prior to staining. However, it is possible that some dead cells were detached from the substrate and thus, not included in the total cell viability calculation, skewing the results slightly towards higher than actual cell viability. Percent viability was calculated by counting the total cells stained green with CellTracker or the live cells stained green with Calcein AM and the dead cells stained red with EthD-1 as:

$$\%\ Cell\ Viability = \frac{Total\ Cells - Dead\ Cells}{Total\ Cells} * 100 \quad (2)$$

2.8 ZnO NW conditioned media preparation and analysis of cell response

ZnO NWs conditioned media (Con. Media) was prepared by soaking ZnO NW grown on SiO_2/Si chips in 200 μL of either DMEM or RPMI 1640 media for 48 h. U87 and NIH 3T3 cells cultured on tissue culture polystyrene (TCP) in complete medium (10% FBS, 1% pen/strep) for 24 h were then exposed to ZnO NWs conditioned media for 48 h and imaged under optical microscope at 0, 24, and 48 h to observe cell spreading (Figure 1B). Additionally, to determine whether the presence of SWCNTs affected cell viability in ZnO NWs conditioned media, and to exclude the possibility that the SWCNTs presence was affecting cell spreading/viability, cells were cultured on SiO_2/Si chips for the reference (as control) and SWCNTs grown on SiO_2/Si chips and positioned in the wells of multi-well plates. At 24 and 48 h, both the cells that were on the well bottom (in the same well plates as SiO_2/Si chips and SWCNTs; labeled as TCP) and the cells on top of the SiO_2/Si chips and SWCNTs were imaged. Images of cells on TCP (on the well bottom) were taken through an inverted microscope (Zeiss, Axiovert 200M, Oberkochen, Baden-Württemberg, Germany). Cells on the SiO_2/Si chips and SWCNTs were stained with 4 μM of EthD-1 and 2 μM Calcein AM for 30 min at 37 °C and imaged with an upright fluorescent microscope as described above. Cell viability was calculated via Eq. 2.

Dynamic light scattering (DLS; Malvern Panalytical, Zetasizer Nano ZS, Malvern, United Kingdom) analysis was performed for the conditioned media to determine whether ZnO NW particulates were released in the medium during soaking. Particulate size was compared between conditioned and unconditioned media.

2.9 Zn^{2+} concentration determination in conditioned media

Conditioned media analyses were performed on ZnO NWs and ZnO NWs/SWCNTs samples grown by CVD on SiO_2/Si before and after they were soaked in media. A total of 6 samples were tested, 4 of which were ZnO NWs and 2 samples were ZnO NWs/SWCNTs heterostructures. The Zn^{2+} concentration in the cell media released from the ZnO NWs was approximated as follows: the average number of ZnO NWs were calculated per unit area of the samples/chips such as ZnO NWs/SiO_2/Si and ZnO NWs/SWCNTs/SiO_2/Si, using SEM imaging. Average length and diameter of the NWs were also determined from SEM images, thus providing us with the unit of measure of an average estimated volume of the ZnO materials to further determine the concentration of Zn^{2+} ions in each medium. For consistency, SEM images of all samples were processed in the same way: dividing each chip into three-by-three quadrants, thus analyzing nine regions. In accordance with the experimental details above, the nanomaterials were soaked in complete cell media for 48 h before being dried and reimaged in the same quadrants as before. SEM image files were imported into MATLAB and ImageJ software was used to evaluate percent coverage. The amount of material before and after dissolution was compared and from there, the percent dissolution of ZnO was estimated.

2.10 Statistical analysis

Data points are shown as average ± standard deviations from 3 independent experiments with up to 3 samples per experiment. For cell analysis from microscopy images, multiple images were taken per sample and up to 150 cells were analyzed per condition. When testing for statistical difference between experimental conditions, GraphPad Prism software was utilized to conduct two-wailed t-tests between 2 conditions, and a one-way ANOVA with *post hoc* Tukey test to compare greater than 2 conditions. Significance is reported as $p < 0.05$.

3 Results

3.1 Nanomaterial characterization

Nanomaterials undergo significant morphological changes upon incorporation into heterostructures, necessitating precise characterization to quantify their quality and morphology alterations. This study employed SEM imaging to verify the morphology of individual nanomaterial components. SWCNTs grew horizontally as monolayers, exhibiting lengths ranging from 2.6 to 17.6 μm (Figure 2A). On the other hand, ZnO NWs grew preferentially in vertical orientations in densely packed arrangements resembling forests. The length and diameter of ZnO NWs ranged from 0.9 to 3.2 μm and 47.3–99.2 nm, respectively (Figure 2B; Supplementary Figure S1A, B). The percentage coverage of SWCNTs on SiO_2/Si was observed to trend lower than that of ZnO NWs and the heterostructures. This phenomenon could be attributed to the fact that some

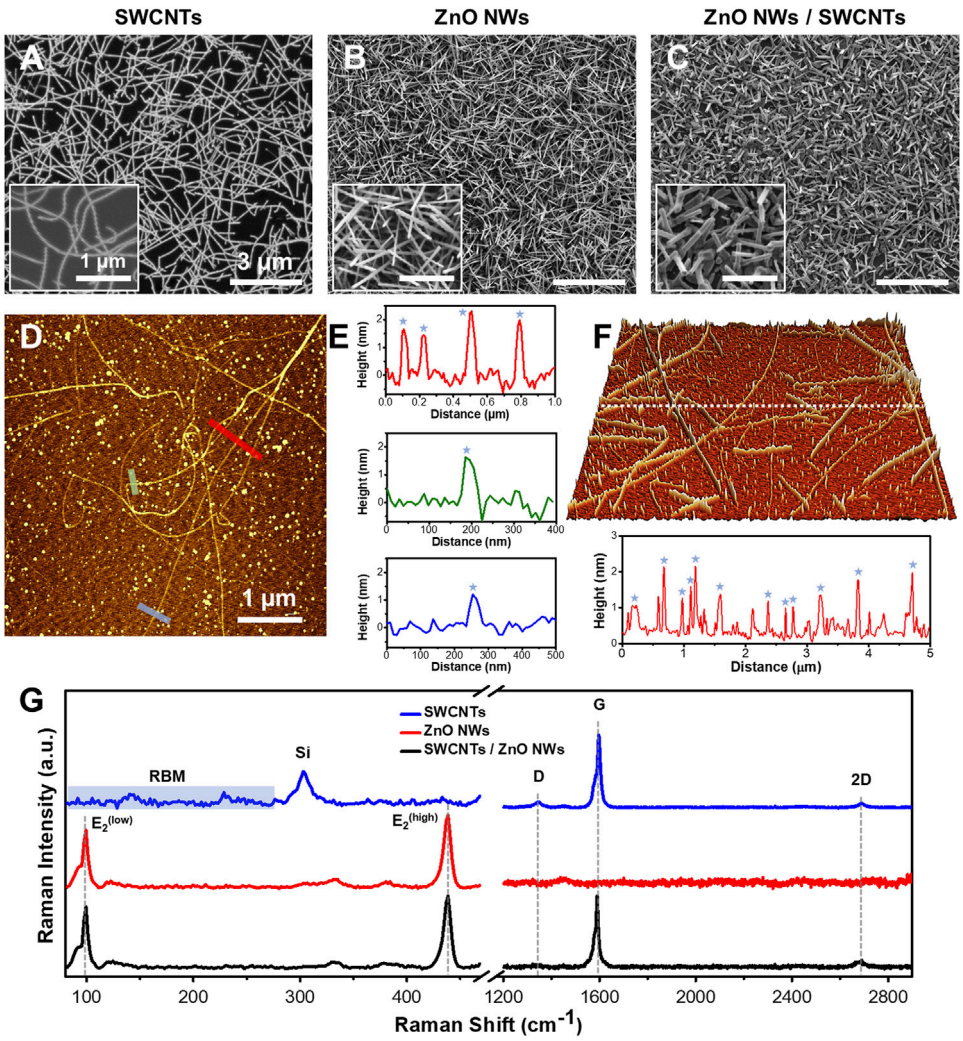

FIGURE 2
SEM, AFM, and Raman of SWCNTs, ZnO NWs, and SWCNTs/ZnO NWs heterostructures. SEM images of **(A)** SWCNTs, **(B)** ZnO NWs, and **(C)** SWCNTs/ZnO NWs heterostructures on SiO_2/Si substrate demonstrating uniformity and high density. Scale = 3 µm. Insets are high-magnification SEM images of each sample. Scale = 1 µm. **(D)** AFM image of SWCNTs with **(E)** line profiles showing the height of the SWCNTs (blue star) at the specified color-coded locations. **(F)** 3D AFM topographic image (for a 5x5 µm square area) of SWCNTs grown on SiO_2/Si substrate with a line profile shown below. **(G)** Raman spectral plots of representative spots on each sample of each nanomaterial featuring G and D and 2D bands for SWCNTs presence and the E_2^{low} and E_2^{high} peaks for ZnO NWs presence. RBM modes in the SWCNTs Raman plot can also be seen at the low-frequency range.

catalytic particles (as seen Figures 2D, F) did not participate in SWCNTs growth but would have been reactivated during ZnO NWs to nucleate ZnO NWs. Furthermore, in the fabricated heterostructures, consisting of ZnO NWs grown on SWCNTs, only the ZnO NWs were discernible (Figure 2C), underscoring the successful integration of the two nanomaterial components into a heterostructure configuration. The length and diameter of ZnO NWs grown on SWCNTs ranged from 0.5 to 1.5 and 66.5–133.5 nm, respectively (Supplementary Figures S1C, D).

The contact angles measurements conducted on the surfaces of the nanomaterials were conducted to evaluate their surface wettability (Supplementary Figure S2). The reported values represent averaged values from six samples. The average contact angles of SWCNTs, ZnO NWs, and ZnO NWs/SWCNTs were determined to be 79.5°, 119.6°, and 128.5°, respectively. Notably, ZnO NWs and ZnO NWs/SWCNTs values can be categorized as hydrophobic, attributed to their high aspect ratio, vertical orientation, and subsequently inherent high surface roughness (Mohammad Karim, 2023). Further, wettability of ZnO NWs is contingent upon the crystallographic orientation of the NWs where the surface of ZnO can be categorized as polar and non-polar (Mardosaitė et al., 2021). The nonpolar facets exhibit low surface energy, thus facilitating the contraction of liquid droplets, while the polar facets exhibit high surface energy and facilitate liquid spreading (Ghannam et al., 2019; Mardosaitė et al., 2021). We have previously characterized our CVD-grown ZnO NWs using X-ray diffraction and showed that they exhibit predominantly non-polar facet termination (Alameri et al., 2017a), thus suggesting that our samples could have tendencies towards hydrophobicity. The observed lower values of the contact angle for the SWCNTs can be attributed to the lower surface coverage and flat surface morphology. Moreover, the areas of the SiO_2/Si surface that were not covered by SWCNTs contributed to more hydrophilic manifestations as compared to the densely packed ZnO NWs samples.

The representative AFM image (Figure 2D) obtained on SiO_2/Si substrates reveals the diameter distribution of SWCNTs within the 1.7–2.2 nm range, as depicted in three topographic line profiles (Figure 2E). The SWCNTs diameters are denoted by stars in the line profiles, while other discernible peaks correspond to nanocatalyst particles that have aggregated during the growth process. These observations corroborate the predominantly single-walled composition of the SWCNTs. In Figure 2F, a 3D-AFM image acquired from another sample and the line profile shown below showed a sub-nanometer roughness of 0.62 nm root mean square (RMS) value. The diameter distribution also confirms the typical range from 1.2 to 2.25 nm for SWCNTs. Notably, all measured diameters of the SWCNTs remained consistent, affirming the uniformity of SWCNTs across different samples. Note that the AFM analysis also revealed the presence of the aggregated larger nano-catalyst particles on the SWCNTs samples, which were likely participating in a nucleation process of the ZnO NWs in the subsequent heterostructure formation. As a result, the average diameter of ZnO NWs grown on top of the SWCNTs within the heterostructure were larger, as compared to ZnO NWs sample grown directly on SiO_2/Si substrates, as seen in the SEM images in Supplementary Figure S1.

The quality of the nanomaterials was assessed by Raman spectroscopy (Figure 2G). SWCNTs have unique Raman signals in the radial breathing mode (RBM) (~100–350 cm^{-1}), the D-band (~1,350 cm^{-1}), and the G-band (~1,580 cm^{-1}). It was found from the RBM Raman shifts that the diameters of the SWCNTs were between 1.7 and 2.3 nm, which also confirms our direct AFM measurement results (Jorio et al., 2001) In addition, Raman data show the full width at half maximum (FWHM) of the G-band, of the SWCNTs was in the range of 18–21 cm^{-1} for both samples, namely, SWCNTs and ZnO NWs/SWCNTs, indicative of high crystallinity. At the same time the G- and D-band intensity ratio (I_G/I_D) was found to be in the range of 10–25 (Alameri et al., 2017b). These results are evidentiary of the high quality of the SWCNTs. It also verifies that SWCNTs are not being compromised (no defects were created) during the growth of the ZnO NWs on top of the SWCNTs in the process of the heterostructure formation. ZnO NWs also display characteristic Raman spectra, which respectively allow us to evaluate their quality and crystallinity. ZnO NWs have wurtzite crystal structure (Geng et al., 2004; Zhu et al., 2012; Al-Asadi et al., 2017). The lattice optical phonon with A_1, E_1, and E_2 being most Raman active. E_2 mode shows the crystallinity level of as-grown ZnO NWs. Raman spectra of representative positions show high-intensity modes for E_2^{low} and E_2^{high} (98.7 and 436.9 cm^{-1}), which are associated with Zn and O_2 sublattices, respectively. The FWHM of the most intense E_2^{high} peak in the Raman spectra of ZnO NWs and ZnO NWs/SWCNTs is ~7.6 cm^{-1}, indicating a high level of crystallinity in both cases. Raman spectra collected from the heterostructure samples show SWCNTs and ZnO NWs characteristic main peaks and demonstrate preserved integrity of both materials.

3.2 Cell spreading and viability on SWCNTs, ZnO NWs, and ZnO NWs/SWCNTs

To study the effects of SWCNTs, ZnO NWs, and ZnO NWs/SWCNTs on cell area, shape factor, and viability, U87 glioblastoma cells and NIH 3T3 fibroblast cells were used. The cells were chosen as the model cells for a commonly used cancer cell type (U87 cells) and a commonly used normal cell type (NIH 3T3) to capture possible differing effects of the nanomaterials on normal vs. cancer cells. U87 glioblastoma cells were chosen for this study due to previous studies indicating ZnO nanostructure suppression of glioblastoma tumor cell viability (Wahab et al., 2011; Zhu et al., 2012). NIH 3T3 fibroblast cells have also been commonly used for *in vitro* toxicity studies, due to being the most abundant cell types within all connective tissues (Boncler et al., 2019).

Cell spreading and circularity as a function of nanomaterial composition were similar for both cell types (Figure 3). For both U87 and NIH 3T3 cells, we noted decrease in cell spreading and increase in cell circularity for cells on the ZnO NW and the ZnO NWs/SWCNTs heterostructures compared to all other conditions, possibly indicating ZnO cytotoxicity or inability to support cell spreading. There was no significant difference between cell spreading or circularity on the ZnO NWs or ZnO NWs/SWCNTs, indicating that the effect of ZnO NWs was dominant. This was not surprising, since the ZnO NWs were grown on top of the SWCNTs, so it is possible that cells were only able to sense the ZnO NWs due to direct contact mostly with the ZnO NWs layer. For both cell types seeded on ZnO NWs and ZnO NWs/SWCNTs we observed a significant ~2-fold decrease in cell area and ~2-fold increase in circularity as compared to cells on SWCTNs or control samples/chips. For both cell types, spreading area was highest on the SWCNTs, and it was significantly higher than the controls for U87 cells. This was also expected as we and others have previously shown that SWCNTs facilitate cell spreading (Imaninezhad et al., 2018).

Live/dead staining for U87 and NIH 3T3 showed more live cells with elongated morphologies on SiO_2/Sicontrols and SWCNTs compared to ZnO NWs or ZnO NWs/SWCNTs heterostructures (Figure 4). The higher cell viability for cells on control SiO_2/Si control samples/chips and SWCNTs, compared to ZnO NWs and ZnO NWs/SWCNTs corroborated the cell spreading data, indicating that decreased cell spreading could be due to decreased cell viability. For both cell types, there was no significant difference between cell viability on SiO_2/Si chips and SWCNTs, with viability being >80% for all conditions. On ZnO NWs and ZnO NWs/SWCNTs, U87 cell viability decreased to ~25%, and for NIH 3T3 cells it decreased even further to ~6%.

3.3 Cell filopodia on SWCNTs, ZnO NWs, and ZnO NWs/SWCNTs

Upon closer observation of the cells through SEM imaging, we were able to qualitatively observe cell filopodia on each nanostructure, albeit with some pronounced differences between conditions. For U87 cells (Figure 5A), cells extended long and dense filopodia on the SiO_2/Si controls and SWCNTs, with an evident decrease in filopodia length and density for cells on ZnO NWs and ZnO NWs/SWCNTs. Similar observations were made for NIH 3T3 cells, where cells on the SWCNTs seemed to have denser and longer filopodia than cells on the control SiO_2/Si, and both were higher than the ZnO NWs and ZnO NWs/SWCNTs (Figure 5B). By quantifying the lengths of filopodia from cells for

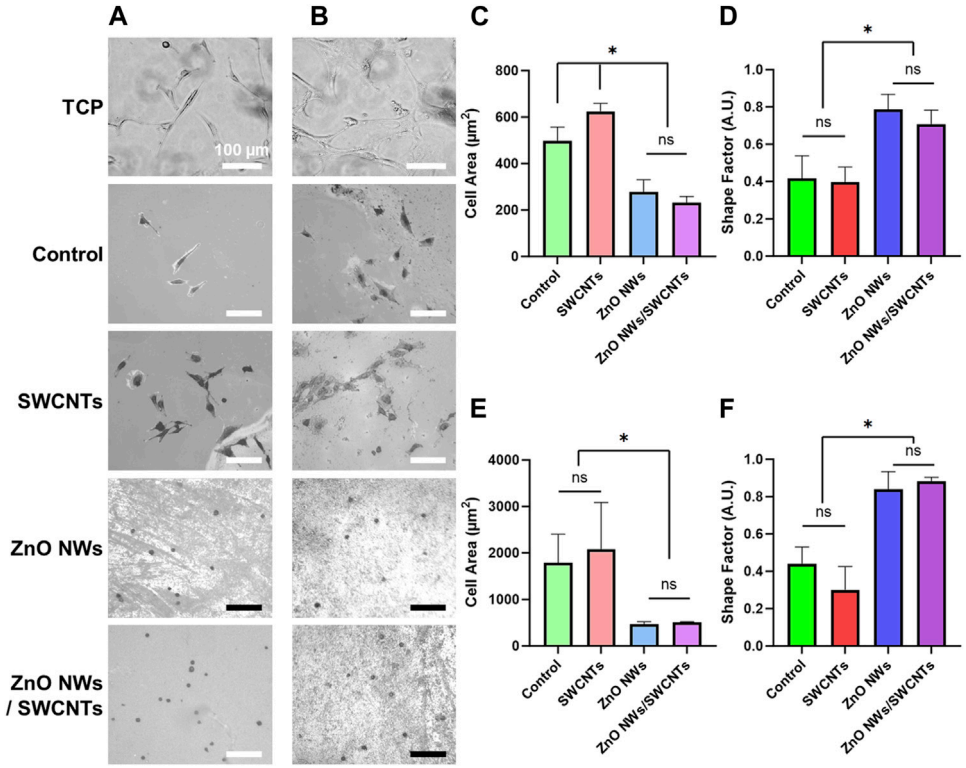

FIGURE 3
NIH 3T3 and U87 cell area and shape factor on TCP, SiO_2/Si control/reference samples (Control), SWCNTs, ZnO NWs, and ZnO NWs/SWCNTs at 24 h of culture. **(A)** Phase contrast microscopy images of NIH 3T3 cells and **(B)** U87 cells on each nanomaterial as well as SiO_2/Si control samples/chips (Control) without nanomaterials and tissue culture polystyrene (TCP). Scale bar = 100 µm. **(C)** Cell area and **(D)** Shape factor of NIH 3T3 cells as a function of nanomaterial composition. **(E)** Cell area and **(F)** Shape factor for U87 cells as a function of nanomaterial composition. * designates significant differences (n = 6 for NIH 3T3, n = 3 for U87, $p < 0.05$).

each condition, it was found that cells on SWCNTs generally had longer filopodia than all other conditions. The most noticeable difference was the increase of filopodia lengths of NIH 3T3 cells on SWCNT, compared to the control SiO_2/Si (Figure 5C). NIH 3T3 filopodia on SWCNTs were an average of 24.7 µm, which was much larger than filopodia averages of 2.0 and 3.3 µm on ZnO NWs, and ZnO NWs/SWCNTs, respectively. Note that due to vastly divergent dimensions, it was challenging to show high resolution images for both cells and cell filopodia and the underlying SWCNTs; hence, separate images with the focus adjusted to show the underlying SWCNTs is shown in Supplementary Figure S3. Lastly, filopodia lengths were lowest for ZnO NWs and ZnO NWs/SWCNTs for both cell types.

Though cell area decreased, and shape factor increased on nanomaterials containing ZnO NWs, for both NIH 3T3 and U87 cells, there was still filopodia extensions on the ZnO NWs. Upon closer inspection, NIH 3T3 cells in areas of varying ZnO NWs density had different filopodia numbers and length. On areas of highest ZnO NWs density, there were short but numerous filopodia extending from the cells. On areas of lesser ZnO NWs density, the cells had fewer filopodia, and decreased cell area. For areas of the least ZnO NWs density, the cells did not seem to extend filopodia and had a round morphology (Supplementary Figure S4). This data suggests that though NIH 3T3 fibroblasts and U87 glioma cells show decreased proliferation and cell area on ZnO NWs, they still can interact with the ZnO NWs, perhaps in a density dependent manner.

3.4 ZnO NWs conditioned media effect on NIH 3T3 and U87 cell spreading and viability

Due to the decreased cell area and increased shape factor, as well as decreased viability for ZnO NWs and heterostructures, we sought to further study ZnO NWs' toxicity to U87 and NIH 3T3 cells by exposing them to ZnO NW conditioned media. We characterized the conditioned media via DLS and compared it to non-conditioned media. DLS analysis of the ZnO NWs conditioned media showed that particle sizes in the media were similar to the unconditioned media (Supplementary Figure S5), suggesting that there are no agglomerated or nano-or micro-size particles from the ZnO NWs. This data implies that the toxic effect from the ZnO NWs conditioned media should be from soluble/degradation compounds, such as ions, released in the media, rather than NWs structures or particulates being released from the ZnO NWs/SiO_2/Si samples.

To test the effect of ZnO NWs releasates on cells, we first cultured cells on TCP and then exposed them to ZnO NWs conditioned or non-conditioned media for 48 h (Figure 6). After exposing U87 cells to ZnO NWs conditioned media, cell area

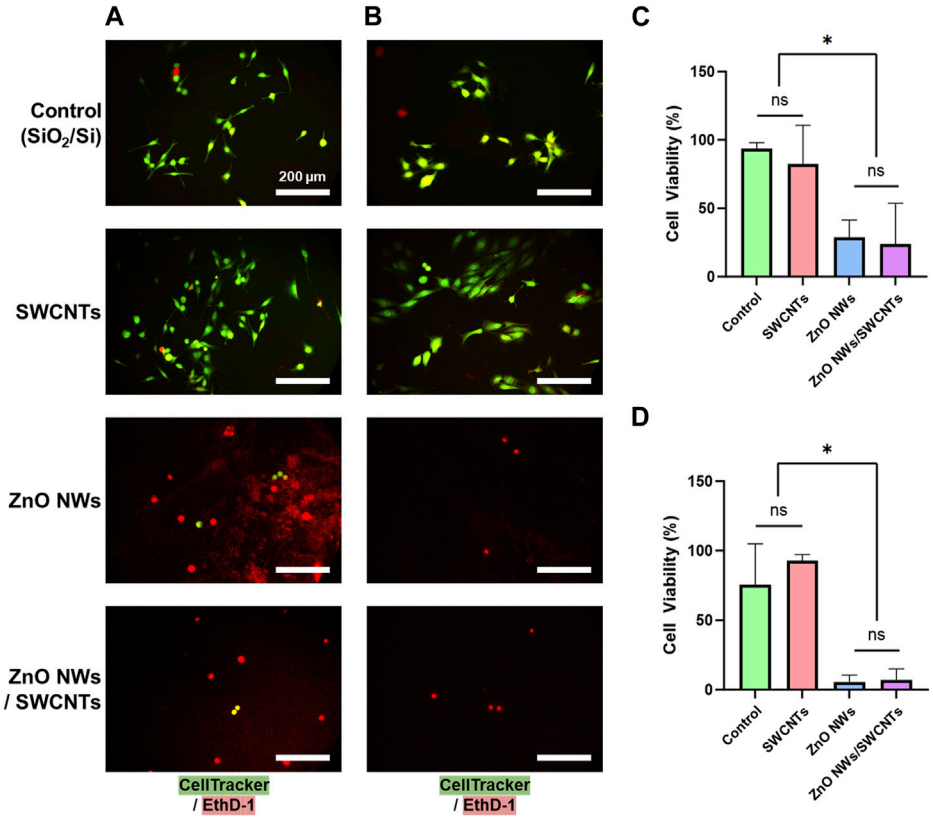

FIGURE 4
NIH 3T3 and U87 cell viability on SiO_2/Si reference/control samples (Control) and nanomaterial; SWCNTs, ZnO NWs, and ZnO NWs/SWCNTs. **(A)** Fluorescence microscopy images of U87 cells on nanomaterials. **(B)** Fluorescence microscopy images of NIH 3T3 cells on nanomaterials. Green = Calcein AM (stains live cells), Red = EthD-1 (stains nuclei of dead cells). Scale bar = 200 µm. **(C)** U87 cell and **(D)** NIH 3T3 cell viability on each nanomaterial as calculated from live/dead staining. * designates significant differences (n = 3, $p < 0.05$).

noticeably decreased after 24 and 48 h of exposure (Figures 6A, B). The shape factor of U87 cells at 48 h with non-conditioned growth media was an average of 0.30 ± 0.05, while U87 cells at 48 h exposure to conditioned media was much higher, at 0.70 ± 0.08, indicative of a round morphology (Figure 6C). NIH 3T3 cells also significantly decreased in cell area with exposure to conditioned media after 48 h (Figure 6D). Cells with non-conditioned media on TCP had an average area of 1,100.1 ± 103.2 µm^2, while cells on TCP exposed to conditioned media had an average cell area of 379.0 ± 46.9 µm^2 (Figure 6E). As seen in Figure 6F, the shape factor had also decreased at 24 and 48 h. At 48 h, the shape factor of NIH 3T3 cells on TCP with growth media was an average of 0.34 ± 0.06, while cells exposed to conditioned media had an increased shape factor to 0.73 ± 0.05 (Figure 6F).

Overall, both cell types experienced similar changes in spreading and morphology when exposed to ZnO NWs conditioned media for 48 h. Compared to non-conditioned media, we noted a significant decrease in cell spreading area and a significant increase in shape factor for both U87 and NIH 3T3 cells, showing that while cells were well spread and elongated in non-conditioned media, they were round in conditioned media indicating toxicity.

In addition to cultured cells on TCP, we also examined the effect of ZnO NWs conditioned media towards cells cultured on the SiO_2/Si control samples and on the SWCNTs samples to determine whether those substrates provided rescue towards cell viability and spreading (Figure 7). Corroborating TCP results at 48 h of exposure, U87 and NIH 3T3 cells showed significantly decreased cell areas and increased shape factor (i.e., round morphology) compared to unconditioned media for both cells on SiO_2/Si controls and on SWCNTs (Figures 7A, C). Also, qualitative evaluation showed a substantially decreased cell presence for both cell types when exposed to ZnO NWs conditioned media independent of the growth substrate, indicative of toxicity.

We further used live/dead staining of U87 and NIH 3T3 cells to investigate cell viability. U87 cells visually decreased in cell number and had a higher ratio of EthD-1-stained dead cells when exposed to ZnO NW conditioned media (Figures 7A, C). U87 cells on the SiO_2/Si controls and on the SWCNTs/SiO_2/Si samples had high viability of 88.1% ± 4.1% and 91.4% ± 5.5%, respectively. U87 cells on the controls and on the SWCNTs samples showed decreased cell viability when exposed to conditioned media, by 16.2-fold and 4.3, respectively. The cell viability on the control sample was 81.6% ± 11.6% and on SWCNTs it was 96.6% ± 1.8% (Figure 7B). This pattern was also seen for NIH 3T3 cells, where cell viability on the control conditioned media, cell viability decreased 3.6-fold and 3.2-fold for cells on SiO_2/Si controls and SWCNTs samples, respectively (Figure 7D). Similarly to U87 and NIH 3T3 cells cultured on SiO_2/Si controls and the SWCNTs

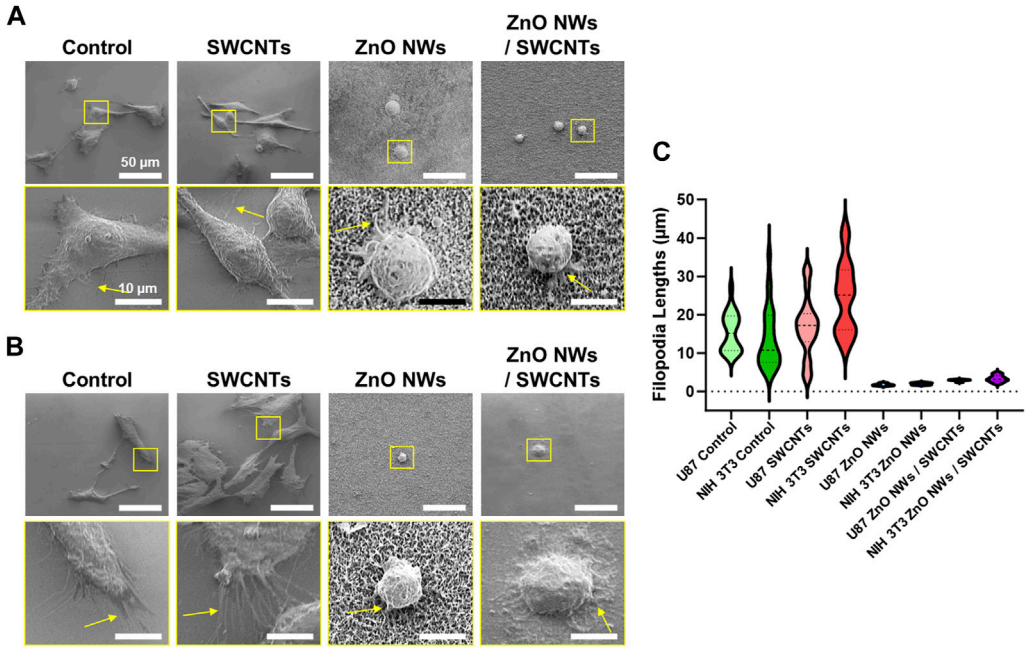

FIGURE 5
Cell filopodia characterization on SiO_2/Si reference/control samples (Control), as well SWCNTs, ZnO NWs, and ZnO NWs/SWCNTs. Cells were cultured for 24 h on each substrate. **(A)** SEM images of U87 cells on each nanomaterial, with the corresponding zoomed-in insets to observe the filopodia. Scale = 50 µm and 10 µm, respectively. **(B)** NIH 3T3 cells on top of each nanomaterial, with zoomed in insets to observe the filopodia. Scale = 50 µm. **(C)** Filopodia lengths for each condition.

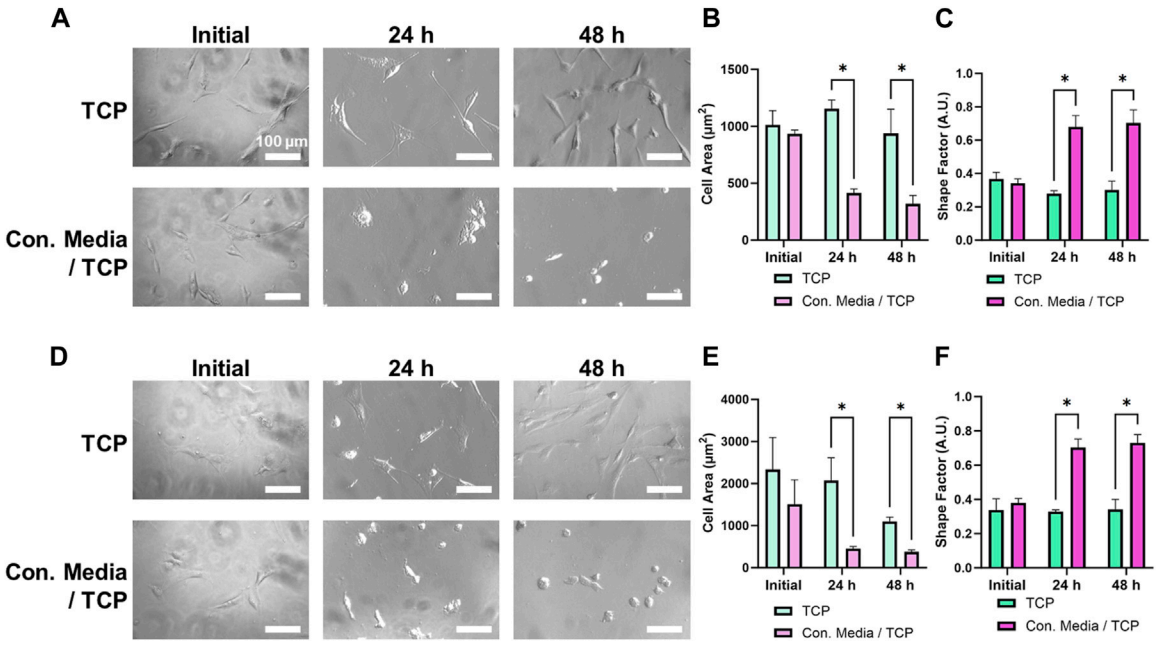

FIGURE 6
U87 and NIH 3T3 cells cultured on TCP for 24 h, then exposed to conditioned media for 48 h. **(A)** Phase contrast images of U87 cells on TCP exposed to non-conditioned or conditioned media. Scale bar = 100 µm. U87 cell area **(B)** and shape factor **(C)** as a function of media conditioning. **(D)** Phase contrast images of NIH 3T3 cells on TCP exposed to non-conditioned or conditioned media. Scale bar = 100 µm. NIH 3T3 cell area **(E)** and shape factor **(F)** as a function of media conditioning. * designates significant differences (n = 3, $p < 0.05$).

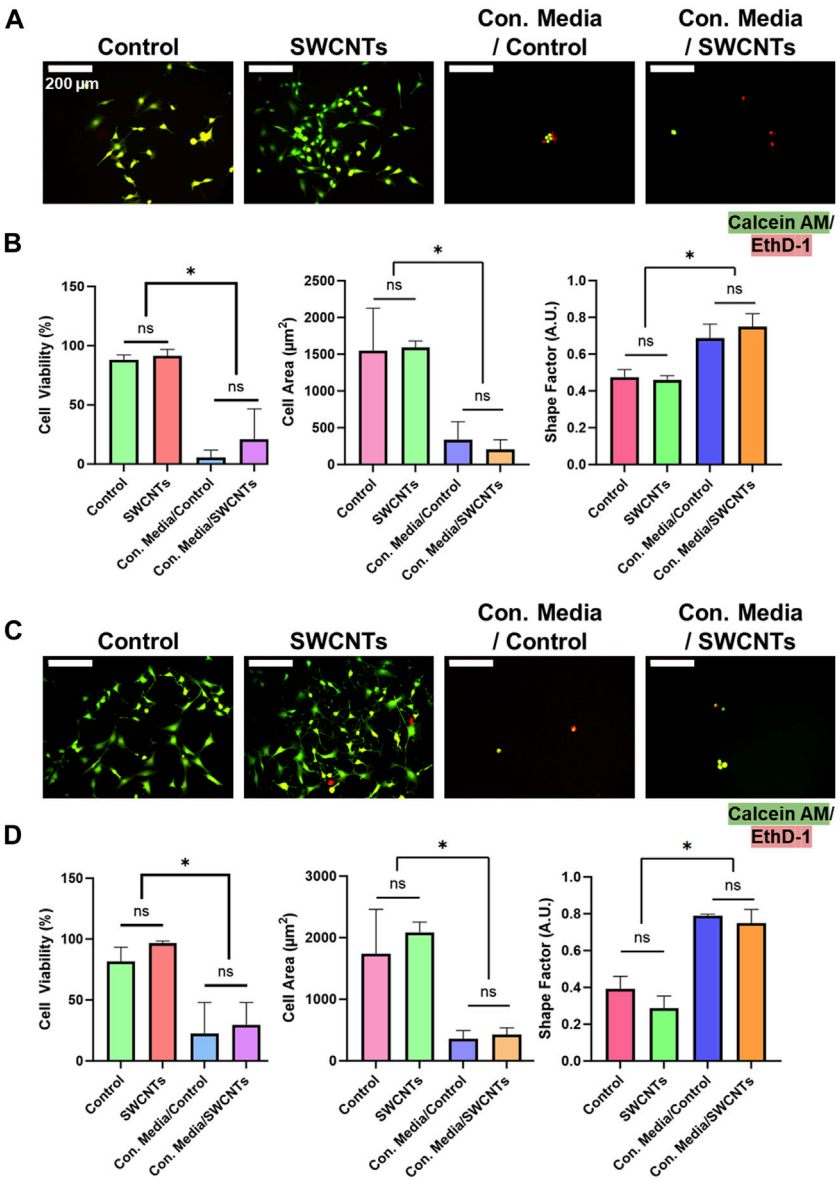

FIGURE 7
NIH 3T3 and U87 cell viability, area, and shape factor on SiO_2/Si control samples (Control) and SWCNTs, when exposed to conditioned media for 48 h. **(A)** Fluorescence microscopy images of U87 cells on nanomaterials. Green = Calcein AM (stains live cells), Red = EthD-1 (stains nuclei of dead cells). Scale bar = 200 µm. **(B)** U87 cell viability, area and shape factor when exposed to ZnO NWs conditioned media on Control and SWCNTs. **(C)** Fluorescence microscopy images of NIH 3T3 cells on nanomaterials. Scale bar = 200 µm. **(D)** NIH 3T3 cell viability, area and shape factor when exposed to ZnO NWs conditioned media on the SWCNTs and Control samples. * designates significant differences (n = 3, $p < 0.05$).

samples, cells that were found in the TCP wells next to the substrates with nanomaterials on them, showed reduced viability when exposed to ZnO NWs conditioned media (Supplementary Figure S6). This result indicated that any loss in cell viability was not due to the underlying substrate (the SiO_2/Si or the SWCNTs), but only the conditioned media.

Previous studies (Li et al., 2011; Liao et al., 2020) have indicated that the cytotoxicity of ZnO nanomaterials may be attributed to the dissolution of Zn^{2+} from the materials, potentially leading to adverse effects upon cellular uptake. To investigate this, the Zn^{2+} concentration in the cell media was estimated using average length/diameter and the surface coverage data provided by high resolution SEM images. Supplementary Table S1 shows the calculated concentration of Zn^{2+} ions to be in the range of 2.3–10.2 µg/mL for the ZnO NWs samples soaked in RPMI compared to a similar range of 2.8–10.2 µg/mL when soaked in DMEM, hence, there is not a significant difference between the two media types used for cell culture. However, for the ZnO NWs/SWCNTs heterostructure samples soaked in RPMI, concentration of Zn^{2+} ions ranged from 1.3–4.6 µg/mL, and for the heterostructures soaked in DMEM, Zn^{2+} ion concentration ranged from 1.5–5.2 µg/mL Although there appears to be no difference in dissolution across the 2 cell medias, there is a clear lower dissolution in the case of

ZnO NWs/SWCNTs heterostructure samples as compared to the solely ZnO NWs.

4 Discussion

In this study we used CVD synthesis to fabricate high quality nanomaterials such as SWCNTs, ZnO NWs and the heterostructures ZnO NWs/SWCNTs on SiO_2/Si substrates with controlled morphology (Figures 1, 2) to examine behaviors of two different cell lines, namely, U87 glioblastoma and NIH 3T3 fibroblast cells, chosen to represent both a cancerous and a normal cell type. While the 2 cell types are representative, a more comprehensive cell panel could be tested in the future to broaden our understanding of cell-nanomaterial interactions. One-dimensional nanomaterial prepared either in lateral monolayer networks (such as SWCNTs) or vertically oriented forests (such as ZnO NWs) have unique biomedical relevance. Heterostructures made from these one-dimensional nanomaterials can add additional versatility in creating compound platforms with dual purposes in biomedical applications. The goal was to study cell viability, spreading, and morphology on top of the SWCNTs, ZnO NWs, and their heterostructure to gain knowledge on the suitability of the nanomaterials as cell substrates or testbeds. While there are multitude of studies of cell behaviors on SWCNTs including by our team, there have been fewer studies involving highly crystalline ZnO NWs. On the other hand, heterostructures of ZnO NWs/SWCNTs have not been explored. Additionally, there are conflicting reports on the toxicity of ZnO. For example, ZnO NWs have been shown as a promising neuronal substrate (Onesto et al., 2019), while ZnO nanorods have been shown to resist cell adhesion (Lee et al., 2008), and yet others have shown that ZnO in the form of a flat film, nanorods or nanowires is toxic to cells (Ghaffari et al., 2019).

In our study we showed that cells cultured onto ZnO NWs and ZnO NWs/SWCNTs decreased in cell area and became more circular, which also corresponded to a significant decrease in cell viability (Figures 3, 4). Our results corroborate a study that observed that NIH 3T3 cells do not have initial spreading on ZnO NWs, nor filopodia formation, due to the inability of cells to adhere to the nanowire substrates and the effects of substrate surface on cell growth (Lee et al., 2008). Another study found that the presence of ZnO NWs, along with toxic by-products after longer periods of culture, may slow down initial cell adhesion and growth rate (Gaetani et al., 2022).

For cells on SWCNTs, we noted larger cell spreading and smaller shape factors. Cell spreading on the SWCNTs is dependent on cell integrin binding facilitated by adsorption of serum and cell-secreted adhesive proteins onto the SWCNTs, as shown by us previously (Imaninezhad et al., 2018). Furthermore, integrin attachment enhances the signaling of growth factors, to which then FAK acts as a downstream target. FAK plays an important role in cell migration, adhesion and regulation for U87 and NIH 3T3 cells (Riemenschneider et al., 2005). Note that while some literature, where nano-powder SWCNTs were used, suggests that SWCNTs are suppressive towards U87 glioblastoma cells (Minchenko et al., 2016), this was not the case in this study as discussed above. This may be due to the fact that cells were grown on top of the CVD-synthesized SWCNTs networks which are attached to the growth substates, and not in media with dispersed SWCNTs powders, as reported in other studies. Here, the as-grown SWCNTs were attached (prepared directly) onto the SiO_2/Si substrate, hence not available for cell endocytosis due to their strong van der Waals attraction to the SiO_2/Si growth substrate (Dai et al., 2001).

On further examining cell morphology, we noted that NIH 3T3 filopodia on SWCNTs were an average of 24.7 μm, which was significantly larger than filopodia averages of 2.0 μm and 3.3 μm on ZnO NWs, and ZnO NWs/SWCNTs, respectively (Figure 5). Fibroblasts also favor probing rigid substrates with filopodia extensions before migration (Wong et al., 2014), hence the larger filopodia length on the SWCNTs was indicative of a more favorable substrate for cell adhesion and migration compared to ZnO NWs. This could also be due to a flatter (nanotextured) surface of the SWCNTs networks-bed as compared to a more 'spiky' ZnO NWs forest interfaces. While both cell types exhibited longer filopodia on the SWCNTs compared to the other nanomaterials, NIH 3T3 fibroblasts had overall more elongated morphology than the U87 cells, which had a more epithelial-like shape (Supplementary Figure S3).

We then aimed to determine whether the lower cell viability and spreading on the ZnO NWs and ZnO NWs/SWCNTs heterostructure was due to the vertical and 'spiky' morphology of the ZnO NWs or due to NWs degradation products. Others have previously shown that cells, specifically neural-like PC12 cells, could extend filopodia, spread and retain high cell viability on vertical collagen-coated ZnO NWs (Ciofani et al., 2012). Beyond ZnO, significant previous research on vertical NW arrays has shown not only that cells can adhere and grow on vertical arrays, but that NW density and diameter can be used to control cell adhesion, morphology, motility, and differentiation (Qi et al., 2009; Persson et al., 2015; Li et al., 2018). For example, breast cancer cells showed an overall lower cell areas and larger focal adhesions at the cell edges for lower diameter NWs compared to higher spreading areas and punctate focal adhesions on larger diameter NWs (Li et al., 2018). Further, increased NW density was shown to increase motility of fibroblasts, but a reduced cell proliferation was noted irrespective of NW density (Persson et al., 2015). Another study of human hepatic and hepatoma cell lines showed that vertical NWs supported cell adhesion and growth and enhanced cell-substrate adhesion force, but restricted cell spreading. The authors attributed the lower cell spreading area on the spiky morphology of the nanowires, where cells were able to extend filopodia and form focal adhesions initially, but were not able to reach out at a distance from their first contact point (Qi et al., 2009).

Hence, we hypothesized that the spiky morphology might be responsible for the lower cell spreading, but it should not be responsible for the lower cell viability. To test for that we used ZnO NW-conditioned media (ZnO NWs soaked in media for up to 48 h) on cells seeded on TCP only or on TCP in the presence of SWCNTs (Figures 6, 7). ZnO NWs have been reported to initiate degradation in ~30 min, which results in the release Zn^{2+} ions (Milano et al., 2018). With the released Zn^{2+} ions, the ZnO NWs may generate reactive oxygen species (ROS). In turn, these compounds may cause cytotoxic cellular effects that include intracellular calcium flux, mitochondrial depolarization, and plasma membrane leakage (George et al., 2010). Therefore,

decreased cell area with ZnO NWs conditioned media may be attributed to the cytotoxic effects from soluble compounds present in the media, which is what our data indicated. Another study on ZnO NWs conditioned media found that cytotoxicity was occurring due to accumulation of by-products from ZnO NWs with 3 days of incubation in 1 mL of medium per sample area of 1 cm^2. In addition to a decrease in cell survival, cells on ZnO NWs retained round morphology, which pointed towards poor cell adhesion (Gaetani et al., 2022). This may also explain the decrease in cell counts for cells in conditioned media and on structures including ZnO NWs, since cells may have been washed off during handling for fixation and live/dead staining.

From the dissolution analysis, it was determined that regardless of whether the medium was RPMI or DMEM, the medium containing the ZnO NWs samples had an approximate Zn^{2+} concentration ranging from 2.3 μg/mL to 10.2 μg/mL (as shown in Supplementary Table S1). Our results seem to be in line with the previously reported studies, which state that at similar concentrations the medium showed to be toxic (Liao et al., 2020). Previous studies have also shown that Zn^{2+} ions released from ZnO structures were responsible for PC12 neural-like cell death, regardless of whether the ZnO were nanorods, nanowires or solid thin films (Ghaffari et al., 2019). The medium containing the ZnO NWs/SWCNTs heterostructures had slightly lower Zn^{2+} ion concentration ranging from 1.3 μg/mL to 5.2 μg/mL. The lower dissolution could potentially be attributed to the enhanced interaction between the ZnO NWs with the SWCNTs networks due to a direct synthesis of one material on top of another. On the other hand, the presence of the SWCNTs could also effectively increase the hydrophobic surface area, thus decreasing the ZnO -solvent interactions.

Overall, our studies indicated that ZnO NWs were not conducive to cell growth for the cell types and growth conditions tested here. This was not due to the inability of cells to adhere to the ZnO NWs or due to their vertically oriented 'spiky' surface topography. In fact, cells were able to extend filopodia on NWs even when they still decreased in spreading area. The filopodia extensions despite the 'spiky' morphology were not surprising as other have shown that cells, specifically neuronal cells, were able to form neuronal networks when grown on ZnO NWs over 7 days (Onesto et al., 2019). The decrease in cell area and cell viability was instead attributed to the release of Zn^{2+} from the nanostructures. While cells were able to spread and retain high viability on SWCNTs as expected, SWCNTs were not able to 'rescue' cell growth in the heterostructures as we had hoped despite decreasing the Zn^{2+} concentration. Note that one limitation to the study was that we used live-dead staining to assess cell viability, so it is possible that some cells were washed off the surface during staining due to weak adhesion (e.g., rounded cells, which might otherwise be alive could not be stained) or due to necrosis (hence dead cells were not stained). Despite that, the decrease in cell spreading and cell presence clearly pointed to the toxic effect of the ZnO NWs on the cells. Despite previous reports on the selective negative effect of ZnO on cancer cells compared to normal cells, we observed similar toxicity for both cell types, possibly because of the high dose of Zn^{2+} ions released in the media due to the high density and volume of the ZnO NWs on which the cells were seeded. Previous studies have shown that the toxicity of ZnO is concentration dependent. For Zn^{2+} concentrations of ~2–10 μg/mL, it was generally being found to be cytotoxic (Liao et al., 2020). Even for the heterostructures which contained a lower Zn^{2+} concentration of ~1–5 μg/mL, this was still found to be in the cytotoxic range (Alameri et al., 2017b). Future investigations focusing on varying densities of ZnO NWs and SWCNTs which could be modulated by growth parameters would be interesting to pursue.

It is important to note that we determined the extracellular Zn^{2+} ions released by ZnO NWs through measuring the ZnO NWs dissolution. Despite finding that the percent dissolution was similar in both DMEM and RPMI media and that the ZnO NWs/SWCNTs samples had less dissolution than ZnO NWs samples, there could be potential interactions with various components in the cell media that could affect cellular uptake of these ions. For example, RPMI has a lower amino acid concentration (~1,000 mg/L) than DMEM (~1,600 mg/L) which has been shown to decrease Zn^{2+} toxicity as the amino acids can complex and effectively remove Zn^{2+}, which would not be detected via our Zn^{2+} concentration determination method (Li et al., 2011). However, with many competing factors present in cell media, it can be hard to predict what the overall effect would be (Li et al., 2011; Li et al., 2013). In future studies, using a fluorescent sensing method to measure the intracellular labile Zn^{2+} can be beneficial in discerning more of the cell media effect (Pratt et al., 2021). Furthermore, measuring the rate of cellular uptake of Zn^{2+} will give more insight into the mechanism behind cell death and whether the morphology of the underlying nanomaterials plays a role in the cellular uptake of these ions.

Altogether, our results have several important implications. They suggest that the surface topography of both SWCNTs (horizontal networks) and ZnO NWs structures (vertically oriented forests) are amenable for use as cell substrates in biomedical applications. The use of SWCNTs and ZnO in biomedical applications needs further investigation and possibly consideration of other nanomaterials such as two-dimensional (2D) graphene (Gr) in combination with patterned 2D ZnO nanostructures which could offer an additional level of local control in preparation of heterostructures and predetermined coverage and amount of ZnO NWs interacting with cells, while as the same time offering an ability to observe selective and localized cell behaviors on patterned vs. unpatented surfaces and substrates. Further investigations should also include a variety of cell types to provide a more comprehensive understanding of nanomaterial-cell interactions as a function of cell type.

Our results indicate that SWCNTs, ZnO NWs, and ZnO NWs/SWCNTs heterostructures could be valuable substrates in future biomedical applications. For example, if SWCNTs are prepared to contain high percentages of CVD grown metallic SWCNTs or multiwalled carbon nanotubes (MWCNTs), which are also predominately metallic, thus having higher thermal and electrical conductivity, then biomedical uses of such systems in heterostructure form could expand its further scope. In particular, the applications could involve effective thermal stimulation of cells or embedding heterostructures into hydrogel matrices or other types of biomaterials used as drug delivery vehicles. Our study indicated that the presence of carbon nanotubes in the heterostructures affected the rate of dissolution of ZnO, therefore further studies using other forms of carbon, such

as 2D graphene or nanodiamond films in the heterostructure assemblies could provide new insights into the nature of carbon - zinc oxide interaction in the cell media environments.

5 Conclusion

Here we used chemical vapor deposition to fabricate substrates with coatings of semiconducting SWCNTs, ZnO NWs and ZnO NWs/SWCNTs heterostructures and investigated their effect on cell viability and spreading for representative normal and cancer cells seeded on top of the nanomaterials. We first confirmed the high quality of the grown nanomaterials by several different methods, including SEM, AFM and Raman spectroscopy. We found that the nanomaterials containing ZnO NWs decreased viability and cell spreading for both U87 and NIH 3T3 fibroblast cell types, even though cells were able to extend filopodia on the ZnO NWs. Further studies of cell viability in ZnO NWs conditioned media, showed that the apparent ZnO NWs toxicity was due to dissolution by-products, such as Zn^{2+} ions released from the nanomaterials, rather than the ZnO NWs surface topography. Our results may inform future uses of SWCNTs, ZnO NWs, and ZnO NWs/SWCNTs heterostructures in biomedical applications.

Data availability statement

The original contributions presented in the study are included in the article/Supplementary Material, further inquiries can be directed to the corresponding authors.

Ethics statement

Ethical approval was not required for the studies on humans in accordance with the local legislation and institutional requirements because only commercially available established cell lines were used.

Author contributions

EL: Formal Analysis, Investigation, Validation, Visualization, Writing–original draft. BA: Formal Analysis, Investigation, Validation, Visualization, Writing–original draft, Writing–review and editing. YK: Formal Analysis, Validation, Visualization, Writing–original draft, Writing–review and editing. ML: Investigation, Validation, Visualization, Writing–review and editing. PJ: Formal Analysis, Writing–review and editing. SZ: Conceptualization, Formal Analysis, Funding acquisition, Methodology, Project administration, Writing–review and editing. IK: Conceptualization, Formal Analysis, Funding acquisition, Methodology, Project administration, Supervision, Writing–review and editing.

Funding

The author(s) declare that financial support was received for the research, authorship, and/or publication of this article. This research was partially supported through a President's Research Fund awarded to IK and SZ from Saint Louis University. IK also acknowledges support of Billiken Boost Program sponsored and funded by the Provost's Office in collaboration with the Faculty Gender Equity Committee, Faculty Fellow for Equity Issues, and the Division of Diversity and Innovative Community Engagement. The research was also partially funded through two ILEX funds awarded to EL and ML from the Honors Program at Saint Louis University.

Acknowledgments

The authors acknowledge Dr. Alaina Baker-Nigh for access to and assistance with an upright fluorescent microscope for cell imaging studies.

Conflict of interest

The authors declare that the research was conducted in the absence of any commercial or financial relationships that could be construed as a potential conflict of interest.

The author(s) declared that they were an editorial board member of Frontiers, at the time of submission. This had no impact on the peer review process and the final decision.

Publisher's note

Supplementary material

The Supplementary Material for this article can be found online at: https://www.frontiersin.org/articles/10.3389/frcrb.2024.1400664/full#supplementary-material

References

Alameri, D., Ocola, L. E., and Kuljanshvili, I. (2017a). Controlled selective CVD growth of ZnO nanowires enabled by mask-free fabrication approach using aqueous Fe catalytic inks. *Adv. Mater. Interfaces* 4, 1700950. doi:10.1002/ADMI.201700950

Alameri, D., Ocola, L. E., and Kuljanshvili, I. (2017b). Controlled selective CVD growth of ZnO nanowires enabled by mask-free fabrication approach using aqueous Fe catalytic inks. *Adv. Mater. Interfaces* 4, 1700950. doi:10.1002/admi.201700950

Al-Asadi, A. S., Henley, L. A., Wasala, M., Muchharla, B., Perea-Lopez, N., Carozo, V., et al. (2017). Aligned carbon nanotube/zinc oxide nanowire hybrids as high performance electrodes for supercapacitor applications. *J. Appl. Phys.* 121, 121. doi:10.1063/1.4979098

Bacakova, L., Grausova, L., Vacik, J., Fraczek, A., Blazewicz, S., Kromka, A., et al. (2007). Improved adhesion and growth of human osteoblast-like MG 63 cells on biomaterials modified with carbon nanoparticles. *Diam. Relat. Mater.* 16, 2133–2140. doi:10.1016/j.diamond.2007.07.015

Bisht, G., and Rayamajhi, S. (2016). ZnO nanoparticles: a promising anticancer agent. *Nanobiomedicine (Rij)* 3, 9. doi:10.5772/63437

Boncler, M., Lukasiak, M., Dastych, J., Golanski, J., and Watala, C. (2019). Differentiated mitochondrial function in mouse 3T3 fibroblasts and human epithelial or endothelial cells in response to chemical exposure. *Basic and Clin. Pharmacol. Toxicol.* 124, 199–210. doi:10.1111/bcpt.13117

Ciofani, G., Genchi, G. G., and Mattoli, V. (2012). ZnO nanowire arrays as substrates for cell proliferation and differentiation. *Mater. Sci. Eng. C* 32, 341–347. doi:10.1016/j.msec.2011.11.001

Cui, H., Liu, Q., Li, R., Wei, X., Sun, Y., Wang, Z., et al. (2020). ZnO nanowire-integrated bio-microchips for specific capture and non-destructive release of circulating tumor cells. *Nanoscale* 12, 1455–1463. doi:10.1039/c9nr07349c

Dai, H. (2001). "Nanotube growth and characterization," in *Carbon nanotubes: synthesis, structure, properties, and applications*. Editors M. S. Dresselhaus, G. Dresselhaus, and P. Avouris (Berlin, Heidelberg: Springer Berlin Heidelberg), 29–53. doi:10.1007/3-540-39947-X_3

Dai, K., Dawson, G., Yang, S., Chen, Z., and Lu, L. (2012). Large scale preparing carbon nanotube/zinc oxide hybrid and its application for highly reusable photocatalyst. *Chem. Eng. J.* 191, 571–578. doi:10.1016/j.cej.2012.03.008

Dineshkumar, B., Krishnakumar, K., Bhatt, A. R., Paul, D., Cherian, J., John, A., et al. (2015). Single-walled and multi-walled carbon nanotubes based drug delivery system: cancer therapy: a review. *Indian J. Cancer* 52, 262–264. doi:10.4103/0019-509x.176720

Gaetani, R., Derevyanchuk, Y., Notargiacomo, A., Pea, M., Renzi, M., Messina, E., et al. (2022). Biocompatibility and connectivity of semiconductor nanostructures for cardiac tissue engineering applications. *Bioengineering* 9, 621. doi:10.3390/bioengineering9110621

Geng, C., Jiang, Y., Yao, Y., Meng, X., Zapien, J. A., Lee, C. S., et al. (2004). Well-Aligned ZnO nanowire arrays fabricated on silicon substrates. *Adv. Funct. Mater.* 14, 589–594. doi:10.1002/adfm.200305074

George, S., Pokhrel, S., Xia, T., Gilbert, B., Ji, Z., Schowalter, M., et al. (2010). Use of a rapid cytotoxicity screening approach to engineer a safer zinc oxide nanoparticle through iron doping. *ACS Nano* 4, 15–29. doi:10.1021/nn901503q

Ghaffari, M., Moztarzadeh, F., and Safavi, M. (2019). A comparative study on the shape-dependent biological activity of nanostructured zinc oxide. *Ceram. Int.* 45, 1179–1188. doi:10.1016/j.ceramint.2018.09.302

Ghannam, H., Chahboun, A., and Turmine, M. (2019). Wettability of zinc oxide nanorod surfaces. *RSC Adv.* 9, 38289–38297. doi:10.1039/C9RA05378F

Hong, H., Shi, J., Yang, Y., Zhang, Y., Engle, J. W., Nickles, R. J., et al. (2011). Cancer-targeted optical imaging with fluorescent zinc oxide nanowires. *Nano Lett.* 11, 3744–3750. doi:10.1021/nl201782m

Imaninezhad, M., Kuljanishvili, I., and Zustiak, S. P. (2017). A two-step method for transferring single-walled carbon nanotubes onto a hydrogel substrate. *Macromol. Biosci.* 17, 1600261. doi:10.1002/mabi.201600261

Imaninezhad, M., Schober, J., Griggs, D., Ruminski, P., Kuljanishvili, I., and Zustiak, S. P. (2018). Cell attachment and spreading on carbon nanotubes is facilitated by integrin binding. *Front. Bioeng. Biotechnol.* 6, 129. doi:10.3389/fbioe.2018.00129

Jorio, A., Saito, R., Hafner, J. H., Lieber, C. M., Hunter, M., McClure, T., et al. (2001). Structural (n,m) determination of isolated single-wall carbon nanotubes by resonant Raman scattering. *Phys. Rev. Lett.* 86, 1118–1121. doi:10.1103/PhysRevLett.86.1118

Kuljanishvili, I., Dikin, D. A., Rozhok, S., Mayle, S., and Chandrasekhar, V. (2009). Controllable patterning and CVD growth of isolated carbon nanotubes with direct parallel writing of catalyst using dip-pen nanolithography. *Small* 5, 2523–2527. doi:10.1002/smll.200900841

Lee, J., Kang, B. S., Hicks, B., Chancellor, T. F., Chu, B. H., Wang, H.-T., et al. (2008). The control of cell adhesion and viability by zinc oxide nanorods. *Biomaterials* 29, 3743–3749. doi:10.1016/j.biomaterials.2008.05.029

Li, M., Lin, D., and Zhu, L. (2013). Effects of water chemistry on the dissolution of ZnO nanoparticles and their toxicity to *Escherichia coli*. *Environ. Pollut.* 173, 97–102. doi:10.1016/J.ENVPOL.2012.10.026

Li, M., Zhu, L., and Lin, D. (2011). Toxicity of ZnO nanoparticles to *Escherichia coli*: mechanism and the influence of medium components. *Environ. Sci. Technol.* 45, 1977–1983. doi:10.1021/es102624t

Li, Z., Persson, H., Adolfsson, K., Oredsson, S., and Prinz, C. N. (2018). Morphology of living cells cultured on nanowire arrays with varying nanowire densities and diameters. *Sci. China Life Sci.* 61, 427–435. doi:10.1007/s11427-017-9264-2

Li, Z., Yang, R., Yu, M., Bai, F., Li, C., and Wang, Z. L. (2008). Cellular level biocompatibility and biosafety of ZnO nanowires. *J. Phys. Chem. C* 112, 20114–20117. doi:10.1021/jp808878p

Liao, C., Jin, Y., Li, Y., and Tjong, S. C. (2020). Interactions of zinc oxide nanostructures with mammalian cells: cytotoxicity and photocatalytic toxicity. *Int. J. Mol. Sci.* 21, 6305. doi:10.3390/ijms21176305

Mardosaitė, R., Jurkeviciute, A., and Rackauskas, S. (2021). Superhydrophobic ZnO nanowires: wettability mechanisms and functional applications. *Cryst. Growth and Des.* 21, 4765–4779. doi:10.1021/acs.cgd.1c00449

Milano, G., D'Ortenzi, L., Bejtka, K., Mandrile, L., Giovannozzi, A. M., Boarino, L., et al. (2018). Tuning ZnO nanowire dissolution by electron beam modification of surface wetting properties. *J. Phys. Chem. C* 122, 8011–8021. doi:10.1021/acs.jpcc.8b01158

Minchenko, O. H., Tsymbal, D. O., Minchenko, D. O., Prylutska, S. V., Cherepanov, V. V., Prylutskyy, Y. I., et al. (2016). Single-walled carbon nanotubes affect the expression of the CCND2 gene in human U87 glioma cells: Einwandige Kohlenstoff-Nanoröhren beeinflussen die Expression des CCND2-Gens in humanen U87 Glioma-Zellen. *Mater. Werkst.* 47, 180–188. doi:10.1002/mawe.201600462

Mohammad Karim, A. (2023). Physics of droplet impact on various substrates and its current advancements in interfacial science: a review. *J. Appl. Phys.* 133, 30701. doi:10.1063/5.0130043

Murali, A., Lokhande, G., Deo, K. A., Brokesh, A., and Gaharwar, A. K. (2021). Emerging 2D nanomaterials for biomedical applications. *Mater. Today* 50, 276–302. doi:10.1016/j.mattod.2021.04.020

Onesto, V., Villani, M., Narducci, R., Malara, N., Imbrogno, A., Allione, M., et al. (2019). Cortical-like mini-columns of neuronal cells on zinc oxide nanowire surfaces. *Sci. Rep.* 9, 4021. doi:10.1038/s41598-019-40548-z

Parikh, S. D., Dave, S., Huang, L., Wang, W., Mukhopadhyay, S. M., and Mayes, D. A. (2020). Multi-walled carbon nanotube carpets as scaffolds for U87MG glioblastoma multiforme cell growth. *Mater. Sci. Eng. C* 108, 110345. doi:10.1016/j.msec.2019.110345

Persson, H., Li, Z., Tegenfeldt, J. O., Oredsson, S., and Prinz, C. N. (2015). From immobilized cells to motile cells on a bed-of-nails: effects of vertical nanowire array density on cell behaviour. *Sci. Rep.* 5 (1), 18535–18612. doi:10.1038/srep18535

Pratt, E. P. S., Damon, L. J., Anson, K. J., and Palmer, A. E. (2021). Tools and techniques for illuminating the cell biology of zinc. *Biochimica Biophysica Acta (BBA) - Mol. Cell Res.* 1868, 118865. doi:10.1016/J.BBAMCR.2020.118865

Qi, S., Yi, C., Ji, S., Fong, C. C., and Yang, M. (2009). Cell adhesion and spreading behavior on vertically aligned silicon nanowire arrays. *ACS Appl. Mater Interfaces* 1, 30–34. doi:10.1021/am800027d

Riemenschneider, M. J., Mueller, W., Betensky, R. A., Mohapatra, G., and Louis, D. N. (2005). *In situ* analysis of integrin and growth factor receptor signaling pathways in human glioblastomas suggests overlapping relationships with focal adhesion kinase activation. *Am. J. Pathology* 167, 1379–1387. doi:10.1016/s0002-9440(10)61225-4

Rudnytska, O. V., Khita, O. O., Minchenko, D. O., Tsymbal, D. O., Yefimova, Y. V., Sliusar, M. Y., et al. (2021). The low doses of SWCNTs affect the expression of proliferation and apoptosis related genes in normal human astrocytes. *Curr. Res. Toxicol.* 2, 64–71. doi:10.1016/j.crtox.2021.02.001

Ryoo, S.-R., Kim, Y.-K., Kim, M.-H., and Min, D.-H. (2010). Behaviors of NIH-3T3 fibroblasts on graphene/carbon nanotubes: proliferation, focal adhesion, and gene transfection studies. *ACS Nano* 4, 6587–6598. doi:10.1021/nn1018279

Schaper, N., Alameri, D., Kim, Y., Thomas, B., McCormack, K., Chan, M., et al. (2021). Controlled fabrication of quality ZnO NWs/CNTs and ZnO NWs/gr heterostructures via direct two-step CVD method. *Nanomater. (Basel)* 11, 1836. doi:10.3390/nano11071836

Sharma, D. K., Shukla, S., Sharma, K. K., and Kumar, V. (2022). A review on ZnO: fundamental properties and applications. *Mater. Today Proc.* 49, 3028–3035. doi:10.1016/j.matpr.2020.10.238

Shooshtari, M., Pahlavan, S., Rahbarpour, S., and Ghafoorifard, H. (2022). Investigating organic vapor sensing properties of composite carbon nanotube-zinc oxide nanowire. *Chemosensors* 10, 205. doi:10.3390/chemosensors10060205

Simon, J., Flahaut, E., and Golzio, M. (2019). Overview of carbon nanotubes for biomedical applications. *Mater. (Basel)* 12, 624. doi:10.3390/ma12040624

Wahab, R., Kaushik, N. K., Verma, A. K., Mishra, A., Hwang, I. H., Yang, Y.-B., et al. (2011). Fabrication and growth mechanism of ZnO nanostructures and their cytotoxic effect on human brain tumor U87, cervical cancer HeLa, and normal HEK cells. *JBIC J. Biol. Inorg. Chem.* 16, 431–442. doi:10.1007/s00775-010-0740-0

Wang, X., Liu, L.-H., Ramström, O., and Yan, M. (2009). Engineering nanomaterial surfaces for biomedical applications. *Exp. Biol. Med.* 234, 1128–1139. doi:10.3181/0904-mr-134

Wong, S., Guo, W.-H., and Wang, Y.-L. (2014). Fibroblasts probe substrate rigidity with filopodia extensions before occupying an area. *Proc. Natl. Acad. Sci.* 111, 17176–17181. doi:10.1073/pnas.1412285111

Yin, L., Zhou, J., Gao, L., Zhao, C., Chen, J., Lu, X., et al. (2017). Characterization and osteogenic activity of SrTiO3/TiO2 nanotube heterostructures on microporous titanium. *Surf. Coatings Technol.* 330, 121–130. doi:10.1016/j.surfcoat.2017.09.075

Zhang, Y., Ram, M. K., Stefanakos, E. K., and Goswami, D. Y. (2012). Synthesis, characterization, and applications of ZnO nanowires. *J. Nanomater.* 2012, 1–22. doi:10.1155/2012/624520

Zhou, W., Bai, X., Wang, E., and Xie, S. (2009). Synthesis, structure, and properties of single-walled carbon nanotubes. *Adv. Mater.* 21, 4565–4583. doi:10.1002/adma.200901071

Zhu, G., Zhou, Y., Wang, S., Yang, R., Ding, Y., Wang, X., et al. (2012). Synthesis of vertically aligned ultra-long ZnO nanowires on heterogeneous substrates with catalyst at the root. *Nanotechnology* 23, 055604. doi:10.1088/0957-4484/23/5/055604

frontiers | Frontiers in Carbon

TYPE Review
PUBLISHED 25 July 2024
DOI 10.3389/frcrb.2024.1393077

OPEN ACCESS

EDITED BY
Derek Hao,
RMIT University, Australia

REVIEWED BY
Peng Li,
RMIT University, Australia
Zijun Yong,
RMIT University, Australia
Qilong Wu,
University of Wollongong, Australia

*CORRESPONDENCE
Elisa S. Orth,
elisaorth@ufpr.br

RECEIVED 28 February 2024
ACCEPTED 23 May 2024
PUBLISHED 25 July 2024

CITATION
Gonçalves MG, Costa VO, Martinez AHG, Régnier BM, Gomes GCB, Zarbin AJG and Orth ES (2024), Functionalization of graphene oxide via epoxide groups: a comprehensive review of synthetic routes and challenges. *Front. Carbon* 3:1393077. doi: 10.3389/frcrb.2024.1393077

Functionalization of graphene oxide via epoxide groups: a comprehensive review of synthetic routes and challenges

Mayara G. Gonçalves, Vinícius O. Costa, André H. G. Martinez, Bernardo M. Régnier, Gabriel C. B. Gomes, Aldo J. G. Zarbin and Elisa S. Orth*

Universidade Federal do Paraná (UFPR), Chemistry Departament, Curitiba, Brazil

Graphene oxide (GO) has attracted significant attention from the scientific community due to its mechanical, optical, electrical, and chemical properties. This review outlines synthetic methods for GO functionalization, including those involving covalent and noncovalent bonds with organic molecules. In a novel contribution to this field, particular emphasis is placed on functionalization via epoxy ring opening, a poorly studied and understood topic. We first provide an overview of the basic structure and properties of graphene oxide. We then explore the various methods employed to functionalize graphene oxide, noting the complexity of these reactions, which sometimes occur in a non-specific manner. However, there are some strategies for targeted functionalization. Furthermore, we present a critical analysis of the covalent functionalization through epoxy groups, demonstrating important aspects to be considered when choosing the reaction medium. An alkaline environment seems to favor this reaction, and there is no consensus regarding the advantages and disadvantages of using basic pH in functionalization reactions. We also demonstrate some challenges involving the characterization and confirmation of the functionalization, mainly in the basal plane, and we show advances in characterization techniques that can be explored in future studies. Finally, some current challenges and future research directions are presented to contribute to the advancement of the field.

KEYWORDS

functionalized graphene, epoxy groups, covalent derivatization, epoxide opening, nucleophilic reactions

1 Introduction

Graphene oxide (GO) is a remarkable material derived from graphene, featuring a two-dimensional arrangement of carbon atoms bonded in hexagons along with oxygen functional groups (Brisebois and Siaj, 2020; Vacchi et al., 2020; Guo et al., 2022; Donato et al., 2023). This unique structure enables GO to disperse in aqueous solutions and serve as a support for various functional groups, enabling a multitude of applications. These applications range from sensors (Shahdost-fard and Roushani, 2017; Devi et al., 2018; Jayaraman et al., 2022; Alves et al., 2023) and catalysts (Xue et al., 2015; Flores et al., 2020; Hao et al., 2020; Hostert et al., 2020; Santos et al., 2022; Santos et al., 2023; Xie et al., 2023) to membranes (Kumar et al., 2012; Nair et al., 2012; Zhang et al., 2015; Feng et al., 2018;

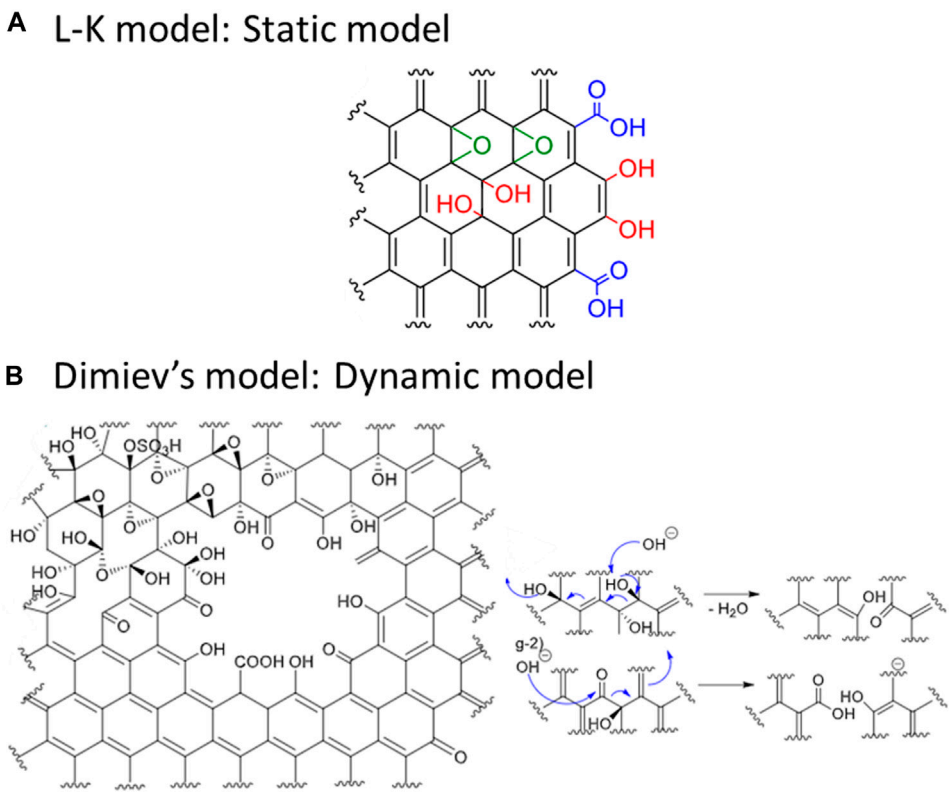

FIGURE 1
Structure models of GO. **(A)** LK model, static model (Kasprzak et al., 2018). **(B)** Dimiev's model, dynamic model (Monteiro et al., 2020). Reprinted with permission from Beilstein-Institut (2018) and Wiley-VCH (2020).

Meng et al., 2019; Tan et al., 2022), solar cells (Liu et al., 2012; Lima et al., 2016; Gao et al., 2022), energy storage (Georgakilas et al., 2016; Zhang et al., 2016; Payami et al., 2020; Tian et al., 2021), and even biomedical therapies (Mirzaie et al., 2019; Monteiro et al., 2020; Ranishenka et al., 2021).

One of the most utilized techniques for obtaining GO involves the chemical oxidation of graphite, followed by exfoliation. However, this process introduces structural defects in the sp^2 network due to the oxidative cutting of graphene sheets (Komeily-Nia et al., 2021). Although the oxygenated groups are spread throughout the whole structure, the defect regions present a different prioritization of groups (Feicht and Eigler, 2018). Epoxides, a functional group found in GO, are formed during the initial stages of oxidation due to their kinetic favorability (Pancharatna et al., 2020). Apart from epoxides, GO also contains other oxygenated groups such as carboxyl, hydroxyl, and carbonyl groups, which can be found in the edges and defects in the structure. The composition of these groups varies depending on the preparation method and the extent of oxidation (Komeily-Nia et al., 2021). Consequently, GO is not a material with a fixed composition and structure but rather a material with significant variation in size and oxidation degree (Donato et al., 2023).

It is crucial to acknowledge the structural complexity when studying the functionalization and application of GO in various fields. Several models have been proposed for GO structure, three of which are highlighted: the L-K model introduced by Lerf and Klinowski (Figure 1A) (Lerf et al., 1998), the two-component structure model (Rourke et al., 2011), and the Dynamic Structure Model (DSM) (Dimiev, 2016) (Figure 1B).

These models provide valuable insights into the structure of GO and its properties. For example, the L-K model suggests that the epoxy and hydroxyl functional groups are attached to the basal plane of GO, while the carboxyl functional groups are linked to the edges. This model has been updated to explain the high acidity, defects, and partial heterogeneity of GO. Among these updates, Rourke et al. (2011) have suggested the partial heterogeneity of GO obtained by the Hummers method. Rourke's "two-component structural model" divides GO into bwGO (base-washed graphene oxide) and OD (oxygenated debris), relating its properties based on these two components and their interaction. ODs are small fragments that can be separated from GO by alkaline washing, accounting for about one-third of its total mass. In neutral or acidic environments, ODs are tightly bonded to GO, while in alkaline environments, the deprotonation of functional groups in OD detaches it from bwGO. This process cannot be reversed once the components are separated. Dimiev (2016) proposed a dynamic structure model (DSM) for GO based on a study of the origin and structural evolution of its acidity. This model attributes the acidity of GO to its enol groups and suggests that the structure of GO is constantly changing in the presence of water. The study also reported a significant change between the freshly prepared GO and the same GO after 2 months.

An increasing number of researchers are now exploring the anchoring of various chemical species in GO, thus creating novel composites with unique chemical and physical properties and expanding their applications (Yu et al., 2020). This can be achieved through both non-covalent (involving intermolecular interactions) and covalent functionalization involving reactions between carboxylic acids, hydroxyls, or epoxides of graphene oxide with other molecules (Yu et al., 2020). A known challenge in this area is corroborating the intended modification with different characterization techniques and answering questions such as where the modification was made, what group was anchored, and what the degree of functionalization is (Kasprzak et al., 2018; Vacchi et al., 2020).

The covalent functionalization approach, which will be the main scope of this review, utilizes a range of classic organic reactions, including carboxylic acids, alcohols, and epoxides (Kasprzak et al., 2018). This field is still very challenging since it is difficult to extend organic reactions to complex structures such as GO (Kasprzak et al., 2018). For example, shifts in reactivity sometimes require changes to the reaction conditions, such as solvent and temperature. Derivatization in carboxylic acid groups via amidation or esterification is a popular choice for the chemical modification of GO—extensively discussed in Georgakilas et al. (2012), Yu et al. (2020), Guo et al. (2022), and Liu et al. (2022) —and offers the benefits of mild pH and temperature conditions (Vacchi et al., 2020). However, this approach is limited by the low quantity of carboxylic acid groups due to their location on the GO sheets' edges (Guo et al., 2020a).

On the other hand, the functionalization of basal groups, particularly epoxides, has been significantly overlooked, as Kumar et al. (2022) have highlighted. Both hydroxyls and epoxides can be functionalized, but epoxides are more susceptible to nucleophilic attack and will be the focus of this review. Nucleophilic attack promotes epoxide ring opening, with the nucleophile becoming covalently attached to the GO (Thomas et al., 2014; Taniguchi et al., 2015; Ranishenka et al., 2021; Kumar et al., 2022). Researchers have highlighted several advantages of this method, including the abundance of epoxides and the absence of coupling reagents commonly used in functionalization via carboxylic acids (Ranishenka et al., 2021; Kumar et al., 2022). Furthermore, the opening of epoxides generates additional hydroxyls that can be functionalized in subsequent reactions (Khan et al., 2021). Also, the modification of basal oxygen groups can yield materials with specific properties distinct from those functionalized at the edges; it is important to explore these differences thoroughly. However, there are also some drawbacks and limitations associated with this approach. First, the characterization and quantification of epoxide groups in GO are challenging as they are in a region where there are many steric hindrances (Piñeiro-García and Semetey, 2023); thus, differentiating hydroxyls and epoxides using spectroscopic methods is difficult (Rabchinskii et al., 2022). Second, there is a preference for alkaline media in these reactions (Taniguchi et al., 2015; Fallah-Mehrjardi et al., 2018; Piñeiro-García and Semetey, 2023), although certain studies caution against functionalization under alkaline conditions due to the potential reduction and destabilization of the GO colloidal system (Guo et al., 2020a; Guo et al., 2020b; Vacchi et al., 2020; Guo et al., 2022). It is important to highlight that some researchers seek out the effects evoked by functionalization via epoxide in an alkaline medium and do not view it as a drawback (Gao et al., 2010; Thomas et al., 2013; Thomas et al., 2014; Kumar et al., 2022). This will be evident when we discuss the pH effects on these reactions.

In fact, the functionalization route via GO epoxides is very promising, but there are still several crucial aspects that require thorough analysis and discussion. We have thus conducted a comprehensive review, compiling studies that have employed this route, showing the proposed mechanisms, and highlighting the main characterization techniques as well as the difficulties associated with them. We expect that this research will contribute to the advancement of studies on the functionalization of GO and provide clarity for future investigations in this field.

2 Strategies for functionalizing GO

Two primary approaches exist in the field of GO functionalization: covalent and non-covalent (Yu et al., 2020; Liu et al., 2022). In this section, we will discuss some general aspects regarding these two types of functionalization, placing particular emphasis on covalent functionalization targeting carbon atoms or oxygen functional groups of GO. This excludes the discussion of functionalization through epoxy groups, which will be detailed in subsequent sections. Additionally, we will explore cases where multiple molecules are incorporated into distinct functional sites of GO, resulting in multifunctionalization.

Non-covalent functionalization is the simplest way of functionalizing; (Table 1) it involves the incorporation of molecules, ions, atoms, or particles of interest into GO through diverse intermolecular interactions (Georgakilas et al., 2012; Georgakilas et al., 2016). For example, molecules that possess a π-conjugate system can be introduced to GO via π–π stacking interaction with the aromatic rings of the graphene plane. The success of this interaction is influenced by factors such as the molecule's ability to donate or withdraw electrons, its planarity, and its molecular size (Georgakilas et al., 2016). The surface of graphene can also interact with molecules or polymers with high hydrophobic characteristics through London scattering forces. On the other hand, the oxygenated functions present on the surface of GO allow Keesom (permanent dipole–permanent dipole) and Debye (permanent dipole–induced dipole) interactions, hydrogen bonds, and ion–dipole interactions (Georgakilas et al., 2012; Georgakilas et al., 2016). Figure 2 illustrates non-covalent interactions between graphene oxide and pharmaceutical molecules (PhAs).

Georgakilas et al. (2012) comprehensively reviewed the non-covalent functionalization of graphene oxide and demonstrated the diverse range of molecules that can be incorporated based on specific interaction types. Polymers and carbon allotropes (such as fullerenes) via π–π interactions can be added for application in solar cells and the formation of gels and thin films, respectively. Furthermore, the incorporation of medicines and biomolecules through hydrogen bonds with oxygenated functional groups can enable biomedical applications.

Despite the simplicity and maintenance of the chemical structure of graphene oxide, there is a drawback when it

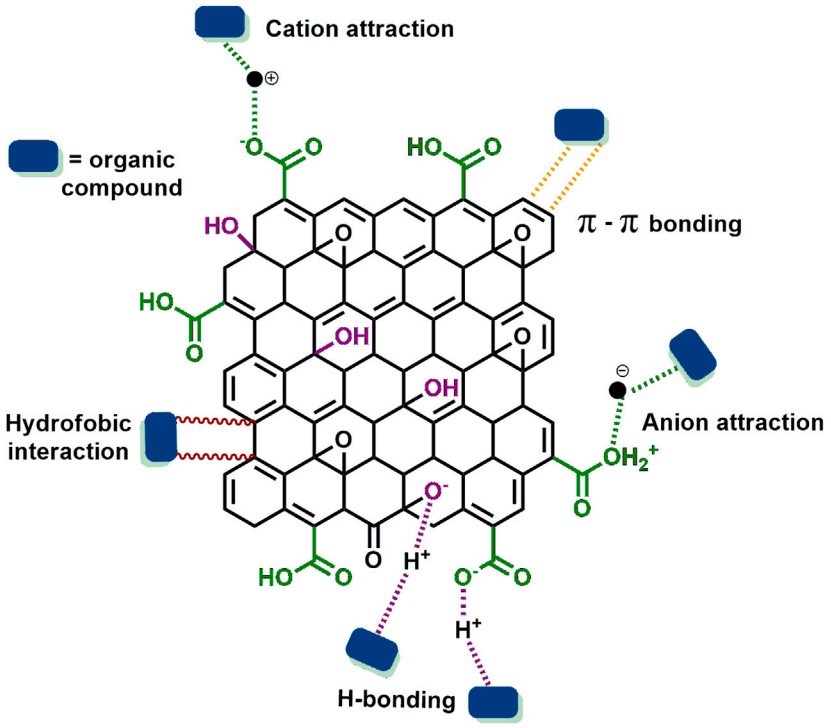

FIGURE 2
Non-covalent interaction between graphene oxide and pharmaceuticals (PhAs). See Khan et al. (2017).

TABLE 1 Non-covalent functionalization of GO, interactions, and applications.

Agents	Interaction	Applications	References
Polymers: polyethylenimine, PEDOT	π-π	Solar cells, Nano-Devices, Biotherapeutics, Drug carriers	Liu et al. (2010), Dehsari et al. (2014), Wang H. et al. (2015)
Metal oxides: TiO_2, Fe_3O_4/Cu_2O	Physisorption, Ionic interactions	Energy, Solar Cells, Catalysis	Kong et al. (2014), Wang et al. (2014), Wang Z. et al. (2015), Yang et al. (2015)
Carbon nanostructures: nanotubes, and hydrophilic nanotubes	π-π, Hydrogen bonds	Removal of dyes from water, Supercapacitor	Liu et al. (2014), Georgakilas et al. (2015)
Polyethylene glycol	Hydrogen bonds	Membranes for oil/water separation	He et al. (2019)
Sodium dodecyl benzene sulfonate (SDBS)	Ionic interactions	Product packaging	Ge et al. (2017)

comes to materials obtained by non-covalent functionalization: the weakly bound molecules can be easily lixiviated (Georgakilas et al., 2012; Lopez and Liu, 2020). Covalent functionalization addresses this drawback by creating stronger attachments between the molecules and the GO structure (Georgakilas et al., 2012; Lopez and Liu, 2020), which is crucial for applications that require material durability over multiple cycles, such as catalysis (Orth et al., 2013; Silvestri et al., 2022). The main reactions of covalent functionalization will be discussed below (see also Figure 3).

When covalent functionalization is employed, reactions can occur directly in the sp^2 carbon network or in the oxygenated functional groups of the graphene oxide (Yu et al., 2020; Liu et al., 2022). Some methodologies that primarily focus on functionalizing the carbon plane are thiol-ene reactions (including the Michael addition) (Piñeiro-García et al., 2021; Piñeiro-García and Semetey, 2023) (Figures 3A), diazotization (Ossonon and Bélanger, 2017) (Figures 3B), and Diels–Alder reactions (Tang et al., 2017) (Figures 3C). The thiol-ene process involves the addition of a thiol compound to an alkene in an anti-Markovnikov orientation (Piñeiro-García et al., 2021; Piñeiro-García et al., 2022; Piñeiro-García and Semetey, 2023); it encompasses thiol-ene radical addition and thiol-ene Michael addition, initiated by radical or base catalysts, respectively (Piñeiro-García and Semetey, 2023). Thiol-ene radical addition occurs in three stages. Firstly, an initiating radical interacts with a thiol molecule, forming thiyl radicals. These then react with a carbon–carbon double bond, creating a central radical in the adjacent carbon. Subsequently, the newly formed central carbon radical can stabilize by extracting a hydrogen atom from another

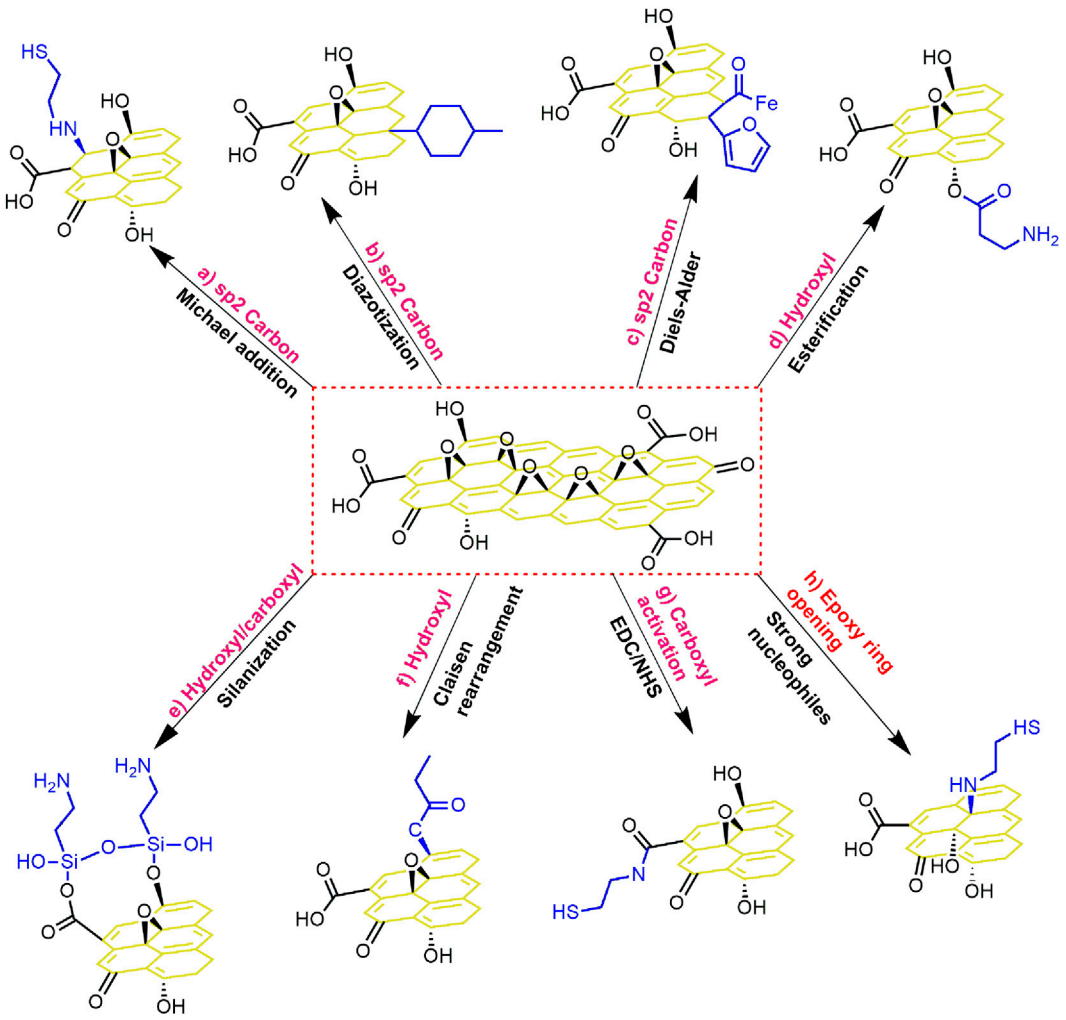

FIGURE 3
Examples of covalent functionalization through different routes in GO. **(A)** Michael addition (Piñeiro-García et al., 2021). **(B)** Diazotization (Ossonon and Bélanger, 2017). **(C)** Diels–Alder (Rahimpour et al., 2022). **(D)** Esterification (Zhang et al., 2011). **(E)** Silanization (Serodre et al., 2019). **(F)** Claisen rearrangement (Collins et al., 2011a), **(G)** Q31 Carboxyl activation with EDC/NHS (Santos et al., 2022). **(H)** Epoxy-ring opening (Santos et al., 2023).

thiol molecule, generating a fresh thiyl radical that perpetuates the reaction (Piñeiro-García et al., 2021).

A thiol-ene Michael addition (Figures 4A,B) involves adding a nucleophile to the β carbon of an α,β-unsaturated carbonyl or carboxyl acid (Guo et al., 2020b; Piñeiro-García et al., 2021; Piñeiro-García and Semetey, 2023). This reaction can serve as a method for functionalizing GO alkenes (acting as electrophiles–Michael acceptors) and hydroxyls (acting as nucleophiles–Michael donors). In the first method, a nucleophile attacks GO's active C=C bonds, which are the double bonds in the beta position of ketones or carboxylic acids. This functionalization can occur under conditions similar to nucleophilic substitution reactions via open epoxide rings, which require nucleophilic attack and employ basic catalysts. Hence, it is highly likely that the nucleophilic attack occurs on both the Michael acceptors and the epoxides (Figure 4A), although the epoxides are more abundant. Therefore, to favor the Michael reaction, the use of reduced graphene oxide (rGO; containing fewer epoxide groups) is recommended (Piñeiro-García et al., 2021) (Figure 4B). The second method, where GO acts as a Michael donor, will be discussed with other functionalization methods involving hydroxyls.

Another common method for functionalizing C=C bonds is diazotization (Figure 3B). It involves a cycloaddition between, which employs aryl diazonium salts (ArN_2+, Ar=aryl). In this method, electron transfer from the carbon substrate to the ion reduces diazonium ions to aryl diazonium radicals and enables their addition to the C=C bonds of GO and the formation of a C–C covalent bond between the carbon and the aryl group (Ossonon and Bélanger, 2017; Monteiro et al., 2020; Yu et al., 2020; Guo et al., 2022). This reaction is compatible with different groups (Guo et al., 2022) and is usually performed in organic solvents to avoid collateral reactions with water (Monteiro et al., 2020).

Finally, the Diels–Alder reaction is a significant method for functionalizing C=C bonds (Figures 3C). It involves a cycloaddition between a diene (an electron-rich alkene) and a dienophile (an electron-poor alkene). The conjugated double bonds of GO can act as both a diene and a dienophile and result in the saturation of conjugated sp^2 hybridized carbon atoms. A carbonyl group adds an

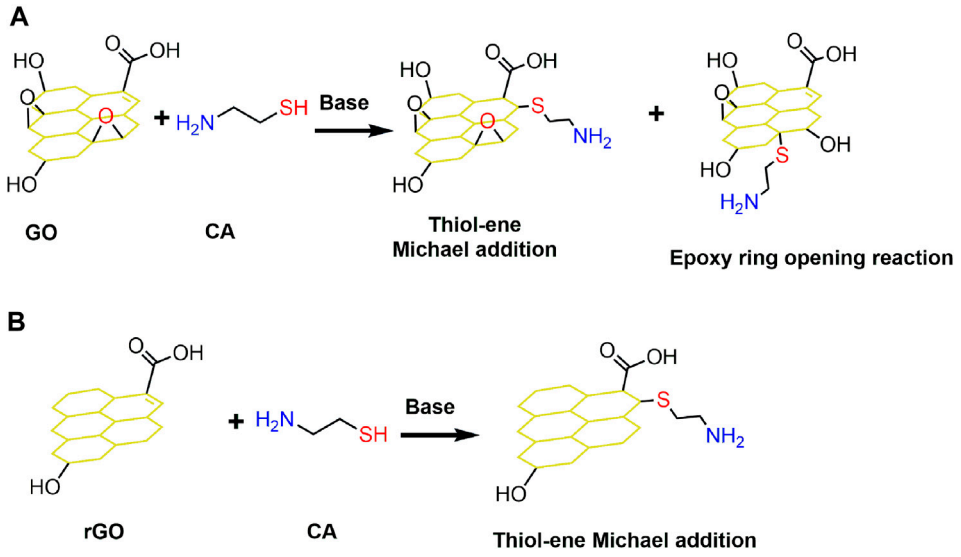

FIGURE 4
(A) Functionalization of GO with cysteamine – CA, using a base catalyst where two possible products are shown: Michael addition and epoxy ring opening reaction by SH. **(B)** Functionalization of rGO with CA by Michael addition. See Piñeiro-García et al. (2021).

extra electron to the graphene π-system, while an epoxy group removes two π-electrons from neighboring sites in the sublattice (Donato et al., 2023). Therefore, the dienophilic nature of the GO surface prevails over its diene behavior due to the large amount of epoxides and hydroxyls (Tang et al., 2017). The main reactions that will be discussed below are illustrated in Figure 3.

The most widely explored functionalization methods have focused on the oxygen functional groups of GO, and we will didactically show the reactions separated by oxygenated functions, starting with hydroxyls, although some reactions are not selective and occur in different groups. Michael additions can ensue using hydroxyl groups, but unlike the process mentioned above, the GO hydroxyls in this case act as Michael donors, attacking other α,β-unsaturated carbonyl molecules. For example, Guo et al (2020b) added benzoquinone (a Michael acceptor) to GO hydroxyls using Michael addition. Hydroxyl groups can also be modified to produce ester (Yu et al., 2020) or carbodiimide (Zhang et al., 2011) (Figures 3D). These reactions offer a great opportunity to customize GO and the attachment of different chemical species, thereby enhancing its properties. For example, esterification with biocompatible polymers greatly improves the dispersibility of GO in physiological solutions (Monteiro et al., 2020). Another approach is to condense GO hydroxyl groups with organosilanes to produce silica-decorated graphene oxide (Figures 3E) (Ma et al., 2016; Serodre et al., 2019). Another functionalization method that initially leverages the reactivity of hydroxyl groups involves the reaction of N, N-dimethylacetamide dimethyl acetal (DMDA) with GO. In this case, the hydroxyl group condenses with DMDA to form a vinyl ether intermediate, which undergoes a Claisen sigmatropic rearrangement with the carbon surface, resulting in the formation of a new C–C bond (Figures 3F) (Sydlik and Swager, 2013).

The carboxyl functionalization of GO, which is the most applied method, requires an activation step followed by anchoring of the group of interest to form an ester or amide bond (Figures 3G). Reagents such as thionyl chloride ($SOCl_2$), N,N-dicyclohexylcarbodiimide (DCC), and 1-ethyl-3-(3-dimethylaminopropyl)-carbodiimide (EDC) are commonly used to activate the carboxyl (Yu et al., 2020). These reagents react with the hydroxyl groups of the carboxylic acid of GO, resulting in an intermediate called o-acylurea, which is more susceptible to nucleophilic attack. However, in some reactions, a direct attack on o-acylurea is not favored, resulting in slow reactions. To overcome this issue, a step before the attack is performed by adding reagents that increase the stability of the intermediate, such as N-hydroxysuccinimide (NHS) reagent (Kasprzak et al., 2018). This methodology is used to add nucleophiles such as cysteamine (Orth et al., 2014; Santos et al., 2023), hydroxamic acid (Hostert et al., 2020), and ethylene diamine (Maslekar et al., 2020) but is not restricted to small nucleophiles since enzymes (Paz-Cedeno et al., 2021) and polymeric materials such as polyethylene glycol (Hao et al., 2020), polyethyleneimine (Oh et al., 2021), alginate (Golkar et al., 2023), and chitosan (Rana et al., 2011; Mirzaie et al., 2019) can also be attached. Table 2 provides a summary of some covalent functionalization on the surface of GOs, taking into consideration different methods and applications.

In addition to the research mentioned in Table 2, other studies have demonstrated the applications of covalently functionalized GO in fields such as desalination (Nair et al., 2012), healthcare products (Liu et al., 2008; Kumar et al., 2019; Shetti et al., 2019), oil–water separation (Feng et al., 2018), solar cells (Liu et al., 2008; Xue et al., 2015), energy storage (Cakici et al., 2017; Tian et al., 2021), and coatings (Ma et al., 2016). Some other studies have discussed the influence of the neighboring effect on functionalized materials, further emphasizing the importance of controlling selectivity in

TABLE 2 Summary of some covalent functionalization of GO, along with conditions and applications.

Site of GO targeted	Method	Conditions	Application	Ref.
Epoxy	Ring opening by strong nucleophiles	Basic medium 25°C – 60 °C	Catalysis Membranes	Santos et al. (2022), Tan et al. (2022), Santos et al. (2023)
Carboxyl	Activation by EDC/NHS	Basic medium; room temperature	Catalysis	Hostert et al. (2017), Hostert et al. (2020), Santos et al. (2022)
Hydroxyl	Williamson reaction	Basic medium; room temperature	Nanomedicine	Vacchi et al. (2016)
Hydroxyl	Silanization	Non aqueous medium	Additive in polymeric matrices, solar cells, and coatings	Ma et al. (2016), Serodre et al. (2019), Gao et al. (2022)
Hydroxyl	Esterification	Non aqueous medium	Energy storage	Hao et al. (2020)
sp2 Carbon	Activation with sodium malononitrile	THF; 60 °C	Polymer composites	Collins et al. (2011a)

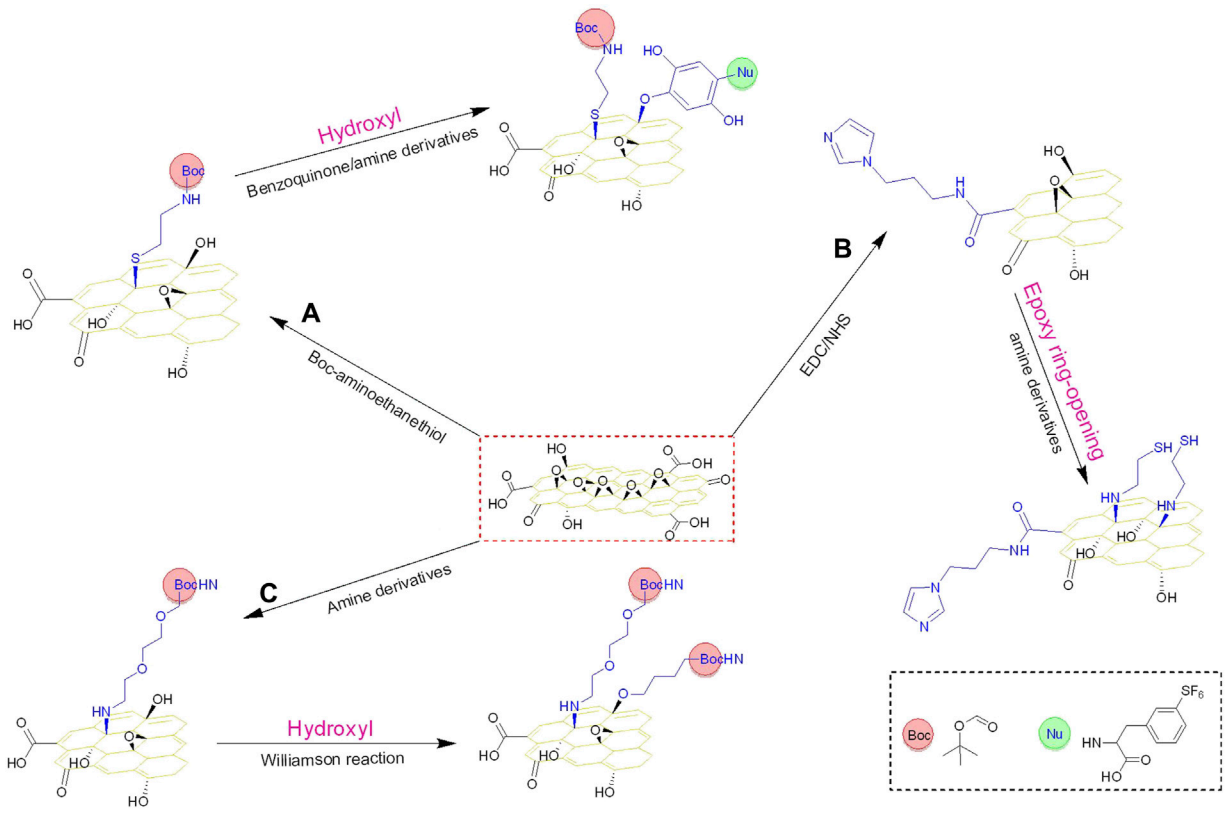

FIGURE 5
Examples of covalent bifunctionalization through different routes in GO. Path **(A)** epoxy-ring opening + Michael addition (See Guo et al., 2020b). Path **(B)** Carboxyl activation + epoxy-ring opening (See Santos et al., 2022). Path **(C)** epoxy-ring opening + Williamson reaction (See Vacchi et al., 2020).

the diverse applications of functionalized GO (Santos et al., 2022; Santos et al., 2023).

Bifunctionalization or multifunctionalization of GO is also an interesting approach to producing advanced materials and is an underexplored subject. Many approaches exist, such as combining epoxy ring opening with Michael addition on hydroxyl groups (Guo et al., 2020b), amidation of carboxyl groups combined with epoxy ring opening (Santos et al., 2022), and epoxy ring opening combined with Williamson reaction on hydroxyl groups (Vacchi et al., 2020). These examples are illustrated in Figure 5.

Path a) is appropriate for introducing different functional groups, considering that benzoquinone is widely used as a coupling agent and can also react with azides, phosphines, and thiol groups. Conjugation takes place through a Michael addition between benzoquinone and the amine or hydroxyl groups, with this

method being performed in mild conditions without any heating. Path b) was surprisingly studied for application in catalysis—modified GO with the lowest degree of functionalization had the best performance in catalytic performance. This was attributed to a dependence on the neighboring groups of GO due to steric effects or non-ideal positioning of the groups. Considering this, the application of bifunctionalized GO in catalysis still lacks a full understanding of its reactions and mechanisms. Path c) utilizes two orthogonally protected amino chains to allow selective cleavage of these protecting groups, allowing further derivatization (such as amidation) with molecules of interest under mild conditions and thus preserving the structure of GO. The Williamson reaction forms an ether bond between an organohalide and deprotonated alcohol via a substitution reaction. This functionalized GO has a high potential in nanomedicine for therapeutic and imaging applications.

Some other underexplored studies show free-radical covalent functionalization on the carbonaceous surface with two different groups, thereby increasing structure complexity (Pennetreau et al., 2014). Another study explored the multifunctionalization of GO with both -NH_2 and -NH_3^+ groups, achieving bifunctional graphene oxide through a microwave-assisted method. In this research, GO was functionalized using N-isopropylidene–3-aminopropyl–triethoxysilane (ITES), with this nanocomposite being utilized in epoxide resin coatings and demonstrating exceptional hydrophobic behavior and dual corrosion protection for mild steel in a sodium chloride solution (Ramirez-Soria et al., 2021).

However, studies have reported that when the epoxy ring opening and carboxylation/amidation were combined, the partial reduction of GO led to a lower overall functionalization efficiency, thereby limiting the viability of this method for future applications. Therefore, in this epoxy ring functionalization, pre-treatment of GO with m-chloroperoxibenzoic acid served to increase the number of carbon atoms with this functional group on its surface (Collins et al., 2011b).

3 Functionalization via epoxide ring opening

A variety of functionalization routes toward epoxides have been reported, mostly involving a nucleophilic attack on one of the carbon atoms composing the epoxide ring (Khanra et al., 2012; Thomas et al., 2014; Alzate-Carvajal et al., 2018; Fallah-Mehrjardi et al., 2018; Kasprzak et al., 2018; Elsie et al., 2019; Jiang et al., 2019; Price et al., 2019; Javidparvar et al., 2020; Piñeiro-García et al., 2021; Guo et al., 2022; Kumar et al., 2022; Meng et al., 2022; Sainz-Urruela et al., 2022; Surabhi et al., 2022; Tan et al., 2022; Singh and Kar, 2023). The nucleophilic attack leads to the opening of the epoxide ring, thus binding the nucleophile to the GO (Guo et al., 2020a; Martin-Gullon et al., 2020; Kumar et al., 2022). The attached nucleophile can also be linked to other molecules or atoms, thus increasing the complexity (Kasprzak et al., 2018; Kumar et al., 2022). Some examples of nucleophiles that can be used in this reaction are amines (Li et al., 2020), thiols (Thomas et al., 2014), hydrazine (Gao et al., 2010), and sulfide ions (Kumar et al., 2022).

Applications greatly depend on the molecule to be added to the GO; this route proves to be interesting for the synthesis of catalysts. Santos et al. (2023) carried out a comparative study of the performance of catalysts functionalized with thiol or imidazole at different GO sites—epoxide and carboxylic acid. They thoroughly demonstrated that materials functionalized through epoxide groups were more effective in catalyzing organophosphate neutralization reactions than those functionalized through carboxylic acids. One of the main factors justifying the superior performance of catalysts functionalized via epoxide is the cooperative effect between the added nucleophile (thiol or imidazole) and neighboring groups, such as carboxylic acids present at the edges of graphene oxide. Surabhi et al. (2022) performed the functionalization with imidazole groups, followed by decoration with palladium nanoparticles. The material was used to catalyze the production of amides from aldehydes and amines. This study highlighted the importance of the imidazole groups that were functionalized via epoxide ring opening for the uniform distribution of the metal nanoparticles, avoiding their agglomeration.

In some studies, the application was not experimentally evaluated, even though researchers suggested some possibilities for future use of the material. For example, Guo et al. (2020b) and Vacchi et al. (2020) performed functionalization with biomolecules and proposed future use for multifunctional applications in therapy, biosensing, and bioimaging. Some functionalizations were also made for GO reduction (Khanra et al., 2012; Price et al., 2019; Javidparvar et al., 2020). Table 3 contains studies in which functionalization via epoxide was carried out, along with both tested and suggested applications.

This section will cover the main approaches used in functionalizing the epoxide groups, discussing the influence of the medium, such as the solvent and pH.

3.1 Epoxide functionalization conditions

Some factors that can influence functionalization are the temperature, solvent, and pH of the reaction. Although the defects of the GO structure are a factor that can be considered, due to the positioning of the groups, there are not enough studies on how the defects can influence the functionalization outcome.

Functionalization via the epoxide ring is usually carried out at room temperature and at temperatures up to 90 °C (see conditions in Table 3). Higher temperatures can reduce the GO, so they are usually avoided. At 100 °C for 30 min, GO already loses a large portion of its oxygenated groups, leading to the production of rGO; at 200 °C, practically all GO is converted to rGO (Kumar et al., 2021).

In the majority of studies, the effects of temperature are not discussed, but we can highlight two studies in which the effects of temperature during functionalization via epoxide were evaluated. One evaluated the epoxide opening by amine at room temperature and at 90 °C to investigate the impact of temperature on the reduction process. The results showed that treatment at room temperature did not lead to a reduction while heating to 90 °C resulted in a partial reduction of GO (Ranishenka et al., 2021). Sun et al. (2018) conducted a study of reaction temperature in which GO

TABLE 3 Conditions and applications of some routes of functionalization of GO via the epoxide ring.

Solvent	Conditions (temperature, pH, atmosphere)	Functionalizing	Application	References
Aqueous	Basic pH (approximately 8,5), 60 °C, 6 h of stirring. Possibility of undergoing further functionalization	Imidazole and palladium nanoparticles	Catalysis: oxidative amidation of aldehydes	Surabhi et al. (2022)
	Neutral pH, 35 °C–40 °C, 72 h	Bakers yeast	Environmentally friendly reduction of GO to rGO	Khanra et al. (2012)
	Acid pH, 80 °C for 24 h	Cysteine	Coating to prevent corrosion of materials	Javidparvar et al. (2020)
Ethanol 20%	Argon atmosphere, room temperature, 72 h	(tert-butoxycarbonyl) aminoethanethiol	Potential for future applications in biomedicine	Guo et al. (2020b)
DMSO	N_2 atmosphere, 50 °C, 5.5 h	Potassium thioacetate	Potential for future applications in catalytic and electrochemical reactions	Thomas et al. (2014)
Ethanol	48 h, reflux	Sulfanilic acid	Potential application for high capacitance electrodes	Khan et al. (2021)
		2-amino naphthoquinone		
DMF	4 h, addition of base catalyst (N,N-diisopropylethylamine, triethylamine, 1,8-diazabicyclo [5.4.0]undec-7-ene)	Cysteamine hydrochloride	Potential application in drug delivery, depollution, and diagnostic agents	Piñeiro-García et al. (2021)
	48 h, room temperature	Boc-monoprotected triethylene glycol	Potential use for nanomedicine	Vacchi et al. (2020)
H_2SO_4	80 °C, 2 h	n-pentanol	Transforming GO to rGO	Price et al. (2019)
		t-butanol		
Ionic liquid (IL)	Imidazolium-based ionic liquids, 24 h, room temperature	Following a mass ratio of GO/IL=5	Membranes for ion separation	Tan et al. (2022)

was modified with p-phenylenediamine (PPD) in aqueous media for 24 h. There was no pH adjustment, and different samples were obtained by controlling the reaction temperature to 10, 30, 50, 70, and 90 °C. Based on the characterizations, the authors concluded that when the reaction temperature was 10–70 °C, GO was linked with PPD through non-covalent interactions such as ionic interactions ($–COO^- – H_3^+N–R$) and hydrogen bonds ($C–OH\ldots H_2N–X$). When the reaction temperature reached 90 °C, GO was functionalized with PPD through covalent C–N bonds, which they attributed to the attack of PPD on the carboxyl and epoxy groups of GO. In this study, a higher temperature was necessary to form the covalent bond. However, the effects of temperature are expected to vary for each grafting group and for each type of mechanism. A change in the pH of the medium could also modify the formation of the covalent bond at lower temperatures.

According to Le et al. (2018), the atmosphere in which a reaction occurs can also influence it; reactions at high temperatures in the air lead to the reaction of the carbonaceous skeleton with oxygen, whereas, in non-oxidative atmospheres and at high temperatures, it leads to the loss of functional groups, maintaining the carbonaceous structure.

Functionalization via epoxides can be conducted in solvents such as water, dimethylformamide (DMF) (Piñeiro-García et al., 2021), tetrahydrofuran (THF) (Collins et al., 2011b; Ha et al., 2016), and dimethyl sulfoxide (DMSO) (Thomas et al., 2014). In choosing the solvent, it is important to consider some points, the first being the solubility of the GO in the chosen solvent. GO can be dispersed in water and even interact with polar solvents. This is determined by the quantity of oxygenated groups in the structure; GO can thus be partially soluble in high-polar solvents such as DMSO.

The dispersibility of GO in polar solvents is related to the dipole moment and the superficial tension of the solvent; solvents that have high dipole moments, like NMP, propanol, and water, can be used to achieve GO dispersion, changing the stability of the dispersion depending on the solvent used (Paredes et al., 2008; Sainz-Urruela et al., 2022). With the dispersion of GO, it is possible to functionalize the structure. In addition to temperature, atmosphere and solvent, the pH is another factors that can influence the functionalization outcome. In changing the pH, the mechanism for functionalization can change, and although they are not well-established, much of the discussion is usually based on classic epoxide ring-opening reactions (i.e., without the GO structure).

Functionalization with polymers such as polyaniline (PANI) and poly 3, 4-ethylenedioxythiophene (PEDOT) shows great results and can be made in aqueous and non-aqueous media. With further study, it is possible to relate the pH effect on polymers as well as functionalization, as this effect is not well established in functionalization with polymers (Kuilla et al., 2010). Some functionalization reactions and the necessary conditions are shown in Table 3.

In aqueous media, the main factor that can influence the reaction is the pH; different ranges create different conditions,

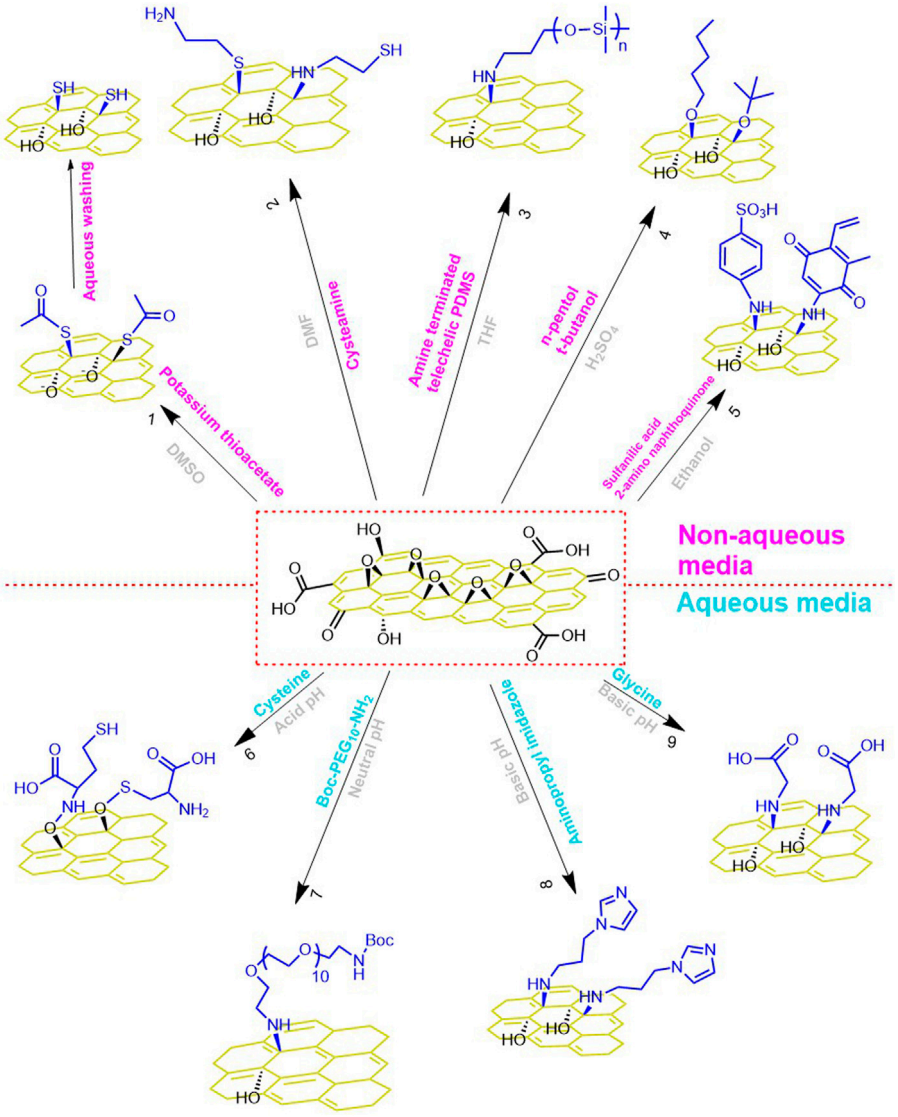

FIGURE 6
General schematics of some reported functionalization routes via epoxy-ring opening in aqueous and non-aqueous media.

changing the temperature at which the reaction can occur and limiting the reagents that can be used under determined conditions (Kasprzak et al., 2018; Price et al., 2019; Guo et al., 2022; Sainz-Urruela et al., 2022). The use of non-aqueous media can produce harsher conditions than with aqueous media, with higher temperatures and longer reactions; however, the use of different solvents means that functionalization might not happen in an aqueous medium. Figure 6 shows some functionalizations and the conditions of each reaction.

3.2 pH effects

Functionalizing the epoxide group in water offers better environmental conditions and often does not need a coupling reagent for the attachment of new nucleophilic groups (Kasprzak et al., 2018). The functionalization reaction will occur with the epoxide ring opening, with pH being the main factor affecting the reaction (Thomas et al., 2014; Fallah-Mehrjardi et al., 2018; Guo et al., 2020a). The use of a basic solution is one of the main methods of opening the epoxide ring, following an S_N2 mechanism, with a nucleophilic attack on the electrophilic carbon from the epoxide (S_N2) (Figures 7–I) or the carbon double bond which is adjacent to the epoxy moiety (S_N2') (Figure 7-I') (Thomas et al., 2014; Fallah-Mehrjardi et al., 2018). This modification of GO is possible due to the high nucleophilicity of the ligand, making it possible to perform an attack at 180° on the carbon in an S_N2 reaction, breaking the C–O bond and generating a GO–Nu bond (Kumar et al., 2022) (Figures 7–II). If the attack occurs in the electrophilic carbon, the nucleophilic group has to make the interaction in the opposite face; otherwise, if the attack occurs in the double-bound carbon, the approach can be in the same face or the opposite, creating a hydroxyl group

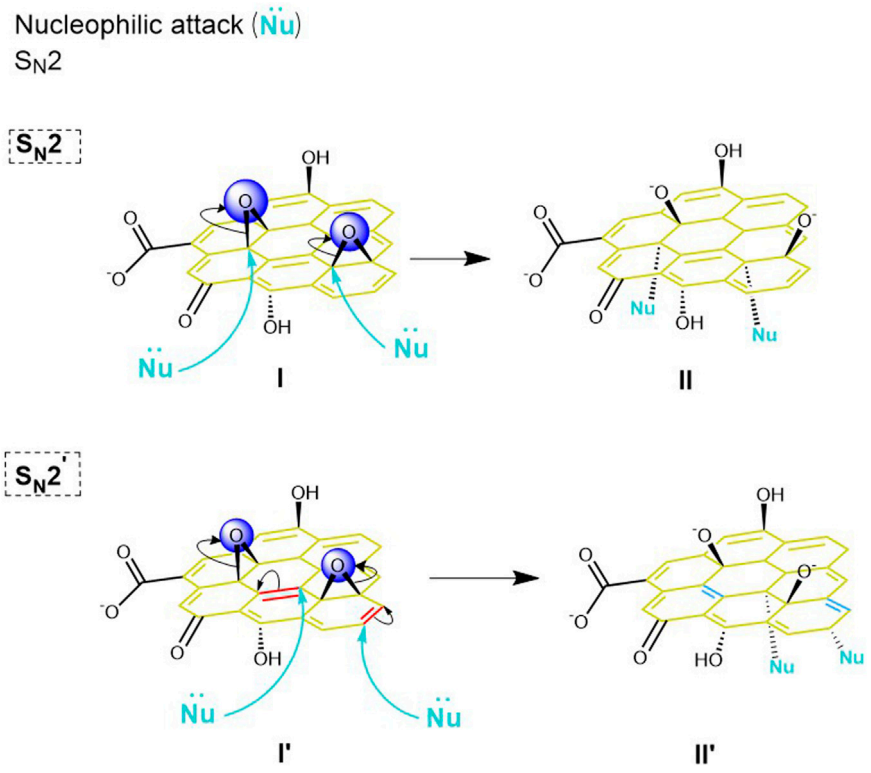

FIGURE 7
General mechanism of functionalization via the epoxide route in a basic medium. See Thomas et al., 2014; Fallah-Mehrjardi et al., 2018.

(Thomas et al., 2014; Fallah-Mehrjardi et al., 2018). With the opening of the epoxide ring, it is possible to functionalize with a nucleophilic group, with multiple reported cases of functionalization with basic solutions and the use of nucleophilic groups (Thomas et al., 2014; Fallah-Mehrjardi et al., 2018).

There is evidence that a high pH can cause the reduction of GO (Guo et al., 2022), and it is possible to observe a minimum effect on pH 8,5. However, with the increase in pH, the reduction of GO is intensified, leading the GO to have fewer oxygenated groups and more defects on its basal plan, affecting functionalization (Guo et al., 2020a; Guo et al., 2022). Research is still conflicting regarding the pH range in which the reduction will be harsh on the GO structure. Some studies indicate that the reduction of GO at pH levels as high as 13 is not sufficient to reduce its structure (Guo et al., 2020a), and others indicate that it is possible to observe low levels of reduction with basic treatment with sodium hydroxide because GO is unstable after treatment with strong bases (Guo et al., 2020a; Guo et al., 2022). The reduction of GO must be avoided in functionalization reactions since reduction makes GO lose most of its oxygenated groups, leaving fewer active sites for functionalization (Guo et al., 2020a). After alkaline treatment, GO becomes much more sensitive to temperature influence; at approximately 40 °C GO becomes unstable, leading to the rupture of its carbon backbone. If the epoxide ring opens at a higher temperature (70 °C), the reaction becomes irreversible. These conditions can cause the reduction of GO, creating defects and the eventual disintegration of the flakes (Guo et al., 2022).

Surabhi et al. (2022) performed the functionalization with 1-(3-aminopropyl) imidazole on the GO structure via an epoxide ring opening made with KOH in aqueous media; see Figure 6.8 for a general schematic. It was further functionalized with palladium nanoparticles (Pd NP) for nanocatalysis of oxidative amidation of aldehydes. In this synthesis, a harsher condition was used in comparison to other functionalizations on the epoxide ring, but these conditions were not enough to cause reduction and any kind of defects in the GO structure (Guo et al., 2022; Surabhi et al., 2022). However, at this temperature (60 °C) the reaction will be irreversible (Guo et al., 2022).

Guo et al. (2020a) studied different types of functionalizations O-(2-aminoethyl)-O0 -[2-(Boc-amino)ethyl]decaethylene glycol (BocNH-PEG10-NH2). In this study, the functionalization of the epoxide ring was made at a neutral pH (Figure 6.7). Other types of functionalization besides epoxide functionalization were compared: other functionalizations with carboxylic acids were made, making use of activating agents, and hydroxyl functionalization to increase the amount of carboxylic acid in the structure. The number of amino-PEG groups in the GO structure was quantified with the Kaiser test. The study showed that after further functionalization of the GO structure, part of the functionalized groups was partially removed from the structure. This was probably because the reduction of the GO structure, caused by the amount of NaOH used, created a highly alkaline solution that reduced GO. The reaction was repeated with a lower concentration of NaOH, achieving pH ranges of 9–13. It was observed that solutions with

a higher pH had suffered a higher reduction. XPS analysis did not show the expected increase in the amount of carboxyl groups, and epoxy groups also suffered a reduction. Even though the results showed that GO had been reduced, this was not severe, so it was possible to make further functionalizations in the epoxy groups at a neutral pH for 3 days. It was possible for Guo et al. (2020a) to see the benefits of the epoxide ring opening without any further functionalization and how strong basic conditions affect GO structure.

Khanra et al. (2012) conducted a study to develop an eco-friendly and cost-effective method for functionalizing and reducing GO. The functionalization was achieved at neutral pH using baker's yeast to utilize the enzyme nicotinamide adenine dinucleotide phosphate (NADPH) as a reducing agent, thereby facilitating the GO reduction. The functionalization was carried out under mild conditions, resulting in the expected GO reduction.

Acid pH can also be used to functionalize the epoxide ring, although the mechanism is not yet well established for the GO structure. In general, the mechanism in epoxides will be an S_N1, with the attack occurring at the more substituted carbon, but research is necessary to establish this type of mechanism for GO (Fallah-Mehrjardi et al., 2018). Tanighuti et al. (2015) studied the influence of pH on the opening of GO epoxide rings and proposed that in an acidic environment, the reaction occurs through a mechanism involving the formation of carbocations and hydroxyl. The reaction of the hydroxyl group with the carbocation occurs preferentially, generating a highly reactive protonated epoxy group that can be cleaved by weak nucleophiles such as water, ultimately generating two hydroxyls. Furthermore, the delocalization of positive charges leads to lower reactivity of the protonated epoxy groups in the GO plane. As a result, much less epoxy ring opening reaction in GO occurs at a neutral or acidic pH.

Javidparvar et al. (2020) carried out functionalization with cysteine on the GO structure (Figure 6.6). This study used a sustainable nanocarrier with the capacity to absorb cerium ions to improve its anti-corrosion properties. To functionalize GO, a pH range of 2–3 was used (Javidparvar et al., 2020). Functionalization in acidic pH is not usual but there are some reports benefiting from this condition. In this range of pH, the reduction of the GO is avoided; however, temperatures as high as 80 °C as used in the study can cause a reduction.

Functionalization in aqueous media is possible in different ranges of pH but is easier with basic pH and is consequently a faster way of achieving functionalization in aqueous media (Khanra et al., 2012; Kasprzak et al., 2018; Price et al., 2019; Javidparvar et al., 2020; Piñeiro-García et al., 2021; Guo et al., 2022; Surabhi et al., 2022; Singh and Kar, 2023). Moreover, functionalization in neutral or acidic pH can occur at higher temperatures, and those conditions can also change depending on the stability of the functionalization and GO (Khanra et al., 2012; Guo et al., 2020a; Guo et al., 2022; Surabhi et al., 2022; Singh and Kar, 2023). The majority of studies do not explain the use of some pH ranges, temperatures, and mechanisms involving reactions, so it is not possible to draw general conclusions on which pH range to use at certain types of functionalization on the epoxide groups. However, it is possible to observe that the main influences on functionalization in aqueous media are pH, temperature, and time of reaction. Controlling these conditions allows new functionalization reactions in the epoxide ring that would normally not be possible without a basic or neutral medium.

3.3 Functionalization in a non-aqueous solvent

The functionalization reaction by epoxide ring opening can be performed in non-aqueous media if necessary. GO has different solubility and dispersion behavior depending on the solvent used. GO can be dispersed in some solvents like ethanol and dimethyl sulfoxide (DMSO), but the dispersion is not stable, precipitating in a matter of hours or days. Other solvents like tetrahydrofuran (THF), dimethylformamide (DMF), ethylene glycol, n-methyl-2-pyrrolidone (NMP), and water can form stable dispersions that do not precipitate (Paredes et al., 2008). Therefore, some factors that affect the planning of GO functionalization on non-aqueous media are the behavior of GO in the medium and the solubility of the functionalization in the medium. Other decisive factors in the choice of the solvent can be the use of catalysts (Ramírez-Jiménez et al., 2018; Piñeiro-García et al., 2021) or synergistic effects between the solvent and reagents. Using aprotic polar solvents such as DMF can facilitate S_n2 reactions, which include the epoxide ring-opening reaction because these solvents can solvate positively charged ions while not interacting as well with anions, therefore increasing their reactivity as nucleophiles and thus enhancing reaction rates (Clayden et al., 2012; Solomons et al., 2016). Therefore, when using anionic nucleophile reagents, the utilization of polar aprotic solvents can be considered. Epoxide ring opening functionalization has been reported in many solvents, like DMF (Shim et al., 2012; Vacchi et al., 2016; Ramírez-Jiménez et al., 2018; Vacchi et al., 2020; Piñeiro-García et al., 2021), DMSO (Thomas et al., 2014), ethanol (Lin et al., 2010; Guo et al., 2020b; Khan et al., 2021), sulfuric acid (Price et al., 2019), and THF (Collins et al., 2011b; Ha et al., 2016).

Polymer/GO composite synthesis is done in aqueous and non-aqueous media (Kuilla et al., 2010; Shim et al., 2012; Lowe, 2014; Gao, 2015; Ha et al., 2016). For elastomers produced with poly (dimethylsiloxane) (PDMS) and GO, THF was used because of its ability to solubilize PDMS. The objective of this study was to create a facile method for producing elastomers with polymers and GO in which the GO showed capabilities of crosslinking and filling the polymer to form a solid product with the added function of acting as a gas barrier. The authors used functional telechelic PDMS, functionalized at both ends with primary amines, which were dissolved in THF; GO was then added and dispersed by sonication in an ice bath. After drying in a Teflon dish for 3 days (2 days normal atmosphere, 1 day vacuum) at room temperature, a liquid solution of uncrosslinked PDMS/GO was obtained, which was then heated to 160 °C in a vacuum oven for 24 h to form the solid crosslinked PDMS/GO elastomer. This temperature is known to thermally reduce GO (Jung et al., 2008; Gao, 2015), which the authors did not acknowledge. The elastomer formed was mechanically resistant, as verified by rheological testing, and showed a reduction in single gas permeability compared to the neat PDMS, which was attributed to the gas adsorption in the GO dispersed phase. FTIR and XPS were used to characterize the polymer composite (Ha et al., 2016).

Functionalization via epoxide ring opening proved to be useful when multi-functionalizing because it is done mostly under moderate conditions without modifying other oxygenated groups of GO while also increasing hydroxyl moieties as a by-product of

epoxide ring opening. The study by Khan et al. (2021) is an example, where many bifunctionalized GOs were synthesized to endow the composites with redox and acidic properties and to develop proton conductive electrodes and high capacitance electrodes. They utilized an epoxide ring opening followed by a Michael addition reaction with *α, and β*-unsaturated carbonyl compounds as a method of double functionalization with the synergistic approach mentioned previously. This study synthesized eleven different functionalized GOs, six of which were monofunctionalized to serve as a comparison. Khan et al. (2021) made use of three different solvents—water, ethanol, and toluene. For the sake of this review and the topic to be discussed, only the functionalization with ethanol as a solvent will be addressed since aqueous media was already explored in the previous sections and toluene is utilized as a solvent for the Michael addition reaction step.

The epoxide ring opening reaction utilized two compounds with a primary amine, which proved to be a good nucleophile in this regard—the first was sulfanilic acid for its proton conductivity function, and the second compound was 2-amino naphthoquinone for its redox-active function. The primary amine compounds were dissolved in ethanol and added to a GO aqueous dispersion. The mixture was sonicated and then refluxed for 48 h, followed by purification via centrifugation and washing. All the functionalized GO thus obtained were characterized via FTIR and XPS, confirming the nature of the GO composites. The double-functionalized samples showed an increment in properties (proton conductivity and capacitance) compared to monofunctionalized samples; the results confirm the efficiency of the double-functionalization method proposed and highlight the capabilities of modulating the physical and chemical properties of GO in mild conditions (Khan et al., 2021).

The epoxide ring opening reaction needs a nucleophilic attack to open the epoxide ring; a strong nucleophile is the thiolate anion that is obtained by removing the hydrogen proton from a thiol moiety. A good source of thiolate anion is potassium thioacetate, used by Thomas et al. (2014) to functionalize GO. The authors proposed a facile method for epoxide ring opening functionalization in DMSO. First, the GO was base washed to remove oxidative debris, leading to bwGO that was dispersed in DMSO via sonication. The dispersion was submitted to an N_2 atmosphere, followed by the addition of potassium thioacetate. When the synthesis was completed, the material was washed multiple times. The aqueous washing was expected to result in the hydrolysis of the thioacetate, leaving surface-bound thiol groups. The material obtained was named GO–SH and was characterized by FTIR, XPS, EDX, solid-state RMN, TEM, and TGA, confirming the study's propositions. Thiol is a hanging group on the surface plane of GO, which can lead to multiple new syntheses and applications. Thomas et al. (2014) anchored gold nanoparticles (AuNP) due to the strong interaction between sulfur and gold, as well as the ability to add a butane moiety to the thiol, demonstrating the diversity of possibilities of the material. Some of the applications suggested were in catalysis and electrochemistry due to the selectivity and reactivity of AuNP, as well as grafting polymers via thiol-ene "click" reactions (Lowe, 2014; Thomas et al., 2014; Piñeiro-García and Semetey, 2023).

Base catalysts, also known as non-nucleophilic bases, can be used to enhance the nucleophilicity of compounds by deprotonation of acidic hydrogen; one example was in the functionalization of GO with cysteamine by Piñeiro-García et al. (2021). They utilized three different base catalysts—N,N-diisopropylethylamine (DIPEA), triethylamine (NEt_3), and 1,8-diazabicyclo [5.4.0]undec-7-ene (DBU) —to generate the thiolate anion on the cysteamine molecule and thus improve its nucleophilicity. Four materials were produced in THF as a solvent, three with the addition of the different base catalysts, and one for control. Samples characterizations were made with XPS and STEM, while a colorimetric titration was performed to quantify the primary amine moieties after GO functionalization. Cysteamine has two different nucleophilic groups, an amine (-NH_2>) and a thiol (-SH). Due to the lower pKa of the thiol group than the amine group in this molecule, the thiolate anion was formed when base catalysts were added. This is a stronger nucleophile than the amine, which means that secondary amine moieties were not found on the functionalized GO samples, which is confirmed by the XPS's N1s deconvolution analysis. Therefore, the addition of base catalysts to polar aprotic solvents can determine which of the nucleophiles in cysteamine will react, thus breeding a selective medium. This study was done to learn about the competing reactions of epoxide ring opening and thiol-ene Michael addition, concluding that both reactions happen simultaneously on the GO sample (Piñeiro-García et al., 2021).

Epoxide ring opening reactions may also occur in non-aqueous acidic conditions, such as when utilizing sulfuric acid as a solvent. GO was functionalized by Price et al. (2019) with n-pentanol and t-butanol, named GO-p and GO-tb, respectively, with the purpose of studying the wettability and dispersibility of the modified GO. The functionalized GO was prepared with sulfuric acid as a solvent, then extracted with hexane and washed with HCl and ethanol. The samples were characterized via TGA, FTIR, Raman spectroscopy, XPS, and DRX. The researchers concluded that the functionalization was successful and that the samples suffered a mild reduction due to the temperature and extremely acidic medium. Epoxide ring opening was not the only pathway of functionalization in this case—it is possible that a Fischer esterification occurred simultaneously. The addition of the alcohols and the reduction of the GO modified its hydrophilicity, turning the material hydrophobic and changing its dispersibility in apolar organic solvents like hexane. Since the reaction is not selective and the conditions are considerably harsh, this functionalization methodology deviates from those typically done via epoxide ring opening, offering a different approach for GO functionalization (Price et al., 2019).

In conclusion, the use of non-aqueous solvents offers a good alternative in cases where water is impractical. It also has synergistic effects when the nucleophile utilized is anionic, thus facilitating the S_n2 epoxide ring opening reaction (Clayden et al., 2012; Solomons et al., 2016).

4 Characterization techniques

Good characterization of GO and its modifications can lead to a better understanding of the chemoselectivity and regioselectivity of each route of GO modification, making correctly characterizing GO and its modifications a difficult

TABLE 4 Some techniques used to characterize epoxy functionalized GO.

Technique	Application in epoxy GO functionalizations	Limitations	References
FTIR	Assign bands to GO and its news functional groups	Some functional groups are difficult to access due to similarity to the background and bands can be ambiguous at the fingerprint region. With low degrees of functionalization, it is usually hard to assign bands.	Xue et al. (2015), Zhang et al. (2015), Cakici et al. (2017), Zhu et al. (2018), Elsie et al. (2019), Meng et al. (2019), Payami et al. (2020), Yu et al. (2020), Zheng et al. (2021), Khan et al. (2021), Kumar et al. (2022), Meng et al. (2022), Tan et al. (2022), Ding et al. (2023)
Raman	Quantify GO defects, assign typical bands of GO.	Information is not decisive about the functionalized group.	Kudin et al. (2008), Kuilla et al. (2010), Khanra et al. (2012), Monteiro et al. (2020)
TEM	Details different thickness levels in GO morphology	Expensive and complex procedure. Information is not decisive about the functionalized group.	Zhang et al. (2016), Chau et al. (2017), Alzate-Carvajal et al. (2018), Jiang et al. (2019), Kang et al. (2019), Meng et al. (2019), Shi et al. (2020), Meng et al. (2022)
SEM	Morphology	Complex procedure Information is not decisive about the functionalization and the group	Chau et al. (2017), Alzate-Carvajal et al. (2018), Jiang et al. (2019), Kang et al. (2019), Meng et al. (2019), Payami et al. (2020), Shi et al. (2020), Meng et al. (2022)
AFM	Topographic map and mechanical properties	Information is not decisive about the functionalization and the group.	Jiang et al. (2019), Meng et al. (2019), Meng et al. (2022)
AFM-IR and AFM-Raman	Maps functionalization on samples	Complex and expensive procedure	Bartlam et al. (2018), Liu et al. (2018), Liu et al. (2019), Pérez et al. (2019)
TGA	Shows profile of weight loss per temperature, assigning a percentage of functionalization via epoxide groups in GO.	Difficult to access the percentage of functionalization considering the molar mass of the introduced nucleophile.	Chai et al. (2013), Chau et al. (2017), Alzate-Carvajal et al. (2018), Zhu et al. (2018), Elsie et al. (2019), Jiang et al. (2019), Zheng et al. (2021), Meng et al. (2022), Ding et al. (2023)
NMR	Identify new structures on GO and assign functionalization specifically via epoxy ring opening.	Limited to a large number of samples (10 mg). Needs to strongly optimize the analyses and takes a long time to obtain the spectra.	Casabianca et al. (2010), Vacchi et al. (2016), Vacchi et al. (2020)
XRD	Crystallinity and interlayer distances	Information is not decisive about the functionalized group.	Thomas et al. (2014), Xue et al. (2015), Payami et al. (2020), Ding et al. (2023)
XPS	Assign GO functionalization via epoxy ring opening by the formation of new bonds with epoxide carbon, even with a low degree of functionalization.	Expensive technique and difficult data analysis	Zhang et al. (2015), Chau et al. (2017), Zhu et al. (2018), Krishna and Philip (2022), Santos et al. (2022), Surabhi et al. (2022), Ding et al. (2023)
N_2 porosimetry	Determine the surface area in GO samples	Limited to a large number of samples. Information is not decisive about functionalization and group.	Payami et al. (2020), Zheng et al. (2021), Surabhi et al. (2022)

and necessary challenge. Due to its various forms of storage and its highly complex structure, several interferences and limitations can occur; some of them are due to the overlap of data in the same analysis or to insufficient or hard-to-optimize instrumental equipment (Guo et al., 2022).

The characterization of functionalized GO aims to understand its morphology, possible uses, and the extent of the nanomaterial's successful functionalization. To achieve this, techniques such as FTIR spectroscopy (Acik et al., 2011), X-ray photoelectron spectroscopy (XPS) (Yang et al., 2009), solid-state NMR spectroscopy (SSNMR) (Casabianca et al., 2010), electrochemical methods (Chua and Pumera, 2013), and thermogravimetric analysis (TGA) are utilized (Sharma et al., 2013; Rani et al., 2014). Particle size may also be characterized in solution using DLS and other laser scattering methods (Hong et al., 2012) or solid-state techniques such as TEM (Kumar et al., 2012) or AFM (Lu et al., 2010). Techniques can also characterize the surface area, such as BET methods (Brunauer et al., 1938), and the interlayer spacing in the powdered GO material can be determined via powder X-ray diffraction (Mu et al., 2013). The extent of defects in the lattice as well as the number of layers in the stacked structure can be measured using Raman spectroscopy (Kudin et al., 2008). Other advanced techniques have also been reported, such as integrated differential phase contrast scanning transmission electron microscopy (iDPC-STEM) (Wu et al., 2023), thermogravimetry-Fourier transform infrared spectroscopy-mass spectrometry (TG-IR-MS) (Liu et al., 2023), X-ray absorption spectroscopy (XAS), and X-ray absorption near edge structure (XANES) (Han et al., 2020).

Some characterization techniques are summarized in Table 4, and this section will cover the techniques usually used for GO modified via epoxy ring opening. It will consist of a brief explanation of the data that each technique provides and then an explanation, if necessary, to detect the functionalization of GO samples.

4.1 Fourier transform infrared (FTIR)

FTIR spectroscopy makes it possible to easily determine and identify functional groups grafted to GO using the vibrational modulus of the bonds formed between the grafted species and GO (Pintus et al., 2023). The experimental modes that are most used are the attenuated total reflection (ATR) and the use of KBr pellets. These are differentiated mainly in the sample preparation, which may be necessary as a function of how it was stored (powder, film, or dispersion) or responds to the experiment (Trikkaliotis et al., 2021; Pintus et al., 2023).

GO characterization using FTIR data has been widely reported (Khanra et al., 2012; Thomas et al., 2014; Zhang et al., 2015; Zhang et al., 2016; Javidparvar et al., 2020; Piñeiro-García et al., 2021; Trikkaliotis et al., 2021; Guo et al., 2022; Surabhi et al., 2022). The analysis of both the non-functionalized GO and the functionalized spectrums—for example, the immobilization of imidazolium-based ionic liquids on GO—was supported in Zheng Y. et al. (2021) and Tan et al. (2022) with the appearance of N–H and C–N stretching. The new modulus is thus identified and attributed to the GO–ligand bond, evidencing functionalization (Payami et al., 2020; Zheng Y. et al., 2021; Khan et al., 2021). It is also possible to assign the epoxide band in the pure GO sample and compare its intensity in the functionalized one; there is expected to be a decrease in this band after functionalization (Ha et al., 2016). One good example was reported by Zheng Y. et al., 2021, where the authors functionalized rGO with octylamine, decylamine, and dodecylamine via epoxide ring opening. Comparing all the functionalized spectra with those from the precursor, the decrease in epoxide band intensity is clearly evident (Ha et al., 2016; Zheng A. et al., 2021).

However, FTIR encounters limitations in determining bands in samples with low degrees of functionalization and in identifying a wide range of functional groups due to their similarity to GO's background and fingerprint region (Pintus et al., 2023). Identifying and quantifying hydroxyls and epoxides in GO for confirmation of functionalization presents an even greater challenge. The assignment of epoxide bands in GO using FTIR often leads to conflicting outcomes.

Advancements in characterizing groups within basal planes using polarized ATR-IR have emerged as a solution. Polarization techniques offer a means of differentiating the contributions of various molecular orientations in the IR spectrum, yielding insights into the organization of molecules on the sample surface. This approach has been successfully applied to a variety of materials, including polymers (Hikima et al., 2019; Perret et al., 2021), molybdate composites (Davantès and Lefèvre, 2016; Botella and Lefèvre, 2022), proteins (Ausili et al., 2011), and graphene derivatives (Wang et al., 2016; Botella et al., 2022). Botella et al. (2022) demonstrated the potential of polarized ATR-IR spectroscopy in the characterization of graphene oxide (GO). By applying polarization angles of 0° and 90°, the researchers were able to analyze GO layers aligned along the x–y plane, identifying differences in both x–y (parallel components) and z (perpendicular component) orientations. Additional investigations within the 1,500–1,000 cm^{-1} range helped elucidate specific band assignments, revealing disparities in epoxide vibrations between the edge and basal plane groups. For instance, GO shows signals at 1,152 cm^{-1} for epoxides on the basal plane and 1,053 cm^{-1} for those at the edges (Botella et al., 2022).

4.2 Raman spectroscopy

Raman spectroscopy is often used since conjugated and double carbon–carbon bonds lead to high Raman intensities (Kudin et al., 2008). This method of characterization provides a simple structural characterization of graphene derivatives by the appearance of bands typical of these nanomaterials (Kuila et al., 2012). Bands typical of GO consist of the D and G bands, where the D band, present at 1,356 cm^{-1}, is related to defects in its surface, and the G band, present at 1,583 cm^{-1}, corresponds to plane vibrations of sp2 carbon (Kudin et al., 2008).

Utilizing the measurement of the band area in the obtained spectra can extract the I_D/I_G ratio values, which offer insights into the level of disorder present in the structure. This disorder can occur due to the interaction between oxygenated and functionalizing groups. Therefore, a greater ID/IG predicts a higher disorder in the functionalized GO structure, indicating more groups on its surface, although there is debate about this (Monteiro et al., 2020).

At around 2,650 cm^{-1}, we have a band known as the 2D band, which is related to the structural organization of GO sheets, indicating the number of layers (Kuila et al., 2012). Considering this, it has been deduced that Raman spectroscopy could clearly distinguish between a single layer, a bilayer, and several layers, given that the number of layers alters the shape of the band (Monteiro et al., 2020). Other bands are observed at 2,930 and 3,170 cm^{-1}, corresponding to the D+G and 2G bands, respectively, which are also characteristic of these materials (Kaniyoor and Ramaprabhu, 2012).

The information from Raman analysis can produce evidence of functionalization, but cannot prove it. Once the epoxy ring opens on a basic medium, it can lead to the formation of new defects or even to a reduction of the carbon structure (Guo et al., 2022). Moreover, it is important for reliable data to have many regions analyzed.

4.3 Microscopic techniques

Atomic force microscopy (AFM), transmission electron microscopy (TEM), and scanning electron microscopy (SEM) can be all used to characterize GO's morphology and structure (Zhang et al., 2016; Chau et al., 2017; Alzate-Carvajal et al., 2018; Jiang et al., 2019; Kang et al., 2019; Meng et al., 2019; Payami et al., 2020; Shi et al., 2020; Zheng A. et al., 2021; Ranishenka et al., 2021), thickness (Alzate-Carvajal et al., 2018; Jiang et al., 2019; Meng et al., 2019; Meng et al., 2022), and porosity (Zheng A. et al., 2021). These microscopy techniques are commonly used together: AFM mainly generates the topographic and mechanical proprieties map, while SEM and TEM work mostly to visualize the GO sheets. A comparison of differences between non-functionalized and functionalized can elucidate some properties. Shi et al. (2020) used AFM and SEM to justify the increase in mechanical stability after the 1-octadecylamine and 1,12-diaminododecane were grafted, with the images showing that the functionalized sample became relatively more ordered

than GO (Alzate-Carvajal et al., 2018; Meng et al., 2022). Meng et al. (2022) used these three techniques to measure GO and grafted GO: the thickness was determined with AFM measurements, while SEM and TEM were used to better understand the surface roughness and how the addition of a group affected the interaction between GO sheets and the interlayer spacing.

These characterizations can detect some evidence of chemical modification of GO with changes in morphology or roughness, although microscopy is the least reliable for confirming functionalization because the conditions of the reactions can cause changes in morphology and roughness even if the functionalization does not occur. It is important to analyze these data, knowing that it is a complementary analysis of GO functionalization.

Although microscopy techniques alone do not produce much information about functionalization, when combining AFM with spectroscopic techniques, it is possible to map the functional groups (Bartlam et al., 2018; Liu et al., 2018; Liu et al., 2019; Pérez et al., 2019). The outstanding combinations are AFM coupled with FTIR (AFM-IR) (Bartlam et al., 2018; Liu et al., 2018; Liu et al., 2019) and Raman (AFM-Raman) (Pérez et al., 2019). These techniques' main disadvantages are high equipment costs and difficult sample preparation. However, their main advantage is that they can give valuable information on the nature of the functional groups and their distribution.

Using AFM-IR, Liu et al. (2019) mapped the functional groups on GO sheets, demonstrating that different groups can be found on the basal plane and borders. They also successively characterized GO groups in a way that is usually difficult, such as differentiating ketones from the carbonyl groups in the infrared spectra. Therefore, a spectrum of specific regions of a modified GO can be used to prove not just the modification but whether it occurred on the basal plane or border (Bartlam et al., 2018; Liu et al., 2018; Liu et al., 2019).

Experiments such as AFM-Raman yield important information about defects in structure and how the intensity of the D and G bands is distributed throughout the sample. This makes it possible to map the I_D/I_G distribution, as reported by Pérez et al. (2019), who mapped the D and I_D/I_G. With this map, they could understand which regions have more oxygenated groups and where it was modified most.

4.4 X-ray photoelectron spectroscopy (XPS)

XPS usually is used to obtain the chemical composition of nanomaterials and information about surface functionalization (Zhang et al., 2015; Chau et al., 2017; Zhu et al., 2018; Krishna and Philip, 2022; Ding et al., 2023). It can also be a tool for characterizing layer thickness, adsorbates, and even nanoparticle size (Krishna and Philip, 2022). Through XPS, it is possible to demonstrate the modification with different groups and calculate the ratio between the abundance of certain atoms in the sample (Chau et al., 2017; Zhu et al., 2018; Ding et al., 2023). Analyzing the changes between the non-functionalized and functionalized GO makes it easy to confirm the grafting of different ligands (Zhang et al., 2015; Ding et al., 2023).

Estimating the presence of hydroxyls and epoxides poses a challenge because of the subtle variations in binding energies within the X-ray photoelectron spectra (XPS) of C 1s and O 1s. Rabchinskii et al. (2022) employed a technique involving the analysis of XPS spectra alongside data from NMR and infrared (IR) spectroscopy. By utilizing density functional theory calculations, they successfully pinpointed and characterized distinct spectral components linked to epoxide and hydroxyl groups within the C 1s spectra.

The decrease of C 1s peaks associated with epoxy and hydroxyl groups, Surabhi et al. (2022) was assigned to the functionalization via epoxy ring opening in the reaction between GO and 1-(3-aminopropyl) imidazole. They also identified another peak appearing after the functionalization attributed to N 1s, corresponding to the imidazole nitrogen. This process is widely used; another example is Khanra et al. (2012), who functionalized it with baker's yeast and reduced GO. Both events were visible in XPS, in which the decrease in intensity in the oxygenated groups is relatable to the reduction and new amine groups appearing from the functionalization with amine groups from baker's yeast.

In the various techniques, XPS stands out for confirming functionalization. As it gives precise and quantitative information about the bonds, it is easy to identify the formation of new bonds and the decrease of the bond in the exact position where the new ligands were grafted. XPS also provides quantitative information about bonds, enabling the identification of new bond formations and reductions in bond intensity at the precise positions where new ligands were grafted (Meng et al., 2022). It proves to be a valuable tool for identifying new bond formations even at low degrees of functionalization (Krishna and Philip, 2022). Santos et al. (2022) confirmed bi-functionalization in carboxylic acid groups by distinguishing bands related to the cysteamine and imidazole derivatives anchored on graphene oxide and estimating the percentage of these groups. They also observed that signals corresponding to amides closely resembled the quantity of added groups.

4.5 Nuclear magnetic resonance (NMR)

Materials coming from graphite are often heterogeneous, noncrystalline, and insoluble, so obtaining structural data from them has been a difficult task. However, NMR can provide this crucial information about GO and modified GO, which is why solid-state NMR (SSNMR) has been employed (Casabianca et al., 2010; Vacchi et al., 2016).

Casabianca et al. (2010) studied the modeling of functionalized graphene from the analysis of GO. They showed that the combination of multidimensional experiments and chemical shift calculations is a great tool for constructing a model capable of reproducing the chemical structure. Vacchi et al. (2016) also used magic angle spinning (MAS) SSNMR, but this time aimed to elucidate the chemical reactivity of GO toward amine derivatives once it has a high reactivity due to the variety of oxygenated moieties, which can lead to many simultaneous reactions. They were able to determine that amines preferably react with the epoxy groups, not with carboxylic acids (Vacchi et al., 2016). NMR is a powerful

technique for calculating the percentage of each functional group in the GO sheet; other techniques cannot be that exact (Vacchi et al., 2020).

SSNMR analysis enables the structural characterization of GO and derivatives (Casabianca et al., 2010; Vacchi et al., 2016) and the control of their derivatization by understanding the information of chemical reactivity (Vacchi et al., 2016) and estimating the constituent functional groups in different GO samples (Vacchi et al., 2020). Although this has great advantages, SSNMR does entail difficulties. It is hard to obtain a usable spectrum due to the higher number of interactions in the sample, the low resolution and intensity of signals, the need to strongly optimize the analyses, and the time for it—the experiment usually takes days to perform.

4.6 Thermogravimetric analysis

TGA analysis is usually performed at approximately 100 °C in an inert atmosphere (nitrogen or argonium). With this analysis, the curve shows the weight loss in each temperature range, making it possible to take the first derivative to obtain the differential thermal analysis (TGA-DTA), which helps elucidate the TGA curves (Alzate-Carvajal et al., 2018; Jiang et al., 2019). All GO samples must be analyzed in this way, making it possible to understand whether there was a bond between the GO and the target group. This is done by analyzing whether there is new weight loss at a certain temperature. Many studies use TGA analysis to confirm functionalization (Alzate-Carvajal et al., 2018; Elsie et al., 2019; Jiang et al., 2019) and to estimate an approximate degree of chemical modification (Alzate-Carvajal et al., 2018; Zhu et al., 2018; Elsie et al., 2019; Jiang et al., 2019; Ding et al., 2023).

Alzate-Carvajal et al. (2018) used such data to support the functionalization of GO with a group of various amines. The first and second weight loss (between 100 °C and approximately 230 °C) was attributed to the loss of oxygenated groups, and it reported a different weight loss, which was attributed to functionalization (Khanra et al., 2012; Javidparvar et al., 2020; Piñeiro-García et al., 2021). As shown above, Guo et al. (2020a) studied the functionalization of GO with O-(2-aminoethyl)-O0 -[2-(Boc-amino)ethyl]decaethylene glycol (BocNH-PEG10-NH2). They used TGA to demonstrate functionalization, showing a new weight loss of approximately 200 °C–400 °C after the modification of GO.

TGA characterization provides important information about samples, giving clues as to whether functionalization occurred. It is possible with a control sample to estimate the number of molecules grafted on GO (Alzate-Carvajal et al., 2018; Elsie et al., 2019; Jiang et al., 2019). The method cannot identify which group was grafted, so it is usually accompanied by methods such as FTIR or XPS.

4.7 X-ray diffraction (XRD)

The suspended GO sheets tend to undergo a re-stacking process after solvent removal or due to some kind of crosslinking due to functionalization. The resulting re-stacked solid can be analyzed by X-ray diffractometry. The crystallographic analysis can provide excellent information about the interlayer distance between sheets, how the ligands are arranged between sheets, and how the functionalization process affects crystallography (Xue et al., 2015; Ding et al., 2023). Knowing the initial basal reflections of GO enables an understanding of how the new ligands are intercalated in the basal planes by calculating the shifting of the peaks (Xue et al., 2015; Payami et al., 2020). With this information, the stitching of GO with functional groups, such as ethylenediamine, can be evidenced (Xue et al., 2015; Zhang et al., 2016; Ranishenka et al., 2021), making it possible to notice that with the increase in EDA ethylenediamine, there is an increase of the peak at 26,6° with a shifting of the 12,3° peak to lower values.

The XRD peak will appear even if the bonding between GO and the functionalizing group is not a covalent bond or if it is just adsorbed on the GO surface, although the interplanar distance may change, leading to a shifting of the GO natural peaks (Xue et al., 2015). XRD also cannot precisely identify what group was added via epoxy ring opening—other techniques are required.

4.8 Brunauer–Emmett–Teller (BET) isotherms

The absorption-desorption of N_2 on GO sheets is used to estimate the surface area and pore diameter (Payami et al., 2020; Zheng A. et al., 2021). For this, the Brunauer–Emmett–Teller (BET) isotherms (Brunauer et al., 1938) are usually used for the surface area and Barrett–Joyner–Halenda (BJH) for pore size distribution (Zheng A. et al., 2021). Related to this is that the functionalization of GO can lead to an increase in the interlayer spacing (Zheng A. et al., 2021). The BET isotherms clarify the porous structures of GO and GO derivatives in their powder or colloidal forms.

Surabhi et al. (2022) used BET analysis to demonstrate that the material has a large superficial area, making it possible to incorporate Pd NP (Surabhi et al., 2022). As noted above, another use of the technique is to estimate the pore size and diameters of alkylamines in rGO hydrogels acting as spacers that lead to an increase in interlayer spacing (Zheng A. et al., 2021).

The change in surface area or pore size distribution indicates that there was probably a modification, but this is far from an accurate result. The synthesis conditions can lead to a rearrangement of the material or changing the carbon structure (Zheng A. et al., 2021), leading to modifications in the surface area.

5 Summary and future perspectives

We here present a critical analysis of the covalent functionalization of graphene oxide via epoxy groups. This is an under-explored method with great potential and stands out due to the large number of epoxide groups present in graphene oxide and the absence of coupling reagents. These generally make functionalization more expensive. Indeed, the functionalization process using epoxides can be conducted in different solvents. When selecting a solvent, it is crucial to consider the solubility of both the GO and the molecule being added. However, opting for aqueous media not only offers a more environmentally friendly approach but also ensures excellent GO dispersibility, so the use of aqueous media is recommended whenever possible. In addition, the

success of the functionalization reaction depends on the pH of the medium, which has a significant impact on the nucleophilic attack. The preference for alkaline media in this reaction has been identified by different researchers. Although some discourage functionalization in alkaline media to avoid the reduction of graphene oxide, others highlight its advantages. For example, an alkaline wash prior to epoxide functionalization can eliminate oxidative debris and facilitate nucleophilic attack on graphene oxide sheets. Furthermore, the possibility of producing materials with properties that differ from those functionalized primarily at the edges is yet another reason why we believe this route to be worth further exploration. Two major challenges were highlighted in this review: the development of controllable methodologies and characterization to confirm the modified groups. The majority of studies focus only on confirming the occurrence of functionalization without worrying about distinguishing whether more than one group was modified. However, in studies seeking controlled functionalization, some techniques adopted include pH control, the use of coupling reagents, and the reduction of graphene oxide, which may favor one synthesis route over another.

Another challenge addressed in this review is characterization. Identifying and quantifying hydroxyls and epoxides in graphene oxide (GO) and confirming their functionalization is a known challenge for all routes, but its challenge is even greater in epoxide functionalization. A specific issue arises with the assignment of epoxide bands in GO using FTIR, as different studies often produce conflicting results. Recently, advances in the characterization of groups in basal planes have been made using polarized FTIR. Furthermore, we explained that estimating the presence of hydroxyls and epoxides is made difficult by the small differences in binding energies in the XPS of C 1s and O 1s. The recent progress in XPS and theoretical studies has allowed the differentiation and characterization of spectral components associated with epoxide and hydroxyl groups in C 1s spectra. These developments contribute to ongoing research for more accurate characterization, and successful implementation of these characterization methods is essential in the epoxide or hydroxyl functionalization of materials.

The improvement of functionalization methods and the development of characterization techniques are very important for fundamental studies and for the practical use of graphene oxide materials. Strategic functionalization can broaden and improve applications in fields including catalysis, energy, and the environment. Our aspiration is that this review plays a significant role in understanding the functionalization of graphene oxide, contributing to future exploration in this field.

Author contributions

MG: Conceptualization, Formal Analysis, Visualization, Writing–original draft, Writing–review and editing, Investigation, Methodology. VC: Conceptualization, Investigation, Methodology, Visualization, Writing–original draft, Writing–review and editing. AM: Investigation, Visualization, Writing–original draft, Writing–review and editing. BR: Investigation, Visualization, Writing–original draft, Writing–review and editing, Formal Analysis. GG: Formal Analysis, Investigation, Visualization, Writing–original draft, Writing–review and editing. AZ: Formal Analysis, Investigation, Writing–original draft, Writing–review and editing, Funding acquisition, Methodology, Resources, Validation. EO: Formal Analysis, Funding acquisition, Resources, Writing–original draft, Writing–review and editing, Conceptualization, Project administration, Supervision, Visualization.

Funding

The authors declare that financial support was received for the research, authorship, and/or publication of this article. This work was supported by UFPR, CNPq, CAPES, L'Oréal-UNESCO-ABC, PhosAgro/UNESCO/IUPAC, the National Institute of Science and Technology of Nanomaterials for Life (INCTNanovida), the National Institute of Science and Technology of Carbon Nanomaterials (INCTNanocarbon), and the Academic Cooperation Program in Public Security and Forensic Sciences-CAPES.

Conflict of interest

The authors declare that the research was conducted in the absence of any commercial or financial relationships that could be construed as a potential conflict of interest.

Publisher's note

References

Acik, M., Lee, G., Mattevi, C., Pirkle, A., Wallace, R. M., Chhowalla, M., et al. (2011). The role of oxygen during thermal reduction of graphene oxide studied by infrared absorption spectroscopy. *J. Phys. Chem. C* 115 (40), 19761–19781. doi:10.1021/jp2052618

Alves, L. S. M., Neves, M. F. F. D., Benatto, L., Ramos, M. K., Eising, M., de Oliveira, CKBQM, et al. (2023). Influence of nanostructuring sensors based on graphene oxide and PEDOT:PSS for methanol detection. *IEEE Sensors J.* 23 (3), 1845–1853. doi:10.1109/jsen.2022.3228954

Alzate-Carvajal, N., Acevedo-Guzmán, D. A., Meza-Laguna, V., Farías, M. H., Pérez-Rey, L. A., Abarca-Morales, E., et al. (2018). One-step nondestructive functionalization of graphene oxide paper with amines. *RSC Adv.* 8, 15253–15265. doi:10.1039/c8ra00986d

Ausili, A., Corbalán-García, S., Gómez-Fernández, J. C., and Marsh, D. (2011). Membrane docking of the C2 domain from protein kinase Cα as seen by polarized ATR-IR. The role of PIP2. *Biochimica Biophysica Acta (BBA) - Biomembr.* 1808 (3), 684–695. doi:10.1016/j.bbamem.2010.11.035

Bartlam, C., Morsch, S., Heard, K. W. J., Quayle, P., Yeates, S. G., and Vijayaraghavan, A. (2018). Nanoscale infrared identification and mapping of chemical functional groups on graphene. *Carbon* 139, 317–324. doi:10.1016/j.carbon.2018.06.061

Botella, R., and Lefèvre, G. (2022). A deep look into the diverse surface speciation of the mono-molybdate/lepidocrocite system by ATR-IR and polarized ATR-IR

spectroscopy. *Colloids Surfaces A Physicochem. Eng. Aspects* 647, 129065. doi:10.1016/j.colsurfa.2022.129065

Botella, R., Piñeiro-García, A., Semetey, V., and Lefèvre, G. (2022). Polarized ATR-IR spectroscopy for the identification of material structure: the case of graphene oxide. *Mater. Lett.* 320, 132352. doi:10.1016/j.matlet.2022.132352

Brisebois, P. P., and Siaj, M. (2020). Harvesting graphene oxide – years 1859 to 2019: a review of its structure, synthesis, properties and exfoliation. *J. Mater. Chem. C* 8 (5), 1517–1547. doi:10.1039/c9tc03251g

Brunauer, S., Emmett, P. H., and Teller, E. (1938). Adsorption of gases in multimolecular layers. *J. Am. Chem. Soc.* 60 (2), 309–319. doi:10.1021/ja01269a023

Cakici, M., Kakarla, R. R., and Alonso-Marroquin, F. (2017). Advanced electrochemical energy storage supercapacitors based on the flexible carbon fiber fabric-coated with uniform coral-like MnO2 structured electrodes. *Chem. Eng. J.* 309, 151–158. doi:10.1016/j.cej.2016.10.012

Casabianca, L. B., Shaibat, M. A., Cai, W. W., Park, S., Piner, R., Ruoff, R. S., et al. (2010). NMR-based structural modeling of graphite oxide using multidimensional 13C solid-state NMR and *ab initio* chemical shift calculations. *J. Am. Chem. Soc.* 132 (16), 5672–5676. doi:10.1021/ja9030243

Chai, N., Zeng, J., Zhou, K., Xie, Y., Wang, H., Zhang, H., et al. (2013). Free-radical-promoted conversion of graphite oxide into chemically modified graphene. *Chem. – A Eur. J.* 19 (19), 5948–5954. doi:10.1002/chem.201203819

Chau, N. D. Q., Reina, G., Raya, J., Vacchi, I. A., Ménard-Moyon, C., Nishina, Y., et al. (2017). Elucidation of siRNA complexation efficiency by graphene oxide and reduced graphene oxide. *Carbon* 122, 643–652. doi:10.1016/j.carbon.2017.07.016

Chua, C. K., and Pumera, M. (2013). Covalent chemistry on graphene. *Chem. Soc. Rev.* 42 (8), 3222–3233. doi:10.1039/c2cs35474h

Clayden, J., Greeves, N., and Warren, S. (2012) *Organic chemistry*. 2nd ed.

Collins, W. R., Lewandowski, W., Schmois, E., Walish, J., and Swager, T. M. (2011a). Claisen rearrangement of graphite oxide: a route to covalently functionalized graphenes. *Angew. Chem. Int. Ed.* 50 (38), 8848–8852. doi:10.1002/anie.201101371

Collins, W. R., Schmois, E., and Swager, T. M. (2011b). Graphene oxide as an electrophile for carbon nucleophiles. *Chem. Commun.* 47 (31), 8790–8792. doi:10.1039/c1cc12829a

Davantès, A., and Lefèvre, G. (2016). Molecular orientation of molybdate ions adsorbed on goethite nanoparticles revealed by polarized *in situ* ATR-IR spectroscopy. *Surf. Sci.* 653, 88–91. doi:10.1016/j.susc.2016.06.007

Dehsari, H. S., Shalamzari, E. K., Gavgani, J. N., Taromi, F. A., and Ghanbary, S. (2014). Efficient preparation of ultralarge graphene oxide using a PEDOT:PSS/GO composite layer as hole transport layer in polymer-based optoelectronic devices. *RSC Adv.* 4 (98), 55067–55076. doi:10.1039/c4ra09474c

Devi, N. R., Sasidharan, M., and Sundramoorthy, A. K. (2018). Gold nanoparticles-thiol-functionalized reduced graphene oxide coated electrochemical sensor system for selective detection of mercury ion. *J. Electrochem Soc.* 165 (8), B3046–B3053. doi:10.1149/2.0081808jes

Dimiev, A. M. (2016). "Mechanism of formation and chemical structure of graphene oxide," in *Graphene oxide* (Chichester, UK: John Wiley & Sons, Ltd), 36–84.

Ding, L., Li, S., Yuan, X., Chang, W., Li, C., and Zheng, X. (2023). Preparation and tribological properties of Phenyl-Functionalized thermally reduced GrapheneOxide. *Chem. Eng. Sci.* 278, 118869. doi:10.1016/j.ces.2023.118869

Donato, K. Z., Tan, H. L., Marangoni, V. S., Martins, M. V. S., Ng, P. R., Costa, M. C. F., et al. (2023). Graphene oxide classification and standardization. *Sci. Rep.* 13 (1), 6064. doi:10.1038/s41598-023-33350-5

Elsie, S., Green, A., Rubavathi, D., Angamuthu, A., Gopal, B., and Bhagavathsingh, J. (2019). Tris-(2-aminoethyl)amine-Intercalated graphene oxide as an efficient 2D material for cerium-ion fluorescent sensor applications. *ACS Omega* 4, 22431–22437. doi:10.1021/acsomega.9b03089

Fallah-Mehrjardi, M., Kiasat, A. R., and Niknam, K. (2018). Nucleophilic ring-opening of epoxides: trends in β-substituted alcohols synthesis. *J. Iran. Chem. Soc.* 15, 2033–2081. doi:10.1007/s13738-018-1400-5

Feicht, P., and Eigler, S. (2018). Defects in graphene oxide as structural motifs. *ChemNanoMat* 4 (3), 244–252. doi:10.1002/cnma.201700357

Feng, Y., Wang, Z., Zhang, R., Lu, Y., Huang, Y., Shen, H., et al. (2018). Anti-fouling graphene oxide based nanocomposites membrane for oil-water emulsion separation. *Water Sci. Technol.* 77 (5), 1179–1185. doi:10.2166/wst.2017.634

Flores, K., Valdes, C., Ramirez, D., Eubanks, T. M., Lopez, J., Hernandez, C., et al. (2020). The effect of hybrid zinc oxide/graphene oxide (ZnO/GO) nano-catalysts on the photocatalytic degradation of simazine. *Chemosphere* 259, 127414. doi:10.1016/j.chemosphere.2020.127414

Gao, Q., Yan, J., Wan, L., Zhang, C., Wen, Z., Zhou, X., et al. (2022). High-efficiency graphene-oxide/silicon solar cells with an organic-passivated interface. *Adv. Mater. Interfaces* 9 (24), 2201221. doi:10.1002/admi.202201221

Gao, W. (2015). Graphene oxide: reduction recipes, spectroscopy, and applications. Graphene oxide: reduction recipes. *Spectrosc. Appl.*, 1–147. doi:10.1007/978-3-319-15500-5

Gao, X., Jang, J., and Nagase, S. (2010). Hydrazine and thermal reduction of graphene oxide: reaction mechanisms, product structures, and reaction design. *J. Phys. Chem. C* 114 (2), 832–842. doi:10.1021/jp909284g

Ge, X., Li, H., Wu, L., Li, P., Mu, X., and Jiang, Y. (2017). Improved mechanical and barrier properties of starch film with reduced graphene oxide modified by <scp>SDBS</scp>. *J. Appl. Polym. Sci.* 134 (22). doi:10.1002/app.44910

Georgakilas, V., Demeslis, A., Ntararas, E., Kouloumpis, A., Dimos, K., Gournis, D., et al. (2015). Hydrophilic nanotube supported graphene–water dispersible carbon superstructure with excellent conductivity. *Adv. Funct. Mater.* 25 (10), 1481–1487. doi:10.1002/adfm.201403801

Georgakilas, V., Otyepka, M., Bourlinos, A. B., Chandra, V., Kim, N., Kemp, K. C., et al. (2012). Functionalization of graphene: covalent and non-covalent approaches, derivatives and applications. *Chem. Rev.* 112 (11), 6156–6214. doi:10.1021/cr3000412

Georgakilas, V., Tiwari, J. N., Kemp, K. C., Perman, J. A., Bourlinos, A. B., Kim, K. S., et al. (2016). Noncovalent functionalization of graphene and graphene oxide for energy materials, biosensing, catalytic, and biomedical applications. *Chem. Rev.* 116, 5464–5519. doi:10.1021/acs.chemrev.5b00620

Golkar, N., Sarikhani, Z., Aghaei, R., Heidari, R., Amini, A., and Gholami, A. (2023). An oral nanoformulation of insulin: development and characterization of human insulin loaded graphene oxide-sodium alginate-gold nanocomposite in an animal model. *J. Drug Deliv. Sci. Technol.* 82, 104309. doi:10.1016/j.jddst.2023.104309

Guo, S., Garaj, S., Bianco, A., and Ménard-Moyon, C. (2022). Controlling covalent chemistry on graphene oxide. *Nat. Rev. Phys.* 4, 247–262. doi:10.1038/s42254-022-00422-w

Guo, S., Nishina, Y., Bianco, A., Ménard-Moyon, C., and Ménard, C. (2020b). A flexible method for covalent double functionalization of graphene oxide. *Angew. Chem. Int. Ed.* 59 (4), 1542–1547. doi:10.1002/anie.201913461

Guo, S., Raya, J., Ji, D., Nishina, Y., Ménard-Moyon, C., and Bianco, A. (2020a). Is carboxylation an efficient method for graphene oxide functionalization? *Nanoscale Adv.* 2 (9), 4085–4092. doi:10.1039/d0na00561d

Ha, H., Park, J., Ha, K. R., Freeman, B. D., and Ellison, C. J. (2016). Synthesis and gas permeability of highly elastic poly(dimethylsiloxane)/graphene oxide composite elastomers using telechelic polymers. *Polym. Guildf.* 93, 53–60. doi:10.1016/j.polymer.2016.04.016

Han, G. F., Li, F., Zou, W., Karamad, M., Jeon, J. P., Kim, S. W., et al. (2020). Building and identifying highly active oxygenated groups in carbon materials for oxygen reduction to H2O2. *Nat. Commun.* 11 (1), 2209. doi:10.1038/s41467-020-15782-z

Hao, B., Lu, G., Zhang, S., Li, Y., Ding, A., and Huang, X. (2020). Gold nanoparticles standing on PEG/PAMAM/thiol-functionalized nanographene oxide as aqueous catalysts. *Polym. Chem.* 11 (25), 4094–4104. doi:10.1039/d0py00471e

He, M., Zhang, R., Zhang, K., Liu, Y., Su, Y., and Jiang, Z. (2019). Reduced graphene oxide aerogel membranes fabricated through hydrogen bond mediation for highly efficient oil/water separation. *J. Mater. Chem. A* 7 (18), 11468–11477. doi:10.1039/c9ta01700c

Hikima, Y., Morikawa, J., and Kazarian, S. G. (2019). Analysis of molecular orientation in polymeric spherulite using polarized micro attenuated total reflection Fourier transform infrared (ATR-FTIR) spectroscopic imaging. *Anal. Chim. Acta* 1065, 79–89. doi:10.1016/j.aca.2019.02.017

Hong, B. J., Compton, O. C., An, Z., Eryazici, I., and Nguyen, S. T. (2012). Successful stabilization of graphene oxide in electrolyte solutions: enhancement of biofunctionalization and cellular uptake. *ACS Nano* 6 (1), 63–73. doi:10.1021/nn202355p

Hostert, L., Blaskievicz, S. F., Fonsaca, J. E. S., Domingues, S. H., Zarbin, A. J. G., and Orth, E. S. (2017). Imidazole-derived graphene nanocatalysts for organophosphate destruction: powder and thin film heterogeneous reactions. *J. Catal.* 356, 75–84. doi:10.1016/j.jcat.2017.10.008

Hostert, L., Zarbin, A. J. G., and Orth, E. S. (2020). Hydroxamic acid-functionalized graphene thin films as nanocatalysts towards organophosphate degradation. *J. Phys. Mater.* 3 (3), 034003. doi:10.1088/2515-7639/ab854c

Javidparvar, A. A., Naderi, R., and Ramezanzadeh, B. (2020). L-cysteine reduced/functionalized graphene oxide application as a smart/control release nanocarrier of sustainable cerium ions for epoxy coating anti-corrosion properties improvement. *J. Hazard. Mater.* 389, 122135. doi:10.1016/j.jhazmat.2020.122135

Jayaraman, N., Palani, Y., Jonnalagadda, R. R., and Shanmugam, E. (2022). Covalently dual functionalized graphene oxide-based multiplex electrochemical sensor for Hg(II) and Cr(VI) detection. *Sensors Actuators B Chem.* 367, 132165. doi:10.1016/j.snb.2022.132165

Jiang, X., Lu, G., Huang, X., Li, Y., Cao, F., Chen, H., et al. (2019). Thermo-responsive graphene oxide/poly(ethyl ethylene phosphate) nanocomposite via ring opening polymerization. *Nanomaterials* 9, 207. doi:10.3390/nano9020207

Jung, I., Dikin, D. A., Piner, R. D., and Ruoff, R. S. (2008). Tunable electrical conductivity of individual graphene oxide sheets reduced at "low" temperatures. *Nano Lett.* 8 (12), 4283–4287. doi:10.1021/nl8019938

Kang, S., Qiao, S., Hu, Z., Yu, J., Wang, Y., and Zhu, J. (2019). Interfacial polymerized reduced graphene oxide covalently grafted polyaniline nanocomposites for high-performance electromagnetic wave absorber. *J. Mater Sci.* 54, 6410–6424. doi:10.1007/s10853-019-03347-5

Kaniyoor, A., and Ramaprabhu, S. (2012). A Raman spectroscopic investigation of graphite oxide derived graphene. *AIP Adv.* 2 (3). doi:10.1063/1.4756995

Kasprzak, A., Zuchowska, A., and Poplawska, M. (2018). Functionalization of graphene: does the organic chemistry matter? *Beilstein J. Org. Chem.* 14, 2018–2026. doi:10.3762/bjoc.14.177

Khan, A., Wang, J., Li, J., Wang, X., Chen, Z., Alsaedi, A., et al. (2017). The role of graphene oxide and graphene oxide-based nanomaterials in the removal of pharmaceuticals from aqueous media: a review. *Environ. Sci. Pollut. Res.* 24 (9), 7938–7958. doi:10.1007/s11356-017-8388-8

Khan, R., Miyagawa, K., Bianco, A., and Nishina, Y. (2021). Covalent double functionalization of graphene oxide for proton conductive and redox-active functions. *Appl. Mater. Today* 24, 101120. doi:10.1016/j.apmt.2021.101120

Khanra, P., Kuila, T., Kim, N. H., Bae, S. H., Yu, D. sheng, and Lee, J. H. (2012). Simultaneous bio-functionalization and reduction of graphene oxide by baker's yeast. *Chem. Eng. J.* 183, 526–533. doi:10.1016/j.cej.2011.12.075

Komeily-Nia, Z., Qu, L. T., and Li, J. L. (2021). Progress in the understanding and applications of the intrinsic reactivity of graphene-based materials. *Small Sci.* 1 (2), 2000026. doi:10.1002/smsc.202000026

Kong, D., He, H., Song, Q., Wang, B., Lv, W., Yang, Q. H., et al. (2014). Rational design of MoS_2@graphene nanocables: towards high performance electrode materials for lithium ion batteries. *Energy Environ. Sci.* 7 (10), 3320–3325. doi:10.1039/c4ee02211d

Krishna, D. N. G., and Philip, J. (2022). Review on surface-characterization applications of X-ray photoelectron spectroscopy (XPS): recent developments and challenges. *Appl. Surf. Sci. Adv.* 12, 100332. doi:10.1016/j.apsadv.2022.100332

Kudin, K. N., Ozbas, B., Schniepp, H. C., Prud'Homme, R. K., Aksay, I. A., and Car, R. (2008). Raman spectra of graphite oxide and functionalized graphene sheets. *Nano Lett.* 8 (1), 36–41. doi:10.1021/nl071822y

Kuila, T., Bose, S., Mishra, A. K., Khanra, P., Kim, N. H., and Lee, J. H. (2012). Chemical functionalization of graphene and its applications. *Prog. Mater. Sci.* 57 (7), 1061–1105. doi:10.1016/j.pmatsci.2012.03.002

Kuilla, T., Bhadra, S., Yao, D., Kim, N. H., Bose, S., and Lee, J. H. (2010). Recent advances in graphene based polymer composites. *Prog. Polym. Sci.* 35 (11), 1350–1375. doi:10.1016/j.progpolymsci.2010.07.005

Kumar, P., Bajpai, H., Gopinath, C. S., and Luwang, M. N. (2022). Sulfur functionalization via epoxide ring opening on a reduced graphene oxide surface to form metal (II) organo-bis-[1,2]-oxathiin. *Inorg. Chem.* 61 (1), 279–286. doi:10.1021/acs.inorgchem.1c02819

Kumar, P., Divya, N., and Ratan, J. K. (2021). Study on the physico-chemical properties of reduced graphene oxide with different degrees of reduction temperature. *J. Iran. Chem. Soc.* 18 (1), 201–211. doi:10.1007/s13738-020-02014-w

Kumar, R., Xu, C., and Scott, K. (2012). Graphite oxide/Nafion composite membranes for polymer electrolyte fuel cells. *RSC Adv.* 2 (23), 8777–8782. doi:10.1039/c2ra20225e

Kumar, S., Bukkitgar, S. D., Singh, S., Pratibha, M., Singh, V., Reddy, K. R., et al. (2019). Electrochemical sensors and biosensors based on graphene functionalized with metal oxide nanostructures for healthcare applications. *ChemistrySelect* 4 (18), 5322–5337. doi:10.1002/slct.201803871

Le, G. T. T., Manyam, J., Opaprakasit, P., Chanlek, N., Grisdanurak, N., and Sreearunothai, P. (2018). Divergent mechanisms for thermal reduction of graphene oxide and their highly different ion affinities. *Diam. Relat. Mater.* 89, 246–256. doi:10.1016/j.diamond.2018.09.006

Lerf, A., He, H., Forster, M., and Klinowski, J. (1998). Structure of graphite oxide revisited. *J. Phys. Chem. B* 102 (23), 4477–4482. doi:10.1021/jp9731821

Li, D., Wang, J., Yu, S., Ye, S., Zou, W., Zhang, H., et al. (2020). Highly regioselective ring-opening of epoxides with amines: a metal- and solvent-free protocol for the synthesis of β-amino alcohols. *Chem. Commun.* 56 (15), 2256–2259. doi:10.1039/c9cc09048g

Lima, L. F., Matos, C. F., Gonçalves, L. C., Salvatierra, R. V., Cava, C. E., Zarbin, A. J. G., et al. (2016). Water based, solution-processable, transparent and flexible graphene oxide composite as electrodes in organic solar cell application. *J. Phys. D. Appl. Phys.* 49 (10), 105106. doi:10.1088/0022-3727/49/10/105106

Lin, Z., Liu, Y., and Wong, C. P. (2010). Facile fabrication of superhydrophobic octadecylamine-functionalized graphite oxide film. *Langmuir* 26 (20), 16110–16114. doi:10.1021/la102619n

Liu, J., Chen, S., Liu, Y., and Zhao, B. (2022). Progress in preparation, characterization, surface functional modification of graphene oxide: a review. *J. Saudi Chem. Soc.* 26, 101560. doi:10.1016/j.jscs.2022.101560

Liu, J., Jiang, X., Xu, L., Wang, X., Hennink, W. E., and Zhuo, R. (2010). Novel reduction-responsive cross-linked polyethylenimine derivatives by click chemistry for nonviral gene delivery. *Bioconjugate Chem.* 21 (10), 1827–1835. doi:10.1021/bc100191r

Liu, J., Xue, Y., Gao, Y., Yu, D., Durstock, M., Dai, L., et al. (2012). Hole and electron extraction layers based on graphene oxide derivatives for high-performance bulk heterojunction solar cells. *Adv. Mater.* 24 (17), 2228–2233. doi:10.1002/adma.201104945

Liu, J., Yu, H., Wang, L., Vatsadze, S. Z., Chen, D., Wu, X., et al. (2023). Preparation of graphene oxides functionalized with ferrocene for the thermal decomposition of ammonium perchlorate. *Mol. Catal.* 550, 113572. doi:10.1016/j.mcat.2023.113572

Liu, Y., Jiang, X., Li, B., Zhang, X., Liu, T., Yan, X., et al. (2014). Halloysite nanotubes@reduced graphene oxide composite for removal of dyes from water and as supercapacitors. *J. Mater. Chem. A* 2 (12), 4264. doi:10.1039/c3ta14594h

Liu, Z., Nørgaard, K., Overgaard, M. H., Ceccato, M., Mackenzie, D. M. A., Stenger, N., et al. (2018). Direct observation of oxygen configuration on individual graphene oxide sheets. *Carbon* 127, 141–148. doi:10.1016/j.carbon.2017.10.100

Liu, Z., Rios-Carvajal, T., Ceccato, M., and Hassenkam, T. (2019). Nanoscale chemical mapping of oxygen functional groups on graphene oxide using atomic force microscopy-coupled infrared spectroscopy. *J. Colloid Interface Sci.* 556, 458–465. doi:10.1016/j.jcis.2019.08.089

Liu, Z., Robinson, J. T., Sun, X., and Dai, H. (2008). PEGylated nanographene oxide for delivery of water-insoluble cancer drugs. *J. Am. Chem. Soc.* 130 (33), 10876–10877. doi:10.1021/ja803688x

Lopez, A., and Liu, J. (2020). Covalent and noncovalent functionalization of graphene oxide with DNA for smart sensing. *Adv. Intell. Syst.* 2 (11). doi:10.1002/aisy.202000123

Lowe, A. B. (2014). Thiol–ene "click" reactions and recent applications in polymer and materials synthesis: a first update. *Polym. Chem.* 5 (17), 4820–4870. doi:10.1039/c4py00339j

Lu, G., Zhou, X., Li, H., Yin, Z., Li, B., Huang, L., et al. (2010). Nanolithography of single-layer graphene oxide films by atomic force microscopy. *Langmuir* 26 (9), 6164–6166. doi:10.1021/la101077t

Ma, Y., Di, H., Yu, Z., Liang, L., Lv, L., Pan, Y., et al. (2016). Fabrication of silica-decorated graphene oxide nanohybrids and the properties of composite epoxy coatings research. *Appl. Surf. Sci.* 360, 936–945. doi:10.1016/j.apsusc.2015.11.088

Martin-Gullon, I., Pérez, J. M., Domene, D., Salgado-Casanova, A. J. A., and Radovic, L. R. (2020). New insights into oxygen surface coverage and the resulting two-component structure of graphene oxide. *Carbon* 158, 406–417. doi:10.1016/j.carbon.2019.11.003

Maslekar, N., Mat Noor, R. A., Kuchel, R. P., Yao, Y., Zetterlund, P. B., and Agarwal, V. (2020). Synthesis of diamine functionalised graphene oxide and its application in the fabrication of electrically conducting reduced graphene oxide/polymer nanocomposite films. *Nanoscale Adv.* 2 (10), 4702–4712. doi:10.1039/d0na00534g

Meng, C., Chen, Q., Li, X., and Liu, H. (2019). Controlling covalent functionalization of graphene oxide membranes to improve enantioseparation performances. *J. Membr. Sci.* 582, 83–90. doi:10.1016/j.memsci.2019.03.087

Meng, Z., Lu, S., Zhang, D., Liu, Q., Chen, X., Liu, W., et al. (2022). Grafting macromolecular chains on the surface of graphene oxide through crosslinker for antistatic and thermally stable polyethylene terephthalate nanocomposites. *RSC Adv.* 12, 33329–33339. doi:10.1039/d2ra06725k

Mirzaie, A., Hasanzadeh, M., and Jouyban, A. (2019). Cross-linked chitosan/thiolated graphene quantum dots as a biocompatible polysaccharide towards aptamer immobilization. *Int. J. Biol. Macromol.* 123, 1091–1105. doi:10.1016/j.ijbiomac.2018.11.139

Monteiro, A. R., Neves, MGPMS, and Trindade, T. (2020). Functionalization of graphene oxide with porphyrins: synthetic routes and biological applications. *ChemPlusChem* 85, 1857–1880. doi:10.1002/cplu.202000455

Mu, S. J., Su, Y. C., Xiao, L. H., Liu, S. D., Hu, T., Tang, H. B., et al. (2013). X-ray difraction pattern of graphite oxide. *Chin. Phys. Lett.* 30 (9), 096101. doi:10.1088/0256-307x/30/9/096101

Nair, R. R., Wu, H. A., Jayaram, P. N., Grigorieva, I. V., and Geim, A. K. (2012). Unimpeded permeation of water through helium-leak–tight graphene-based membranes. *Science* 335 (6067), 442–444. doi:10.1126/science.1211694

Oh, J. S., Park, J. S., and Lee, E. J. (2021). Enhanced effect of polyethyleneimine-modified graphene oxide and simvastatin on osteogenic differentiation of murine bone marrow-derived mesenchymal stem cells. *Biomedicines* 9 (5), 501. doi:10.3390/biomedicines9050501

Orth, E. S., Fonsaca, J. E. S., Almeida, T. G., Domingues, S. H., Ferreira, J. G. L., and Zarbin, A. J. G. (2014). Functionalized graphene oxide as a nanocatalyst in dephosphorylation reactions: pursuing artificial enzymes. *Chem. Commun.* 50 (69), 9891–9894. doi:10.1039/c4cc03262d

Orth, E. S., Fonsaca, J. E. S., Domingues, S. H., Mehl, H., Oliveira, M. M., and Zarbin, A. J. G. (2013). Targeted thiolation of graphene oxide and its utilization as precursor for graphene/silver nanoparticles composites. *Carbon* 61, 543–550. doi:10.1016/j.carbon.2013.05.032

Ossonon, B. D., and Bélanger, D. (2017). Functionalization of graphene sheets by the diazonium chemistry during electrochemical exfoliation of graphite. *Carbon* 111, 83–93. doi:10.1016/j.carbon.2016.09.063

Pancharatna, P. D., Jhaa, G., and Balakrishnarajan, M. M. (2020). Nature of interactions between epoxides in graphene oxide. *J. Phys. Chem. C* 124 (2), 1695–1703. doi:10.1021/acs.jpcc.9b10262

Paredes, J. I., Villar-Rodil, S., Martínez-Alonso, A., and Tascón, J. M. D. (2008). Graphene oxide dispersions in organic solvents. *Langmuir* 24, 10560–10564. doi:10.1021/la801744a

Payami, E., Teimuri-Mofrad, R., Ahadzadeh, I., and Mohammadi, R. (2020). A novel composite electrode material derived from bisferrocenyl-functionalized GO and PANI

for high performance supercapacitor. *Electrochimica Acta* 354, 136712. doi:10.1016/j.electacta.2020.136712

Paz-Cedeno, F. R., Carceller, J. M., Iborra, S., Donato, R. K., Godoy, A. P., Veloso de Paula, A., et al. (2021). Magnetic graphene oxide as a platform for the immobilization of cellulases and xylanases: ultrastructural characterization and assessment of lignocellulosic biomass hydrolysis. *Renew. Energy* 164, 491–501. doi:10.1016/j.renene.2020.09.059

Pennetreau, F., Riant, O., and Hermans, S. (2014). One-step double covalent functionalization of reduced graphene oxide with xanthates and peroxides. *Chem. – A Eur. J.* 20 (46), 15009–15012. doi:10.1002/chem.201405148

Pérez, L. A., Bajales, N., and Lacconi, G. I. (2019). Raman spectroscopy coupled with AFM scan head: a versatile combination for tailoring graphene oxide/reduced graphene oxide hybrid materials. *Appl. Surf. Sci.* 495, 143539. doi:10.1016/j.apsusc.2019.143539

Perret, E., Sharma, K., Tritsch, S., and Hufenus, R. (2021). Reversible mesophase in stress-annealed poly(3-hydroxybutyrate) fibers: a synchrotron x-ray and polarized ATR-FTIR study. *Polym. Guildf.* 231, 124141. doi:10.1016/j.polymer.2021.124141

Piñeiro-García, A., and Semetey, V. (2023). The "how" and "where" behind the functionalization of graphene oxide by thiol-ene "click" chemistry. *Chem. Weinheim der Bergstrasse, Ger.* 29, e202301604. doi:10.1002/chem.202301604

Piñeiro-García, A., Vega-Díaz, S. M., Tristán, F., Meneses-Rodríguez, D., Labrada-Delgado, G. J., and Semetey, V. (2021). New insights in the chemical functionalization of graphene oxide by thiol-ene Michael addition reaction. *FlatChem* 26, 100230. doi:10.1016/j.flatc.2021.100230

Piñeiro-García, A., Vega-Díaz, S. M., Tristan, F., Meneses-Rodríguez, D., and Semetey, V. (2022). Functionalization and soft photoreduction of graphene oxide triggered by the photoinitiator during thiol-ene radical addition. *FlatChem* 33, 100349. doi:10.1016/j.flatc.2022.100349

Pintus, A., Mantovani, S., Kovtun, A., Bertuzzi, G., Melucci, M., and Bandini, M. (2023). Recyclable GO-arginine hybrids for CO2 fixation into cyclic carbonates. *Chem. Weinheim der Bergstrasse, Ger.* 29, e202202440. doi:10.1002/chem.202202440

Price, E. K., Bansala, T., Achee, T. C., Sun, W., and Green, M. J. (2019). Tunable dispersibility and wettability of graphene oxide through one-pot functionalization and reduction. *J. Colloid Interface Sci.* 552, 771–780. doi:10.1016/j.jcis.2019.05.097

Rabchinskii, M. K., Shnitov, V. V., Brzhezinskaya, M., Baidakova, M. V., Stolyarova, D. Y., Ryzhkov, S. A., et al. (2022). Manifesting epoxide and hydroxyl groups in XPS spectra and valence band of graphene derivatives. *Nanomaterials* 13 (1), 23. doi:10.3390/nano13010023

Rahimpour, S., Luo, L., and Teimuri-Mofrad, R. (2022). Preparation of ferrocenyl-furan modified graphene oxide via Diels-Alder click reaction and using of its polypyrrole nanocomposites as supercapacitor electrode material. *Electrochimica Acta* 416, 140285. doi:10.1016/j.electacta.2022.140285

Ramírez-Jiménez, R., Franco, M., Rodrigo, E., Sainz, R., Ferritto, R., Lamsabhi, A. M., et al. (2018). Unexpected reactivity of graphene oxide with DBU and DMF. *J. Mater. Chem. A* 6, 12637–12646. doi:10.1039/c8ta03529f

Ramirez-Soria, E. H., León-Silva, U., Lara-Ceniceros, T. E., Bazán-Díaz, L., Advíncula, R. C., and Bonilla-Cruz, J. (2021). Graphene oxide bifunctionalized with NH2/NH3+ and their outstanding-performance against corrosion. *Appl. Surf. Sci.* 561, 150048. doi:10.1016/j.apsusc.2021.150048

Rana, V. K., Choi, M., Kong, J., Kim, G. Y., Kim, M. J., Kim, S., et al. (2011). Synthesis and drug-delivery behavior of chitosan-functionalized graphene oxide hybrid nanosheets. *Macromol. Mater. Eng.* 296 (2), 131–140. doi:10.1002/mame.201000307

Rani, S., Kumar, M., Kumar, R., Kumar, D., Sharma, S., and Singh, G. (2014). Characterization and dispersibility of improved thermally stable amide functionalized graphene oxide. *Mater. Res. Bull.* 60, 143–149. doi:10.1016/j.materresbull.2014.07.019

Ranishenka, B., Ulashchik, E., Tatulchenkov, M., Sharko, O., Panarin, A., Dremova, N., et al. (2021). Graphene oxide functionalization via epoxide ring opening in bioconjugation compatible conditions. *FlatChem* 27, 100235. doi:10.1016/j.flatc.2021.100235

Rourke, J. P., Pandey, P. A., Moore, J. J., Bates, M., Kinloch, I. A., Young, R. J., et al. (2011). The real graphene oxide revealed: stripping the oxidative debris from the graphene-like sheets. *Angew. Chem. Int. Ed.* 50 (14), 3173–3177. doi:10.1002/anie.201007520

Sainz-Urruela, C., Vera-López, S., Paz San Andrés, M., and Díez-Pascual, A. M. (2022). Surface functionalization of graphene oxide with tannic acid: covalent vs non-covalent approaches. *J. Mol. Liq.* 357, 119104. doi:10.1016/j.molliq.2022.119104

Santos, Y. H., Martinez, A. H. G., Veiga, A. G., Rocco, M. L. M., Zarbin, A. J. G., and Orth, E. S. (2022). Neighboring effects on the selective bifunctionalization of graphene oxide for nanocatalytic organophosphate neutralization. *ACS Appl. Nano Mater.* 5, 6001–6012. doi:10.1021/acsanm.2c00832

Santos, Y. H., Martinez, A. H. G., Veiga, A. G., Rocco, M. L. M., Zarbin, A. J. G., and Orth, E. S. (2023). Site-selective mono- and bifunctionalization of graphene oxide: screening nanocatalysts for organophosphate degradation. *ChemCatChem* 16. doi:10.1002/cctc.202301440

Serodre, T., Oliveira, N., Miquita, D., Ferreira, M., Santos, A., Resende, V., et al. (2019). Surface silanization of graphene oxide under mild reaction conditions. *J. Braz Chem. Soc.* doi:10.21577/0103-5053.20190167

Shahdost-fard, F., and Roushani, M. (2017). Designing an ultra-sensitive aptasensor based on an AgNPs/thiol-GQD nanocomposite for TNT detection at femtomolar levels using the electrochemical oxidation of Rutin as a redox probe. *Biosens. Bioelectron.* 87, 724–731. doi:10.1016/j.bios.2016.09.048

Sharma, P., Tuteja, S. K., Bhalla, V., Shekhawat, G., Dravid, V. P., Suri, C. R., et al. (2013). Bio-functionalized graphene–graphene oxide nanocomposite based electrochemical immunosensing. *Biosens. Bioelectron.* 39 (1), 99–105. doi:10.1016/j.bios.2012.06.061

Shetti, N. P., Malode, S. J., Nayak, D. S., Bagihalli, G. B., Reddy, K. R., Ravindranadh, K., et al. (2019). A novel biosensor based on graphene oxide-nanoclay hybrid electrode for the detection of Theophylline for healthcare applications. *Microchem. J.* 149, 103985. doi:10.1016/j.microc.2019.103985

Shi, L., Wang, Z., Yang, G., Yang, H., and Zhao, F. (2020). A novel electrochemical immunosensor for aflatoxin B1 based on Au nanoparticles-poly 4-aminobenzoic acid supported graphene. *Appl. Surf. Sci.* 527, 146934. doi:10.1016/j.apsusc.2020.146934

Shim, S. H., Kim, K. T., Lee, J. U., and Jo, W. H. (2012). Facile method to functionalize graphene oxide and its application to poly(ethylene terephthalate)/graphene composite. *ACS Appl. Mater Interfaces* 4 (8), 4184–4191. doi:10.1021/am300906z

Silvestri, S., and Gonçalves, M. G. (2022). "Carbon composites and catalysts for decomposition of organic pollutants," in *Carbon composite catalysts*. Editors M. Jawaid and A. Khan (Springer Nature), 337–369.

Singh, R., and Kar, R. K. (2023). Dynamic properties of graphene oxide functionalized with l-cysteine. *J. Phys. Chem. C* 127, 17438–17453. doi:10.1021/acs.jpcc.3c04469

Solomons, T. W. G., Fryhle, C. B., and Snyder, S. A. (2016) *Organic chemistry*. 12th ed.

Sun, H. J., Liu, B., Peng, T. J., and Zhao, X. L. (2018). Effect of reaction temperature on structure, appearance and bonding type of functionalized graphene oxide modified P-phenylene diamine. *Materials.* 11 (4), 647. doi:10.3390/ma11040647

Surabhi, S. D., Sah, D., Shabir, J., Gupta, P., and Mozumdar, S. (2022). Imidazole-functionalized porous graphene oxide nanosheets loaded with palladium nanoparticles for the oxidative amidation of aldehydes. *ACS Appl. Nano Mater* 5, 5776–5792. doi:10.1021/acsanm.2c00859

Sydlik, S. A., and Swager, T. M. (2013). Functional graphenic materials via a Johnson–Claisen rearrangement. *Adv. Funct. Mater.* 23 (15), 1873–1882. doi:10.1002/adfm.201201954

Tan, S., Zhang, D., Nguyen, M. T., Shutthanandan, V., Varga, T., Rousseau, R., et al. (2022). Tuning the charge and hydrophobicity of graphene oxide membranes by functionalization with ionic liquids at epoxide sites. *ACS Appl. Mater Interfaces* 14 (16), 19031–19042. doi:10.1021/acsami.2c02366

Tang, S., Wu, W., Liu, L., Cao, Z., Wei, X., and Chen, Z. (2017). Diels-Alder reactions of graphene oxides: greatly enhanced chemical reactivity by oxygen-containing groups. *Phys. Chem. Chem. Phys.* 19 (18), 11142–11151. doi:10.1039/c7cp01086a

Taniguchi, T., Kurihara, S., Tateishi, H., Hatakeyama, K., Koinuma, M., Yokoi, H., et al. (2015). PH-driven, reversible epoxy ring opening/closing in graphene oxide. *Carbon* 84 (1), 560–566. doi:10.1016/j.carbon.2014.12.054

Thomas, H. R., Day, S. P., Woodruff, W. E., Vallés, C., Young, R. J., Kinloch, I. A., et al. (2013). Deoxygenation of graphene oxide: reduction or cleaning? *Chem. Mater.* 25 (18), 3580–3588. doi:10.1021/cm401922e

Thomas, H. R., Marsden, A. J., Walker, M., Wilson, N. R., and Rourke, J. P. (2014). Sulfur-functionalized graphene oxide by epoxide ring-opening. *Angew. Chem. - Int. Ed.* 53 (29), 7613–7618. doi:10.1002/anie.201404002

Tian, Y., Yu, Z., Cao, L., Zhang, X. L., Sun, C., and Wang, D. W. (2021). Graphene oxide: an emerging electromaterial for energy storage and conversion. *J. Energy Chem.* 55, 323–344. doi:10.1016/j.jechem.2020.07.006

Trikkaliotis, D. G., Christoforidis, A. K., Mitropoulos, A. C., and Kyzas, G. Z. (2021). Graphene oxide synthesis, properties and characterization techniques: a comprehensive review. *ChemEngineering* 5, 64. doi:10.3390/chemengineering5030064

Vacchi, I. A., Guo, S., Raya, J., Bianco, A., and Ménard-Moyon, C. (2020). Strategies for the controlled covalent double functionalization of graphene oxide. *Chem. – A Eur. J.* 26 (29), 6591–6598. doi:10.1002/chem.201905785

Vacchi, I. A., Spinato, C., Raya, J., Bianco, A., and Ménard-Moyon, C. (2016). Chemical reactivity of graphene oxide towards amines elucidated by solid-state NMR. *Nanoscale* 8 (28), 13714–13721. doi:10.1039/c6nr03846h

Wang, H., Bi, S. G., Ye, Y. S., Xue, Y., Xie, X. L., and Mai, Y. W. (2015). An effective non-covalent grafting approach to functionalize individually dispersed reduced graphene oxide sheets with high grafting density, solubility and electrical conductivity. *Nanoscale* 7 (8), 3548–3557. doi:10.1039/c4nr06710j

Wang, J. T. W., Ball, J. M., Barea, E. M., Abate, A., Alexander-Webber, J. A., Huang, J., et al. (2014). Low-temperature processed electron collection layers of graphene/TiO_2 nanocomposites in thin film perovskite solar cells. *Nano Lett.* 14 (2), 724–730. doi:10.1021/nl403997a

Wang, X., Wang, W., Liu, Y., Ren, M., Xiao, H., and Liu, X. (2016). Characterization of conformation and locations of C–F bonds in graphene derivative by polarized ATR-FTIR. *Anal. Chem.* 88 (7), 3926–3934. doi:10.1021/acs.analchem.6b00115

Wang, Z., Hu, G., Liu, J., Liu, W., Zhang, H., and Wang, B. (2015). Coordinated assembly of a new 3D mesoporous Fe_3O_4@Cu_2O–graphene oxide framework as a

highly efficient and reusable catalyst for the synthesis of quinoxalines. *Chem. Commun.* 51 (24), 5069–5072. doi:10.1039/c5cc00250h

Wu, Q., Zou, H., Mao, X., He, J., Shi, Y., Chen, S., et al. (2023). Unveiling the dynamic active site of defective carbon-based electrocatalysts for hydrogen peroxide production. *Nat. Commun.* 14 (1), 6275. doi:10.1038/s41467-023-41947-7

Xie, Z., Sun, B., Lin, H., Fu, M., Zhang, Y., Ma, Z., et al. (2023). Bifunctional reduced graphene oxide/polyelectrolyte/NiFe layered double hydroxide composites for efficient catalyzed dephosphorylation and 4-nitrophenol reduction. *J. Water Process Eng.* 1, 53. doi:10.1016/j.jwpe.2023.103624

Xue, B., Zhu, J., Liu, N., and Li, Y. (2015). Facile functionalization of graphene oxide with ethylenediamine as a solid base catalyst for Knoevenagel condensation reaction. *Catal. Commun.* 64, 105–109. doi:10.1016/j.catcom.2015.02.003

Yang, D., Velamakanni, A., Bozoklu, G., Park, S., Stoller, M., Piner, R. D., et al. (2009). Chemical analysis of graphene oxide films after heat and chemical treatments by X-ray photoelectron and Micro-Raman spectroscopy. *Carbon* 47 (1), 145–152. doi:10.1016/j.carbon.2008.09.045

Yang, S., Cao, C., Huang, P., Peng, L., Sun, Y., Wei, F., et al. (2015). Sandwich-like porous TiO $_2$/reduced graphene oxide (rGO) for high-performance lithium-ion batteries. *J. Mater. Chem. A* 3 (16), 8701–8705. doi:10.1039/c5ta01744k

Yu, W., Sisi, L., Haiyan, Y., and Jie, L. (2020). Progress in the functional modification of graphene/graphene oxide: a review. *RSC Adv.* 10, 15328–15345. doi:10.1039/d0ra01068e

Zhang, B., Chen, Y., Xu, L., Zeng, L., He, Y., Kang, E. T., et al. (2011). Growing poly(*N* -vinylcarbazole) from the surface of graphene oxide via RAFT polymerization. *J. Polym. Sci. A Polym. Chem.* 49 (9), 2043–2050. doi:10.1002/pola.24633

Zhang, J., Gao, J., Song, Q., Guo, Z., Chen, A., Chen, G., et al. (2016). N-Substituted carboxyl polyaniline covalent grafting reduced graphene oxide nanocomposites and its application in supercapacitor. *Electrochimica Acta* 199, 70–79. doi:10.1016/j.electacta.2016.03.003

Zhang, Z. B., Wu, J. J., Su, Y., Zhou, J., Gao, Y., Yu, H. Y., et al. (2015). Layer-by-layer assembly of graphene oxide on polypropylene macroporous membranes via click chemistry to improve antibacterial and antifouling performance. *Appl. Surf. Sci.* 332, 300–307. doi:10.1016/j.apsusc.2015.01.193

Zheng, A. L. T., Boonyuen, S., Li, G. Y., Ngee, L. H., and Andou, Y. (2021). Design of reduced graphene hydrogel with alkylamine surface functionalization through immersion/agitation method and its adsorption mechanism. *J. Mol. Struct.* 1245, 131008. doi:10.1016/j.molstruc.2021.131008

Zheng, Y., Li, S., Han, D., Kong, L., Wang, J., Zhao, M., et al. (2021). Eco-friendly preparation of epoxy-rich graphene oxide for wound healing. *ACS Biomater. Sci. Eng.* 7 (2), 752–763. doi:10.1021/acsbiomaterials.0c01598

Zhu, J., Wang, S., Gu, Y., Xue, B., and Li, Y. (2018). A new and efficient method of graphene oxide immobilized with ionic liquids: promoted catalytic activity for CO2 cycloaddition. *Mater. Chem. Phys.* 208, 68–76. doi:10.1016/j.matchemphys.2018.01.031

frontiers | Frontiers in Carbon

TYPE Original Research
PUBLISHED 03 January 2025
DOI 10.3389/frcrb.2024.1363919

OPEN ACCESS

EDITED BY
Junchao Wei,
Nanchang University, China

REVIEWED BY
Elif Seven,
C-Dots Nanotec, LLC, United States
Yong Yang,
Northwestern Polytechnical University, China
Jiaolong Wang,
Affiliated Stomatological Hospital of Nanchang University, China

*CORRESPONDENCE
Gisele Eva Bruch,
gisele.bruch@professor.faminas.edu.br

RECEIVED 31 December 2023
ACCEPTED 25 September 2024
PUBLISHED 03 January 2025

CITATION
Bruch GE, Dal Bosco L, Cordeiro AP, Cordeiro MF, Sahoo SK, Peixoto C, Klosterhoff MC, Romano LA, Fantini C, Santos AP and Barros DM (2025) Biodistribution of intravenously delivered PEGylated carbon nanotubes to the rat brain cortex. *Front. Carbon* 3:1363919. doi: 10.3389/frcrb.2024.1363919

Biodistribution of intravenously delivered PEGylated carbon nanotubes to the rat brain cortex

Gisele Eva Bruch[1,2]*, Lidiane Dal Bosco[1,3], Arthur P. Cordeiro[1], Marcos F. Cordeiro[1], Sangram K. Sahoo[4], Carolina Peixoto[1], Marta C. Klosterhoff[5], Luis Alberto Romano[5], Cristiano Fantini[4], Adelina P. Santos[6] and Daniela M. Barros[1]

[1]Laboratório de Neurociências, Instituto de Ciências Biológicas, Universidade Federal do Rio Grande (FURG), Programa de Pós-graduação em Ciências Fisiológicas - Fisiologia Animal Comparada, FURG, Rio Grande, Brazil, [2]Laboratório de Simulação Realística, Faculdade de Minas – Faminas BH, Belo Horizonte, Brazil, [3]Universidade Federal do Pampa (UNIPAMPA), Uruguaiana, Brazil, [4]Departamento de Física, Universidade Federal de Minas Gerais, Belo Horizonte, Brazil, [5]Laboratório de Imunologia e Patologia de Organismos Aquáticos, Instituto de Oceanografia, Universidade Federal do Rio Grande, Rio Grande, Brazil, [6]Centro de Desenvolvimento da Tecnologia Nuclear, CDTN, Belo Horizonte, Brazil

Polyethylene glycol-functionalized single-walled carbon nanotubes (SWCNT-PEG) have been studied for many biomedical applications because of their unique physicochemical properties. Due to their reduced size and high stability in physiological media, SWCNT-PEG are candidates for crossing the blood–brain barrier (BBB), with potential use in treating central nervous system diseases that are currently unresponsive to pharmacological interventions because of the tightly regulated permeability of the BBB. In this study, we investigated the biodistribution of intravenously delivered SWCNT-PEG using Raman spectroscopy, as well as possible toxicological outcomes using morphological, histological, biochemical, and behavioral analyses. SWCNT-PEG were identified in the brain cortex, blood, spleen, and liver of rats. Biochemical and histological analyses did not reveal toxic effects in rats 24 h after SWCNT-PEG injection. Additionally, no behavioral impairments were observed in treated animals subjected to the Morris water maze task. Our preliminary experimental results clearly indicate that SWCNT-PEG were able to cross biological membranes and reach the rat brain cortex parenchyma (but not other brain structures) after systemic administration without the presence of acute toxic effects. The biodistribution of SWCNT-PEG in a specific region of the brain tissue encourages further studies regarding the application of SWCNTs in neuroscience.

KEYWORDS

nanomedicine, carbon nanotubes, polyethylene glycol, biodistribution, Raman spectroscopy

1 Introduction

One of the greatest challenges in neuroscience is the search for an effective and non-invasive treatment for central nervous system (CNS) diseases. The efficacy of available treatments are limited because most therapeutic molecules are unable to permeate the brain parenchyma due to the blood–brain barrier (BBB) (Huang et al., 2017; Fernandes et al., 2018). The BBB is a complex physical and functional barrier that regulates the flux of blood-borne solutes into the brain, protecting the CNS from physical and chemical threats

(Irudayanathan et al., 2016; Pardridge, 2012). To overcome this problem, the use of nanomaterials has been proposed as a non-invasive strategy for the delivery of drugs across the BBB (Khongkow et al., 2019; Tam et al., 2016).

Among the various nanomaterials studied recently, carbon nanotubes (CNTs) have attracted immense interest in the neuroscience field, with promising results regarding BBB permeability and biosafety after local (Dal Bosco et al., 2015a; Dal Bosco et al., 2015b; Lee et al., 2011; Nunes et al., 2012) and systemic (Yang et al., 2007; Kafa et al., 2015; Kafa et al., 2016; Soligo et al., 2021) administration in rodents. Because of their small and controllable dimensions, unique physicochemical properties, and ease of chemical modification to improve biocompatibility either by covalent bonding (e.g., with polyethylene glycol—PEG) or by adsorption (e.g., with DNA), CNTs are considered strong candidates for many neurobiological applications. Furthermore, the unique properties of single-walled carbon nanotubes (SWCNTs), including their near-infrared photoluminescence with minimal tissue interference, make them ideal optical probes for biological applications (Fernandes et al., 2018).

Despite several possible applications of CNTs in biomedicine and neuroscience, much remains to be known about their biological implications. Although many studies have examined CNT effects using *in vitro* systems, there is a lack of information about the interactions of these materials with the CNS of animals under physiological conditions. It is thus essential to consider the importance of a detailed investigation of the effects of different types of CNTs (single walled–SWCNT and multi walled–MWCNT), with different levels of functionalization and purity, and diverse states of aggregation (Mann et al., 2022; Metternich et al., 2023).

Kafa et al. (2015) used two different methods to demonstrate the ability of MWCNTs to cross the BBB using a BBB co-culture *in vitro* model comprising primary porcine brain endothelial cells and primary rat astrocytes exposed to amino-functionalized MWCNTs, and an *in vivo* analysis consisting of the systemic administration of MWCNT radio-labelled with fluorescein isothiocyanate in mice. Another study showed that the intracerebroventricular injection of amine-modified SWCNTs resulted in brain protection from ischemic damage by reducing apoptosis, inflammation, and glial cell activation in a rat stroke model (Lee et al., 2011). In addition, studies using pristine SWCNTs (Yang et al., 2007), angiopep-2 targeted chemically-functionalized MWCNTs (Kafa et al., 2016), and Gd (L2) and Gd (L3) loaded onto different functionalized MWNTs (Costa et al., 2018) have been developed in order to enhance the biodistribution of CNTs and the ability to cross the BBB.

When in aqueous media, pristine SWCNTs tend to form aggregates that are associated with several toxic responses (Alshehri et al., 2016; Elsaesser and Howard, 2012; Kavosi et al., 2018; Pinals et al., 2020; Gravely et al., 2022). One of the most successful strategies for overcoming this limitation is the functionalization of SWCNTs with PEG chains (SWCNT-PEG), which results in CNTs with more hydrophilicity and electrical neutrality (Dos Santos et al., 2007; Yang et al., 2020; Son et al., 2023; Lemos et al., 2023; Iverson et al., 2013). However, very little information is presently available regarding the rate and brain region-specific biodistribution of SWCNT-PEG in the CNS.

SWCNT-PEG are promising nanomaterials for many biomedical applications, thus requiring a better understanding of their behavior in biological systems (Zhu, 2017). Therefore, the aim of this study was to determine the presence of SWCNT-PEG in the CNS after intravenous injection in Wistar rats and to assess possible implications in spatial memory. We also investigated the presence of SWCNT-PEG in important organs for metabolization and excretion (liver, spleen, and kidney) and evaluated their interactions with the blood. Raman spectroscopy was used to detect nanotubes in the tissues because of its strong sensitivity based on resonance phenomena.

2 Results

2.1 Biodistribution

SWCNT-PEG distribution was assessed using Raman spectroscopy. SWCNT-PEG Raman signatures were observed in the liver, bone, blood, CNS (cerebral cortex), lung, and spleen (Figures 1A–F, respectively). The data provide direct evidence for the presence of SWCNT-PEG in the analyzed tissues. The detection of SWCNT-PEG was based on both the radial breathing mode (RBM) and tangential graphite-like phonon mode (G band). Our results show that, even though part of the nanomaterial accumulated in the liver and in the spleen, a considerable amount of CNTs were detected in the brain cortex.

2.2 Toxicity

To evaluate any potential toxic effects of SWCNT-PEG in the treated rats, we performed biochemical analyses of hepatic and renal key biomarkers. All tested parameters were within normal limits, not showing any obvious toxic effects in the liver or in the kidney after SWCNT-PEG treatment (Supplementary Figure S2).

We investigated the effects the presence of SWCNT-PEG in blood by assessing hematological parameters. The only variations observed were in the indexes for platelet and white blood cells, as there was a decrease in the number of platelets in the animals treated with higher concentrations of SWCNT-PEG (Table 1). Additionally, monocytosis and eosinophilia were observed in animals treated with the highest concentration of SWCNT-PEG (Figures 2A, B, respectively), while no differences were detected among treatments in the number of neutrophils, lymphocytes, and basophils (Figures 2C–E, respectively).

No toxic effects were detected based on necropsy, histology, and overall health (such as weight loss and fatigue) in rats injected with SWCNT-PEG. Similarly, histological analysis of the brain (Figure 3), lung, spleen, and kidney (Figure 4) showed no evidence for extensive cell injury, even though SWCNT-PEG could be identified within the tissues.

2.3 Behavioral testing

Considering the presence of SWCNT-PEG in the brain cortex, we subjected the animals to the Morris water maze (MWM) to

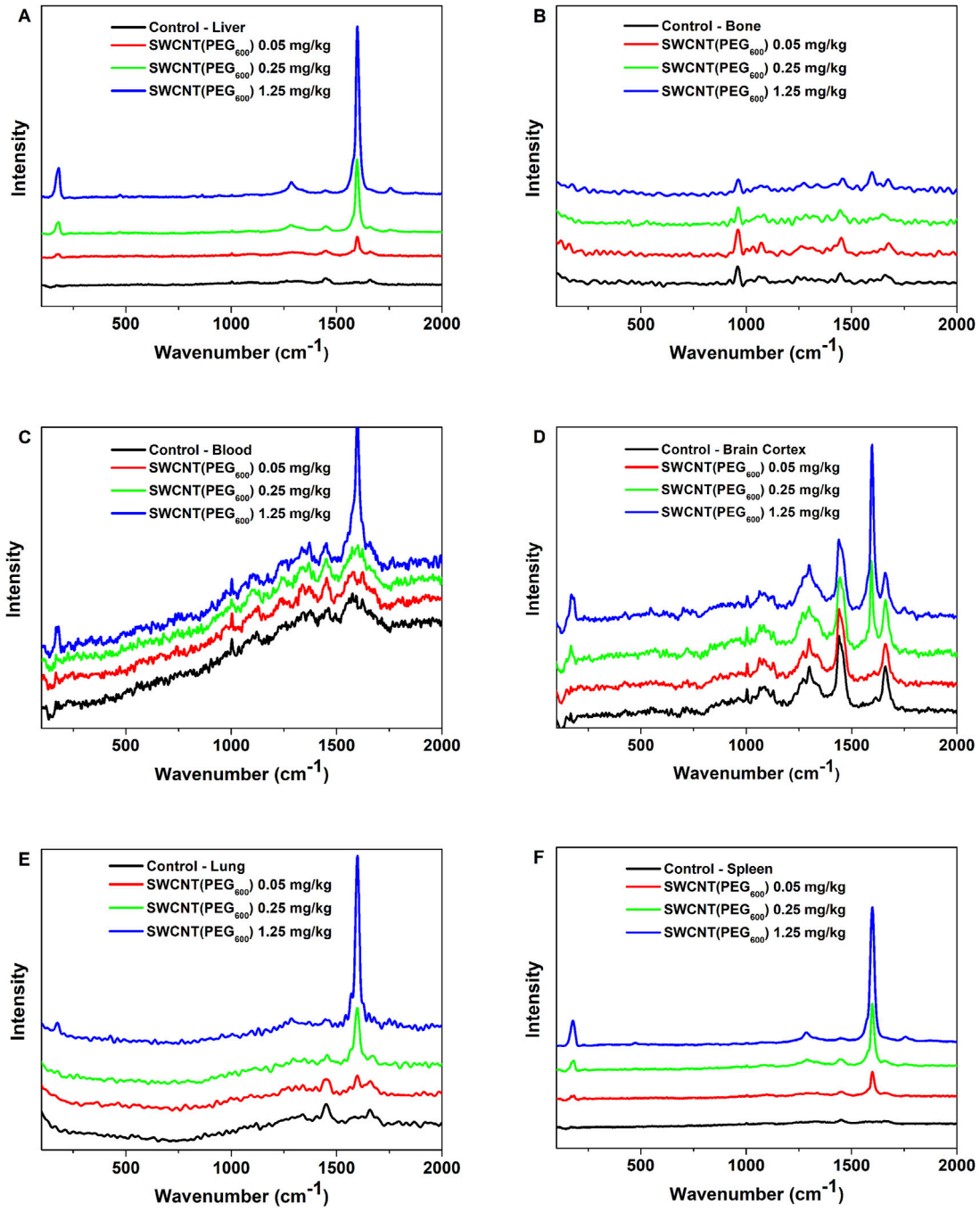

FIGURE 1
Raman spectra of lyophilized tissue samples 24 h after SWCNT-PEG intravenous delivery. Liver **(A)**, bone **(B)**, blood **(C)**, brain cortex **(D)**, lung **(E)**, and spleen **(F)** after injection of SWCNT-PEG dispersions at different concentrations (n=5 per group).

evaluate possible implications of the presence of these nanomaterials in the CNS. The animals were trained for 5 days and were able to learn the task as expected, showing no difference in total traveled distance (Supplementary Figure S3). They were treated with SWCNT-PEG or saline after the last training session, and the test session was performed 24 h later. SWCNT-PEG did not cause impairments in spatial learning 24 h after treatment. Interestingly, the groups treated with the two lowest tested doses showed an improvement in memory evocation, observed by the time spent in the TQ during the test session (Figure 5).

3 Discussion

SWCNT are usually not observable through optical microscopy, but this was possible in the present case because they were found to lodge in the biological tissue in the form of large aggregates. The

TABLE 1 Hematological parameters.

Parameter	Control	SWCNT-PEG 0.05 mg/kg	SWCNT-PEG 0.25 mg/kg	SWCNT-PEG 1.25 mg/kg
RBC (10^{12}/L)	8.47 ± 0.31	8.57 ± 0.18	7.98 ± 0.18	8.25 ± 0.40
HGB (g/L)	15.5 ± 0.46	15.9 ± 0.25	14.9 ± 0.28	15.1 ± 0.85
MCV (fL)	51.1 ± 0.39	51.8 ± 0.38	52.8 ± 0.51	51.5 ± 0.57
HCT (%)	43.4 ± 1.37	44.5 ± 0.68	42.1 ± 0.64	42.3 ± 1.75
MCH (pg)	18.3 ± 0.20	18.5 ± 0.18	18.7 ± 0.18	18.3 ± 0.23
MCHC (g/L)	35.6 ± 0.34	35.7 ± 0.11	35.3 ± 0.12	35.6 ± 0.20
PLT (10^9/L)	703.2 ± 42.3	737.0± 53.0	595.4 ± 45.0	373.2 ± 78.0 *
MPV (fL)	67.4 ± 2.7	68.4 ± 1.3	71.7 ± 1.8	75.0 ± 3.4
PCT (%)	0.47 ± 0.017	0.50 ± 0.026	0.40 ± 0.034	0.35 ± 0.033*
WBC (10^9/L)	4.85 ± 0.72	5.20 ± 0.58	5.36 ± 0.40	4.80 ± 0.60

Red blood counting (RBC), blood count hemoglobin (HGB), mean corpuscular volume (MCV), hematocrit (HCT), mean corpuscular hemoglobin (MCH), mean corpuscular hemoglobin concentration (MCHC), platelet count (PLT), mean platelet volume (MPV), plateletcrit (PCT), and white blood cell count (WBC) from blood samples of animals treated with saline (Control) or different amounts of SWCNT-PEG. * = $p < 0.05$ compared to the control group (one-way ANOVA, followed by Tukey's post-test) (n=5 per group). All data are expressed as mean ± SEM.

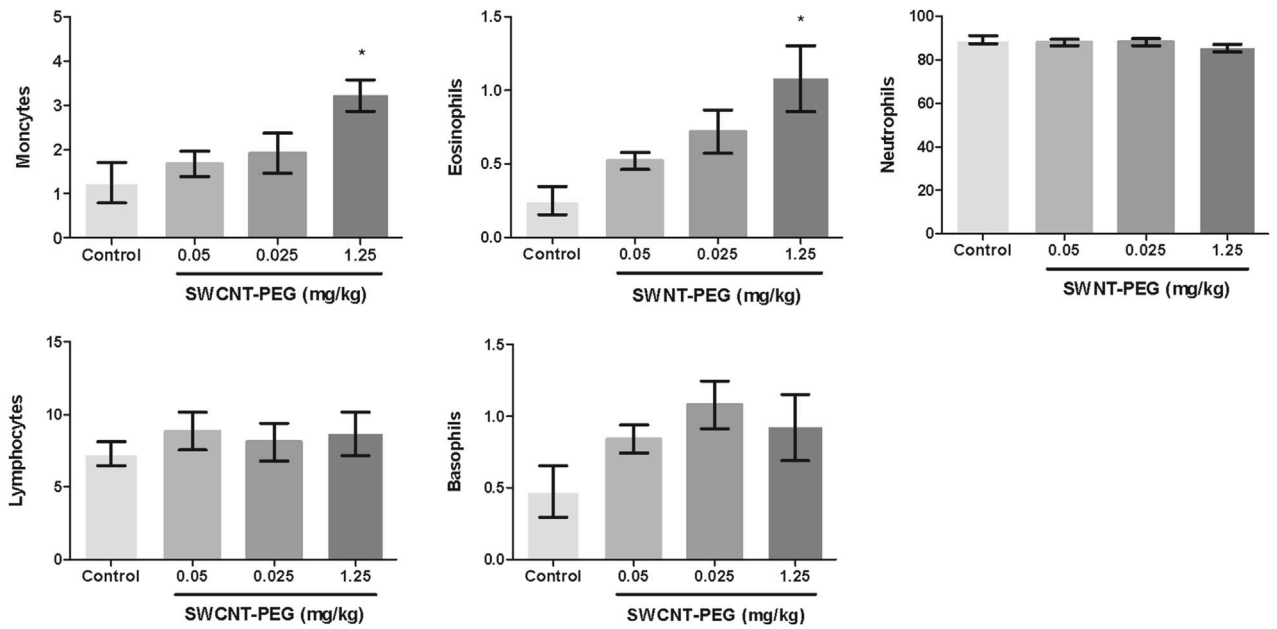

FIGURE 2
White blood cell differential count number of monocytes, eosinophils, neutrophils, lymphocytes, and basophils in blood samples of animals treated with saline or SWCNT-PEG suspensions at different concentrations. * = $p < 0.05$ compared to the control group (one-way ANOVA followed by Tukey's post-test) (n=5 per group). All data are expressed as mean ± SEM.

sample used in this experiment was dispersed in water, and the characterization by TEM analysis (Weber et al., 2014) showed that the SWCNT-PEG used in this study were functionalized in bundles (two to five tubes) that were occasionally connected by polymeric masses that presumably led to the formation of larger aggregates. Long periods of bath-sonication were not sufficient to separate the aggregates, which probably become even larger with time. As suggested by the zeta potential of −60 mV and as observed by TEM analysis, the PEGylation of our sample was not homogeneous and was considerably unstable, featuring uncovered portions in the SWCNT surface that were free to interact with the molecules of the biological medium. This outcome is explainable by the combination of the functionalization method and the length of the PEG chains we used. SWCNTs were subjected to a strong acid treatment for the addition of carboxyl groups, introduced to interact with PEG hydroxyl groups (Sacchetti et al., 2013). It is both possible that some carboxyl groups did not react with PEG (as a result of steric hindrance) and that the PEG chains were not long enough to completely cover the SWCNT surface (Zhao et al., 2005). Thus, not only were the uncovered areas hydrophobic, as is common with

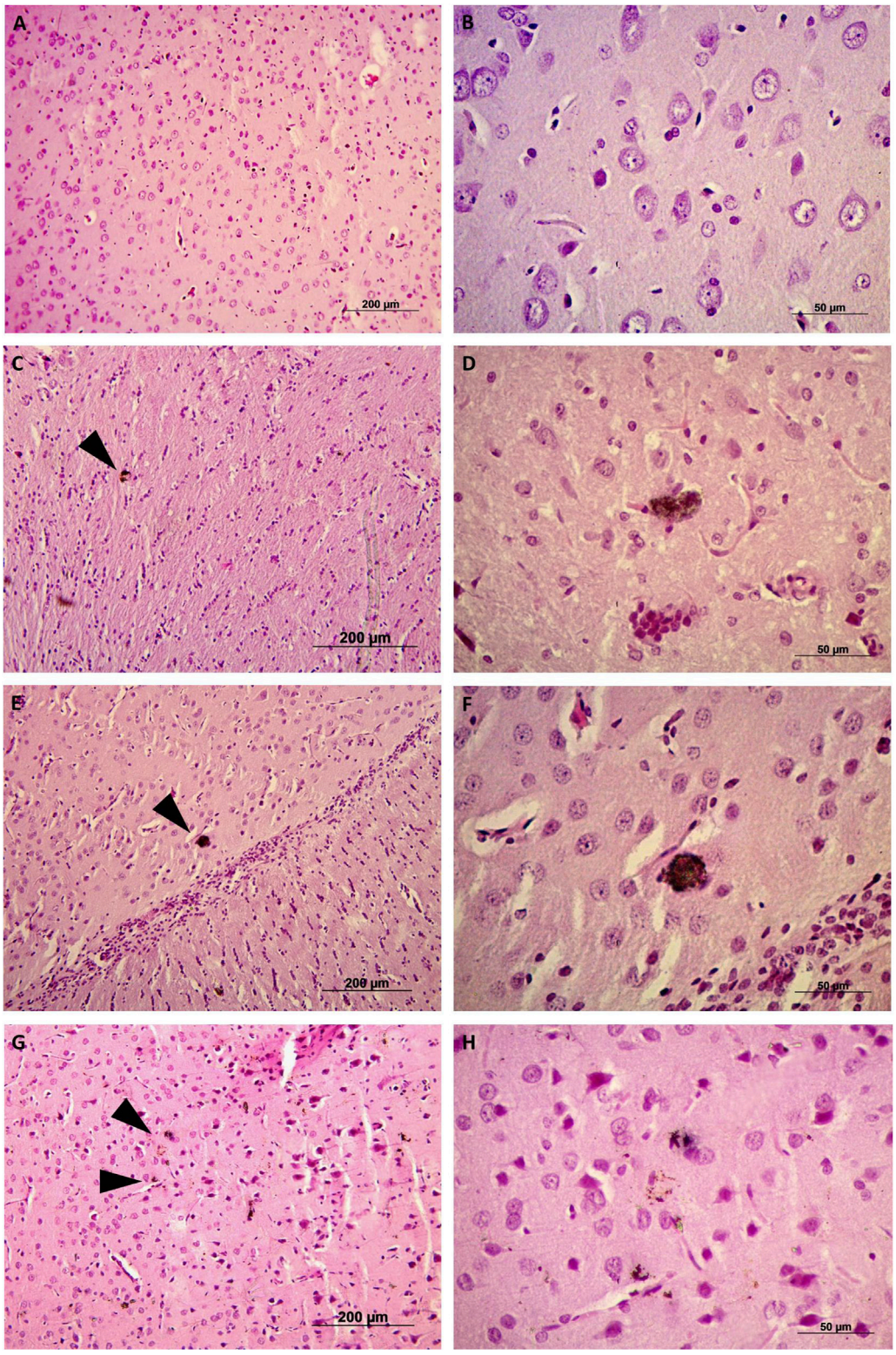

FIGURE 3
Histological analysis of brain tissues from rats injected with a saline solution or SWCNT-PEG dispersions. Representative images of brain coronal sections of control animals **(A, B)** and animals treated with SWCNT-PEG dispersions at concentrations of 0.05 mg/kg **(C, D)**, 0.25 mg/kg **(E, F)**, or 1.25 mg/kg **(G, H)** 24 h after infusion. Black arrowheads in C, E, and G indicate the presence of SWCNT-PEG in the tissue parenchyma without signs of cellular or tissue damage. B, D, F, and H micrographs are high-magnification images of specific areas in A, B, C, and D, respectively (n=5 per group).

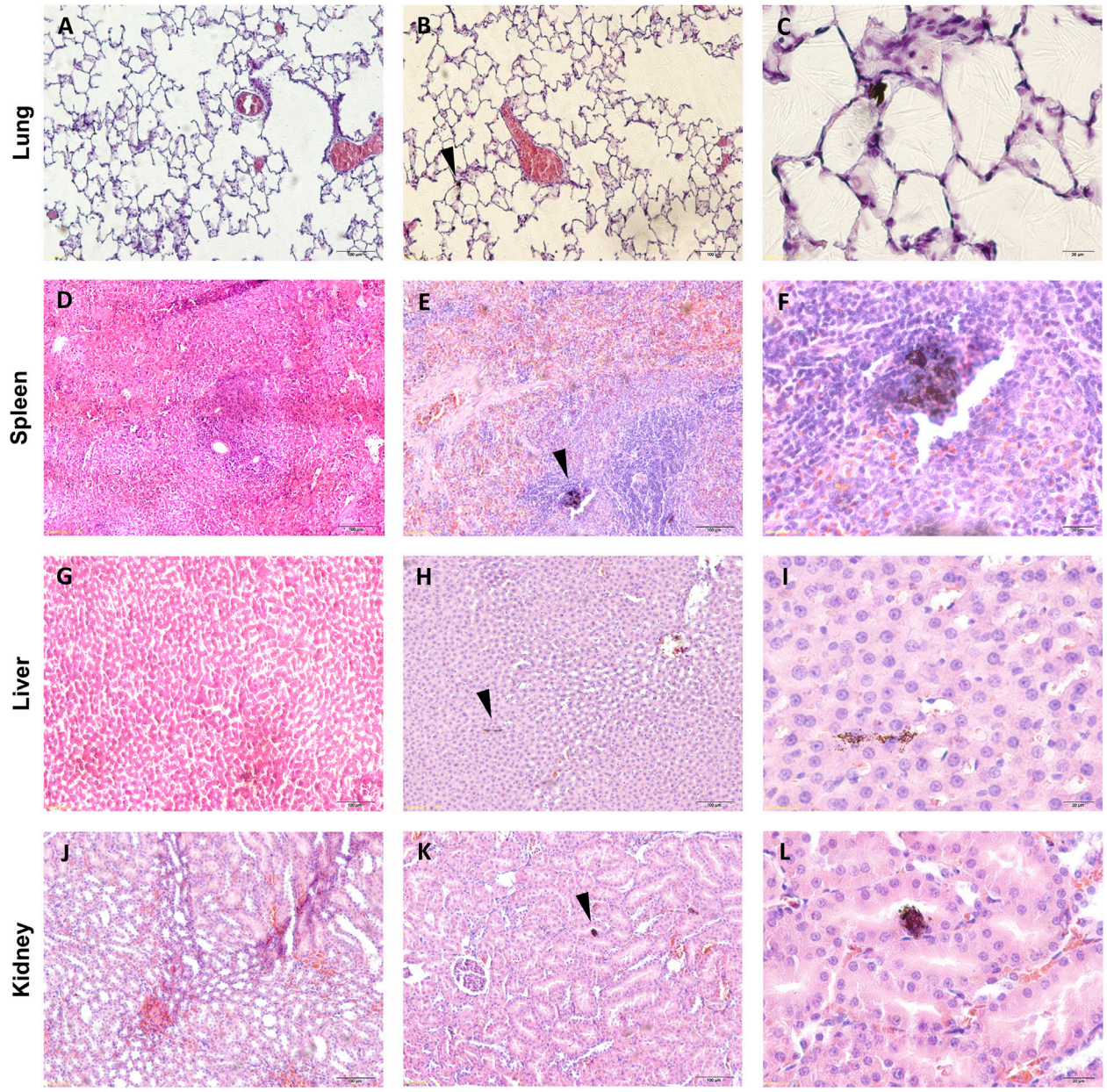

FIGURE 4
Histological analysis of tissues from rats injected with a saline solution or SWCNT-PEG. Representative images of histological sections of the lung, spleen, liver, and kidney of control animals **(A, D, G,** and **J)** and animals treated with SWCNT-PEG dispersions at 1.25 mg/kg. Black arrows in **(B, E, H,** and **K)** indicate the presence of SWCNT-PEG in the tissue parenchyma without signs of cell or tissue damage. **(C, F, I,** and **L)** are high-magnification micrographs of specific areas in **(B, E, H**, and **K)** (n= 5 per group).

non-functionalized SWCNT, but they also contained carboxyl groups that were free to interact with the many different molecules present in the biological medium.

Our histological analysis revealed that SWCNT-PEG accumulated in both the liver and the spleen, which can be explained due to opsonization and scavenging by the mononuclear phagocytic system (MPS) (García et al., 2014; Liu et al., 2008). It is well-known that the size, shape, degree, and arrangement of functionalization are important variables for CNT pharmacokinetics, biodistribution, and tissue penetration (Lemos et al., 2023; García et al., 2014; Serpell et al., 2016). As reported by Liu et al. (2007), PEGylation reduces CNT uptake by the liver and the spleen and increases the blood circulation of SWCNT-PEG5400 (PEG, MW = 5,400 Da), avoiding rapid *in vivo* clearance. Elsewhere, Liu et al. (2008), showed that the PEG chain length and structure (branched or linear) as well as the quality and coverage of PEGylation affect CNT *in vivo* biodistribution. Important characteristics to highlight are the aggregation state of nanotubes in the dispersion. Xue et al. (2016) reported that individualized and aggregated SWCNTs exhibit different bioactivities. They found that the intracranial delivery of aggregated SWCNTs attenuated the increase of extracellular dopamine release induced by

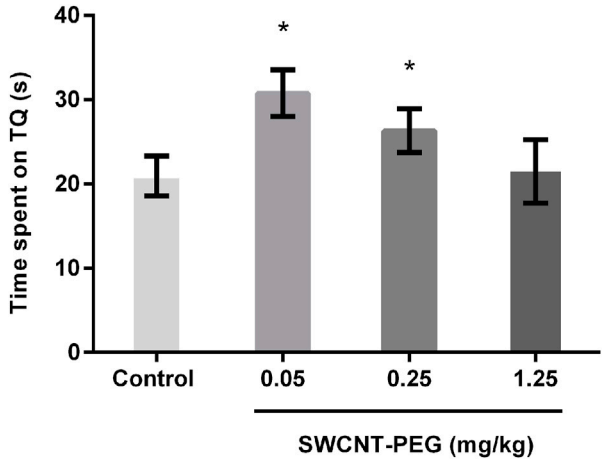

FIGURE 5
Effects of SWCNT-PEG intragingival vein injection on spatial memory, as assessed with the Morris water maze task. Animals treated with the least concentrated SWCNT-PEG suspensions spent more time in the target quadrant (TQ) than controls, suggesting that SWCNT-PEG can improve spatial memory. * = $p < 0.05$ compared to the control group (one-way ANOVA followed by Tukey's post-test) (n=7-9 per group). All data are expressed as mean ± SEM.

methamphetamine in the ventral striatum through the oxidation of tyrosine and dopamine.

Our results are consistent with these findings and show the presence of SWCNT-PEG in the brain. Al-Jamal et al. (2011) previously showed that MWCNTs were able to successfully deliver siRNA to rat brain cells, confirming direct membrane penetration. Interestingly, we could only detect SWCNT-PEG in the brain cortex (Figure 1D) and not in other brain structures (Supplementary Figure S4). To the best of our knowledge, this is the first report of the biodistribution of SWCNT-PEG in a specific region of the brain tissue after intravenous injection. This raises several questions and hypotheses about the interactions of CNTs with the BBB and specific brain regions. However, it is possible that the SWCNT-PEG went from the bloodstream to the brain parenchyma in regions other than the cerebral cortex but below the detection limit of our methodology. The BBB spreads throughout the brain in a nonhomogeneous fashion, possibly containing regions that are more permeable to the SWCNT-PEG near the cortex. Paviolo et al. (2019) showed the presence of individual SWCNTs (functionalized with phospholipid-polyethylene glycol—PL-PEG) in the CA1 and dentate gyrus (DG) of rat hippocampal organotypic slices and the presence of carbon nanotubes in the cortex, striatum, hippocampus, and ventral midbrain in mouse acute slices either by incubation (organotypic slices) or injection into the cerebral lateral ventricle of live adult mouse (acute slices). This study provides interesting information about the understanding of SWCNT diffusion in different brain extracellular space.

Moreover, Kateb et al. (2007) demonstrated the spontaneous uptake of MWCNTs by the microglia. If SWCNT-PEG of smaller particle size were able to penetrate the brain tissue in other regions, it is possible that the cerebral defenses affected the material, hindering its detection.

Blood analysis revealed an increase in platelets and white blood cells. This observation probably indicates platelet activation resulting from an acute inflammatory response due to the contact of blood cells with SWCNT-PEG (Budak et al., 2016). Although the SWCNTs were pre-coated with PEG in order to form stable dispersions in biological milieu, it has been shown that this does not prevent the activation of the complementary system (Rybak-Smith and Sim, 2011). PEG functionalization did not cover the entire CNT structure, and this uncoated portion was probably almost immediately covered by a corona composed of proteins naturally found in the biological medium which triggers immune responses (Pinals et al., 2020; Yang et al., 2020; Budak et al., 2016; Rybak-Smith and Sim, 2011). Vlasova et al. (2012), demonstrated that these unprotected areas of the CNT may be the primary sites for oxidative damage and the degradation of the nanomaterial. When the immune system recognizes SWCNT-PEG, the first cellular lines of defense of the body, such as monocytes/macrophages and neutrophils (Yang et al., 2019), are among the first to encounter the nanomaterials injected into the blood stream.

The highest SWCNT-PEG dose resulted in monocytosis and eosinophilia. Monocyte activation and inflammation apparently were the first event after the intravenous injection of our SWCNT-PEG. Eosinophil activation is associated with lung dysfunction (such as cystic fibrosis) (Davies et al., 2008) and it is probably related to the biodegradation and clearance of the SWCNT-PEG injected into blood stream that were quickly trapped in the lungs (Vlasova et al., 2012; Ijaz et al., 2023).

To evaluate whether the presence of SWCNT-PEG in the CNS could have led to alterations in behavior, we subjected the animals to the MWM as a method of assessing spatial or place learning. The prefrontal cortex is one of the brain structures involved in learning and memory in this task (Vorhees and Williams, 2006). The MWM has already been used by Yang et al. (2010) as one parameter to evaluate therapeutic effects of SWCNT-acetylcholine in a mouse model for Alzheimer disease. SWCNT-PEG did not lead to behavioral impairments in this task. On the contrary, the animals treated with the two lowest doses showed an improvement in memory evocation according to the tested parameters (more time spent in the target quadrant during the test session). It is important to highlight that, in the biodistribution analysis using Raman spectroscopy, we did not detect the presence of nanotubes in the cerebral cortex at the lowest concentration (0.05 mg/kg). This may be due to the concentration being below the detection limit of the technique, despite the memory improvement observed in the MWM experiment at this dose. Furthermore, at lower nanomaterial concentrations, less aggregation is expected. Consequently, the increased dispersion of nanomaterials may lead to a greater biological effect. However, this possible effect of unknown underlying mechanisms requires further confirmation.

Based on our results, we suggest that the tested nanomaterial can cross the BBB and reach the brain cortex without leading to acute toxicity. These findings encourage the use of SWCNT-PEG in small bundles as a platform for applications in the CNS. Further studies, such as more detailed behavioral tasks, BBB penetration assays, and toxicological tests involving different routes of administration and long-term effects, need to be performed to determine the safest approach for the *in vivo* use of CNT.

4 Materials and methods

4.1 SWCNT-PEG dispersions and characterization

SWCNTs (Sigma-Aldrich, St. Louis, MO, United States) were synthesized by electric arc discharge and functionalized with PEG (MW = 600 Da). SWCNT-PEG preparation was carried out following our previous protocol (Weber et al., 2014). In brief, we prepared the dispersion in deionized water at a high concentration (greater than 2 mg/mL). A multi-step process employing several cycles of sonication, high-shear mixing, centrifugation, and ultracentrifugation was required to prepare a stable dispersion. SWCNT-PEG were previously characterized in another study from our group (Weber et al., 2014) and showed ~25 wt% of grafted PEG, ~60 wt% of SWCNT, and ~20 wt% of 20–40 nm diameter carbon-coated catalyst particles (Ni–Y). As detailed in Weber et al. (2014) and Dal Bosco et al. (2015b), low-resolution TEM analyses showed that this commercial SWCNT-PEG sample formed large aggregates in water even after prolonged bath sonication. The concentration of the final dispersion obtained after the entire process was of approximately 2.1 mg/mL. The Zeta potential of the sample was approximately −60 mV, indicating the presence of many unreacted carboxylic acid groups (–COOH).

4.2 Animals and treatments

Male Wistar rats (2–3 months old, weighing 250–320 g) were purchased from the breeding colony at the Federal University of Rio Grande–FURG (Rio Grande, RS, Brazil) and randomly distributed up to five animals per cage. The animals were kept under standard laboratory conditions (12 h light/dark photoperiod and 23°C ± 1°C) with free access to food pellets and water. The animals were subjected to intragingival vein administration of SWCNT-PEG dispersion (1 mg/mL) at 0.05, 0.25, and 1.25 mg/kg or to saline (control group). Intragingival vein administration was performed under light anesthesia with halothane. The animal was held in a supine position, and the lower lip was retracted to expose the gingiva. A 28–30 gauge needle was then inserted at a 20°–25° angle, approximately 2 mm into the gingiva. (de Oliveira et al., 2009). All procedures were performed according to the guidelines of the Brazilian National Council for the Control of Animal Experimentation (CONCEA) and authorized by the Ethics Committee for Animal Use of the Federal University of Rio Grande–FURG (permission number P006/2014).

4.3 Raman spectroscopy

All animals were killed by decapitation 24 h post-injection, and the organs of interest were carefully removed for biodistribution analysis. Samples were lyophilized, sprayed with mortar, and Raman spectroscopy was performed using a FT-Raman spectrometer (RAM II - Bruker Inc., Karlsruhe, Germany) with excitation source at 1,064 nm (1.16 eV) and 150 mW. This excitation energy is below the self-fluorescence range of the tissues, allowing us to obtain background-free Raman spectra (Supplementary Figure S1). The characteristic Raman spectrum of SWCNT-PEG in the lyophilized tissues presented peaks approximately 180, 1,300, and 1,600 cm^{-1}, corresponding to RBM, D, and G bands, respectively. The laser excitation energy used was in resonance with the second optical transitions (E22S) of semiconducting SWCNT. All spectra were normalized to the 1,448 cm^{-1} band, relative to the proteins obtained from the control group.

4.4 Histological analysis

The animals were euthanized and tissues of interest were isolated, fixed in 10% neutral buffered formalin for 12 h at room temperature, and processed according to histological routine. The samples were embedded in paraffin, sectioned at 5 µm, and stained with hematoxylin and eosin (H&E). The sections were observed and examined under a clear field microscope (Zeiss Primo Star) by a certified pathologist (L.A.R.).

4.5 Behavioral assessment

The implications of SWCNT administration on spatial memory were evaluated using the model described by Morris (1984). This Morris water maze (MWM) apparatus consisted of a circular tank divided into four imaginary quadrants and filled with water (24°C ± 1°C) dyed with non-toxic food colorant. A black platform was placed in one of the quadrants (2 cm below water surface level) and visual cues were distributed on the walls of the room. On the first training day, animals were subjected to a four-stage training session (120 s with 70 s interval), starting each stage in a different quadrant. The training sessions were repeated for another 4 days, and the learning progress—time taken to find the platform—was quantified. At the end of the last training session (day 5), the animals received an injection of SWCNT-PEG or saline. On the sixth day, the platform was removed, and the animals were placed in the tank to swim freely for 90 s (test session). Memory consolidation was assessed as the time spent by the animals in the quadrant where the platform was previously placed. Data for this test were acquired using a video tracking system (EthoVision® 3.2, Noldus).

4.6 Hematological and biochemical analysis

Blood was collected 24 h after injection. The rats were euthanized, and blood was collected by cardiac puncture into ethylenediamine tetra acetic acid (EDTA) bottles to evaluate hematological parameters. We performed red blood counting (RBC), blood count hemoglobin (HGB), mean corpuscular volume (MCV), hematocrit (HCT), mean corpuscular hemoglobin (MCH), mean corpuscular hemoglobin concentration (MCHC), platelet count (PLT), mean platelet volume (MPV), plateletcrit (PCT), and white blood cell count (WBC) for monocytes, neutrophils, lymphocytes, eosinophils, and basophils using an automated dialysis machine. For the biochemical analysis, another portion of blood was dispensed into plain bottles, allowed to clot, and centrifuged at 3,500 rpm for 10 min, and the clear sera were

aspirated for biochemical evaluation. Creatinine, alanine aminotransferase (ALT), and aspartate aminotransferase (AST) were analyzed using commercial kits obtained from Doles (Go, Brazil) following the manufacturer's instructions.

4.7 Statistical analysis

Results were analyzed using one-way ANOVA (STATSOFT Statistica, version 7.0) followed by Tukey's *post hoc* test. All data are presented as mean ± SEM, and p-values < 0.05 were considered statistically significant.

5 Conclusions

In this study, we used Raman spectroscopy to detect SWCNT-PEG in the major organs of rats following intravenous administration. The presence of SWCNT-PEG in the liver, bone, blood, lungs, cerebral cortex, and spleen 24 h post-injection was not associated with significant signs of toxicity, as demonstrated by biochemical, histological, and behavioral analyses. These findings are consistent with other studies evaluating the toxicity of PEG-functionalized CNTs. However, certain factors must be considered, such as the length of the PEG chains, the purity of the nanomaterial, and the degree of functionalization. In this study, we utilized a commercial sample of SWCNTs covalently functionalized with PEG (MW = 600 Da), which formed large aggregates in water even after prolonged bath sonication. This aggregation state of the nanotubes in the dispersion may explain why they were observable in biological tissues using optical microscopy, which is uncommon.

Our biodistribution analysis revealed that SWCNT-PEG reached the cerebral cortex but not other brain structures. Despite the presence of these nanomaterials in the CNS, no behavioral impairments were observed in treated animals, as demonstrated by the Morris water maze task. Interestingly, animals injected with the two lowest doses exhibited an improvement in spatial learning based on the tested parameters. This effect on memory evocation was observed even in animals injected with the lowest concentration (0.05 mg/kg), where the SWCNT-PEG Raman signature was not detected. Therefore, we cannot rule out the possibility that this material reached other regions of the brain parenchyma at concentrations below the detection limit of the technique.

This study provides an initial evaluation of the fate and biological effects of PEG-functionalized carbon nanotubes (CNTs) shortly after systemic administration. To achieve a more comprehensive understanding of the safety profile and potential biomedical applications of SWCNT-PEG-based delivery systems, further investigations are required. These should focus on the biodistribution, toxicity, and clearance of these nanomaterials, employing varying dosages, administration routes, and exposure durations.

Data availability statement

The original contributions presented in the study are included in the article/Supplementary Material; further inquiries can be directed to the corresponding author.

Ethics statement

The animal study was approved by Ethics Committee for Animal Use of the Federal University of Rio Grande–FURG (permission number P006/2014). The study was conducted in accordance with the local legislation and institutional requirements.

Author contributions

GB: conceptualization, formal analysis, funding acquisition, investigation, methodology, writing–original draft, writing–review and editing, data curation, and project administration. LD: conceptualization, formal analysis, funding acquisition, investigation, methodology, writing–original draft, and writing–review and editing. AC: data curation, methodology, and writing–original draft. MC: conceptualization, data curation, formal analysis, funding acquisition, investigation, methodology, writing–original draft, and writing–review and editing. SS: formal analysis, investigation, methodology, writing–original draft, and writing–review and editing. CP: funding acquisition, methodology, project administration, and writing–original draft. MK: data curation, formal analysis, methodology, and writing–review and editing. LR: conceptualization, data curation, formal analysis, investigation, methodology, and writing–review and editing. CF: conceptualization, data curation, formal analysis, funding acquisition, investigation, methodology, and writing–review and editing. AS: conceptualization, data curation, formal analysis, funding acquisition, investigation, methodology, project administration, supervision, and writing–review and editing. DB: conceptualization, data curation, formal analysis, funding acquisition, investigation, methodology, project administration, resources, supervision, validation, writing–original draft, and writing–review and editing.

Funding

The authors declare that financial support was received for the research, authorship, and/or publication of this article. This work was partially supported by the Brazilian Institute of Science and Technology (INCT) in Carbon Nanomaterials and the Brazilian agencies Fapemig, CAPES, and CNPq, research grants from Fundação de Amparo à Pesquisa do Estado do Rio Grande do Sul (FAPERGS-PRONEM, process number 11/2037–9), the Nanotoxicology Network (MCTI/CNPq process number 552131/2011–3), and CNPq (Universal, process number 435890/2018–2). Daniela M. Barros, Adelina P. Santos, and Cristiano Fantini were sponsored with productivity research fellowships from the Brazilian National Council of Scientific and Technological Development (CNPq). Gisele Eva Bruch, Lidiane Dal Bosco, and Marcos F. Cordeiro received a graduate scholarship from Coordenação de Aperfeiçoamento de Pessoal de Nível Superior (CAPES). This work was partially supported by the Brazilian Institute of Science and Technology (INCT) in Carbon Nanomaterials—CTI/CNPq/CAPES/FAPs number 16/2014 process number 421701/2017-0.

Acknowledgments

The authors thank the Institute of Science and Technology (INCT) in Carbon Nanomaterials and the Brazilian agencies Fapemig, CAPES, and CNPq for supporting this work, and Beatriz Lopes Tecedor Bassi from Universidade Federal de Minas Gerais (UFMG) for the scientific discussion, contribution to the text, and English correction.

Conflict of interest

The authors declare that the research was conducted in the absence of any commercial or financial relationships that could be construed as a potential conflict of interest.

Publisher's note

All claims expressed in this article are solely those of the authors and do not necessarily represent those of their affiliated organizations, or those of the publisher, the editors, and the reviewers. Any product that may be evaluated in this article, or claim that may be made by its manufacturer, is not guaranteed or endorsed by the publisher.

Supplementary material

The Supplementary Material for this article can be found online at: https://www.frontiersin.org/articles/10.3389/frcrb.2024.1363919/full#supplementary-material.

References

Al-Jamal, K. T., Gherardini, L., Bardi, G., Nunes, A., Guo, C., Bussy, C., et al. (2011). Functional motor recovery from brain ischemic insult by carbon nanotube-mediated siRNA silencing. *Proc. Natl. Acad. Sci.* 108 (27), 10952–10957. doi:10.1073/pnas.1100930108

Alshehri, R., Ilyas, A. M., Hasan, A., Arnaout, A., Ahmed, F., and Memic, A. (2016). Carbon nanotubes in biomedical applications: factors, mechanisms, and remedies of toxicity. *J. Med. Chem.* 59, 8149–8167. doi:10.1021/acs.jmedchem.5b01770

Budak, Y. U., Polat, M., and Huysal, K. (2016). The use of platelet indices, plateletcrit, mean platelet volume and platelet distribution width in emergency non-traumatic abdominal surgery: a systematic review. *Biochem. Medica* 26, 178–193. doi:10.11613/bm.2016.020

Costa, P. M., Wang, J. T. W., Morfin, J. F., Khanum, T., To, W., Sosabowski, J., et al. (2018). Functionalised carbon nanotubes enhance brain delivery of amyloid-targeting Pittsburgh compound B (PiB)-Derived ligands. *Nanotheranostics* 2 (2), 168–183. doi:10.7150/ntno.23125

Dal Bosco, L., Weber, G. E., Parfitt, G. M., Cordeiro, A. P., Sahoo, S. K., Fantini, C., et al. (2015a). "Biopersistence of PEGylated carbon nanotubes promotes a delayed antioxidant response after infusion into the rat hippocampus,". Editor M. Ahmad, 10. doi:10.1371/journal.pone.0129156

Dal Bosco, L., Weber, G. E. B., Parfitt, G. M., Paese, K., Gonçalves, C. O. F., Serodre, T. M., et al. (2015b). PEGylated carbon nanotubes impair retrieval of contextual fear memory and alter oxidative stress parameters in the rat hippocampus. *BioMed Res. Int.* 2015, 1–11. doi:10.1155/2015/104135

Davies, M. J., Hawkins, C. L., Pattison, D. I., and Rees, M. D. (2008). Mammalian heme peroxidases: from molecular mechanisms to health implications. *Antioxidants & Redox Signal.* 10 (7), 1199–1234. doi:10.1089/ars.2007.1927

de Oliveira, D. T., Souza-Silva, E., and Tonussi, C. R. (2009). Technical report: gingival vein punction: a new simple technique for drug administration or blood sampling in rats and mice. *Scand. J. Lab. Anim. Sci.* 36 (2), 109–113. doi:10.23675/sjlas.v36i2.174

Dos Santos, N., Allen, C., Doppen, A. M., Anantha, M., Cox, K. A. K., Gallagher, R. C., et al. (2007). Influence of poly(ethylene glycol) grafting density and polymer length on liposomes: relating plasma circulation lifetimes to protein binding. *Biochimica Biophysica Acta (BBA) - Biomembr.* 1768 (6), 1367–1377. doi:10.1016/j.bbamem.2006.12.013

Elsaesser, A., and Howard, C. V. (2012). Toxicology of nanoparticles. *Adv. Drug Deliv. Rev.* 64 (2), 129–137. doi:10.1016/j.addr.2011.09.001

Fernandes, L. F., Bruch, G. E., Massensini, A. R., and Frézard, F. (2018). Recent advances in the therapeutic and diagnostic use of liposomes and carbon nanomaterials in ischemic stroke. *Front. Neurosci.* 12, 453. doi:10.3389/fnins.2018.00453

García, K. P., Zarschler, K., Barbaro, L., Barreto, J. A., O'Malley, W., Spiccia, L., et al. (2014). Zwitterionic-coated "stealth" nanoparticles for biomedical applications: recent advances in countering biomolecular corona formation and uptake by the mononuclear phagocyte system. *Small* 10 (13), 2516–2529. doi:10.1002/smll.201303540

Gravely, M., Kindopp, A., Hubert, L., Card, M., Nadeem, A., Miller, C., et al. (2022). Aggregation reduces subcellular localization and cytotoxicity of single-walled carbon nanotubes. *ACS Appl. Mater Interfaces* 14 (17), 19168–19177. doi:10.1021/acsami.2c02238

Huang, L., Hu, J., Huang, S., Wang, B., Siaw-Debrah, F., Nyanzu, M., et al. (2017). Nanomaterial applications for neurological diseases and central nervous system injury. *Prog. Neurobiol.* 157, 29–48. doi:10.1016/j.pneurobio.2017.07.003

Ijaz, H., Mahmood, A., Abdel-Daim, M. M., Sarfraz, R. M., Zaman, M., Zafar, N., et al. (2023). Review on carbon nanotubes (CNTs) and their chemical and physical characteristics, with particular emphasis on potential applications in biomedicine. *Inorg. Chem. Commun.* 155, 111020. doi:10.1016/j.inoche.2023.111020

Irudayanathan, F. J., Trasatti, J. P., Karande, P., and Nangia, S. (2016). Molecular architecture of the blood brain barrier tight junction proteins--A synergistic computational and *in vitro* approach. *J. Phys. Chem. B* 120 (1), 77–88. doi:10.1021/acs.jpcb.5b09977

Iverson, N. M., Barone, P. W., Shandell, M., Trudel, L. J., Sen, S., Sen, F., et al. (2013). *In vivo* biosensing via tissue localizable near infrared fluorescent single walled carbon nanotubes. *Nat. Nanotechnol.* 8 (11), 873–880. doi:10.1038/nnano.2013.222

Kafa, H., Wang, J. T. W., Rubio, N., Klippstein, R., Costa, P. M., Hassan, HAFM, et al. (2016). Translocation of LRP1 targeted carbon nanotubes of different diameters across the blood–brain barrier *in vitro* and *in vivo*. *J. Control. Release* 225, 217–229. doi:10.1016/j.jconrel.2016.01.031

Kafa, H., Wang, J. T. W., Rubio, N., Venner, K., Anderson, G., Pach, E., et al. (2015). The interaction of carbon nanotubes with an *in vitro* blood-brain barrier model and mouse brain *in vivo*. *Biomaterials* 53, 437–452. doi:10.1016/j.biomaterials.2015.02.083

Kateb, B., Van Handel, M., Zhang, L., Bronikowski, M. J., Manohara, H., and Badie, B. (2007). Internalization of MWCNTs by microglia: possible application in immunotherapy of brain tumors. *NeuroImage.* 37, S9–S17. doi:10.1016/j.neuroimage.2007.03.078

Kavosi, A., Hosseini Ghale Noei, S., Madani, S., Khalighfard, S., Khodayari, S., Khodayari, H., et al. (2018). RETRACTED ARTICLE: the toxicity and therapeutic effects of single-and multi-wall carbon nanotubes on mice breast cancer. *Sci. Rep.* 8 (1), 8375. doi:10.1038/s41598-018-26790-x

Khongkow, M., Yata, T., Boonrungsiman, S., Ruktanonchai, U. R., Graham, D., and Namdee, K. (2019). Surface modification of gold nanoparticles with neuron-targeted exosome for enhanced blood-brain barrier penetration. *Sci. Rep.* 9 (1), 8278. doi:10.1038/s41598-019-44569-6

Lee, H. J., Park, J., Yoon, O. J., Kim, H. W., Lee, D. Y., Kim, D. H., et al. (2011). Amine-modified single-walled carbon nanotubes protect neurons from injury in a rat stroke model. *Nat. Nanotechnol.* 6 (2), 121–125. doi:10.1038/nnano.2010.281

Lemos, J. d. A., Soares, D. C. F., Pereira, N. C., Gomides, L. S., Silva, J. d. O., Bruch, G. E., et al. (2023). Preclinical evaluation of PEG-Multiwalled carbon nanotubes: radiolabeling, biodistribution and toxicity in mice. *J. Drug Deliv. Sci. Technol.* 86, 104607. doi:10.1016/j.jddst.2023.104607

Liu, Z., Cai, W., He, L., Nakayama, N., Chen, K., Sun, X., et al. (2007). *In vivo* biodistribution and highly efficient tumour targeting of carbon nanotubes in mice. *Nat. Nanotechnol.* 2 (1), 47–52. doi:10.1038/nnano.2006.170

Liu, Z., Davis, C., Cai, W., He, L., Chen, X., and Dai, H. (2008). Circulation and long-term fate of functionalized, biocompatible single-walled carbon nanotubes in mice probed by Raman spectroscopy. *Proc. Natl. Acad. Sci. U. S. A.* 105 (5), 1410–1415. doi:10.1073/pnas.0707654105

Mann, F. A., Galonska, P., Herrmann, N., and Kruss, S. (2022). Quantum defects as versatile anchors for carbon nanotube functionalization. *Nat. Protoc.* 17 (3), 727–747. doi:10.1038/s41596-021-00663-6

Metternich, J. T., Sistemich, L., Nißler, R., Herbertz, S., and Kruss, S. (2023). Rational design of near-infrared fluorescent carbon nanotube biosensors with covalent DNA-anchors. *ChemRxiv* 27. doi:10.26434/chemrxiv-2023-838d6

Morris, R. (1984). Developments of a water-maze procedure for studying spatial learning in the rat. *J. Neurosci. Methods* 11 (1), 47–60. doi:10.1016/0165-0270(84)90007-4

Nunes, A., Bussy, C., Gherardini, L., Meneghetti, M., Herrero, M. A., Bianco, A., et al. (2012). *In vivo* degradation of functionalized carbon nanotubes after stereotactic administration in the brain cortex. *Nanomedicine* 7 (10), 1485–1494. doi:10.2217/nnm.12.33

Pardridge, W. M. (2012). Drug transport across the blood-brain barrier. *J. Cereb. Blood Flow & Metabolism* 32 (11), 1959–1972. doi:10.1038/jcbfm.2012.126

Paviolo, C., Soria, F. N., Ferreira, J. S., Lee, A., Groc, L., Bezard, E., et al. (2019). Nanoscale exploration of the extracellular space in the live brain by combining single carbon nanotube tracking and super-resolution imaging analysis. *Methods San. Diego Calif.* doi:10.1016/j.ymeth.2019.03.005

Pinals, R. L., Yang, D., Rosenberg, D. J., Chaudhary, T., Crothers, A. R., Iavarone, A. T., et al. (2020). Quantitative protein corona composition and dynamics on carbon nanotubes in biological environments. *Angew. Chem. Int. Ed.* 59 (52), 23668–23677. doi:10.1002/anie.202008175

Rybak-Smith, M. J., and Sim, R. B. (2011). Complement activation by carbon nanotubes. *Adv. Drug Deliv. Rev.* 63 (12), 1031–1041. doi:10.1016/j.addr.2011.05.012

Sacchetti, C., Motamedchaboki, K., Magrini, A., Palmieri, G., Mattei, M., Bernardini, S., et al. (2013). Surface polyethylene glycol conformation influences the protein corona of polyethylene glycol-modified single-walled carbon nanotubes: potential implications on biological performance. *ACS Nano* 7 (3), 1974–1989. doi:10.1021/nn400409h

Serpell, C. J., Kostarelos, K., and Davis, B. G. (2016). Can carbon nanotubes deliver on their promise in biology? Harnessing unique properties for unparalleled applications. *ACS Cent. Sci.* 2 (4), 190–200. doi:10.1021/acscentsci.6b00005

Soligo, M., Felsani, F. M., Da Ros, T., Bosi, S., Pellizzoni, E., Bruni, S., et al. (2021). Distribution in the brain and possible neuroprotective effects of intranasally delivered multi-walled carbon nanotubes. *Nanoscale Adv.* 3 (2), 418–431. doi:10.1039/d0na00869a

Son, M., Mehra, P., Nguyen, F. T., Jin, X., Koman, V. B., Gong, X., et al. (2023). Molecular recognition and *in vivo* detection of temozolomide and 5-Aminoimidazole-4-carboxamide for glioblastoma using near-infrared fluorescent carbon nanotube sensors. *ACS Nano* 17 (1), 240–250. doi:10.1021/acsnano.2c07264

Tam, V. H., Sosa, C., Liu, R., Yao, N., and Priestley, R. D. (2016). Nanomedicine as a non-invasive strategy for drug delivery across the blood brain barrier. *Int. J. Pharm.* 515 (1–2), 331–342. doi:10.1016/j.ijpharm.2016.10.031

Vlasova, I. I., Vakhrusheva, T. V., Sokolov, A. V., Kostevich, V. A., Gusev, A. A., Gusev, S. A., et al. (2012). PEGylated single-walled carbon nanotubes activate neutrophils to increase production of hypochlorous acid, the oxidant capable of degrading nanotubes. *Toxicol. Appl. Pharmacol.* 264 (1), 131–142. doi:10.1016/j.taap.2012.07.027

Vorhees, C. V., and Williams, M. T. (2006). Morris water maze: procedures for assessing spatial and related forms of learning and memory. *Nat. Protoc.* 1 (2), 848–858. doi:10.1038/nprot.2006.116

Weber, G. E. B., Dal Bosco, L., Gonçalves, C. O. F., Santos, A. P., Fantini, C., Furtado, C. A., et al. (2014). Biodistribution and toxicological study of PEGylated single-wall carbon nanotubes in the zebrafish (*Danio rerio*) nervous system. *Toxicol. Appl. Pharmacol.* 280 (3), 484–492. doi:10.1016/j.taap.2014.08.018

Xue, X., Yang, J. Y., He, Y., Wang, L. R., Liu, P., Yu, L. S., et al. (2016). Aggregated single-walled carbon nanotubes attenuate the behavioural and neurochemical effects of methamphetamine in mice. *Nat. Nanotechnol.* 11 (7), 613–620. doi:10.1038/nnano.2016.23

Yang, D., Yang, S. J., Del Bonis-O'Donnell, J. T., Pinals, R. L., and Landry, M. P. (2020). Mitigation of carbon nanotube neurosensor induced transcriptomic and morphological changes in mouse microglia with surface passivation. *ACS Nano* 14 (10), 13794–13805. doi:10.1021/acsnano.0c06154

Yang, M., Zhang, M., Nakajima, H., Yudasaka, M., Iijima, S., and Okazaki, T. (2019). Time-dependent degradation of carbon nanotubes correlates with decreased reactive oxygen species generation in macrophages. *Int. J. Nanomedicine* 14, 2797–2807. doi:10.2147/ijn.s199187

Yang, S. tao, Guo, W., Lin, Y., Deng, X. y., Wang, H. f., Sun, H. f., et al. (2007). Biodistribution of pristine single-walled carbon nanotubes *in vivo*. *J. Phys. Chem. C* 111 (48), 17761–17764. doi:10.1021/jp070712c

Yang, Z., Zhang, Y., Yang, Y., Sun, L., Han, D., Li, H., et al. (2010). Pharmacological and toxicological target organelles and safe use of single-walled carbon nanotubes as drug carriers in treating Alzheimer disease. *Nanomedicine Nanotechnol. Biol. Med.* 6 (3), 427–441. doi:10.1016/j.nano.2009.11.007

Zhao, B., Hu, H., Yu, A., Perea, D., and Haddon, R. C. (2005). Synthesis and characterization of water soluble single-walled carbon nanotube graft copolymers. *J. Am. Chem. Soc.* 127 (22), 8197–8203. doi:10.1021/ja042924i

Zhu, Z. (2017). An overview of carbon nanotubes and graphene for biosensing applications. *Nano-Micro Lett.* 9 (3), 25. doi:10.1007/s40820-017-0128-6

Frontiers in Carbon

Explores the development, properties and application of carbon-based materials

A multidisciplinary journal focusing on scientific progress and the technological advances relating to carbon-based materials, from biotechnology to electronics, and modelling to nano-technology

Discover the latest Research Topics

See more →

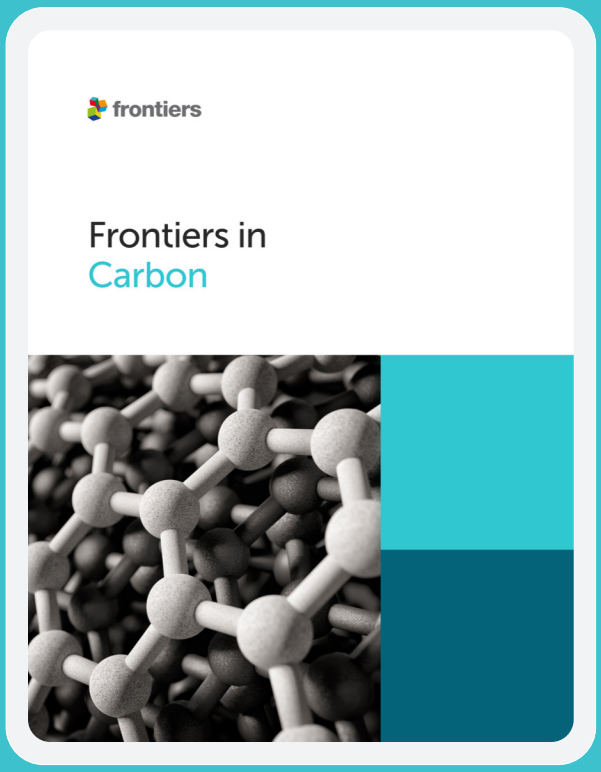

Frontiers

Avenue du Tribunal-Fédéral 34
1005 Lausanne, Switzerland
frontiersin.org

Contact us

+41 (0)21 510 17 00
frontiersin.org/about/contact